Disorder–Property Relationships in Magnetic and Pseudospin Framework Materials

Johnathan Bulled

Balliol College, Oxford

A thesis submitted to the University of Oxford

for the degree of Doctor of Philosophy

Supervisor: Prof. Andrew Goodwin

Inorganic Chemistry Laboratory

University of Oxford

Declaration

This dissertation is the result of my own original work, and where it draws on the work of others, this is acknowledged at appropriate points in the text. Some initial measurements, shown in Figures 3.1, 3.4, and 3.5 , were also originally presented in my undergraduate dissertation. The remainder of this dissertation has not previously been submitted for a degree at Oxford or any other institution.

Johnathan Bulled

Abstract

Framework materials are a diverse set of solids known for their mechanical flexibility, topological diversity, and crystallinity. The ordering temperature of magnetic spins in framework materials is low—typically around a few Kelvin. Analogues can be drawn between magnetic spins and structural 'pseudospin' degrees of freedom, for which ordering occurs at higher temperatures and shows complex interplay with vibrations. The degree and type of disorder in these magnetic and pseudospin have implications for exploitable properties.

In this thesis, I study the spin and pseudospin disorder in four framework materials—$NaMn(HCOO)_3$, $Tb_{1-x}Y_x(HCOO)_3$, $[C(NH_2)_3]Mn_{(1-x)}Fe_{2x/3}(HCOO)_3$, and $Cd(CN)_2$. I investigate the links between their disordered structures and properties—namely, the magnetocaloric effect, heat capacity, ferrimagnetism, and thermal expansion. The degree of disorder is examined and modelled with a range of experimental and theoretical techniques: neutron scattering, magnetometery, heat-capacity measurements, Monte Carlo, and harmonic lattice dynamics calculations. By describing the disordered structure of the system, I can elucidate the role of various structural elements and the mechanism by which they affect the property. In this way, the work sheds light on the kind of disordered structural motif which may be used to induce a certain property.

I show that $Na[Mn(HCOO)_3]$ exhibits three hallmarks of geometric frustration: (i) the suppression of its Néel temperature; (ii) strongly-correlated disorder over a large temperature range; and (iii) a magnetisation pseudo-plateau. The magnetic ground-state is governed by the interplay of geometric frustration and the dipolar interaction. I demonstrate that the resulting model: (i) accounts quantitatively for the magnetic susceptibility; (ii) correctly predicts neutron-scattering measurements over the temperature range; and (iii) can be used to rationalise the existence of the magnetisation pseudo-plateau. A characteristic magnetocaloric effect associated with this pseudo-plateau emerges. Using the theoretical background obtained for this system, the microscopic driving forces behind this effect are investigated.

Next, I study the nonmagnetic doping of terbium formate, revealing that quasi-one-dimensionality leads to a surprisingly sensitive thermodynamic response to doping. I use Monte Carlo and mean-field simulation to understand these effects from a theoretical standpoint, and heat capacity measurements—both theoretical and experimental—to confirm the importance of these effects. Since these results are for thermodynamic variables, they are applicable to a range of quasi–one–dimensional materials involving Ising pseudospins beyond the particular family studied here.

The series $[C(NH_2)_3]Mn_{(1-x)}[Fe_{2x/3}\square_{x/3}](HCOO)_3$ is investigated, in which the B–site of the perovskite structure is occupied by Mn^{2+}, Fe^{3+} and vacancies (denoted $\square$). Unlike the systems studied in the previous chapter, the distribution of these vacancies is not random, but rather highly correlated. An effect of this correlation is the onset of ferrimagnetic order at a critical percolation threshold $x = 0.6$, leading to a significant enhancement of the magnetic moment. I investigate the magnetic interactions present in the system using magnetometery. A Monte Carlo simulation is developed to describe the dual disorder of vacancies and spins based on a simpli-

fied anstaz of the Hamiltonian. Only at intermediate compositions—where atomic configurations are disordered ($0.6 < x < 1.2$)—are long-range magnetic order possible.

Finally, I investigate cadmium cyanide, which has the largest isotropic negative thermal expansion (NTE) of any material. Its performance is greater than that predicted by quantum mechanical simulations and the quasi-harmonic approximation. Recent interest the orientational cyanide pseudospins of the model comes from its mapping onto spin ice. First, at room temperature, I report variable pressure powder inelastic scattering measurements to ascertain the dependence of the lattice dynamics on pressure. This gives an estimate for the Grünisen parameter of the lowest frequency phonon branch.

I use a combination of inelastic neutron scattering (INS) and molecular dynamics simulation to understanding of the interplay between lattice dynamics and cyanide flipping dynamics. I have carried out INS as a function of temperature over the temperature range associated with cyanide order and find evidence for antipolar correlations over nanometer lengthscales, persisting over a large temperature range. A hybrid approach is taken to simulation, coupling an existing Monte Carlo simulation to a supercell lattice dynamics simulation within the harmonic approximation. This approach requires the fitting of a custom forcefield. The results demonstrate that the static structure of cadmium cyanide evolves with temperature below the ordering temperate T_{c} and that phonon localisation occurs just above the transition temperature. However, they are insufficient to explain the signatures of antipolar nanodomains seen experimentally. The results of the experiment and simulation are understood in the context of the large isotropic NTE seen for $T > T_{\mathrm{c}}$.

Acknowledgements

Foremost, I am enormously grateful to my supervisor Prof. Andrew Goodwin, for involving me in this project. This thesis could only be completed as a result of his faith, patience, and ever-present encouragement over the 6 years since we have been working together. I feel very lucky to have such a generous and inspiring supervisor, with an in-depth knowledge of food, science, and how to bring good people together.

On that, I would like to thank all the members of the Goodwin group over the time I have been here. Besides all the help and support, I am particularly grateful to: Arianna, for your constant humour and composure (?!), regardless of sleep; Ella, for your excellent taste in films, bikes, and walks; Nikolaj, for sharing your artistic eye for patterns; Emily, for the friendship and music the whole way; Tom, for always being up to chat and/or pop Menorca; John, for your remarkable cucumber-related culinary skills; Quentin, for your unstoppable comedy; Elodie, for always remembering to check in on me (and reliable reminders to back up my thesis); Phil, Harry, Chloe, Zoe and Emma, for the good times at the start of my DPhil; and all the Part IIs, for the energy and enthusiasm. Thank you to Ana for all your hard work on our behalf, what would we do without you?

I am enormously grateful to my examiners, Lucy Clark and Simon Clarke, for giving their time to understanding this thesis, their useful advice, and kind words.

This work would not be possible without the expertise, hard work, and patience of a multitude of collaborators: Ben Slater, Joe Paddison, Andrew Wildes, Elsa Lhotel, Breogán Pato-Doldán, L. Claudia Gómez-Aguirre, Mario Falsaperna, Paul Saines, Gavin Stenning, Hannah Boström, Jonas Bruckmoser, Alex Willis, Helen Walker and Ross Stewart. The specific nature of each contribution will be acknowledged at the opening of the chapters in which their contribution is presented. I would also like to thank Arianna Minelli, Thomas Nicolas, Artem Korshunov, Arkadiy Simonov, Richard Dixey, Quentin Gueroult and Ella Schmidt, for their work on collaborations which are not covered in the thesis. I have received generous advice from throughout the scientific community. In addition to the people already mentioned, I am especially grateful for conversations with Martin Dove, Arkadiy Simonov, Kieran Orr, Nicola Spalding, Alexei Bossak, Carl Romero, Tara Tosic, Jem Pitcairn, Matt Cliffe, Alexei Bosak, Mark Senn, Richard Cooper, Jamie Nielsen, Tom Fennel, Josh Hill, Mia Baise, and Siân Dutton.

The mistakes in this thesis are my own, and occur because I didn't follow advice and example of all the above people carefully enough.

Finally, I couldn't have got here without the constant support and compassion of too many people to mention here. Without the kindness, support, and welcome distractions of my family—Dougie, Laura, Jack, Chris, Ann, Lin, Frank, gran, mum, dad, and Sammy—and friends—in particular Ben, Joe, Holly, Asang, Casey, Conan, Adam, Liv, Zach, Alex, Eliza, Nicola, Raddon, Kai, Louie, Tom, Momo, Boris, Kumeren, and without a doubt, Maike—I really couldn't have written this thesis. Thank you all for your love and help these last years.

Publications

I include a list of my publications directly relevant to this thesis,

- C. S. Coates, M. Baise, J. M. Bulled, E. H. Wolpert, J. W. Makepeace, H. C. Walker, A. S. Gibbs, A. Dominic Fortes, B. Slater, A. L. Goodwin, "Structure and dynamics of the negative thermal expansion material $Cd(CN)_2$ under pressure" Submitted 2023, *arXiv:2302.09963*,
- J. M. Bulled, M. Falsaperna, A. L. Goodwin, and P. J. Saines, "Thermodynamic signatures of chain segmentation in dilute quasi-one dimensional Ising systems" Submitted 2023, *arXiv:2212.06752*,
- M. Falsaperna, J. M. Bulled, G. B. G. Stenning, A. L. Goodwin, and P. J. Saines, "Anomalous evolution of the magnetocaloric effect in dilute triangular Ising antiferromagnets $Tb_{1-x}Y_x$(HCO2)3", *Phys. Rev. Materials* **6**, 124410 (2022),
- J. M. Bulled, J. A. M. Paddison, A. Wildes, E. Lhotel, S. J. Cassidy, B. Pato-Doldán, L. C. Gómez-Aguirre, P. J. Saines, and A. L. Goodwin "Geometric Frustration on the Trillium Lattice in a Magnetic Metal-Organic Framework", *Phys. Rev. Lett.* **128**, 177201 (2022),

as well as some from projects which I will not detail in the text,

- E. M. Schmidt, J. M. Bulled, and A. L. Goodwin, "Efficient fitting of single-crystal diffuse scattering in interaction space: a mean-field approach" *IUCrJ* **9**, 21-30. (2022),
- E. M. Schmidt, S. Thomas, J. M. Bulled, A. Minelli and A. L. Goodwin, "Interplay of thermal diffuse scattering and correlated compositional disorder in KCl1–xBrx" *Acta Cryst. B* **78**, 385 (2022).

Abbreviations

CDW	charge density wave
COF	covalent organic framework
CSI	classical spin ice
CSL	classical spin liquid
CW	Curie–Weiss
DFT	density functional theory
FC	field-cooled
FF	force field
GULP	general utility lattice program
INS	inelastic neutron scattering
LRO	long-range order
MFT	mean-field theory
MOF	metal organic framework
nDOS	neutron-weighted density of states
nnHAF	nearest-neighbour Heisenberg antiferromagnet
nnHAF+D	nearest-neighbour Heisenberg antiferromagnet with dipolar interactions
PMN	lead manganese nickel oxide
PZT	lead zirconium tungstate
QSI	quantum spin ice
SCLD	supercell lattice dynamics
SQUID	superconducting quantum interference device
SSL	Shastry-Sutherland lattice
TEM	transition electron microscopy
TIA	triangular Ising antiferromagnet
UUD	up-up-down
VCA	virtual crystal approximation
ZFC	zero-field cooled

Contents

Chapter 1

Introduction

1.1 Framework Materials

1.1.1 Overview

Framework materials are a broad class of solids which can be conceptualised as largely consisting of nodes connected by linkers. The broadness of this definition makes this family more of a conceptual linking of various families of material: perovskites, cyanides, zeolites, metal organic frameworks (MOFs), covalent organic frameworks (COFs) and many besides. By varying the coordination number of the node and coordination geometry of the linker, this approach provides a systematic way to design specific network connectivities (in such materials, this is what we mean by 'topology') into materials [1–4]. There are many ways to understand this diversity of network geometries, many of them borrowing heavily from graph theory [5]. One analysis suggests that there are at least 6620 framework topologies realised in crystalline coordination polymers today [6]. Recent developments in machine learning are providing new ways to understand very high-dimensional space of possible topologies [7–10].

Because of the large number of variables, targeting a specific topology is a key challenge in framework materials. By systematically varying the node size and linker geometry, one can navigate the space of possible topologies. An example of this is found in the $AB(HCOO)_3$ ternary perovskites—which are central to this thesis. A geometric tolerance factor can be defined as

$$\alpha = (r_{\mathrm{A,eff.}} + r_{\mathrm{HCOO,eff.}})/(r_{\mathrm{B}} + r_{\mathrm{HCOO,eff.}}) \,, \tag{1.1}$$

depending on the relative sizes of the components [11]. A simple geometric argument

demonstrates how, when limited to atomic cations (A = Rb^+ or Cs^+, B = Mn^{2+}, Co^{2+} or Ni^{2+}), the value of this tolerance factor directs the formate perovskites to one of the three topologies shown in Fig. 1.1(a) [12]. A consequence of this change in topology is that the formate binding mode changes and the implications of this for magnetism are discussed in §3.1. An equally important way to target geometries in framework materials is by tuning the geometry of the linker. An extreme example is found on changing the linear 1,4-bdc linker of MOF-5 to the bent 1,3-bdc linker, the topology changes from a simple pcu topology to a complex, aperiodic 'TRUMOF' topology [13, 14].

Aside topological diversity, framework materials are varied because of the essentially inexhaustible range of nodes and particularly linkers available. It is very useful to relate framework materials with the same topology: the term isorecticular is borrowed from MOF chemistry [3]. The concept is illustrated for the simplest primitive

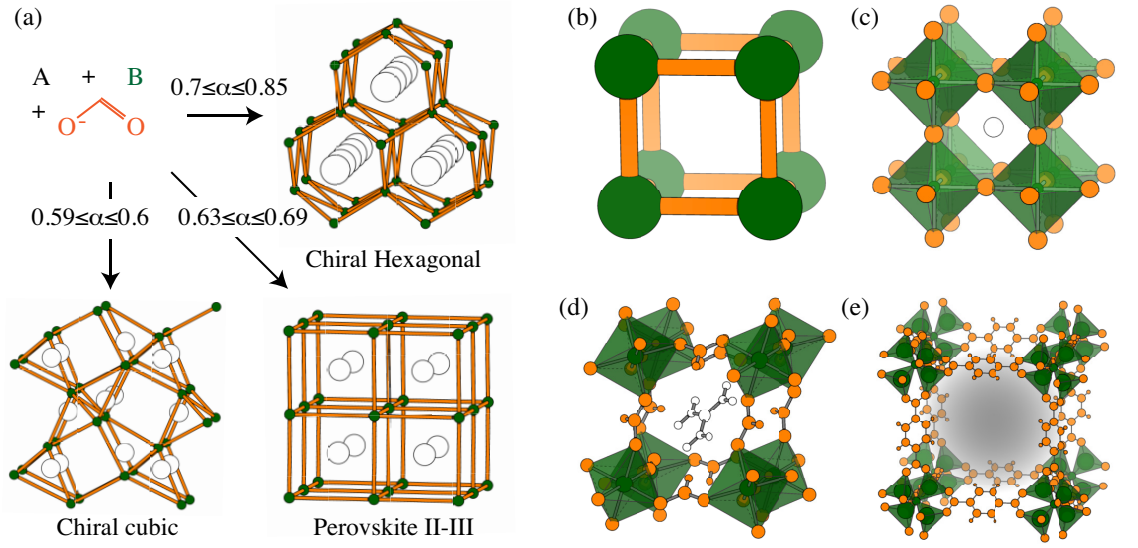

Figure 1.1: (a) Schematic showing the tolerance factor dependence on topology in $AB(HCOO)_3$ formates, based on the tolerance factor, α, described in Equation (1.1) [12]. (b—e) These framework structures all exhibit the pcu topology shown in (b), with nodes shown in green, linkers in orange, and atoms not part of the framework in white. (c) The inorganic perovskite structure, (d) a formate perovskite with Guanidinium on the A site and formate forming the linkers [15] (e) the MOF-5 structure, with the linker 1,4-benzendicarboxylic acid, nodes of [13].

cubic (pcu) topology in Figure 1.1. The simplest framework materials involve single atom nodes—such as metal cations—and single atom linkers—such as oxide anions [16]. The example shown in Figure 1.1(c) is the perovskite structure, where the B–site metal nodes are connected by oxide linkers whilst an atom sits on the A–site and does not participate in the framework. Substituting single atom linkers for molecules gives a class of material typically refereed to a coordination polymers [17]. The example of the hybrid perovskite [Gua]$Mn(HCOO)_3$ [Fig. 1.1(d)] sees oxide substituted for a formate anion and the A site cation for the organic guanadiumium [15]. This approach allows for the design of materials with much bigger pores: in MOF-5 the organic linker (1,4-benzendicarboxylic acid) and stable inorganic Zn_4O cluster allow for the large pore volume needed for gas absorption [13]. This system is really on the low end of size for MOF-linker size and the years since its publication have seen the reticulary approach extended to orders of magnitude larger structures by substituting for larger nodes and linkers [18]. Changing the size and chemistry of linkers across a series gives materials with predictably different properties. This approach allows the chemist to systematically explore compositional space and draw relationships between materials with very different compositions.

The final (optional) ingredients in framework materials are components which are not themselves part of the framework. These can be neutral or charged and may interact strongly or weakly with the underlying framework but do not form part of its backbone. Since these extra-framework atoms and molecules are not bonded to the framework, they are generally more mobile and free to rearrange. This is useful in the design of solid state cathode and electrolyte materials needed for battery technology, allowing charge carriers to move freely throughout the structure [19, 20]. In the case of barocaloric materials, extra-framework atoms can disorder and act as sinks for entropy [21–24]. The ability to host extra-framework atoms in the large pores of Zeolites and MOFs is crucial to their high capacity and selectivity as gas storage materials [25–27]. Although rarely strongly bonded, the extra-framework

components do apply forces to the framework, which depend on their shape, size, and chemical nature. In response to these forces, the ideal framework geometry distorts with a related symmetry that of the extra-framework component [28]. This is the origin of the octahedral tilting seen in [Gua]$Mn(HCOO)_3$ [Fig. 1.1(d)]. The framework rearranges to allow for optimal (in this case, hydrogen) bonding to the framework atoms [15]. Since these deformations depend on which modes of distortion have low energy cost, I explore this impact of this internal pressure further in the next section on flexibility.

In the following sections, I will investigate how the framework approach to understanding such materials has allowed chemists to understand their fundamental characteristics: flexibility and capability to host varying degrees of order. A central theme is understanding these materials in terms of nodes and linkers. The systems which concern the thesis, are on the simple end of the particularistic spectrum (small unit cells, short linkers, single metal clusters). By understanding the relationship between structural motifs, I hope that the concepts developed have broader applicability to more complicated MOFs, Zeolites, battery materials etc.

1.1.2 Flexibility

In the context of framework materials, flexibility refers to the ability of a material to respond structurally to a stimulus [29]. This stimulus can be remarkably diverse, with examples being guest change, temperature change, light irradiation and mechanical forces [17, 30–34]. Framework materials are commonly flexible as a result of their design: nodes can move at a fixed distance from one another through a continuum of geometries. This is the basis of the rigid unit mode (RUM) description of framework materials [Fig. 1.2(a–c)] which aims to characterise the types of motion which may be particularly flexible. This is done by representing framework nodes as rigid polyhedra and linkers with fixed geometries [35–37]. The figure highlights how by varying the nature of the linker from a single atom (e.g. the oxide in ZrW_2O_8 [38]) [Fig. 1.2(a)] to a linear linker (e.g. the cyanide in $Cd(CN)_2$ [39]) [Fig. 1.2(b–c)]

doubles the number of modes available for flexibility. Given that these descriptors only depend on the geometry of the framework, isorecticular mappings like those detailed in Figure 1.1 are useful in seeing links between the types of flexibility seen in framework materials and predicting the types of material that are likely to be flexible.

The mechanical flexibility of these materials is tied to their underlying framework topology. This type of flexibility, the response to hydrostatic pressure or uniaxial strain, is often extreme and unusual in framework materials. In the coordination polymer $Ag_3Co(CN)_6$, applying hydrostatic pressure leads to an expansion—positive linear compressibility—in the a and b direction but a very large contraction—negative linear compressibility (NLC)—in the c-direction [40]. The particular flexibility mode responsible for this involves the linker geometry flexing in order to shrink the volume of the structure as shown in Figure 1.2(d). This mode of flexibility is often referred to as a 'wine-rack' distortion [41], after its resemblance to the common office furniture, and theory shows that this can be seen a consequence of the wine-rack structural motif [42, 43]. But by understanding the underlying framework motif responsible for NLC in $Ag_3Co(CN)_6$, we can find other materials which display the same characteristic by virtue of similar topology. Amongst MOFs the MIL-53 family and MIL-47 both show wine-rack distortions because of their topology [43–45], the hybrid formate $[NH_4]Zn(HCOO)_3$ has a similar topology to $Ag_3Co(CN)_6$ and thus shows NLC [46]. Here, I highlight the wine-rack mode of distortion, but many other structural motifs exhibit their own characteristic flexibility. The perovskite tilts, the helical distortion in Selenium, Tellurium and $Zn[Au(CN)_2]_2$, are named examples [41, 47]. Indeed, the principle is more general: an understanding of the soft modes in a framework allows for the prediction of its mechanical properties. This is true whether the link is drawn through quantitative approaches—ab initio, via RUMs, or recently developments in machine learning [7, 10, 40, 42]—or by the recognition of structural motifs.

Flexibility is not only a response to mechanical stimulus but can come from components inside the framework itself. These internal forces arise from a mismatch between the extra-framework atoms or molecules and their ideal geometry, and this leads to different distortion modes depending type of mismatch. For the atomic extra-framework atoms of the perovskite structure (ideally in the cubic spacegroup $Pm\bar{3}m$), this mismatch is captured by Goldschmidt's geometric tolerance factor [48] and leads to tilts which preserve octahedral geometry [Fig. 1.2(a)] for some values of the factor. Tilts lower symmetry from the $Pm\bar{3}m$ perovskite aristotype in ways well described by group theory [49–51]. In the same way, symmetry lowering due to extra-framework atoms can be understood in coordination polymers like the molecular perovskites. However, the degrees of freedom which result from the 'unconventional tilts' [see Fig. 1.2(b–c)], non-spherical A-site cations, and Jahn-teller distortions make the picture more complex [28]. This approach is useful as it allows for the intentional breaking of inversion-symmetry in controlled ways, with applications in piezo- and ferroelectrics [52–54].

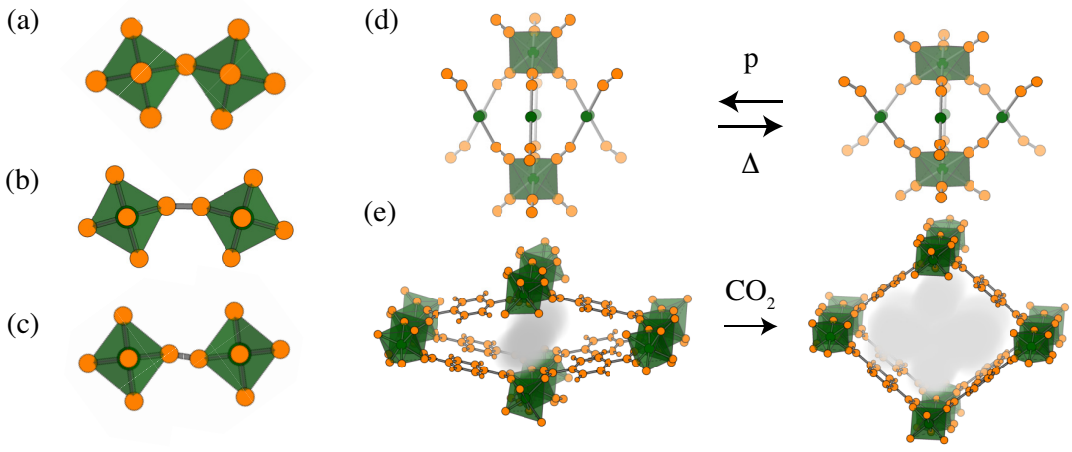

Figure 1.2: Some flexibility modes seen in framework materials. (a) The tilting mode exhibited by two connected octahedra. (b–c) The two modes exhibited when the single atom linker is replaced with a linear linker. (d) The structural distortion is exhibited by $Ag_3Co(CN)_6$ on heating and hydrostatic compression. (e) The 'breathing' mode shown by the MIL-53 family. X-ray scattering density due to gas molecules is represented by the translucent objects inside the pore.

In soft porous crystals, gas adsorption tends to activate the same soft modes which are activated by mechanical pressure or strain. At a certain gas pressure the framework collectively inflates via a 'breathing' mode [Fig. 1.2(e)], which shares the same flexibility mode as the wine-rack distortion discussed previously [31, 55, 56]. Again, this observation is not limited to the tilt and breathing modes discussed here. The 'interdigitation' of $[Cu_2(dhbc)_2(bpy)]_n$ and 'gate opening' motions of MOF-508 being other famous examples [57–60]. A good understanding of the soft modes present allows for predictions about the structural impact of extra-framework component inclusion.

Thermal expansion can be thought of as flexibility in response to temperature change. We have seen how framework materials are soft with well-defined modes, distortions which have a large susceptibility to pressure. This observation can be related to thermal expansion using the fluctuation-dissipation theorem, from which it follows that modes which are susceptible to pressure should accordingly show large fluctuations in volume, proportionally to temperature. Because the modes are often anharmonic, increased fluctuations in these modes should lead to large changes in their average value. So increases in temperature should lead to a large change in these mode coordinates. This is exactly what we see in Figure 1.2(d) for $Ag_3Co(CN)_6$, which shows colossal negative thermal expansion (NTE) along c while showing positive thermal expansion (PTE) along a and b, effectively reversing the action of pressure [40]. The same NTE/PTE behaviour is seen in the other wine rack structures such as $Pd(acac)_2$ and throughout the MIL-53 family [61–63], highlighting its origin as a framework effect.

Negative thermal expansion materials are of interest to the chemist primarily because of their use offsetting the PTE of most materials in composites [64]. State of the art materials can passively athermalize optics or provide ultra-stable struts for telescopes [64]. Broadly, there are two classes of NTE material: (i) those that work by exploiting a phase transition such as charge order or magnetic ordering and (ii)

the phonon-driven NTE materials such as the wine-rack systems discussed above. The first kind shows the largest magnitude of NTE, but because the excitations tend to be rather fermionic (once a charge transfer has happened no more entropy can be stored in the mode), this behaviour is confined to a relatively small temperature range around the phase transition [65]. Phonon excitations on the other hand are bosonic and so persist over a much larger temperature range [65]. While phonon-driven NTE tends to be a lot weaker than transition-driven NTE in hard materials, the extreme flexibility shown by framework materials can give them competitive values [39]. Taking into account both temperature range and magnitude, the NTE-capacity metric shows better values for many framework materials than transfer driven systems [65].

In practice, isotropic NTE of the kind seen in cubic materials is preferred to the anisotropic NTE discussed already in wine-rack-type systems, because it does not lead to strain degradation of materials [66]. The key flexibility motifs which drive NTE here are the tilts such as those shown in Figure 1.2(a–c). This observation is supported by the success of the RUM description in strong cubic NTE materials e.g. ZrW_2O_8 [38]. The presence of additional modes due to linear linkers highlighted in the figure explains the greater magnitude of NTE in MOF-5, $Zn(CN)_2$ and $Cd(CN)_2$ [39, 67], compared with single atom linker systems like ZrW_2O_8. An in-depth analysis of the theory of phonon driven NTE is given in Section 1.5.4.

1.1.3 Spin and Pseudospin (Dis)order

Framework materials are best known for their ability to crystallise into well ordered systems. It is becoming increasingly important to realise that even crystalline framework materials are in many cases inherently disordered, in ways that are sometimes beneficial (or at least important) to those materials' physical properties. In many cases this disorder is not just a result of a material's finite temperature but persists down to absolute zero. This was noted by Pauling for the hydrogen positions in water ice and topically for magnetic analogues of the problem (namely, the spin

ices), where the disorder emerges because the Hamiltonian does not have a unique ground-state [68, 69].

Perhaps the most obvious example of disordered in frameworks are the magnetic MOFs, where other than at very low temperatures, the magnetic moments (spins) are thermally disordered [70]. To a good first approximation [§1.2.1], we can understand these magnetic moments as vectors which reside on the metal nodes of the MOF [Fig. 1.3(a,d)].

Given the large amount of theoretical attention paid to magnetic materials, it makes sense to draw on this wealth of study to understand other degrees of freedom. As such pseudospins are defined as some degree of freedom which is analogous to a spin. Analogous to a Heisenberg spin [Fig. 1.3(d)], is (for instance) the orientation of a linker or guest molecule of a framework material, as illustrated for a diatomic molecule in Figure 1.3(e). When the disorder is discreet (as in the magnetic example shown in Fig. 1.3(a)), an Ising pseudospin should be used [Fig. 1.3(b)]. Examples of this orientational disorder are the disordered linker orientations of IrMOF-5, which can be directed by changing the solvent [71]. An equally important form of disor-

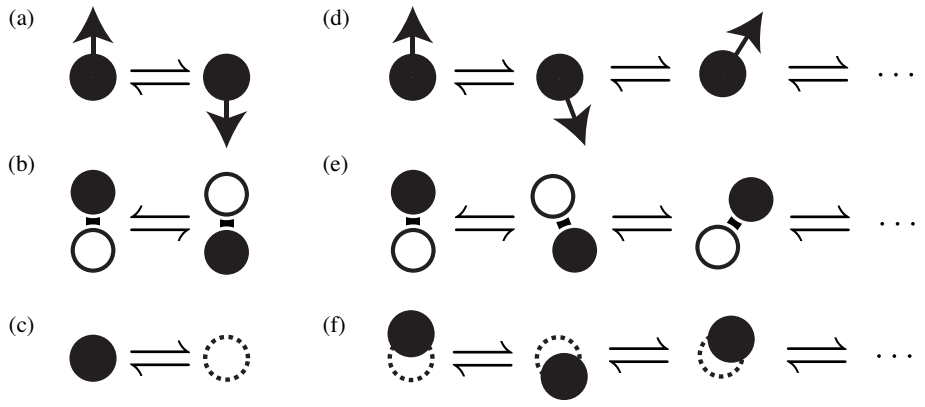

Figure 1.3: Schematic of types of spin and pseudospin disorder which concern this thesis, shown as equilibria between possible states. (a–c) Ising degrees of freedom have two discreet states while (d–f) continuous degrees of freedom can take a continuum of different occupations. The degrees of freedom shown are (a,d) magnetic spins shown in their vector representation, (b,e) the molecular orientations of a diatomic dipolar molecule, (c) site disorder with the two atoms shown as a black and white dot, (f) atomic displacements of an atom (black circle) with its average position shown with a dotted circle.

der which can be treated analogously is site (or occupational) disorder, where two substituents or one substituent and a vacancy jointly occupy one suite in a crystal structure [Fig. 1.3(c)]. This kind of disorder exists in mixed metal MOFs [72–75] and systems like UiO-66 and the Prussian Blues one where a node or linker is partially present [76, 77]. The final form of pseudospin disorder relevant this thesis is displacive disorder [Fig. 1.3(f)], where a single atom displaces from its central position. The theory of this disorder differs from that of Heisenberg spins and molecular orientation because the magnitude of the associated pseudospin can change.

It should be noted that nothing is really *gained* by labelling a degree of freedom as a pseudospin, it rather draws conceptual parallels and facilitates the application of theories developed in magnetic materials.

At sufficiently low temperatures, most of these forms of disorder become correlated. For example in the ferromagnetic MOF-505, this can be used to store magnetic polarisation [78]. The pseudospin analogue of this order (ferroelectricity) has applications in long-term data storage [79]. By understanding the structure and interactions in (pseudo)spin materials, we can govern their ferroic properties.

The entropy associated with both spin and pseudospin disorder is important for understanding the thermodynamic properties of these materials. For example in $[NPr_4]Mn(N(CN)_2)_3$, the pressure-dependant entropy associated with the disorder may promise effective barocaloric cooling [80], while the $Ln(HCOO)_3$ series promises effective magnetocaloric effects [81]. We will see in Section 1.2 that both amount of entropy available and presence of ferroicity at a given temperature are acutely dependant on the geometry of the lattice and the types of (pseudo)spins present. For this reason, a detailed understanding of spin and pseudospin physics is useful for designing new framework materials.

In Section 1.2, I will give an overview of the theory which describes magnetism before detailing in Section 1.4 the extension of these theories to pseudospin systems. I will make a distinction between two forms of disorder in the thesis, discrete and

continuous. The discrete degrees of freedom considered in the thesis take two values, which I will tend to refer to as 'spin-up' and 'spin-down' because the theory to describe these systems was in a large part developed for the field of magnetism, while the continuous ones take values which vary continuously. These variables include the Ising spins described of $Tb(HCOO)_3$, the orientational pseudospins in $Cd(CN)_2$ and the occupational pseudospins which are used do describe the solid solutions in Chapters 4 and 5. The continuous degrees of freedom described in this thesis include the Heisenberg spins residing on Fe^{3+} and Mn^{2+} ions in Chapters 3 and 5.

In this thesis, I will look in more detail at the implications of this magnetic and structural disorder for the properties of systems.

1.1.4 Systems of Interest

The four systems in which I will investigate these relationships have spin and/or pseudospin disorder. These systems were chosen because in each case, there was an important physical property which remained (at least) partially unexplained by an 'ordered' representation of their crystal structure.

I will give a brief overview here of what is known structurally about these systems. In the first system—$NaMn(HCOO)_3$—the geometry of the lattice predisposes its magnetism to disorder down to low temperatures. The second system is a solid solution $Tb_{1-x}Y_x(HCOO)_3$, where the impact of random doping with a nonmagnetic impurity leads to significant changes in magnetic properties. In another solid solution—$[Gua]Mn_{1-x}Fe_{2x/3}(HCOO)_3$—rather than random vacancy positions, there is crystallographic evidence of long-range chequerboard order of vacancies, driven by the 'anti-clustering' tendency of vacancies to avoid sitting on adjacent sites. The final results of this thesis are given about $Cd(CN)_2$, in which the antiferroelectric order of cyanide orientations evolves as a function of temperature.

$NaMn(HCOO)_3$

Sodium manganese(II) formate, $NaMn(HCOO)_3$, is a dense MOF, where magnetism arises from Mn^{2+} ($S = \frac{5}{2}$) ions. The system crystallises in the chiral cubic space group $P2_13$ and has a nearest neighbour Mn–Mn distance of $\sim$5.6 Å [Fig. 1.4(a)]. Formate ions connect neighbouring Mn^{2+} cations to give the Mn–O–C–O–Mn pathway that supports magnetic superexchange [85–88]. Bulk thermodynamic measurements have shown the system to exhibit no sign of magnetic ordering for $T > 2\,\mathrm{K}$, with magnetisation measurements indication antiferromagnetic coupling of the approximate strength $J \sim 1\,\mathrm{K}$ [89].

This system is of interest because of the trillium lattice on which Mn^{2+} sits [Fig. 1.4(b)]. The geometric frustration [§1.2.4] present makes the system liable to disorder, making it an important system for study. Despite the large number of topologies which may exhibit geometric frustration, much of the field has focused on the relatively small set of structure types that are common amongst ceramic materials; *e.g.*, the pyrochlore, triangular, kagome, and face-centred cubic nets. The study of frustration on less common lattices may therefore allow for the discovery of novel magnetic phases and their corresponding physics [90–92].

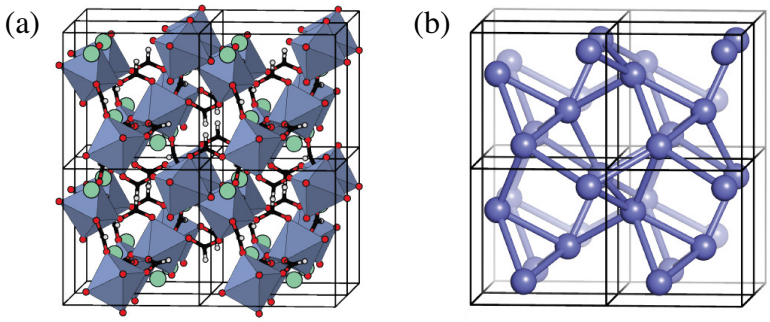

Figure 1.4: (a) The trillium lattice, shown here as a $2 \times 2 \times 2$ supercell of the corresponding cubic unit cell [82]. Each site has six neighbours, arranged at the vertices of a three-bladed propeller (*cf.* the β-Mn net [83]). (b) Representation of the crystal structure of $NaMn(HCOO)_3$; Na, C, H and O atoms shown as green, black, white and red spheres, respectively, and Mn coordination environments shown as filled polyhedra [84]. The Mn atoms decorate a trillium lattice.

$\mathbf{Tb_{1-x}Y_x(HCOO)_3}$

The $Ln(\mathrm{HCOO})_3$ coordination frameworks (Ln = Gd^{3+}, Tb^{3+}, Dy^{3+}, Ho^{3+}, Er^{3+}) have proven to be highly efficient magnetocalorics over a wide temperature range (2–20 K) [93]. While $Gd(HCOO)_3$ has the strongest performance at ultralow temperatures and high applied fields, it has been found that replacing Gd with Ising-like Tb and Ho leads to enhanced performance above 4 K in more modest applied fields of up to 2 T [93]. This behaviour can be seen as emerging from the crystal structure, in which metals sit close in one direction but further in the other [Fig. 1.5(a)], leading to low dimensionality (the consequences of which are discussed in Section 1.2.3) and the chains are arranged on a frustrated triangular lattice [Fig. 1.5(b)] (§1.2.4). My interest of this system follows our recent investigation into the consequences of doping $Tb(HCOO)_3$ with non-magnetic Y following our recent experimental study [94].

A recent investigation [Ref. 94] on the series $Tb_{1-x}Y_x(HCOO)_3$: $0 < x < 0.4$ demonstrated the formation of a solid solution is possible. Given this observation, the impact of this doping on material properties is of interest, particularly with the tuning of the strong magnetocaloric effect in the family. The effect of non-magnetic doping on magnetic properties is discussed in Section 1.2.5 and a mixed experimental

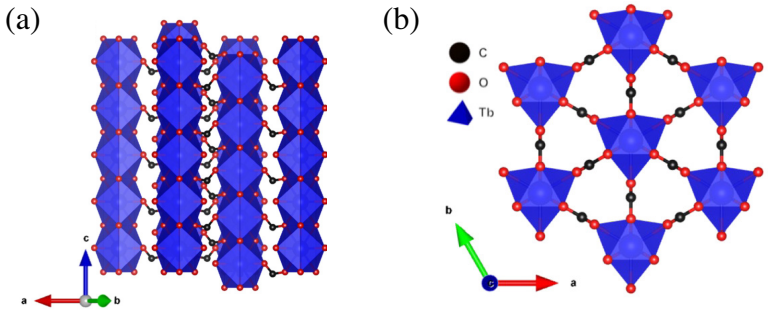

Figure 1.5: The crystal structure of $Tb(HCOO)_3$, shown in two projections. Terbium polyhedra are edge sharing down chains, mediated by strong superexchange. In turn, chains are linked via through the formate superexchange bridge.

and my investigation into the properties can be found in Chapter 4.

$\mathbf{[Gua]Mn_{1-x}Fe_{2x/3}(HCOO)_3}$

The formate perovskites $AB(HCOO)_3$ hold particular currency as candidate multiferroic materials which simultaneously host magnetic and electric polarisation [95–97] for applications in sensors and information storage devices [98, 99]. Effective design of multiferroics in conventional inorganic perovskites is difficult because of the incompatible electronic structure design criteria for polarisation (closed-shell species) and magnetism (open-shell species) [100]. But in hybrid perovskites, there are more routes to generating polarisation; for example, the exploitation of polar A-site cations [95], and a broad range of hybrid improper ferroelectric design strategies based on combining a diverse set of degrees of freedom [28, 101, 102]. Less clear, however, is how to generate hybrid perovskites with bulk magnetic polarisation: nearly all hybrid perovskites are canted antiferromagnets with only weak moments that result from antisymmetric interactions [54, 101, 103]. An obvious challenge is therefore how to develop new routes for enhance magnetisation in hybrid perovskites.

It is in this context that I turn to the solid solution $[Gua]Mn_{1-x}Fe_{2x/3}]\square_{x/3}(HCOO)_3$. In this system, the B–site of the perovskite structure is jointly occupied by Mn^{2+}, Fe^{3+}, and vacancies (denoted $\square$) [104]. Given that vacant sites are deficient in positive charge, we might expect them to avoid sitting adjacent. Evidence for this 'anticlustering' tendency comes on the observation of long-range chequerboard order at a certain concentration threshold [104]. While these cations both have the same electron configuration and are therefore similar magnetically, the imbalance of magnetic moment between metal sites and vacancies may have interesting implications for the magnetism. These implications are investigated in Chapter 5.

$\mathbf{Cd(CN)_2}$

Cubic cadmium(II) cyanide is amongst the most important isotropic negative thermal expansion (NTE) materials (its volumetric expansion coefficient $-61.2\,\mathrm{MK}^{-1}$) [105], with behaviour more than twice as extreme as that of better known systems

such as ZrW_2O_8 ($\alpha_V \simeq -27\,MK^{-1}$) [106]. The high temperature phase crystallises in cubic spacegroup $Pn\bar{3}m$, showing a transition to a low temperature phase which proved impossible to characterise via single crystal X-ray scattering due to problems with twinning [1, 107]. Studies of the phonon spectra of related materials (ZrW_2O_8, $Zn(CN)_2$ etc.) have been essential in understanding the relationship between NTE and low energy phonons. In contrast, relatively little is understood about lattice dynamics of $Cd(CN)_2$. The value of the expansion coefficient for a cubic model of $Cd(CN)_2$ that can be calculated by DFT for fixed cyanide order ($-31.3\,MK^{-1}$). This number is consistent with other DFT studies on NTE in $Cd(CN)_2$, all of which neglect the correlated cyanide orientations [108, 109]. While being a large and negative value, this is considerably more moderate than that measured experimentally [110]. Could the dynamics of the cyanide dipole, which are neglected in these calculations, account for this difference?

The models up to this point have neglected to consider this effect, which can be conceptualised as an orientational pseudospin either oriented in or out of the $Cd(CN)_4$ tetrahedra. As such, the pyrochlore geometry of the pseudospin lattice [Fig. 1.6(a)], maps onto the spin ice Hamiltonian of, for example, Ref. 111 [§1.2.4]. Evidence for preferential pseudospin ordering first came from NMR studies of the

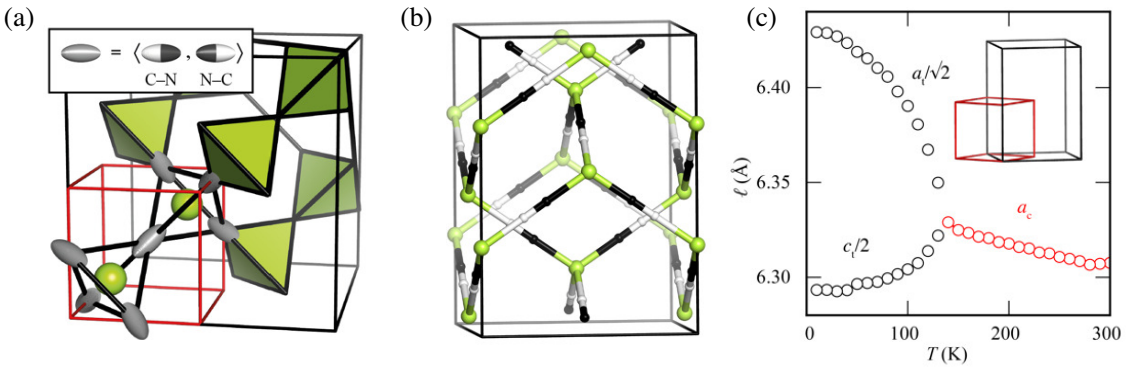

Figure 1.6: (a) The high temperature crystal structure of $Cd(CN)_2$ in which cyanide pseudospins are disordered between the two orientations shown. (b) The high temperature crystal structure of $Cd(CN)_2$. (c) Obtained by Coates and coworkers from Rietveld analysis of powder neutron scattering, Ref. 65.

system, which found that the percentage of Cd environments with the decorations CdC_4 : CdC_3N : CdC_2N_2 : $CdCN_3$: CdN_4 was 2 : 22.8 : 50.3 : 23.2 : 1.7 compared to the random statistical distribution which would be 6.25 : 25 : 37.5 : 25 : 6.25 [112]. The energetic preference for ice-like coordination is supported by ab initio calculations. Further evidence for the preference of ice rules came from X-ray scattering experiments. A characteristic aspherical electron density distribution around the Cd position indicated collective distortions, consistent with the local $O_h \rightarrow C_{2v}$ distortion expected for the CdC_2N_2 environment [113]. In addition diffuse X-ray scattering showed similarities with theoretical predictions for ice rules [113]. The energy integration in these X-ray scattering experiments makes it impossible to know if the scattering arises from static CN correlations or lattice dynamics, which give rise to NTE. Studies of $Cd(CN)_2$ under X-rays are also plagued by extreme radiation damage, which even effects the degree of negative thermal expansion seen [114].

The most definitive evidence for ice-like behaviour in $Cd(CN)_2$ came after the synthesis of an isotopically enriched $^{116}Cd(CN)_2$ sample suitable for neutron experiments. Using this sample Coates and co-workers [65] found that on cooling, $Cd(CN)_2$ undergoes a phase transition (at $T \sim 140\,\mathrm{K}$) to a pseudospin ordered $I4_1/amd$ phase, as predicted by theoretical models (§1.4.3). The impact of cyanide order on the lattice dynamics which drive NTE has not been investigated to date.

1.2 Magnetism

In this section, I introduce the theory of magnetic order in the solid state, which is the root of the models of the thesis. I will derive some key results, crucially pertaining to the relationship between the measurable quantities obtained from magnetometery, specific heat, and neutron scattering and the behaviour of the magnetic models. I will investigate the role of the magnetic lattice geometry on the models and end by introducing a mapping between the spins discussed earlier and pseudospins, which behave similarly and are of interest to the thesis. My treatment follows standard

texts on magnetism [69, 115].

1.2.1 Non-Interacting Ions

In classical mechanics, angular momentum is a continuous variable with three components. The uncertainty principle of quantum mechanics implies that we can only simultaneously know pairs of operator which commute. A useful choice are the observables the magnitude squared $\hat{S}^2$ and projection $\hat{S}_z$ of the spin. Now the angular momentum of the electron is dictated by just two quantum numbers $S = \frac{1}{2}$ and S_z—subject to the quantisation $S_z = -\frac{1}{2}, \frac{1}{2}$. The quantum numbers relate to the observables by their eigenvalue equations

$$\hat{S}^2 |\psi\rangle = S(S+1) |\psi\rangle \tag{1.2}$$

$$\hat{S}_z |\psi\rangle = S_z |\psi\rangle \tag{1.3}$$

Electrons are fermions with the specific value $S = \frac{1}{2}$ so S_z can take two values, $S_z = +\frac{1}{2}$ (spin up) and $S_z = -\frac{1}{2}$ (spin down).

The magnetisation of isolated spins, $M_z = g\mu_0\mu_B S_z$, fluctuates in the absence of field. The relevant casting of the fluctuation dissipation theorem is

$$\chi_0 = \frac{\mu_0}{N k_\mathrm{B} T} \left(\langle M_z^2 \rangle - \langle M_z \rangle^2 \right). \tag{1.4}$$

This explains the $\chi_0 = C/T$ dependence which can be measured by applying a magnetic field and measuring the response. Under the directional averaging that occurs in practice, the Curie constant

$$C = \frac{\mu_0 (g\mu_\mathrm{B})^2 S(S+1)}{3k_\mathrm{B}}, \tag{1.5}$$

is an experimental measure of the quantum number S.

In systems which have two coupled spins, the spin operators of the electrons couple additively ($\hat{\mathbf{S}} = \hat{\mathbf{S}}_1 + \hat{\mathbf{S}}_2$) but the total spin quantum number takes a value which

must sit in the Clebsch-Gordan series $S = |S_1 - S_2|, \ldots, (S_1 + S_2 - 1), (S_1 + S_2)$ with $S_z = -S, \ldots, (S-1), S$. An additional constraint applies to identical particles which ensures the total wavefunction is antisymmetric. Take the two electrons of helium, where the series reduces to $S = 0, 1$. A consequence is Pauli's exclusion principle which stops electrons sharing the same state. Accordingly, helium's electrons must have opposing spins, giving $S = 0$ as the only possibility unless another angular momentum is introduced.

We have been neglecting the orbital angular momentum of electrons which arises because they are circulating around the nucleus. The same equations apply, with L substituting for S and $g_{\mathrm{L}} \simeq 1$ for $g_{\mathrm{S}} \simeq 2$. Within the L-S coupling scheme, total spin angular momentum and total orbital angular momentum couple to make total angular momentum, $\hat{\mathbf{J}} = \hat{\mathbf{S}} + \hat{\mathbf{L}}$. Their quantum numbers combine with another Clebsch-Gordan series $J = |S - L|, \ldots, (S + L - 1), (S + L)$. Hund's rules are a good predictor of which state will be lowest in energy, to be obeyed with decreasing importance: (i) maximise $2S + 1$ (ii) maximise L (iii) if the outer shell is more than half full, maximise J, else minimise J. Hund's first rule is accurate everywhere in the periodic table and (ii—iii) apply only in the rare earths. Anticipating §3 and §5 which use Mn^{2+} and Fe^{3+} rule (i) tells us the ground state must be $J = \frac{5}{2}$, $S = \frac{5}{2}$, $L = 0$. Anticipating §4, for Tb^{3+} we must use all three rules to derive $J = 6$, $S = 3$, $L = 3$ state. Under this treatment the Lande-g factor changes too according to

$$g_J = 1 + \frac{J(J+1) + S(S+1) - L(L+1)}{2J(J+1)}, \tag{1.6}$$

which gives $g_J = 1.5$ for Tb^{3+}.

Crystal Field Effects

So far we have been exploiting the spherical symmetry of isolated ions. In real crystals, the local environment of the magnetic ion breaks this symmetry, leading to crystal-field splitting. However, states with orbital angular momentum $L = 0$ have

symmetric spin distributions which means that they feel all of these charges the same. Consequently, spin-only ions like Mn^{2+} and Fe^{3+} have very limited (and not first order) crystal field effects. Tb^{3+} on the other hand does have an asymmetric angular momentum (since $L = 3$) so in $Tb(HCOO)_3$, the reduction in symmetry breaks the degeneracy of the $J(J+1) = 13$ states. The effect is that instead of the 13 degenerate states expected for the gas phase there are only two, spin-up and spin-down [116]. This has an impact on the maximum magnetocaloric entropy recoverable from Tb^{3+} compounds. Describing this effect requires a complex description of the atomic environment and often requires experimental measurements to know precisely. Theory can get some way to predicting these levels but usually crystal field experiments or NMR experiments are required [117, 118].

The Vector Model of Spins

For systems with large orbital momentum quantum number, it is common to approximate total magnetic moments as three component vectors of length $\sqrt{J(J+1)}$. As $J \to \infty$ magnetic states become closer and closer together until quantisation is no longer important: the difference between saturation ($\propto J$) and fluctuational ($\propto \sqrt{J(J+1)}$) measurements of the magnetic moment evaporates and this approximation becomes exact. The strength of any model comes from its predictive and illustrative power. Although the vector model is not as accurate as a full quantum-mechanical model of magnetism, its easier to treat mathematically and (more importantly) far easier to comprehend.

Rather confusingly, in this model the angular momentum vectors are usually called spins and denoted $\mathbf{S}$, despite in general containing some orbital component. From this point forward I will follow this convention, referring to atomic magnetic moments in general as spins. Anticipating §1.2.2, it will be important to cease using J to represent angular momentum altogether since this term will be used for interactions.

The vector representation gives a useful and common way to approximate the

crystal field identified at the end of the last section with a single parameter. For ions with the appropriate axis of symmetry oriented along $\hat{\mathbf{z}}$, the crystal field effects can be approximated by the single-ion Hamiltonian,

$$\mathcal{H}_{\mathrm{SI}} = -\Delta \sum_i \left(\mathbf{S}_i \cdot \hat{\mathbf{z}}\right)^2 \tag{1.7}$$

In the absence of field ($\mathbf{H}$=0) this Hamiltonian orders in two distinct ways, depending on the sign of Δ, the crystal field splitting parameter. A positive value corresponds to an 'easy–plane' anisotropy and a negative value to 'easy-axis'. In the limit that $\Delta \ll k_{\mathrm{B}}T$, spins are constrained to lie either in the plane in the first case or up/down the easy axis in the second. These are referred to as the XY and Ising models, respectively.

The value of the constant Δ depends on the type of magnetic atom and the local environment. The best fit of this value can be fitted to a crystal field model [119] but like many of the constants I will discuss in this section, it is more commonly derived semi-empirically, by fitting it as a parameter to magnetisation, heat capacity or neutron scattering data [90, 120, 121].

1.2.2 Magnetic Interactions and Conventional Order

The Lattice

In extended solids, spins are not isolated and when they are brought into proximity they interact. All of the interactions that I will discuss in this thesis are pairwise. Nevertheless, the presence of this interaction nearly always leads to a single ground state configuration. The ground state and behaviour at finite temperature are dictated by the interactions present and the lattice on which they operate.

At this stage it is therefore necessary to place spins in the wider solid. In general, magnetism can exist in topologically disordered systems (e.g. amorphous magnets) [122]. This thesis is concerned with systems where the spins sit on an underlying lattice, with a repeated unit cell. Throughout the thesis, I will use the following

conventions to describe the structure of the crystal: the axes of the unit cell are defined by basis vectors **a**, **b** and **c**. Each spin has the position $\mathbf{r}_\sigma$ within the unit cell. I will assume throughout that this position does not vary with magnetic order so the origin of the unit cell can be found at $\mathbf{R} = t_1\mathbf{a} + t_2\mathbf{b} + t_3\mathbf{c} : t_1, t_2, t_3 \in \mathbb{Z}$. I will use this vector $\mathbf{R}$ to refer to an arbitrary unit cell in the crystal. Each spin j in the crystal can be found by its unit cell and site index: $\mathbf{r}_j = \mathbf{R} + \mathbf{r}_\sigma$. The importance of the geometry of this underlying lattice of spins $\{\mathbf{r}_j\}$ is a central concern of this thesis.

This magnetic ordering will require often a larger unit cell than that of the parent structure. This is simplified in the **k**-vector formalism, we can write the σth spin in unit cell with origin at vector $\mathbf{R}$ as a sum over ordering vectors **k** with corresponding components $\boldsymbol{\Psi}_\sigma(\mathbf{k})$:

$$\mathbf{S}_\sigma(\mathbf{R}) = \sum_{\mathbf{k}} \sum_{\mathbf{R}} \boldsymbol{\Psi}_\sigma(\mathbf{k}) \exp 2\pi \mathrm{i} \mathbf{k} \cdot \mathbf{R}. \tag{1.8}$$

While many 'incommensurate' structures with irrational **k**-vectors exist, this thesis is only concerned with structures where **k** can be expressed as a vector of fractions and therefore the supercell is finite. This formalism allows the amount of information needed to describe magnetic structures to be greatly reduced. Usually only a handful of **k**-vectors are required to fully describe a magnetic structure. The amount of information required can be compressed even further when considering the magnetic symmetry [123]. Note that the net magnetisation is reproduced by

$$\mathbf{M} = \sum_{\sigma} \boldsymbol{\Psi}_\sigma(0), \tag{1.9}$$

so is related to magnetic structures with $\mathbf{k} = 0$.

Interactions and Order

For a simple square lattice, some important examples of ordered states are shown in Figure 1.7. Despite all sitting on the same underlying lattice, by tuning the type

of atom sat on the lattice, therefore its magnetic moment and interactions, one can navigate through various structures. These canonical magnetically ordered states—ferromagnets, antiferromagnets, ferrimagnets and canted antiferromagnets—are central to the study of magnetic solids. The figure shows why some of these structures have residual magnetisation, allowing for information storage. In this section, we will discuss the interactions which lead to them.

This thesis is concerned with insulating systems, where the atomic orbitals hosting magnetic moments do not come into close enough contact to directly overlap. This contrasts with metals, where electrons tend to exist in delocalised states and interactions are mediated by direct exchange (e.g. RKKY interaction [115, 124–126]). Instead, in insulators such as the transition metal oxides, indirect exchange is mediated via the non-magnetic atom, such as oxide. The filled orbitals of the oxide mix with the partially filled orbitals on either side leading to exchange interactions along the M–O–M pathway whose strength and sign is dictated by an orbital overlap integral called the 'hopping integral'. The dependence of this interaction on ligand orientation and type, as well as the electron configuration of the metal, means that I will delay its discussion until Section 3.1, when I have introduced the particular systems with which we are concerned. At this stage, it will suffice us to have a good effective description of these interactions, which are usually represented as symmetric and antisymmetric exchange terms.

Symmetric (or Heisenberg) exchange tends to be the leading term magnetic models and has a relatively simple form,

$$\mathcal{H}_{\text{sym}} = J \sum_{\langle i,j \rangle} \mathbf{S}_i \cdot \mathbf{S}_j, \tag{1.10}$$

where the sum over $\langle i, j \rangle$ means a sum over metal ions connected by a superexchange bridge. In perturbation theory, it can be thought of as an interaction between the ground-states of the metals and the exited state of the linking atom. This equation is isotropic, meaning that it does not depend on the orientation of the crystallite.

The groundstate has a trivial degeneracy involving the collective rotation of all spins (a Goldstone mode) [127].

The ground-state of this model on a square lattice is shown in Figure 1.7(a–c). For $J < 0$, spins are encouraged to point in the same direction so the 'ferromagnetic' ground state hosts a large magnetisation. By contrast, for $J > 0$ the interaction favours spins aligned antiparallel, leading to the antiferroelectric structure [Fig. 1.7(b)] with each sublattice exactly cancelling out the other. This results in zero residual magnetisation. However, if one decreases the size of the magnetisation on one sublattice compared to the other, this balance is lost. Figure 1.7(c) demonstrates the residual magnetisation which emerges from this 'ferrimagnetic' structure. An important example of this occurs in the spinels, e.g. Fe_3O_4 where the Fe^{2+} and Fe^{3+} occupy alternating sublattices but have different moments sizes due to their differing electron configurations. I will discuss another approach to 'percolation induced' ferrimagnetism by doping with non-magnetic ions in §5.1.1.

Asymmetric exchange—or the Dzyaloshinsky-Moriya (DM) interaction—arises due to an interaction between the ground state of one ion and the exited state of the other, mediated by the bridging atom. As such, this term is typically weaker

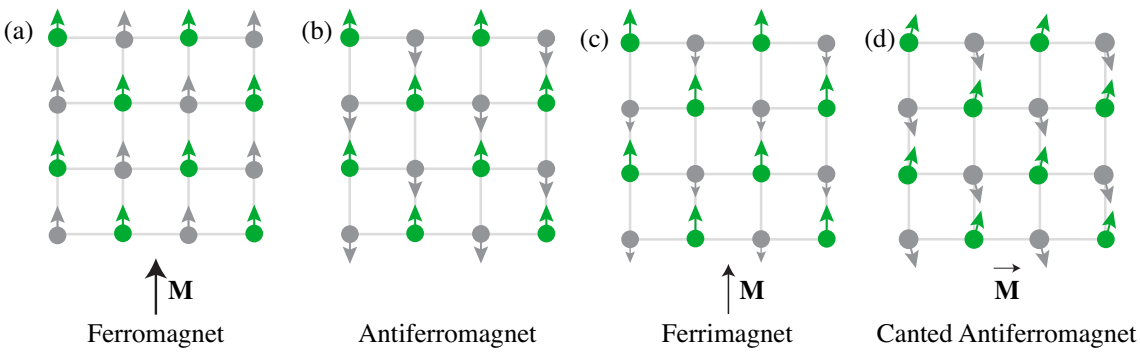

Figure 1.7: Schematic of common ordered magnetic structures expected for different interactions on a square lattice: (a) Ferromagnet (b) Antiferromagnet (c) Ferrimagnet (d) Canted Antiferromagnet. Structures (a), (c), and (d) all have a residual magnetisation shown in black.

than the direct exchange term. It takes the form

$$\mathcal{H}_{\text{asym}} = \sum_{\langle i,j \rangle} \mathbf{D}_{ij} \cdot (\mathbf{S}_i \times \mathbf{S}_j) \,, \tag{1.11}$$

and is parametrised by the vector $\mathbf{D}$, which depends on the metal–ligand–metal geometry. The symmetry dictates the form this vector takes. For example, if a centre of inversion lies between the two metal ions, this vector is necessarily zero.

Systems involving antiferromagnetic direct exchange and weaker DM interaction are common in nature (α-Fe_2O_3, $MnCO_3$, $CoCO_3$). The competition of these terms in such systems leads the spin canted groundstate shown in Figure 1.7(d), where a slight rotation of the moments allows for a small residual magnetisation. The resulting structures are termed 'weak-ferromagnets' because the size of the magnetisation is usually much smaller than that arising from the other two mechanisms mentioned.

All spins interact via the dipole-dipole interaction, which acts over pairs of spins. It is not mediated by any connection so is sometimes called 'through-space coupling'. It takes the form

$$\mathcal{H}_{\text{dip}} = D \sum_{i>j} \frac{\mathbf{S}_i \cdot \mathbf{S}_j + 3(\mathbf{S}_i \cdot \hat{\mathbf{r}}_{ij})(\mathbf{S}_j \cdot \hat{\mathbf{r}}_{ij})}{(r_{ij}/r_1)^3}, \tag{1.12}$$

whose strength D is given by

$$D = \frac{\mu_0 (g_J \mu_{\text{B}})^2}{4\pi r_1^3}, \tag{1.13}$$

where r_1 represents the nearest neighbour separation. The expression depends on the relative orientation of the spins and also interatomic vector. For this reason, the interaction is anisotropic (c.f. symmetric exchange), depending on the orientation of the bond relative to the spins. The equation has an identical form to a electrostatic dipolar interaction.

By taking a mixture of various Hamiltonians $\mathcal{H} = \mathcal{H}_{\text{S.I}} + \mathcal{H}_{\text{sym}} + \mathcal{H}_{\text{asym}} + H_{\text{asym}} +$

..., one can create a magnetic model and in this way try to explain the low temperature structure of the system.

Predicting magnetic entropy changes, heat capacity and ferromagnetic properties require a good description of the disorder present in a magnetic system. At high temperatures, interactions are thermally averaged and systems behave like the isolated ions described in §1.2.1. At the lowest temperatures, the structure of the system is typically ordered and acutely dependant on the lattice and interactions.

Field Induced Transitions

In order to understand the interaction of magnetic models with an external field $\mathbf{H}$, one must introduce the Zeeman interaction to the Hamiltonian:

$$\mathcal{H}_{\text{Zeeman}} = \mu_0 \mathbf{H} \cdot \sum_i \mathbf{S}_i. \tag{1.14}$$

Microscopically, this arises because of the splitting of energy levels by the external field. Macroscopically, the minimisation of this term explains the tendency of all magnetic materials (most importantly, ferromagnets) to align with a magnetic field. When the applied field is small, the effect can be considered perturbatively. In this way, we can arrive at the low-field experimental approaches discussed in Section 2.2.1. When a larger field is applied, it may significantly alter the ground state of the Hamiltonian. Where this occurs discontinuously, we have a field induced transition.

The combination $\mathcal{H} = \mathcal{H}_{\text{S.I.}} + \mathcal{H}_{\text{sym}} + \mathcal{H}_{\text{Zeeman}}$ helps explain the 'spin flop' transition seen in some anisotropic systems. The application of field leads to a switch between two types of behaviour [Fig. 1.8(a,b)], alignment along the easy axis when $|\Delta| > \mu_0|H|$, and alignment along the field orientation when $|\Delta| < \mu_0|H|$. At the field value at which this switch occurs, both states are degenerate so the fluctuations are high. This leads to a jump in the magnetisation $\mathbf{M}(\mathbf{H}) = 1/N \sum_j \mathbf{S}_j$ for certain field orientations, and a corresponding sharp peak in the susceptibility.

However when we measure a polycrystaline sample we are measuring $M(H)$ not $\mathbf{M}(\mathbf{H})$. This is because each of the crystallites contributes to the signal and must be orientationally averaged:

$$M(H) = \frac{1}{4\pi}\int_0^{\pi}\int_0^{2\pi} \left|\mathbf{M}\begin{pmatrix} H\sin\theta\cos\phi \\ H\sin\theta\sin\phi \\ H\cos\theta \end{pmatrix}\right| \sin\theta d\theta d\varphi. \tag{1.15}$$

This spike in the susceptibility expected in a single crystal sample is therefore smoothed out to the behaviour seen in Figure 1.8(c) [128].

The position of this maximum captures information about the relative strength of these terms and thus gives an experimental determination of their relative strength [129]. This one example highlights the usefulness of modelling many magnetic systems: if one can define a Hamiltonian which captures the important behaviour of a system for some values of its parameters, comparison to experiment will allow for direct determination of these parameters.

Note on units

Up to this point, we have taken $\mathbf{S}$ to represent a vector of length $\sqrt{S(S+1)}$ (where S represents the total angular momentum quantum number). In the literature, it is

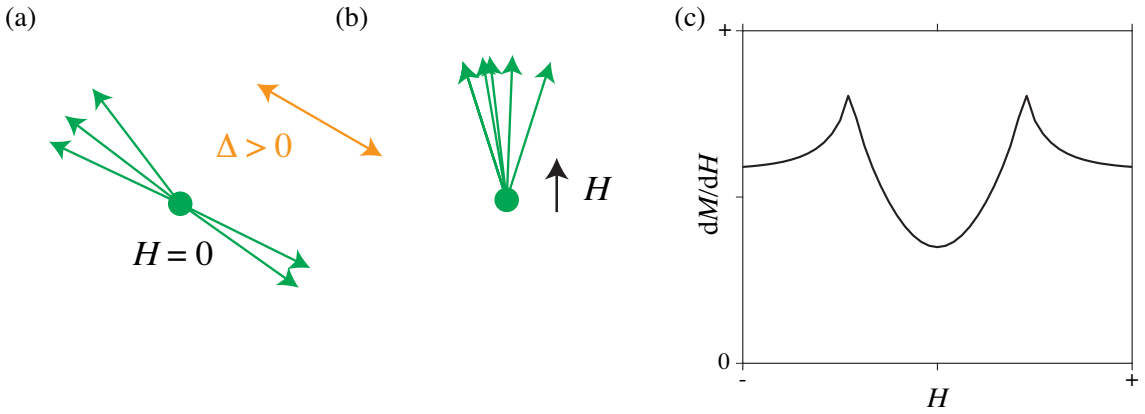

Figure 1.8: Schematic on the spin flop transition and its signature. (a) At low field, magnetic moments (green) tend to be aligned along the east axis (shown in orange). (b) Once field is applied, there is a threshold after which moments tend to be aligned along the direction of the field. (c) The signature of this transition in the polycrystalline is somewhat broad because of an average over crystallite orientations.

more common to define this as a vector of unit length. To do this we must rescale the coupling constants. The convention I will follow in this thesis is to give coupling constants not in units of energy, but of temperature, subsuming $1/k_{\mathrm{B}}$ so that the Hamiltonians of Equations (1.7), (1.10), (1.11), and (1.12) give the energy in units of temperature. In this way we must rewrite the dipolar constant,

$$D = \frac{\mu_0 (g\mu_{\mathrm{B}})^2 S(S+1)}{4\pi r_1^3 k_{\mathrm{B}}}, \tag{1.16}$$

and rescale the parameters Δ, J and $\mathbf{D}$ by a factor $S(S+1)/k_{\mathrm{B}}$. In this way we can compare systems with different magnetic ions, and in due course extend these physics to pseudospin systems.

2D Ising model

The 2D Ising model is the simplest model which displays long-range order of the kind seen in most magnetic systems. (The complications which make the simpler 1D Ising model an inappropriate place to start will be discussed in §1.2.3.) The ground state of the model is shown in Figure 1.7(a). The beauty of the model is that it captures the important characteristics—long range ordering and phase transitions—which are universal across solid state physics.

Onsager's solution for the free energy of the 2D Ising model to give the following formula for the free energy [130]:

$$F = \frac{-k_{\mathrm{B}}T}{2} \log\left(2\sinh\frac{2J}{k_{\mathrm{B}}T}\right) - \frac{k_{\mathrm{B}}T}{4\pi}\int_{-\pi}^{\pi} \cosh^{-1}\left(\cosh\frac{4J}{k_{\mathrm{B}}T}\coth\frac{4J}{k_{\mathrm{B}}T} - \cos q\right) \mathrm{d}q. \tag{1.17}$$

If this formula is differentiated twice with respect to temperature, the result is an expression for the heat capacity (which is plotted in Figure 1.9(a)), which possesses an important characteristic: a logarithmic singularity at a critical temperature $T_{\mathrm{C}} = 2J/\sinh^{-1}(1) \simeq 2.26J$. At this point the heat capacity diverges $C(T_{\mathrm{C}}) \to \infty$, implying that fluctuations in the energy are extensive.

In order to explain the significance of this transition temperature, it is useful to define the correlation function between spins separated by the vector $\mathbf{r}$

$$\langle S_i \cdot S_j \rangle (\mathbf{r}) = \frac{1}{N} \sum_{i,j} S_i S_j \delta(\mathbf{r} - (\mathbf{r}_i - \mathbf{r}_j)). \tag{1.18}$$

This function can be calculated from the model and when expressed as a product of determinants [131, 132] behaves in a markedly different way above and below T_C. Kadanoff found a more comprehensible expansion of these expressions, as

$$\langle S_i \cdot S_j \rangle ([r_x, 0]) = \left(1 - \text{cosech}^4 \frac{2J}{kT}\right)^{\frac{1}{4}} + \frac{A(T) e^{-\frac{r_x}{\xi_1(T)}}}{r_x^{\frac{1}{4}}} + \mathcal{O}\left(e^{-\frac{2r_x}{\xi_1(T)}}\right) \tag{1.19}$$

for $T < T_C$ and

$$\langle S_i \cdot S_j \rangle ([r_x, 0]) = \frac{B(T) e^{-\frac{r_x}{\xi_2(T)}}}{r_x^{\frac{1}{2}}} + \mathcal{O}\left(e^{-\frac{3r_x}{\xi_2(T)}}\right) \tag{1.20}$$

for $T > T_C$ [133]. Functions of this form are shown schematically in Figure 1.9(b). The key difference is in the limit that $R_x \to \infty$, where the correlation function

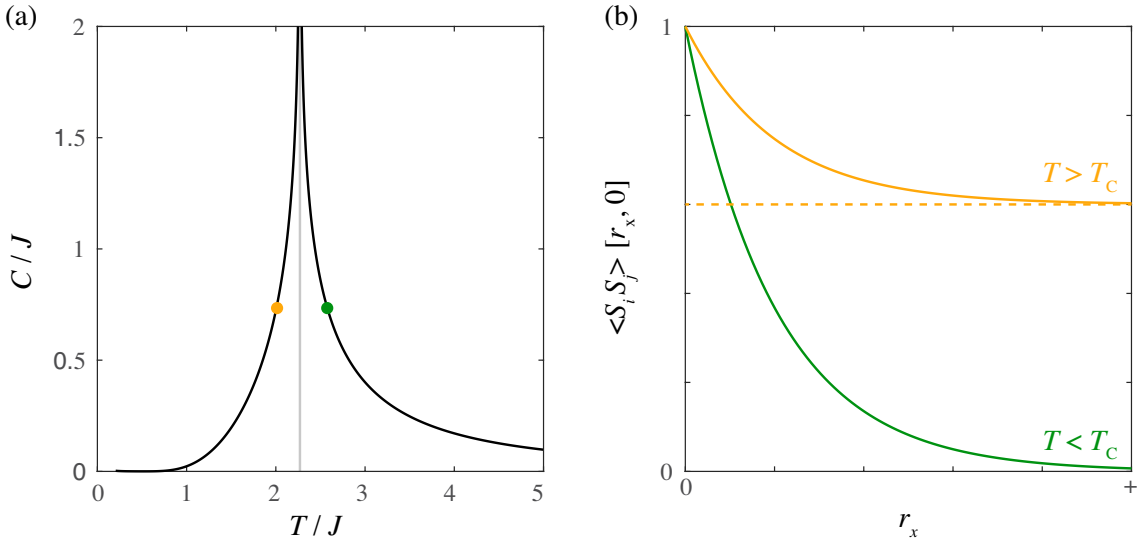

Figure 1.9: (a) The Onsager heat capacity, calculated as the second derivative of Equation (1.17), shows a discontinuity at $T = T_C$, shown with a gray vertical line. The system is said to be ordered below T_C and disordered above T_C.

decays to

$$\langle S_i \cdot S_j \rangle \left([r_x \to \infty, 0]\right) = \begin{cases} 0 & T > T_{\mathrm{C}}; \\ \left(1 - \mathrm{cosech}^4 \frac{2J}{kT}\right)^{\frac{1}{4}} = M^2 & T < T_{\mathrm{C}}. \end{cases} \tag{1.21}$$

This is the key difference between two types of order: at $T < T_{\mathrm{C}}$, the magnetism shows 'long-range order' (LRO) as this correlation function extends over all space. For $T > T_{\mathrm{C}}$, this long-range order does not exist but we can see from Figure 1.9 that correlations persist. This is called 'short-range order' (SRO). An important parameter of this short-range order is the correlation length, ξ, which indicates the distance over which short-range order persists. As $T \to T_{\mathrm{C}}$ from above, $\xi_2 \to \infty$ and so from Equation (1.20) $\langle S_i \cdot S_j \rangle \left([r_x, 0]\right) \propto 1/r_x^{\frac{1}{2}}$ at exactly T_{C}.

The key observation that can be made from the 2D square Ising model—namely, LRO at low temperature a sharp phase transition to SRO on increasing temperature—is seen throughout ordering transitions in the solid state. Unfortunately very few (if any) physical systems are well described by such exactly solvable models. Instead, the approaches taken in this thesis are the approximate methods outlined in Sections 2.4 and 2.5.

1.2.3 Low dimensionality

In the previous section, I discussed the two-dimensional Ising model but neglected to consider its structurally simpler one dimensional counterpart. This is because the 1D Ising model shows an interesting property, failing to show long range order even in the $T \to 0$ limit. This is because the energetic cost of introducing a defect into the structure is always outweighed by the entropic gain from such an introduction. In a chain of L Ising spins, the energetic cost for the flip shown in Figure 1.10(a) is J but because this flip can arise at any point along the chain, the entropy induced

is $N \log 2$. Putting this together, the free energy associated with all possible flips is

$$\Delta_{\text{flip}} F = J - k_{\text{B}} T L \log 2. \tag{1.22}$$

Since in a bulk system $L \to \infty$, this process is favourable for all values of $T > 0$. Compare this with the 3D Ising model (with dimensions $L \times L \times L$), where the energy cost of introducing a domain wall is $\propto L^2$, as the entropy gain is only $\propto L$. This means that in the 3D case, the creation of such domain walls will not be thermodynamically favourable at low temperature, leading to the ordered ground states discussed in the previous section.

The expressions for the heat capacity,

$$C_{\text{mag}}(T) = \frac{J^2}{k_{\text{B}}^2 T^2} \operatorname{sech}^2 \frac{J}{k_{\text{B}} T}, \tag{1.23}$$

and correlation length,

$$\xi(T) = \frac{-1}{\log\left[\tanh(J/k_{\text{B}}T)\right]}. \tag{1.24}$$

are relatively simple and plotted in Figure 1.10(b). Although the heat capacity signature of ordering does not show a singularity as in the 2D case [c.f. Fig. 1.9],

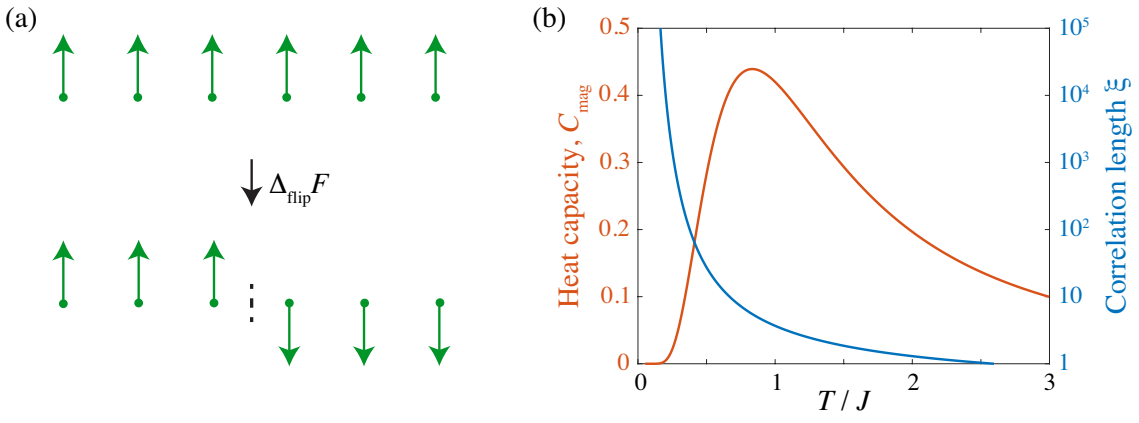

Figure 1.10: (a) Schematic representation of the spin flip inclusion process with free energy described by Equation (1.22). (b) The heat capacity [Eq. (1.23)] and correlation length [Eq. (1.24)] as a function of temperature in the 1D Ising ferromagnet model.

it does show a clear and marked maximum (with associated temperature $T_{1D} = 0.8335$), which decays to zero at the lowest temperatures. The function $C(T)$ is analytically flat as $T \to 0$, meaning that all of its derivatives vanish in this limit. Indeed, the order that exists at $T \ll J$ is short range only in name. While $\xi(T)$ does not diverge until $T_C = 0$, the correlation length becomes large quite quickly below the ordering peak: $\xi(T) \sim 50$ interatomic distances at $T/T_{1D} = 0.5$ and by $T/T_{1D} = 0.1$, $\xi(T) \sim 10^{10}$ interatomic distances, comparable to the size of the crystal. This means that lack of long-range order in the 1D Ising model still does not mean that the model disordered in any real sense at $T \ll J$.

Because of quantum effects due to the disordered groundstate, a range of unconventional behaviours are seen in one dimensional systems which are not exhibited in higher dimensions. These include spin fractionalization whereby the quasiparticles of a system cannot be constructed as combinations of its elementary constituents [134]. Others examples include quantum sine-Gordon physics [135, 136], which may be a pathway to effective quantum computing [137] and the exotic 'Haldane' gap in the antiferromagnetic $S = 1$ spin chains [138, 139]. The realisation of such models is of interest to physicists both to study the fundamentals of models and for the design of devices.

Because of the lack of long range order, the 1D Ising model is much more dynamic at low temperatures than ordered models such as its 2D counterpart [140–142]. A spin flip like that of Figure 1.10(a) could propagate with no energetic cost across the chain, completely changing the spin. This is studied in the 'Glauber' model [143, 144]. This means that the kinetics of one dimensional magnets is often quite different from that of higher dimensional magnets, staying fluid until relatively low temperatures, where a 'blocking transition' occurs, in which the kinetic barrier to reorient the spin determines the rate at which the sample can become magnetised [140]. This situation contrasts with 3D magnets, where the factor limiting magnetisation is the movement of domain walls and tends to set in at T_C [145].

The real world is not one dimensional and real 1D materials are realised as embeddings of 1D chains in 3D space. Spin chain compounds are usually designed to put as much space as possible between adjacent chains. This is achieved in framework materials by exploiting asymmetric exchange pathways or using highly directional linker geometry (§ 3.1). However, it is impossible to completely eliminate the interaction between chains [142]. In the coordination polymer $[(CH_3)_3NH]FeCl_3 \cdot 2H_2O$, the effect of this can be seen in the heat capacity, which is compared in Figure 1.11 to a fit of the asymmetric Onsager model where $J_\perp = 1.2 \times 10^{-3} J_\parallel$ [130]. At $T > 4\,\mathrm{K}$ the curve closely resembles the smooth maximum of Figure 1.10(b) but at T_C, the curve suddenly diverges to $C \to \infty$, a peak associated with final 3D order. It is perhaps surprising that the transition occurs at $T_\mathrm{C} = 3.135\,\mathrm{K}$, much greater than the interaction strength associated with interchain order $J_\perp = 0.022\,\mathrm{K}$. The reason for this can be seen in the fast divergence of the correlation length (Equation (1.24)). We have already noted that the regions of chains which are completely correlated become large (recall that at $T/T_\mathrm{1D} = 0.1$, $\xi(T) \sim 10^{10}$). This

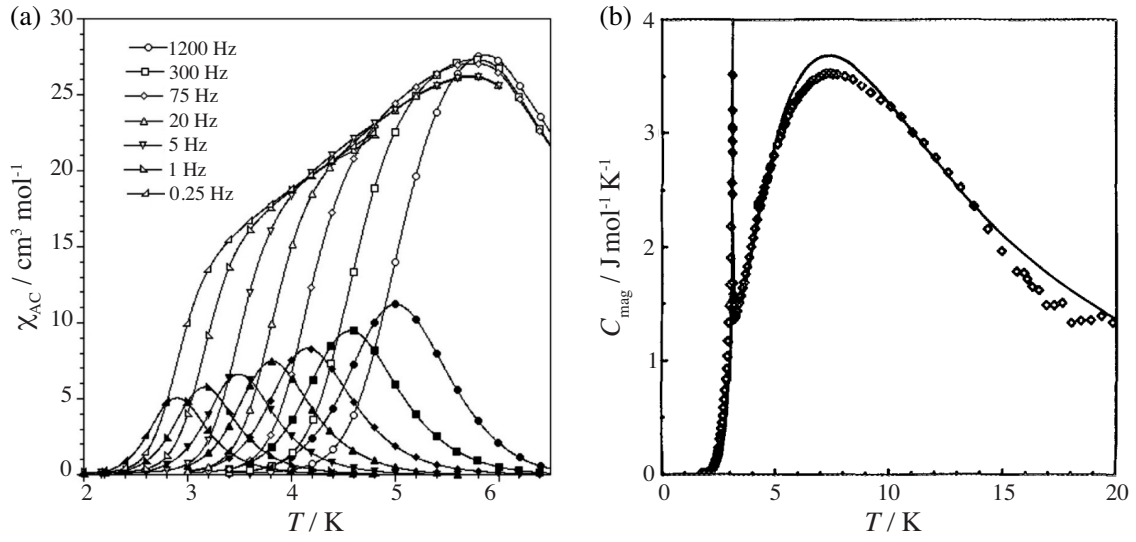

Figure 1.11: Complicating factors in the analysis of real quasi–1D systems. (a) AC susceptability (χ' and χ'' in open and filled markers, respectively) in $Fe^{III}(bpym)(CN)_4$ which shows a 'blocking' peak associated with the dynamical freezing of spins. (b) Magnetic heat capacity for $[(CH_3)_3NH]FeCl_3 \cdot 2H_2O$ compared with a fit to theory [130] where $J_\parallel = 17.4\,\mathrm{K}$ and $J_\perp = 0.022\,\mathrm{K}$. Note: C_mag diverges at $T = T_\mathrm{C} = 3.135\,\mathrm{K}$ reproduced from Ref. 146.

means that the effective interactions between these regions becomes large too. It is for this reason that we can see ordering transitions associated with coupling strengths many orders of magnitude weaker than the transition temperature. A consequence is that quasi one dimensional materials are incredibly sensitive to sometimes quite small interactions between chains.

In two dimensions, while we have seen that the Ising ferromagnet model orders, neither the Heisenberg nor XY models do [147]. Instead, down to arbitrarily low temperature, there are 'vortex' and 'anti-vortex' defects which suppress long range order at any finite temperature, with interesting (but probably distant) applications in data storage [148, 149], as well as being important to understanding the behaviour of superconducting devices [150]. While these 2D systems do not directly concern this thesis, the disorder which arises due to low-dimensionality is similar and observations made for quasi-one-dimensional systems may have implications for quasi-two-dimensional physics.

1.2.4 Geometric Frustration

In frustrated systems, because of the specific geometry of the lattice, the interactions underconstrain the degrees of freedom. The simplest example of this is Ising spins on the vertices of a triangle [Fig. 1.12(a)]. When coupled antiferromagnetically, spins are constrained to lie antiparallel. However, this is made impossible by the geometry of the system: if the spins on two vertices are antiparallel the third spin has no choice but be parallel with one of the first two.

When these triangular units are combined it is not immediately clear whether the size of this degeneracy will grow or not. Figure 1.12(b) shows an example where the combining triangles lifts the frustration. There exists an antiferromagnetic ground state where spins point in opposite directions on successive rows. Systems also exist where the degeneracy grows exponentially as the system is scaled up. An example is an antiferromagnetic Ising model on the kagome lattice [Fig. 1.12(c)], where this exponentially growing degeneracy with the size of the system results in

an entropy, even in the zero temperature limit of the model [151]. Of course the nature of the spins changes the character of the model entirely. The Heisenberg kagome model has a ground state with spins pointing at 120° around a triangle, whilst showing a 'charge ice' state required where the spins are disordered but the total number of spins pointing in or out of each triangle is either ±1 and never ±3 [152]. The presence of such 'local rules' in the absence of long-range magnetic order is a key feature that distinguishes frustrated magnets both from classical paramagnets and ordered magnets, and has led to their being described as as 'spin liquids' or 'cooperative paramagnets' [153, 154]. Despite the wide range of potential topologies, much of the research in this field has focused on a small set of structures commonly found in ceramic materials, such as pyrochlore, triangular, kagome, and face-centered cubic nets. Therefore, studying frustration on less common lattices may lead to the discovery of new magnetic phases and their associated physics [90–92].

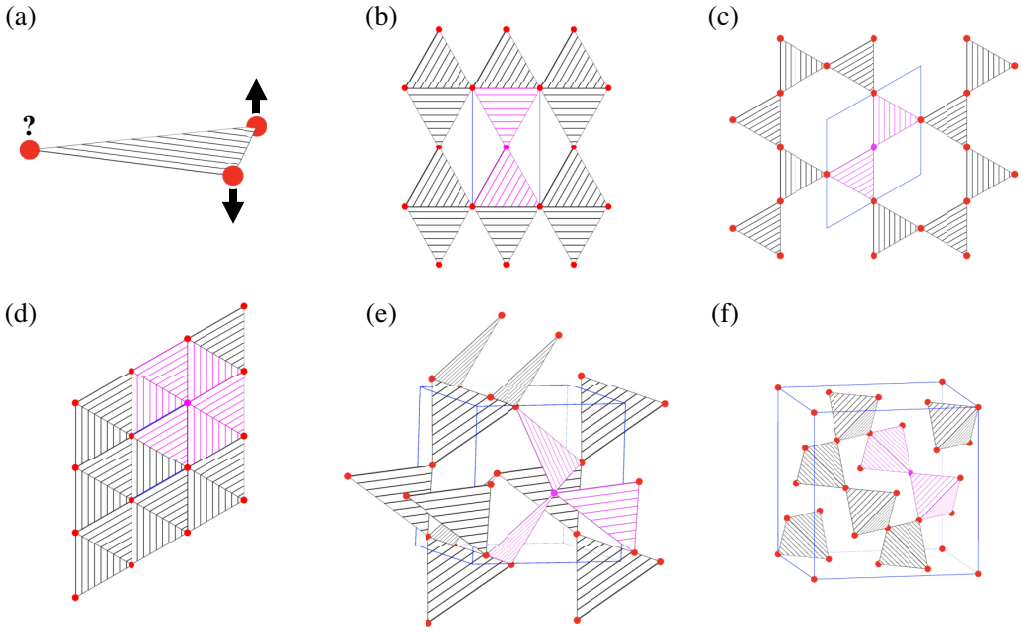

Figure 1.12: Some examples of frustrated geometries: (a) spins on a triangle, (b) a network of corner and edge sharing triangles which has an ordered ground-state, (c) the kagome, (d) triangular, (e) trillium, and (f) pyrochlore lattices. The local environment is shown in pink and the unit cell in blue.

Where an ordered state does arise, the temperature required to induce this order is usually much smaller than we might expect given the energy scale of the interactions responsible for ordering. Since we saw in Equations (2.49) and (2.51) that Θ_W is a measure of the strength of interactions, we define the frustration parameter as

$$f = \frac{T_{\mathrm{N}}}{|\Theta_W|}. \tag{1.25}$$

In systems where $f \gtrsim 10$, interactions are at least order of magnitude stronger than order, so they are termed 'strongly frustrated'.

Probably the most useful consequence of this frustration is a macroscopic degeneracy or near-degeneracy of ground-states. This means that frustrated magnets are highly fluctuating systems and given the fluctuation-dissipation theorem, it is unsurprisingly that these states are highly susceptible to magnetic fields, showing transitions as a function of field [155]. This high susceptibility means that it is easy to induce phase transitions by applying field. This has been observed in a number of different frustrated models at many different values of the magnetisation 1/2, 1/3, 1/4, 1/5, ... [155]. We have already discussed a method of inferring these transitions from experiment—magnetisation curves, where field induced transitions appear as peaks in $\chi(H)$.

Three geometrically frustrated models are of particular interest to this thesis: the Ising triangular antiferromagnet, the Heisenberg trillium antiferromagnet, and spin ice itself.

Triangular Ising Antiferromagnet

The triangular lattice antiferromagnet (TIA) model has been an important two dimensional model in the development of the theories of frustrated magnetism. As early as 1950, it has been known that the model has a disordered groundstate with entropy [156]:

$$S(0) = \frac{2k_{\mathrm{B}}}{\pi} \int_0^{\pi/2} \ln(2\cos\omega)\,\mathrm{d}\omega \simeq 0.3231 k_{\mathrm{B}}. \tag{1.26}$$

The groundstate of the TIA model has a surprising property: correlations decay algebraically rather than exponentially in the plane. This means that—despite the disordered nature of the configuration—the diffuse scattering from this disordered state looks essentially sharp [Fig. 1.13(a)]. Stephenson [157] showed that correlations along one line of the triangular lattice obey

$$\langle \mathbf{S}(0,0,0) \cdot \mathbf{S}(0,y,0) \rangle = \frac{\cos 2\pi y/3}{\sqrt{y}}, \tag{1.27}$$

and since $\sum_{n=1}^{\infty} 1/\sqrt{n}$ diverges, it is perhaps unsurprising that the diffuse scattering gives sharp peaks. This has been verified by Monte Carlo modelling which shows that scattering stays essentially sharp even at non-zero temperature [158].

There are few experimental realisations of the TIA model: for true 2D embeddings, the requirement for a large separation between 2D layers again requires large molecules, as in the case of κ-(BEDT-TFF)$_2$Cu(CN)$_3$ [159]. Many systems which involve well-coupled triangular lattice layers form effective spin liquid candidates, with quantum $S = 1/2$ showing gapless excitations [160].

The system of most interest to this thesis is Tb(HCOO)$_3$, which has been discussed already in Section 1.1.4. A neutron scattering study was used to parametrise a Hamiltonian for the system, which found evidence for strong anisotropy (meaning that this system is very Ising-like), strongly ferromagnetically coupled chains which interact antiferromagnetically with their neighbouring chains [116]. Furthermore, they found the sharp peak, which can be reproduced using a TIA-like model [116]. A reasonably broad heat capacity feature associated with this ordering transition has been measured [161]. The geometric frustration in this system is understood as being the origin of the strong MCE in the system [93, 162].

Trillium Heisenberg Antiferromagnet

The trillium lattice is an obvious target for frustrated magnetism: it is a chiral network of corner-sharing triangles that is intrinsically predisposed to geometric

frustration [Fig. 1.12(d)] [82]. Remarkably few magnets are known to adopt this lattice, but those that do—mostly intermetallics—exhibit a wide range of interesting physics. In MnSi, for example, magnetic skyrmions arise from competition between ferromagnetism and the Dzyaloshinskii-Moriya interaction [163, 164]; EuPtSi and EuPtGe are strongly-correlated spin liquids [165]; and CeIrSi is an Ising trillium spin-ice candidate [166, 167]. Mean-field theory tells us that even the simple nearest-neighbour Heisenberg antiferromagnet (nnHAF) on this lattice should support a classical spin-liquid (CSL) phase over a wide temperature range [82]. The associated diffuse scattering [Fig. 1.13(b)] marks out circles in reciprocal space with $\sqrt{k_x^2 + k_y^2 + k_z^2} = 1/3$. Monte Carlo simulations showed that the model does order with 120° helical order ('Y' phase; $\mathbf{k}_{\text{ord}} = [\frac{1}{3}, 0, 0]$) in the frustrated magnetic ground state [168]. To best of my knowledge, there has not been any experimental realisation of this model system.

Spin Ice

Interest in the pyrochlore lattice as a host of geometric frustration has been long-standing: in 1956, Anderson proposed an Ising antiferromagnet model on this lattice

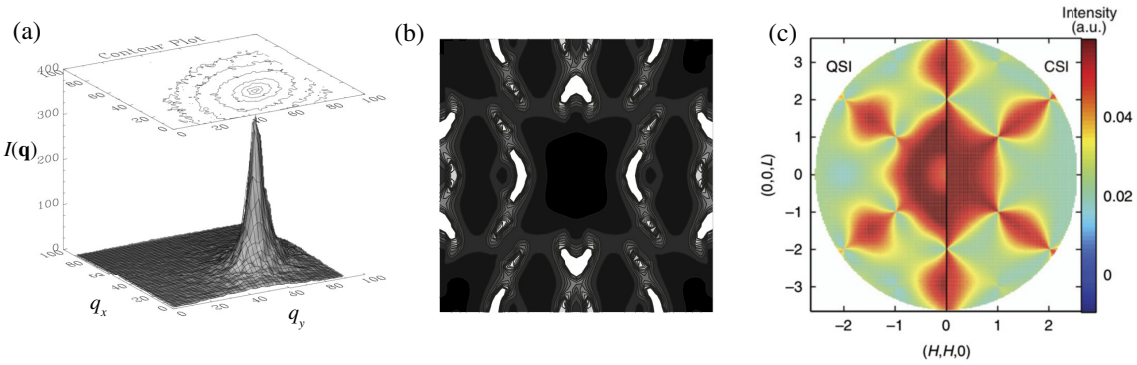

Figure 1.13: Scattering signatures of the three frustrated magnet models discussed. (a) The scattering function arising from the disordered TIA groundstate has essentially sharp scattering peaks. Calculated from Monte Carlo simulation of a 60×60 lattice, reproduced from Ref. 158. (b) The curved diffuse scattering shown in the classical spin liquid phase of the trillium nearest neighbour Heisenberg antiferromagnet model. Calculated via mean-field simulation in Ref. 168. (c) Pinch-point magnetic scattering simulated for the low temperature phase of the spin ice model in $Pr_2Hf_2O_7$, reproduced from Ref. 169. Pinch points are present in both the quantum (QSI) and classical (CSI) models.

as an analogue to Pauling's earlier ice model [68], which exhibits a disordered ground state [170]. However, 50 years after his proposal and investigation of the pyrochlore spinels [171], no systems were found that matched Anderson's model. Bramwell explains that this lack of matching systems is not surprising, considering that the Ising antiferromagnet anisotropy breaks the cubic symmetry of the lattice [172]. A breakthrough came in 1997 when Bramwell instead proposed the 'spin ice' model and identified a candidate system, $Ho_2Ti_2O_7$ [173, 174]. Since this discovery, there have been well over five thousand papers that discuss spin ice [172].

In this model, the spins are arranged on a pyrochlore lattice, which consists of interconnected tetrahedral units. The anisotropy is such that the two spins point either in or out of these tetrahedra. Ferromagnetic interactions drive towards a two-in-two-out arrangement, similar to the arrangement of hydrogen and oxygen atoms in water ice (two long hydrogen bonds and two short covalent bonds) proposed originally by Pauling [68]. The ferromagnetic spin ice model on this lattice, with the Hamiltonian

$$\mathcal{H} = \mathcal{H}_{\text{sym}} + \mathcal{H}_{\text{dip}} + \mathcal{H}_{\text{S.I.}} \tag{1.28}$$

was first proposed for this system by Harris, Bramwell and co-workers [173]. Due to the geometrical frustration inherent in the pyrochlore lattice, the spins cannot simultaneously satisfy all their interactions, leading to a highly degenerate and disordered ground state. Experimental evidence for this was seen in isostructural $Dy_2Ti_2O_7$, which showed the residual entropy $S \simeq R\log(3/2)$ to low temperature [111]. Despite this disorder, the local ferromagnetic rules act to suppress lattice divergence of the magnetization [175]. An experimental signature of the local rules are the pinch points simulated for both a classical and quantum spin ice model in the ground-state diffuse magnetic neutron scattering [Fig. 1.13(c)] [169] and measured for a number of compounds including $Ho_2Ti_2O_7$ [176].

The magnetic excitations of this model are of fundamental interest, taking the form of 'magnetic monopoles'—local environments which break the local two-in-

two-out rules [177]. The monopoles interact via an effective coulomb potential, as is the case in a large class many of these vertex models, so called 'coulomb phases' [172]. As such, the monopole dynamics can be understood in exactly the same way as the Debye-Huckel theory developed for ionic solutions [172, 178]. As in liquids, the excitations of spin ice are not gapped. The search for a system which is truly not gapped down to low temperature has become a common theme in spin-ice literature [179].

1.2.5 Magnetic Dilution

Other than modifying the geometry of a magnetic system, modifying its composition is another way to change its magnetic properties. A solid solution is obtained when two or more elements jointly occupy a site in the crystal structure, homogeneously distributed across the sample. When the difference between the species (e.g. A and B in the $A_{(1-\rho)}B_{\rho}$ solid solution) is small, such as for the Nb-Ta alloys [180, 181], the resulting lattice parameter obeys Vegard's rule [182],

$$a_{A_{(1-\rho)}B_{\rho}} = (1-\rho)\ a_A + \rho\ a_B. \tag{1.29}$$

Deviations from this rule exist where the substituents are of more different size, as seen in models of hard spheres as well as in binary alloys [181, 183]. These deviations can also result from clustering or anticlustering of the substituents, so that obeying Vegard's rule can be used as an indication of randomly arranged vacancies [184]. More rigorous techniques such as transmission electron microscopy exist to test the homogeneity of a solid solution [185].

A common approach to tuning the magnetic behaviour of a system (and the focus of Chapter 4 and 5) is to dilute a known magnetic material where A is magnetic and B non-magnetic. It was noted by Griffiths [186] that incorporating these vacancies randomly would suppress the ordering temperature from its value in the undoped system ($T_G = T_{\mathrm{C}}(\rho = 0)$), as shown in Figure 1.14(a). However, in a infinitely large

crystal, there would exist arbitrarily large regions of perfect order—'rare regions'—which can locally order above the Griffiths temperature [186]. The singularities that result from these regions mean that the between T_G and the final ordering temperature, the model is not analytically solvable but is infinitely differentiable [187]. This region, the Griffiths Phase, shows unusual behaviour which results from these singularities: a continuously varying critical exponent. The presence of these Griffiths singularities, which result from randomness in the underlying magnetic model are far more widespread than simple diluted magnets. Recent examples of its observation are in the disordered bundles of 1D nanowires and as a result of quenched disorder in two dimensional superconductors [188, 189]. $NdSrCoFeO_6$, a disordered double perovskite exhibiting a Griffiths phase, shows magnetocaloric coupling with unusual universality behaviour [190]. This is presumed to be because the rare regions are able to order at very different temperatures than their surroundings. In the perfect 1D Ising model, because of the lack of long range order, no Griffiths phase exists [191], but the impact of doping a quasi-one-dimensional model remains understudied.

So far in this section we have been assuming that the systems are allowed to reach thermodynamic equilibrium but there is a very important class of dilute mag-

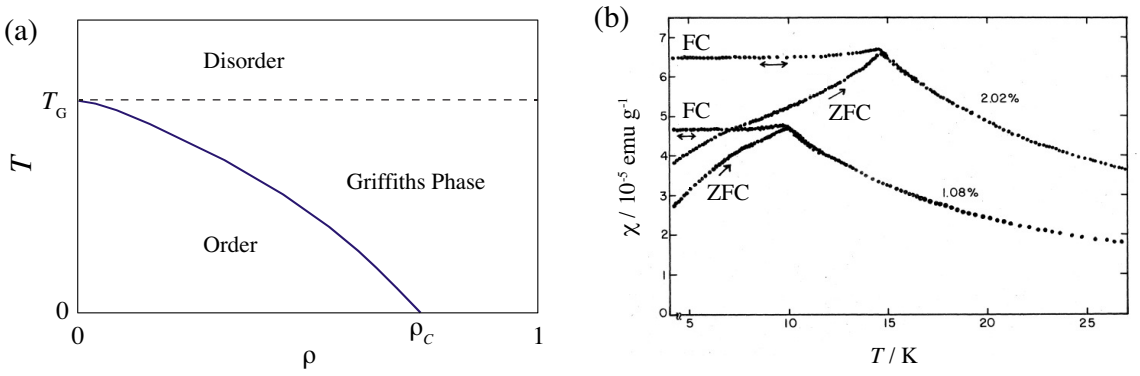

Figure 1.14: (a) Phase behaviour predicted by Griffiths [186] for a dilute magnetic system, showing $T_C(\rho)$ as a blue line. (b) Field cooled and zero filed cooled measurements for two dilute AuMn alloys. Numbers indicate the molar-percentage of Mn. Both traces show a divergence of FC and ZFC susceptibility at T_N. Adapted from Ref. 192.

netic material—Spin Glasses—where this is not the case. What is really surprising about these systems is that ergodicity is broken [193]. This means that even with an infinite amount of time a spin-glass system prepared in a state below its spin glass temperature, there will exist some states of similar energies which the system will never reach. A recent Nobel Prize was awarded for demonstrating that there exist sensible magnetic models where this is the case [194]. The experimental consequence of this is that there are many magnetic systems, particularly those with magnetic disorder, where their magnetism 'freezes' before it reaches its equilibrium ordering temperature, an important challenge for the field of frustrated magnetism [195]. This can be seen experimentally in measurements of the 'field cooled' susceptibility [§2.2.1], which shows a plateau in χ_{FC} corresponding to the freezing temperature, below which it becomes harder to rearrange the spins. The 'field cooled' susceptibility diverges from χ_{FC} because at $T < T_{\mathrm{C}}$ the history dependence means that it 'remembers' being cooled under field [196]. The archetypical example is the alloy CuMn for high levels of dilution (99 % and 98 %), which show the divergence of field cooled and zero field cooled at differing temperature depending on the extent of dilution [Fig. 1.14(b)].

1.3 Lattice Dynamics

This section will give an overview of the theory of lattice dynamics. We start in the harmonic approximation, developing the concept of phonon modes. We will then introduce anharmonicity, first as a small perturbation and finally the effect of extreme anharmonicity in soft mode materials. We will finish by discussing vibration localisation in disordered materials. The analysis leans heavily on standard texts on the subject by Dove [35, 197].

1.3.1 The Harmonic Approximation

Many important physical properties of solids result from the motion of their atoms about their equilibrium positions. In this way crystalline materials differ from the

lattice described. For many solids, the main source of these deviations are lattice vibrations. A convenient way to describe the energy of a solid is to take its Taylor expansion in terms of atomic deviations about the equilibrium positions $\mathbf{u} = \mathbf{r} - \langle \mathbf{r} \rangle$,

$$E = E_0 + \frac{1}{2} \sum_{\substack{i,j, \\ \alpha,\beta}} \frac{\partial^2 E}{\partial u_i^{(\alpha)} \partial u_j^{(\beta)}} u_i^{(\alpha)} u_j^{(\beta)} + \frac{1}{6} \sum_{\substack{i,j,k, \\ \alpha,\beta,\gamma}} \frac{\partial^3 E}{\partial u_i^{(\alpha)} \partial u_j^{(\beta)} \partial u_k^{(\gamma)}} u_i^{(\alpha)} u_j^{(\beta)} u_k^{(\gamma)} \ldots, \quad (1.30)$$

where $u_i^{(\alpha)}$ represents the displacement from its average position of the ith atom in the unit cell, displaced in the $\alpha \in \{x, y, z\}$ direction. If displacements from equilibrium are small, it is sufficient to take the 'harmonic approximation' i.e. to truncate after the second term in the series. The solution of the equations of motion can be written as a sum of normal modes ν with wave vectors $\mathbf{k}_\nu$ and normalisation constant A_ν,

$$u_j^{(\alpha)}(t) = \sum_\nu A_\nu m_j^{-1/2} e_{\nu j}^{(\alpha)} \exp\left(\mathrm{i}[\mathbf{k}_\nu \cdot \mathbf{r}_j - \omega_\nu t]\right). \quad (1.31)$$

In a 3-dimensional system there are $3N$ modes if there are N atoms in the unit cell. The values of the mode frequency $\omega_\nu(\mathbf{k}_\nu)$, representing the energy of a particular vibration mode, and eigenvectors $\mathbf{e}_\nu$, representing the displacements associated with the mode, are solutions to the dynamical equation,

$$\mathbf{e}_\nu \omega_\nu^2 = \mathbf{D}\mathbf{e}_\nu, \quad (1.32)$$

where $\mathbf{D}$ is the dynamical matrix

$$D_{ij\alpha\beta}(\mathbf{k}) = (m_i m_j)^{-1/2} \sum_\alpha \frac{\partial^2 E}{\partial u_i^{(\alpha)} \partial u_j^{(\beta)}} \left(\delta_{ij} - \exp \mathrm{i}\mathbf{k} \cdot \mathbf{r}_{ij}\right). \quad (1.33)$$

The functions $\omega_\nu(\mathbf{k})$ (of which there are $3N$)—the dispersion relations—have a special relevance to the properties of a solid. The lowest energy vibrations are found for the three branches near $\mathbf{k} = 0$. These functions can be directly probed using inelastic neutron scattering, as is shown for the example of fcc lead in Figure 1.15.

The very long wavelength vibrations are sound waves. In three dimensions, $\omega_1(\mathbf{k} = 0) = \omega_2(\mathbf{k} = 0) = \omega_3(\mathbf{k} = 0) = 0$, corresponding to the collective displacement of the whole lattice in each of the three directions which requires no energy. The gradient of the branches out of the origin (Shown in Figure 1.15 as tangent lines) contains information about the sound velocity in that particular direction. The different gradients result from the multiple sound modes which travel through a three dimensional crystal, both transverse and longitudinal sound vibrations often have very different energies which is the origin of s and p waves in seismology [199].

Since the dispersion curves encode the energies of vibrations within a system, they are related to the thermodynamic partition function, and in turn (1.32) contains information about the phonon contribution to the free energy,

$$F_{\text{phon}}(T) = \frac{1}{N} \iiint \sum_{\nu} \frac{1}{2}\hbar\omega_\nu(\mathbf{k}) + k_{\text{B}}T \log\left[1 - \exp\left(-\frac{\hbar\omega_\nu(\mathbf{k})}{k_{\text{B}}T}\right)\right] \mathrm{d}\mathbf{k}, \qquad (1.34)$$

the corresponding equation for the heat capacity can be treated under the approximation that near $\mathbf{k} = 0$, the dispersion relations $\omega(\mathbf{k})$ are linear, up to a certain cut off energy (corresponding to the Debye temperature Θ_D). This is the basis for the Debye equation for the 'lattice' heat capacity, which arises from thermal vibrations

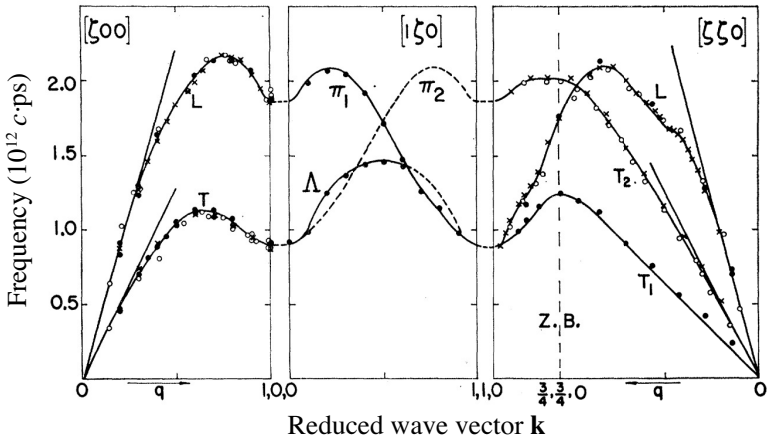

Figure 1.15: Dispersion curves ($\omega_\nu(\mathbf{k})$) of Pb at 100 K measured using neutron diffraction by Brockhouse and co-workers [198], with a fit to an empirical model. Reproduced from Ref. 198

[200],

$$C_{\mathrm{lat}}(T) = 9k_{\mathrm{B}}\left(\frac{T}{\Theta_{\mathrm{D}}}\right)^3 \int_0^{\Theta_{\mathrm{D}}/T} \frac{x^4 e^x}{\left(e^x-1\right)^2}\,dx\,. \tag{1.35}$$

1.3.2 Anharmonicity

Many of the physical phenomena arising in solids—lattice thermal conductivity, thermal expansion, etc.—require further terms than quadratic. When small, the effect of these terms is a perturbation to Equation (1.30), which can be conceptualised as the creation or annihilation of pairs of phonons: cubic terms lead to events involving two phonons, quadratic terms lead to events involving three phonons and so on. The loss of coherence due to these events means one can understand the solution to these equations as a sinusoidal vibration multiplied by an exponential decay, much the same as the damped harmonic oscillator of classical physics. The times associated with this damping $\tau_\nu(\mathbf{k})$ determined how long a phonon survives before annihilating. Since at higher temperature, there are more phonons present to annihilate with, it is usually the case that $\tau \propto 1/T$. Experimentally, this can be seen (for example in neutron scattering) as a broadening at low temperature. Quantitatively, the heat capacity is proportional to the mean-square velocity ($\overline{v^2}$), phonon lifetime and lattice heat capacity (C_{V}),

$$K = \frac{1}{3}\overline{v^2}\tau C_{\mathrm{V}}, \tag{1.36}$$

meaning that at greater anharmonicity decreases τ and lowers the heat capacity.

In more extreme cases, the anharmonic terms in the Hamiltonian introduce wells in the potential energy surface which change the equilibrium values of the mode coordinates at low temperature. Since the new equilibrium position will in most cases break the symmetry of the parent structure, this leads to a phase transition. Where this breaks inversion symmetry, the result is a conventional ferroelectric, as is the case in the perovskite titanates (e.g. $PbTiO_3$). By plotting the free energy F as a function of the mode coordinate η, we can see that there are two possibilities

for how this may happen. In the Landau theory of phase transitions, we write a Taylor expansion of $F(\eta)$ up to η^6

$$F(\eta) = \frac{1}{2}(T - T_0)\eta^2 + \frac{1}{2}b\eta^4 + \frac{1}{6}c\eta^6. \tag{1.37}$$

'Second-order phase transitions' are seen when $b > 0$, as is shown in Figure 1.16(a). The curvature at $\eta = 0$, which corresponds to frequency of the phonon mode associated with η varies continuously to zero at $T \to T_C$. Such modes are called 'soft modes' because they become very low in energy near the transition. Phonon softening can be directly measured via techniques like neutron and Raman scattering. This is shown in the case of the ferroelectric soft mode of $PbTiO_3$ in Figure 1.16(b), with the phonon frequency tending linearly to zero from above.

By contrast, in the 'first-order' case of Equation (1.37), where $b < 0$ and $c > 0$, the equilibrium coordinate η_0 jumps discontinuously at T_C. This means that the frequency associated with the mode never approaches zero as for the second-order

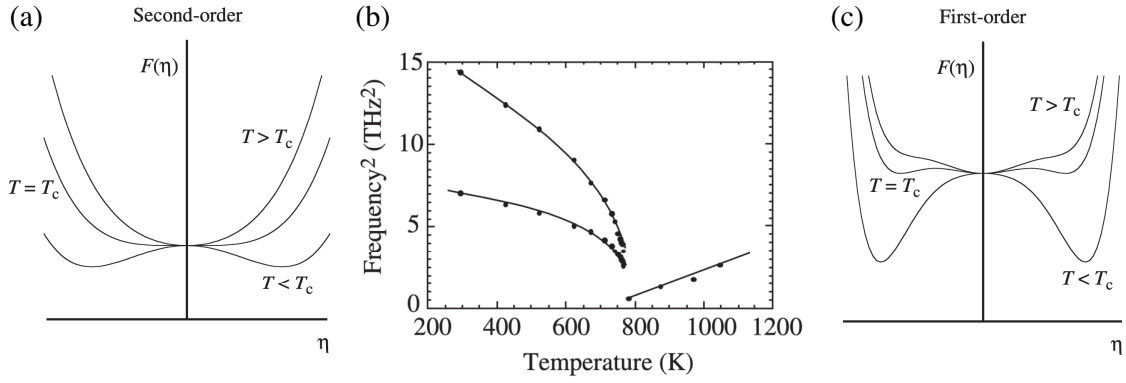

Figure 1.16: (a) The free energy surface F plotted along the 'soft-mode' coordinate η in the second order case ($b > 0$) of Equation (1.37), shown above, at, and below the phase transition temperature. Note that at $T = T_C(b)$ the function is flat at $\eta = 0$. (b) Temperature dependence of the ferroelectric soft mode in PbTiO3. Data in the low-temperature phase are taken from the Raman scattering [201], and data in the high-temperature phase are taken from the inelastic neutron scattering [202]. (c) The free energy surface $F(\eta)$, plotted for the first-order case.

case. There may be several reasons why a phase transition is first order, for example through coupling to spontaneous strain.

1.3.3 Effect of Disorder

The vibrations represented in Equation (1.31) are by their nature extended and coherent across the whole crystal. In real crystals, disorder has a (perhaps) surprising effect on the vibrations which are present in the crystal. We might suspect this to be especially relevant in $Cd(CN)_2$, given the disorder discussed in §1.1.4.

This effect is seen simply in the Anderson model [203]. In this model, the periodicity in crystalline materials is replaced by an 'off-diagonal' disorder. While initially developed for studying the electronic structure on disordered materials, the theories are directly applicable to the vibrations of a disordered model too. The vibrational force constant between two atoms k_{ij} is drawn from a uniform distribution of width W and centre B. Actually this result turns out to be resilient to the form of this distribution [204]. Because of the lack of periodicity in this model, it is improper to define a $\mathbf{k}$ vector and the dynamical matrix spans the whole crystal:

$$D_{ij}^{\alpha\beta} = \delta_{ij} + \langle ij \rangle \, k_{ij}, \tag{1.38}$$

where $\langle ij \rangle = 1$ when sites i and j are adjacent and 0 otherwise.

The strength of the disorder is indicated by W/B, since the ratio captures how much the spring strength varies relative to the average spring strength. The density of states of such a model is shown schematically for various values of the disorder strength in Figure 1.17, focusing on a particular mode. When $W = 0$, the case is completely periodic and we recover a symmetrical density of states with centre ω_0: the mode disperses with a width $\sim B$ and eigenstates are extended across the whole lattice. When the disorder strength is increased, the distribution of eigenvalues widens (unsurprising, since the spring constants are more varied). States at the tails of the distribution are no longer extended (as in the periodic case) but localised

in specific regions of the lattice. The eigenvalues no longer have coherence over a large length-scale. However, states in the centre of the band must be localised when the energy of the individual atomic states varies at random over a range somewhat greater than the width of the band produced by overlap between adjacent sites. This changes at a critical value, which can be shown to correspond to $W/B = \exp(1)$, beyond which all states are localised.

This is the case in highly disordered systems like glasses and liquids, where phonon vibrations are exclusively localised. For this reason, thermal transport cannot occur via the mechanism discussed in the previous section and so is relatively poor. Topically, this is the basis for the 'phonon glass electron crystal' concept for designing effective thermoelectric materials [205, 206]. If it were possible to have a material where the phonons were localised but electrons delocalised, the Seebeck coefficient would be very favourable [206]. The heat capacity of glasses can be understood as local harmonic vibrations and so fit the Einstein model of localised vibrations, rather than the Debye law, which is applicable in crystals [Equation (1.35)] [207]. It is undoubtedly the case that disordered crystals are less disordered than glasses; however in this sense there seems to be a lower limit on the thermal conductivity of disordered systems, meaning that many disordered crystals (e.g. $(KBr)_x(KCN)_{1-x}$, $(NaCl)_x(NaCN)_{1-x}$, $Zr_xY_{1-x}O_2$, and $Ba_xLa_{1-x}F_2$) are as favourable for reduced thermal conductivity as their glassy analogues [208]. This has applications in yttria-stabilized zirconia used for low thermal conductivity in aerospace [209, 210].

At the other extreme of Figure 1.17, where the W/B is small and the disorder weak, the dynamics are only perturbatively different from the ordered case. In this approach, we write the Hamiltonian of the whole crystal as $\mathcal{H} = \overline{\mathcal{H}} + \mathcal{W}$, where the unperturbed $\overline{\mathcal{H}}$ has perfect crystalline symmetry and $\mathcal{W}$ contains the effects of disorder. Neglecting the effect of disorder, we can imagine a 'virtual crystal' with the average properties of the material. This virtual crystal approximation (VCA)

is sufficient to explain many important behaviours involving weak disorder. This approach is easy to implement with DFT, and has been shown to be effective in simulating systems where the difference between the substituents is small. This is effective, for example, for carrier-phonon scattering in the Si_xGe_{1-x} alloys and thermoelasticity across the $K_xNa_{1-x}Cl$ series [211, 212].

However, the virtual crystal approximation breaks down when the disorder becomes more extreme. (Clearly, the VCA cannot predict the localised tails of Figure 1.17.) The approach taken in this thesis is a supercell lattice dynamical simulation (SCLD, §2.6.4), which solves for eigenvalues of a supercell dynamical matrix numerically [214]. For small amounts of disorder the average T-matrix approximation (ATA) is effective. Within the approximation, solutions for the phonon modes keep the same eigenfunctions as in the VCA but with energy spectra broadened and shifted in energy as a result of the disorder [204]. Of course, the true spectral levels of a disordered system are infinitely sharp (since they are eigenvalues of Equation (1.38)) but the solutions of the ATA are not invariant under translations of the

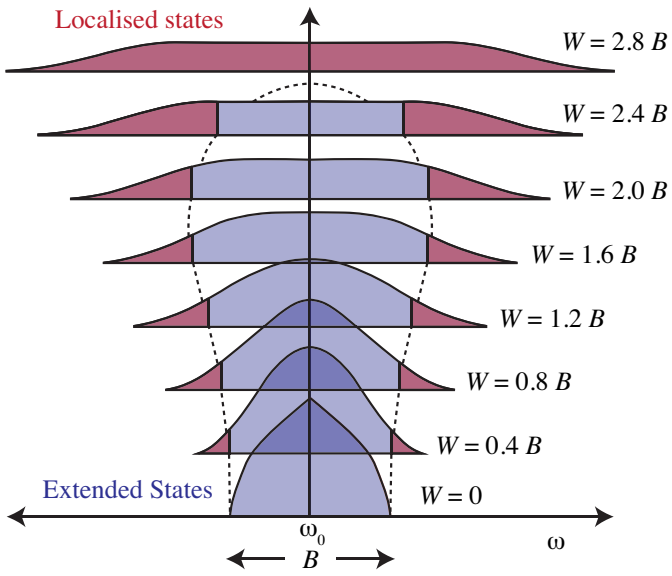

Figure 1.17: The density of states in the Anderson model, plotted for various values of W/B showing entirely localised states for $W/B > e \approx 2.7$ and extended states for $W = 0$. For the intermediate values, a mobility edge divides localised and delocalised states, and the form of this edge is shown with a dotted line. Adapted from Ref. 213

crystal (due to the disorder induced) and so are not true eigenvalues. This approach does have the advantage of giving a picture which is interpretable in the reciprocal space of the virtual crystal. This explains the observation made for small amounts of disorder in the SCLD of the slight broadening of phonon modes [214].

Understanding the impact of disorder on the phonon properties of a crystal is difficult and represents a clear challenge for the future of the field, but as neutron scattering techniques get more powerful and simulations easier the complexity of system that can be probed will continue to increase.

1.4 Pseudospin Systems

The theory developed in §1.2 for magnetic systems has long been recognized as important for non-magnetic systems too. The key complication in such systems is the increased importance of lattice dynamics, which couples in complex ways to the pseudospin dynamics. Important examples include the mixing of alloys studied by Warren and Cowley, orientational glasses, and ferroelectric materials. These pseudospin models fall into the categories highlighted in Figure 1.3: Ising models where the pseudospin takes two values—mapping onto the magnetic Ising model—and vector models, related to the Heisenberg model of Equation (1.10). Where the magnetic models described in Section 1.2 are usually poorly coupled to the lattice dynamics, Pseudospins are far more strongly coupled. Approaches to understanding this link are discussed.

1.4.1 Compositional Pseudospins

Ising variables can be used to represent two-state degrees of freedom. For example in the solid solutions discussed in substitute magnetic and nonmagnetic components on a lattice site. We have visited examples of occupational Ising models in the thesis already [§1.2.5]: in the solid solution $Tb_xY_{1-x}(HCOO)_3$, the joint occupation of Tb and Y on the lattice can be represented as up and down pseudospins. For such rare earth formate systems, the similarity in size, charge, and bonding between rare

earth substituents means that correlations are relatively weak [94, 215]. In models of these systems it is therefore typical to assume that the substituents are randomly distributed subject to the average stoichiometry [216].

In systems where there is a greater difference between the substituents—for example the size difference between Cu and Au in CuAu alloys—the tendency of these substituents to minimise strain leads to an 'effective interaction' between sites [204]. Historically one of the main techniques pioneered by Cowley [217] involved fitting correlation functions. For each shell n around an atom A, the deviation from the bulk of the probability P_n^{AB} of atoms in that shell being different is given by Warren-Cowley parameters, α_n [218]:

$$\alpha_n = 1 - \frac{P_n^{AB}}{P_\infty^{AB}}. \tag{1.39}$$

This approach allows for simple analysis, such as identifying clustering or anti-clustering but, due to the lack of constraints on correlation functions, does not guarantee a self-consistent model. Other approaches to modelling such systems may build a large supercell of the structure, employed in the study of high entropy alloys [219]. When the difference in size is large (such as in the $Ga_{1-x}In_xP$ series [220]) the correction required to these theories requires a more complex treatment to understand the relaxation of the structure around the pseudospin disorder [221]. Evidence for this relaxation can be found experimentally in Huang scattering [222, 223]. But for many systems (such as those investigated in §4–5) it is sufficient to include the effects of these relaxations on the energy only as an *effective* interaction.

Amongst framework materials, the MOF UiO66(Hf) is noteworthy in the existence of correlations in cluster vacancies. Models for this system based on diffuse powder X-ray scattering indicate that vacancies tend to order across regions a few tens of nanometres [77]. A region of this model is show in Figure 1.18(a) illustrating the alternating regions of reo topology, driven by cluster-cluster avoidance. This is analogous to antiferromagnetism, in which like spins avoid sitting adjacent. The model proposed by Cliffe and co-workers was later verified using transmission elec-

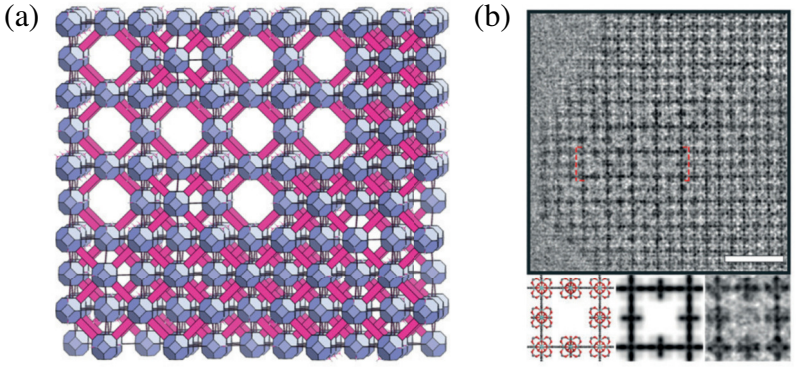

Figure 1.18: (a) Nanodomain model for UiO66(Hf) developed in Ref. 77: cluster vacancies are correlated to give domains of reo topology embedded within the parent fcu framework. (b) High-resolution transmission electron microscopy images of missing-cluster/missing-linker nanodomains in UiO-66 [136].

tron microscopy (TEM), which was able to directly image this domain structure [Fig. 1.18(b)] [136] . These two techniques are complementary: while TEM allows for definitive imaging of domain structures, it is not a bulk technique meaning that it can only give a snapshot of a selected region of the crystal and does not probe the interior volume which makes up most of the crystal. By contrast, diffraction is able to probe the whole crystal.

The model for B-site ordering in $[\mathrm{Gua}]\mathrm{Mn}_{1-x}\mathrm{Fe}_{2x/3}\square_{x/3}(\mathrm{HCOO})_3$ described by Bostrom and co-workers has already been discussed in §1.1.4. While three species occupy the approximately cubic B-sublattice, Mn^{2+} and Fe^{3+} are treated equivalently and vacancies ($\square$) can be represented as the other pseudospin. In this way the anticlustering of vacancies can be described in a similar way to the antiferromagnetic Ising model. The implications of this order for the magnetic properties of the series are the subject of Chapter 5.

1.4.2 Displacive Pseudospins

The soft mode picture of transitions discussed in Section 1.3.2 gives a global view of displacive phase transitions, where atoms across the crystal displace collectively. In some systems, a more local picture is necessary to capture the physics. In such mod-

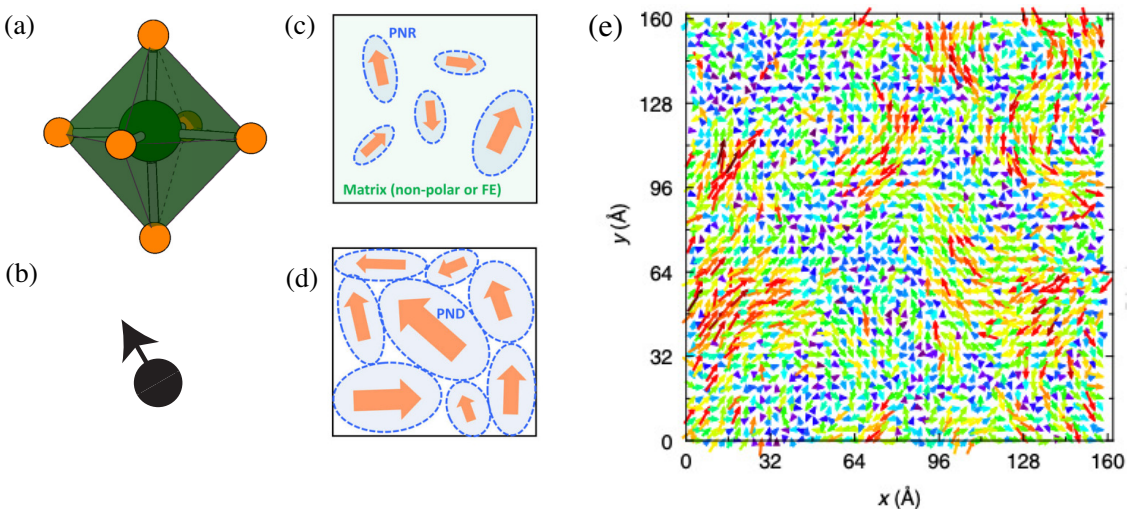

Figure 1.19: (a) The offcentering seen as a result of a second order Jahn Teller effect in the TiO_6 octahedra of $BaTiO_4$ and (b) a corresponding pseudospin representation. (c–d) Two candidate models proposed by Takenaka and collaborators for the relaxor ferroelectric PMN [228], (c) involves polar nanoregions embedded in a non polar matrix while (d) shows polar nanodomains with low angle walls. (e) A slice through the structure of a PMN obtained from reverse Monte Carlo modelling by Erementko and collaborators, arrows indicate Pb-offcentering vectors [229].

els the displacement associated with the 'soft' degree of freedom can be considered as a pseudospin. Take the case of the Jahn Teller dispersion in $KTaO_3$ considered by Höchli [224]: Ta^{5+} displaces away from the centre of the octahedron [Fig. 1.19(a)] in a way which may be represented as a vector. Unlike the majority of magnetic spins discussed in Section 1.2, this 'pseudospin' vector does not have fixed length. Many d^0 cations behave like this but as for magnetism, the way in which displacive pseudospins couple together determines their macroscopic properties. By analogy with the paramagnets, antiferromagnets, and ferromagnets discussed in Section 1.2.2, we have antiferroelectrics like $AgNbO_3$ and $NaNbO_3$ [125, 225], ferroelectrics like $BaTiO_3$ [226] and rarer materials like $SrTiO_3$ which stay paraelectric due to quantum fluctuations down to low temperature [227]. The symmetry breaking seen in the ferroelectric materials is probably the most practically useful.

I will focus in this section on a particularly useful and intriguing family of ferroelectrics called the relaxors. This family includes some of the most commercially

important ferroelectric materials: PZT, PZN, and PNM are solid solutions made up of various off-centering species Pb, Zr, Ti, Nb, Mg, etc., with names represented by the first letter of their chemical symbol (so PZT is $Pb[Zr_xTi_{1-x}]O_3$ etc.). The interaction between the offcentering behaviour of different cations make these systems reminiscent of the Griffiths phases discussed in Section 1.2.5, with the potential to exhibit regions in their structure with different compositions (even the rare regions noted by Griffiths) [230]. These materials are highly effective in piezoelectric response (their polarisation–strain coupling) [231], making them effective sensors and may be effective energy storage materials (because of their strain–energy coupling) [232].

Given the importance of these materials, what is surprising is the lack of consensus about their structure and the mode of their ferroelectricity. One thing that is clear is that these materials are not always equilibrium states, meaning that there is history dependence to their behaviour [233], and it has been noted that the materials may be in nonergodic pseudospin-glass like states [234] but this description is disputed [235].

The pseudospin representation of these systems can be useful in understanding their behaviour. It has been understood for some time that unlike simple ferroelectric materials, which contain macro-domains with electric polarisation, Most commonly, the displacement correlations in PMN are perceived to be manifested as polar nanoregions (PNR), several nanometers in size, which emerge below the so-called Burns temperature of $\sim 620\,\mathrm{K}$ [233, 236, 237]. The clearest evidence for this comes from scattering experiments (both X-ray [238] and neutron [237] [Fig. 1.20(a)]). Another controversy in the field is the question of how these nanodomains are arranged in space. The lack of understanding about the shapes, growth, and dipole patterns of polar nanoregions has led to the characterization of relaxors as 'hopeless messes' [239]. Are there small regions of polarity embedded in a non-polar matrix [Fig. 1.19(c)] or is there no medium separating the polar nanoregions [Fig. 1.19(d)]?

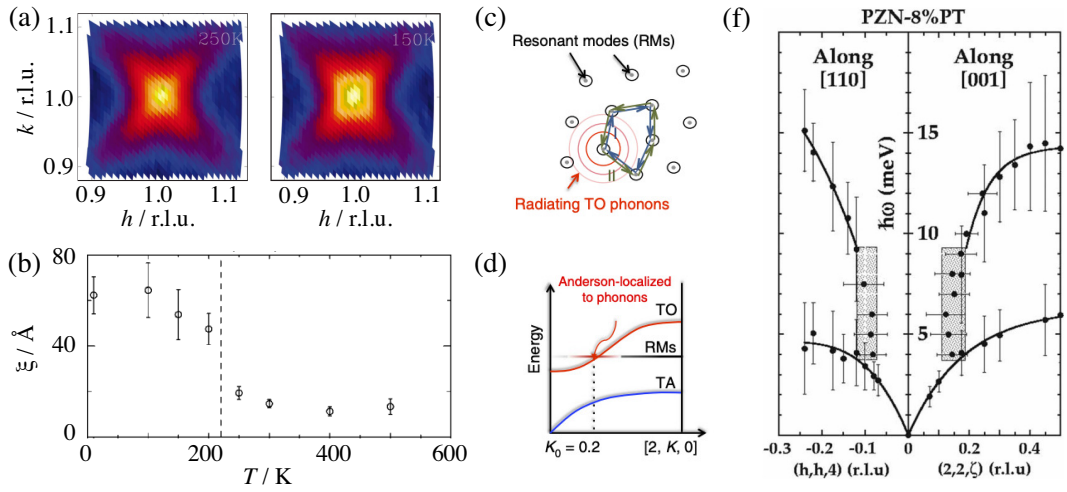

Figure 1.20: Anomalous scattering signatures of polar nanoregions in relaxor ferroelectrics. (a) Elastic neutron scattering measured near the $\langle 100 \rangle$ peak in PMN shows a butterfly form above and below the transition temperature. (b) The associated correlation length remains many unit cells far above the transition temperature $T_C = 213\,\mathrm{K}$. Reproduced from Ref. 236. (c) Anderson localization scheme for ferroelectric TO phonons eminating from and then scattered by resonance modes. Because they remain in phase, radiating ferroelectric phonons following two equal but opposite scattering paths (I, II) constructively interfere on returning to the source. (d) Characteristic inelastic scattering associated with the localisation scheme: Anderson phonons decay with a Lorentzian around the crossing point. (e) The waterfall effect measured by neutron scattering. The waterfall regions around [-0.1,-0.1,4] and [2,2,0.2] see a vertical diffusion. Solid dots represent positions of peak scattered neutron intensity taken from constant-Q and constant-E scans at 500 K along both [110] and [001] symmetry directions. Reproduced from [240].

Evidence for the former comes from the reverse Monte Carlo refinement of 3D X-ray scattering patterns [229]. A plane of the configuration obtained by this method is plotted in Figure 1.20(e), showing a clear separation between polar nanoregions and a nonpolar matrix.

An emerging view, which contradicts the glassy view of nanoregions held historically [234], is that the features emerge dynamically. This concept could help to reconcile the two cartoons proposed by Takenaka [66] [Fig. 1.19(c–d)]. Different measurements are taken with different energy resolutions meaning that they represent averages of the crystal structure for different amounts of time [241]. If the nanodomains of Figure 1.19(d) are constantly in motion, they would average to form a picture similar to that of Figure 1.19(c) over a certain amount of time. Since the

X-ray scattering represents such a time average, the RMC refinement to its scattering data would show regions where the average displacement is low, since they are constantly fluctuating between different polarisations [241].

A recent inelastic neutron scattering study by Manley and collaborators suggests that dynamics could even stabilise the nanostructure present in relaxor PMN-30%PT [242]. The observation of a localised 'resonant mode' was made at $\mathbf{Q} \approx [2, 0.2, 0]$. Fitting the mode to an 'Anderson localised' form, [Fig. 1.20(d)], indicates that the localisation length of the mode is very similar to the size of the nanodomain, suggesting the picture in Figure 1.20(c) [243]. Another important, and perhaps related, inelastic feature present is the sharply dispersing waterfall-like feature [240]. This feature must be related to strong anharmonicity as its presence in a harmonic crystal would imply infinite force constants, and the feature can be produced by a model coupling the pseudospin 'central' mode to the transverse acoustic branch [244].

1.4.3 Orientational Pseudospins

The analogy between spins and pseudospins is perhaps better displayed by those who take the form of fixed-length vectors. A clear example of this is given by the orientational glasses. Cyanide is the simplest dipole moment which is a molecule, making it an excellent ingredient to realise magnetic models.

An example of this is the solid solution $K(CN)_xBr_{1-x}$, which by analogy with the spin glasses can be understood as an 'orientational glass' [246–248]. In the $x = 1$ end member of the series, CN orientations are disordered at high temperature. At intermediate temperature, they partially order in the fashion shown in Figure 1.21(a), while still being disordered between up and down orientations [245]. At the lowest temperatures, these dipoles order in the 'antiferroelectric' manner shown in Figure 1.21(b), which is analogous to the antiferromangetic order which could be seen in spin systems with similar geometry. By doping $(CN)^-$ with the spherically symmetric Br^- anion, a behaviour somewhat analogous to the magnetic dilution

discussed in Section 1.2.5 can be realised. As one might expect for an orientational glass, increasing x suppresses the average interaction strength (measured via a Curie law from the dielectric susceptibility) [Fig. 1.21(c)]. This can be seen in the elastic neutron scattering [Fig. 1.21(d)], which shows a diffuse maximum at 51 K [246].

The key omission in spin glass models of the kind discussed in Section 1.2.5 for applications to $K(CN)_xBr_{1-x}$ is the interplay between pseudospin dynamics and the lattice dynamics. To model the effect of pseudospin disorder on inelastic neutron spectrum (a model developed in the context of an occupational pseudospin model, KH_2PO_4 [249, 250]) one can couple the pseudospin reorientation motion to the lattice dynamics. This model had some success describing the very dilute ($x = 0.03, 0.04$ and 0.05) members of this series, where cyanide dipoles were essentially isolated

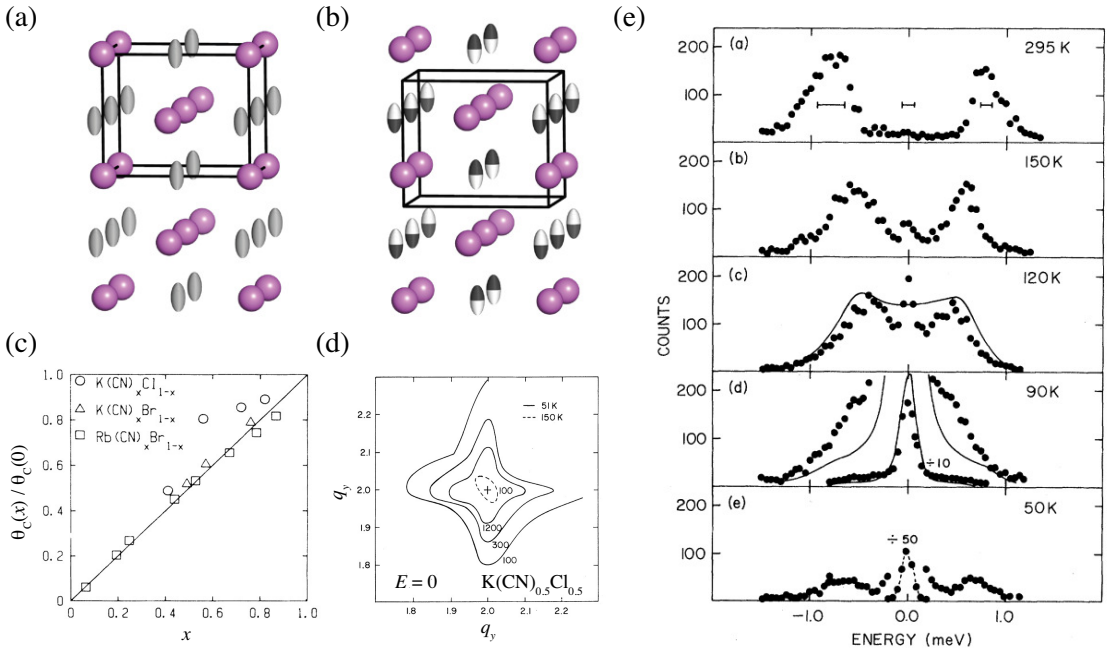

Figure 1.21: (a) The intermediate temperature crystal structure of KCN, K shown as pink spheres and the cyanide anion shown as gray ellipsoids, disordered between up and down orientations. (b) The low temperature, ordered phase of KCN with the N and C end of the anions shown in white and black, respectively. (c) The trend in normalised Θ_C, showing that the $K(CN)_xCl_{1-x}$, $K(CN)_xBr_{1-x}$, $Rb(CN)_xBr_{1-x}$ all show the same linear trend in transition temperatures, reproduced from Ref. 245. (d) Elastic scattering near the 220 peak in $K(CN)_{0.5}Cl_{0.5}$ from Ref. 246. (e) Inelastic neutron scattering of the antipolar phonon mode ($Q = (2.0, 1.9, 0)$) in $K(CN)_{0.5}Cl_{0.5}$, reproduced from Ref. 246.

[247], but theory failed to understand the complex evolution of $S(Q, E)$ for the $x = 0.5$ member of the series [Fig. 1.21(e)] [246]. Qualitatively, we can describe the inelastic scattering results as a dampening (i.e. a broadening in energy) and a softening (i.e. a reduction in energy) of the phonon on cooling accompanied by the emergence of a quasielastic central mode (a mode centred at $E = 0$, but with an energy width larger than the resolution function). The behaviour seen here is qualitatively different from the soft mode transitions [Figure 1.16(b)] in the considerable broadening ('overdamping') and the emergence of a central mode.

In order to understand the pseudospin dynamics of cadmium cyanide, Coates and coworkers [65] developed a model based on the spin ice Hamiltonian of Ramirez and coworkers [111],

$$\mathcal{H} = -J_{\text{eff}} \sum_{\langle ij \rangle_{\text{inter}}} \mathbf{S}_i \cdot \mathbf{S}_j + D \sum_{\langle ij' \rangle_{\text{intra}}} \mathbf{S}_i \cdot \mathbf{S}_{j'} - \Delta \sum_i (\mathbf{S}_i \cdot \hat{\mathbf{z}})^2. \tag{1.40}$$

with three parameters J_{eff}, D and Δ. This Hamiltonian treats two sets of nearest neighbour interactions inequivalent, as shown in Figure 1.22(a). The interaction strength within the framework J_{eff} involves neighbours denoted $\langle ij \rangle_{\text{inter}}$ and the interaction between frameworks D involves neighbours denoted $\langle ij \rangle_{\text{intra}}$. The anisotropic term Δ is far greater than the other terms in the Hamiltonian, forcing cyanide molecules to lie almost exactly linearly along Cd–C–N–Cd. In spin ice models, this term acts to suppress ferromagnetic order [251]. This Hamiltonian truncates dipolar interactions at the nearest neighbour strength, which is a reasonable assumption since the next nearest neighbour is $\sim 20\,\%$ of the strength of the nearest neighbour interactions [69] and studies show that the further dipolar interactions are largely self-screening [252].

The three parameters of Equation (1.40) were parametrised using an NMR study. Previous estimates for the preference of ice rules ($J_{\text{eff}} = 168\,\text{K}$) came from NMR [109, 112], Coates and collaborators obtained a similar number, $J_{\text{eff}} = 205\,\text{K}$ [65]. An accurate estimate for Δ could be obtained from the temperature dependence

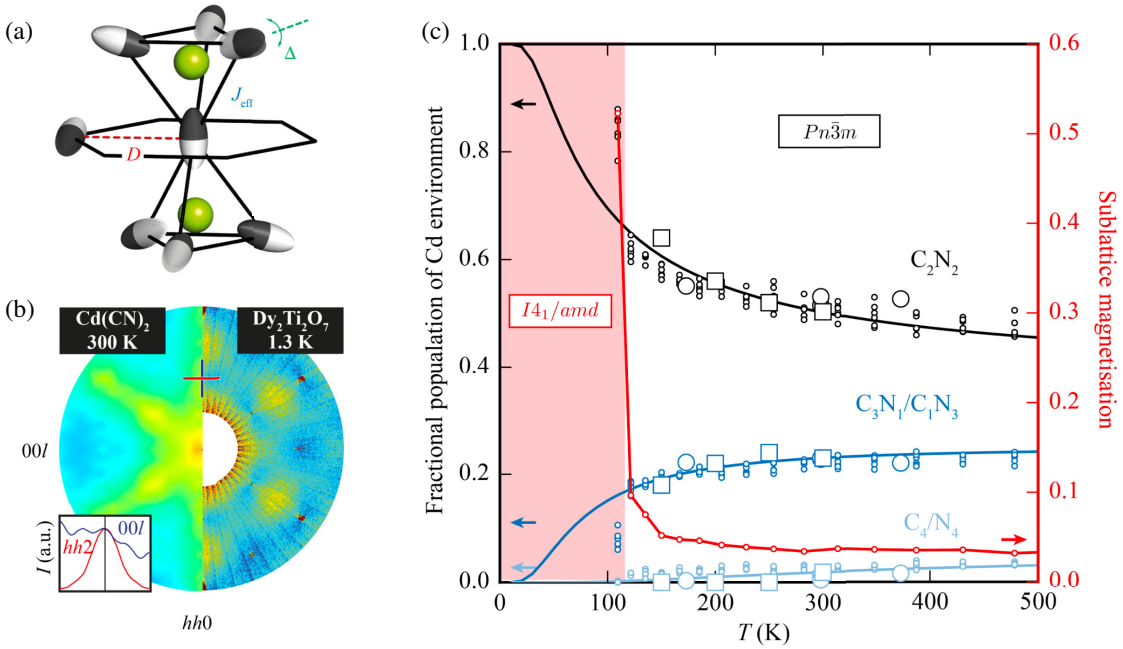

Figure 1.22: (a) Schematic representation of the single ion term (Δ) pairwise intraframework interactions (J_{eff}) and interframework interactions which are mediated by dipolar exchange (D). (b) Effective magnetic diffuse scattering pattern in the hhl plane from a single framework of the pyrochlore structure in the $Cd(CN)_2$ model at 300 K, compared with measured data in $Dy_2Ti_2O_7$ at 1.3 K [253]. The characteristic broadened pinch points are examined with cuts in the inset. (c) Temperature dependence of population of different Cd coordination environments C_4/N_4, C_3N/N_3C and the ice-rules obeying C_2N_2, as determined from MC simulations, neutron PDF measurements, magic angle spinning NMR measurements and combined with the fit of a non-interacting model to NMR data (solid line, Ref. 112). The sublattice magnetisation from the MC simulation is shown alongside, as calculated from MC simulations, representing an order parameter for the $Pn\bar{3}m \rightarrow I4_1/amd$ phase transition. Reproduced from Ref. 65.

of the the rate constant for cyanide flips. 1D selective ^{113}Cd EXSY measurements allowed the rate of CN– flips to be tracked experimentally at different temperatures; from a linear fit over the range 62–85 °C one can obtain a $\Delta = 8800 \pm 600$ K. The dipolar interaction strength $D = 85$ K can be obtained directly from the the dipole moment of cyanide (1.0 D) and the electrostatic equivalent of Equation (1.13).

This experimentally determined set of parameters ($J_{\text{eff}} = 205$ K, $D = 85$ K and $\Delta = 8,800$ K) were found to be consistent with DFT calculations. In order to estimate the dependence of internal energy on cyanide decoration, the relaxed QC energies of a range of small single- and double-network $Cd(CN)_2$ unit cells with

different CN^- orientation decorations were calculated and the Hamiltonian of Equation (1.40) was fitted with the usual three free parameters. In this way, Coates and collaborators were able to obtain $J_{\text{eff}} = 191\,\text{K}$ and $D = 93\,\text{K}$, [65]. To estimate Δ, nudged elastic band energies were calculated as the cyanide ion was flipped, obtaining another estimate of the activation energy for flips. This value $\Delta = 12,800\,\text{K}$ was also consistent with experimental measurements. DFT calculations were made more complex because of the sensitivity of these values (and the nature of the ground state) to the type of functional used [110]. For this reason, the paper (and subsequently my treatment in this thesis) took the experimental values of the parameters.

The model reproduces the cyanide ordering and temperature of the $Pn\bar{3}m \rightarrow I4_1/amd$ phase transition seen on cooling (discussed in Section 1.1.4). The temperature dependence of the model was probed via Monte Carlo simulations using the parametrised Hamiltonian, as shown in Figure 1.22(b). The sublattice magnetisation measures the extent of the phase transition, which is only significant for $T < T_{\text{C}} \simeq 130\,\text{K}$. This value is remarkably similar to the experimental phase transition temperature of $T_{\text{C}} \simeq 150\,\text{K}$. Above T_{C} a significant percentage of environments ($\sim 60\,\%$) obey ice rules [Fig. 1.22(b)]. Indeed the magnetic diffuse scattering calculated from MC configurations reproduced the pinch points seen in spin ice material $Dy_2Ti_2O_7$ [Fig. 1.22(c)]. This is because the Hamiltonian of $Dy_2Ti_2O_7$ is has interaction energies which mirror those in $Cd(CN)_2$: $J_{\text{eff}} = 3.3\,\text{K}$, $D = 1.41\,\text{K}$ and $\Delta \sim 200\,\text{K}$ [254, 255]. Crucially the ratio of interactions ($D/J_{\text{eff}} = 0.43$ and $\Delta/J_{\text{eff}} = 61$) is the same as in $CdCN_2$, where $D/J_{\text{eff}} = 0.49$ and $\Delta/J_{\text{eff}} = 67$ but the absolute scale of the interactions is roughly 60 times greater. This puts the physics of $Cd(CN)_2$ at the thermal scale of room temperature and (crucially for this thesis) on a similar energy scale to the lattice vibrations. The effect of order-disorder behaviour resulting from pseudospin orientations on the lattice dynamics (as has been studied already in the cyanide orientational glasses) will prove to be essential to understanding the behaviour of $Cd(CN)_2$.

1.5 Properties of Interest

The system of interest to the thesis exhibit disordered structures which lead to some useful properties. In this section, I will consider the origin of each property based on the theories introduced earlier, define quantitative measures of the properties, and touch on approaches to designing new functional materials.

1.5.1 Permanent Magnetism

By far the most important magnetic materials are those which are capable of storing a permanent magnetic state. These 'permanent magnets' are so ubiquitous in modern life that it would be impossible to imagine society functioning without them. We have already seen in Section 1.2.2 the strategies for designing permanent magnetism: it can arise due to the long-range ordering of ferromagnetic interactions (ferromagnetism); antiferromagnetic interactions with imbalanced spins (ferrimagnetism); or the competition of symmetric and antisymmetric interactions (canted antiferromagnetism). In each case, the magnetic unit-cell has some non-zero magnetic moment associated with it. This magnetic moment is 'permanent' in the sense that the time expected for the magnetisation of a macroscopic sample to spontaneously reverse is much longer than the age of the universe [145].

Given that permanent magnetism is present, how can we quantify its strength? Naively, one may expect to directly measure the microscopic remanent magnetisation shown in Figure 1.7 directly from the ZFC/FC experiment. However, real samples are rarely prepared as single magnetic domains but rather contain statistically many magnetic domains, which average to give a magnetisation orders of magnitude smaller than the microscopic magnetisation expected from theory.

The hysteresis experiment [Fig. 1.23] offers the solution, by first applying a strong magnetic field, which hopes to saturate the magnetisation of the sample. Then, when the field is removed, one expects one magnetic domain to be present so that the residual magnetisation (after accounting for internal fields as best as possible)

is expected to be representative of the bulk magnetisation of the zero-field state. In practice, it is not always possible to remove all of the domains—as is shown ideally in the blue inset of Figure 1.23—so the estimate of M_{res} tends to be smaller than the microscopic magnetisation of individual domains. However, this value represents the maximum magnetisation practically storable in a material and so is actually more important than the microscopic value. Understanding the mesoscopic domain structure of magnets is essential to predicting the behaviour of magnets, but is beyond the scope of this thesis.

In Chapter 5 of this thesis, I consider the percolation induced ferrimagnetism (PIF) mechanism of introducing permanent magnetism into antiferromagnetic compounds, first described by Timonin [405]. The background of this theory and its application to the (Gua)Mn/Fe(HCOO)$_3$ series are given in detail in the chapter.

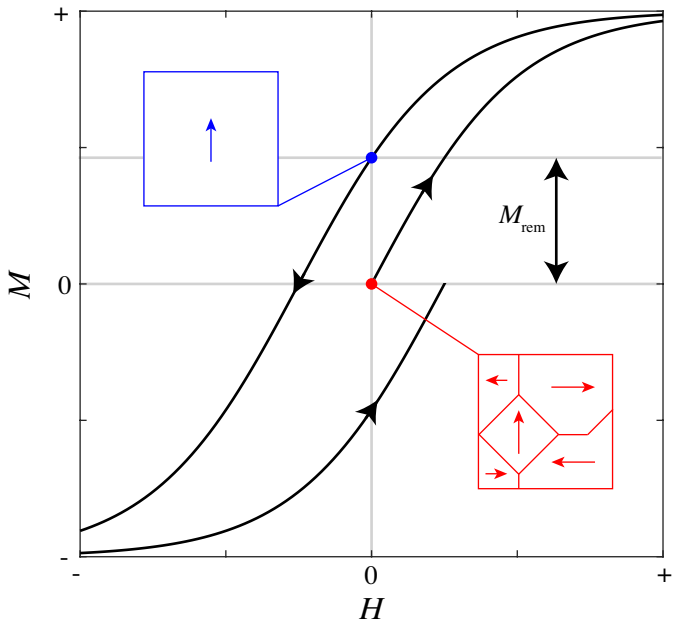

Figure 1.23: Schematic showing hysteresis measurement of magnetisation curves and detailing the remanent magnetisation. The field is cycled through $H = 0 \rightarrow +H_{\text{sat}} \rightarrow -H_{\text{sat}} \rightarrow 0$, with the order of this cycling indicated with arrows. Insets show the domain structure that is present at the start (red) and after the first magnetisation cycle (blue).

1.5.2 The Magnetocaloric Effect

The magnetocaloric effect (MCE) can be used to drive a heat cycle. The principle, shown in Figure 1.24, is the same as for conventional refrigeration, where the simultaneous entropy and volume change between an ordered liquid and disordered gas refrigerant can drive a heat cycle. Here instead the coupling between an entropy change on magnetisation (*ii*-*iii* in the figure) can be used to induce adiabatic cooling (*i*-*ii*).

In a simple sense, this can be understood in the paramagnetic models of Section 1.2.1. In the absence of applied field, these models are fluctuating between a number ($W(0)$) of states. When field is applied, the number drops ($W(\mathbf{H} \to \infty) = 1$). For N isolated ions with angular momentum J this number is $W(0) = (2J+1)^N$. The corresponding maximum entropy change on magnetisation

$$\Delta S = -k_{\mathrm{B}} \log \frac{W(0)}{W(\mathbf{H})} \to -N k_{\mathrm{B}} \log(2J+1). \tag{1.41}$$

In general, an entropy change on the application of field can be used to drive a heat cycle, which brings us to our first disorder induced property: the magnetocaloric effect. This heat cycle has an important application in cooling materials lower than the liquid helium temperature [145].

Magnetocaloric cooling works by alternating steps of isothermal magnetisation and adiabatic demagnetisation. This can be seen on plotting $S(T)$ for various values of the magnetisation. In the isothermal magnetisation step, which is done slowly in thermal contact with the liquid helium heat bath, entropy is removed from the sample because the magnetic moments align with field and absorbed by the helium bath. The maximum amount of entropy removed from the system is given by Equation (1.41). In the next step, adiabatic demagnetisation, sees the instant removal of the magnetic field, without thermal contact. Now the magnetic entropy returns to its starting value, exactly balanced by a decrease in the other entropy in the sample:

spin wave, lattice vibration, etc. One can see this in Figure 1.24(b), the sample is cooled.

The principle here applies beyond isolated ions: maximIsing the degeneracy at low compared to high field ($W(0)/W(\mathbf{H})$) is the key strategy to designing effective magnetocaloric materials.

In interacting spin systems, the ordering discussed in Section 1.2.2 leads to a lack of entropy at zero field and low temperatures. This is modelled in Figure 1.24(b) as a small residual magnetic field at $\mathbf{H} \sim 0$, similar to the mean-field approach discussed in Section 2.4. More accurately, if one can measure or simulate the magnetisation as function of field and temperature $M(H,T)$, as well as the heat capacity $C(H,T)$, it is possible to directly calculate ΔT and ΔS as they appear in Figure 1.24 directly:

$$\Delta T = -\int_{H_0}^{H_1} \left(\frac{T}{C}\right)\left(\frac{\partial M}{\partial T}\right)_H dH, \tag{1.42}$$

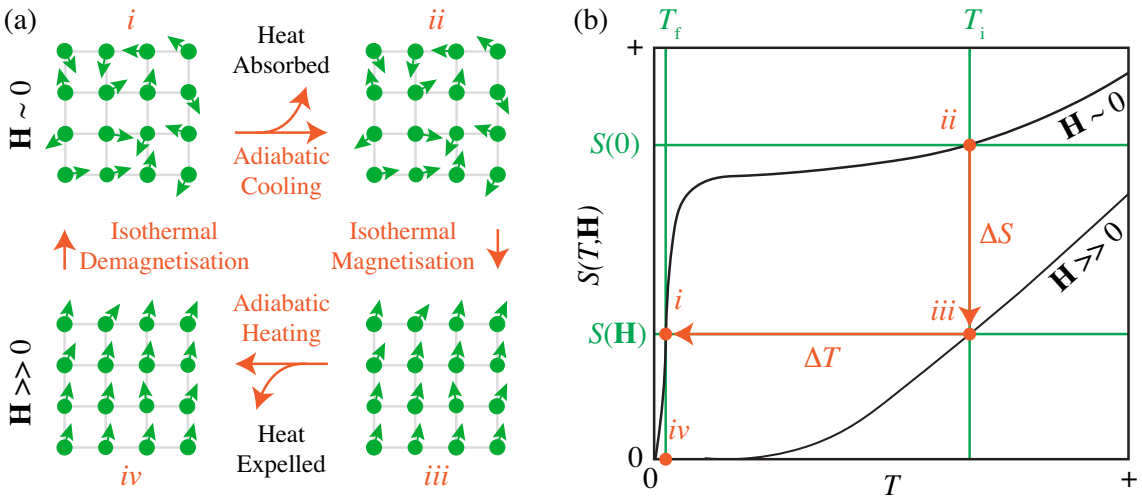

Figure 1.24: (a) Schematic of the isothermal magnetisation process, where the cycle between states (*i*,*ii*,*iii*,*iv*) is used to dive a temperature cycle. (b) The entropy of an idealised paramagnetic salt, with and without a large magnetic field applied. The $\mathbf{B} \sim 0$ curve includes a very small field to model the intrinsic residual magnetisation. The model assumes total angular momentum $J = \frac{1}{2}$ and includes an $S_{\text{lat}} \propto T^3$ term to model the lattice dynamics. The path shown in orange shows the magneto caloric cooling strategy: the path from a to b is isothermal magnetisation, involving entropy change ΔS and from b to c is adiabatic demagnetisation. Adapted from Blundell [145].

$$\Delta S = \int_{H_0}^{H_1} \left(\frac{\partial M}{\partial T} \right) dH. \tag{1.43}$$

Using this approach, it is possible to answer important questions about the strength of MCE in materials: what materials are more effective magnetocalorics? Which interactions lead to strong magnetocaloric effects? How does the strength of the MCE vary with composition? Which lattices give the most effective MCE?

This last question turns out to be particularly useful as the suppression of order seen in geometrically frustrated materials [§1.2.4] can enhance the MCE considerably [256, 257]. This was noticed by Zhitomirsky in 2003 [258] in a set of MC simulations on various lattices. Figure 1.25 shows the enhancement of temperature change seen in the geometrically frustrated pyrochlore and garnet lattices relative to the frustrated cubic lattice.

1.5.3 Specific Heat

The role of C in Equation (1.42) is an example of the importance of the specific heat in many other useful properties. This is unsurprising since the transfer of heat to

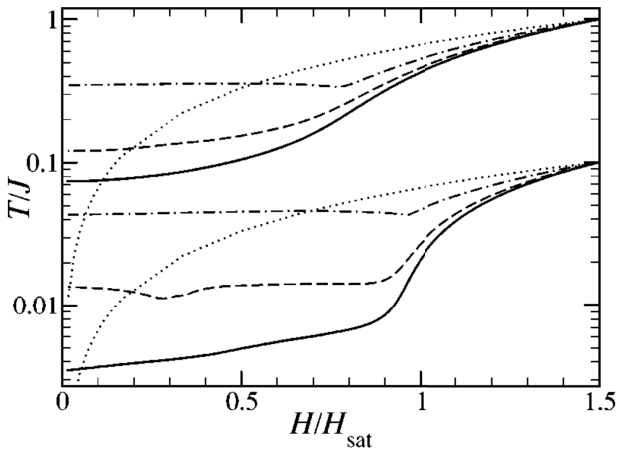

Figure 1.25: Temperature variation during adiabatic demagnetization of a pyrochlore (full line), a garnet (dashed line), and a cubic (dot-dashed line) antiferromagnet. Dotted lines represent demagnetization of an ideal paramagnet (T/H = const). Two traces are shown at initial temperature $T = 1$ and $0.1J$.

work is the basis for many of the thermodynamic properties of matter. We saw in Equation (1.36) that the lattice heat capacity played an important role in thermal transport: if there are no modes in which to put energy, no heat transport will occur. In the most basic sense, materials with a high heat capacity have a high 'inertia' against temperature fluctuations making it an important property in systems (for example, buildings) which need to hold a constant temperature [259].

Heat capacity is also an important characterisation tool: where a phase transition occurs, there will usually be a transfer of heat to the surroundings, the amount of heat associated with the transition may contain information about the degree of freedom being (dis)ordered [260]. Heat capacity also provides a convenient way to measure entropy changes [§2.3], with applications in caloric materials.

Another common way to characterise heat capacity behaviour is to find regions in which the specific heat obeys a power law as a function of temperature ($C \propto T^{\alpha}$). The value of the exponent α contains information about the nature of the degree of freedom being disordered. For example, in the high temperature limit of the heat capacity for a two level system, $C \propto T^{-3}$ [261]. This relation holds for any system which Fermions (in this case, Phonons) can be freely populated, so it is seen at the high temperature limit of a phase transition. By contrast, bosons have a constant heat capacity in the high temperature limit (i.e. $C \propto T^{0}$) since one can always populate more.

Traditionally, a linear dependence of low-temperature heat capacity ($C \propto T^{1}$) has been linked to conduction electrons in metals [262, 263], but it has also been found in nonmetallic materials [264, 265]. In metals, this linearity arises from electrons populating energy levels above the Fermi level [262, 263]. Examples of this have been seem in spin glasses, such as the random magnetic anisotropy alloy Er_xNi_{1-x} and the weakly disordered ludwigite $Co_3Mn_3(O_2BO_3)$ [266, 267]. The linear heat capacity is perhaps a more famous signature of quantum spin-1/2 chains, where it is used as evidence of the gapless excitations which make the systems interesting [268].

The electronic heat capacity of disordered graphene, inorganic insulators, and solid solutions of $(U_{1-x}Th_x)O_2$ which have been irradiated to induce disorder all show the same $C \propto T$ dependence [269–271]. We will see in Chapter 4 another example of a system where linear heat capacity emerges as a result of some fundamental disorder. In many of these cases, a linear heat capacity is used as a signature of whichever kind of disorder is being studied.

1.5.4 Thermal expansion

Thermal expansion, the change of the size of a system with temperature, is an important material property to materials. Understanding and designing a material's response to temperature is critical to a number of applications from metrology—where precise knowledge of a materials dimensions are essential—to civil engineering—where poor predictions of the extent of thermal expansion can have devastating consequences. For a material with molar volume V, we can define an expansion coefficient

$$\alpha_V = \frac{1}{V}\frac{\partial V}{\partial T} \tag{1.44}$$

Most materials, like metals and conventional ceramics have a positive value. $\alpha_V = +20\,\mathrm{MK}^{-1}$ Titanium [272]. Composites of NTE materials with PTE can be created to design materials with zero thermal expansion.

Phonon-driven thermal expansion is of such importance to Chapter 6 that it requires its own section. We have seen how the framework materials of interest to this thesis show extreme thermal expansion behaviour due to the softness of their frameworks. Here, I will derive the origin of this behaviour in the quasi-harmonic approximation, starting from an expression for the free energy of a harmonic crystal. The volume thermal expansion (α_V) can be rewritten

$$\beta = K_T \left(\frac{\partial P}{\partial T}\right)_V = -K_T \frac{\partial^2 F}{\partial T \partial V}, \tag{1.45}$$

where K_T is the isothermal compressibility. We will work within the high temperature limit of Equation (1.34),

$$F(V) = E(V) + \frac{1}{N} \iiint \sum_{\nu} k_{\mathrm{B}} T \log \left(-\frac{\hbar \omega_{\nu}(\mathbf{k})}{k_{\mathrm{B}} T} \right) \mathrm{d}\mathbf{k}, \tag{1.46}$$

allowing an expression for the thermal expansion to be found,

$$\beta = -\frac{K_T k_{\mathrm{B}}}{NV} \iiint \sum_{\nu} \gamma_{\nu}(\mathbf{k}) \mathrm{d}\mathbf{k}, \tag{1.47}$$

in terms of mode Grüneisen parameters,

$$\gamma_{\nu}(\mathbf{k}) = \frac{V}{\omega_{\nu}(\mathbf{k})} \frac{\partial \omega_{\nu}(\mathbf{k})}{\partial V}. \tag{1.48}$$

It is these mode Grüneisen parameters which allow us to predict which kinds of modes lead to negative and positive thermal expansion. So we can see that materials exhibiting large negative thermal expansion should have low energy modes which change considerably in energy with temperature. This was the same conclusion that we came to in Section 1.1.2 about the framework materials.

The mechanism for phonon driven NTE can be predicted theoretically, via DFT or molecular dynamics methods [§2.6] and also probed directly using pressure dependant inelastic neutron scattering [§2.1.4]. Both methods allow for the direct probing of which modes are responsible for NTE. In this way we can understand the structural motifs which lead to NTE in systems and better design NTE materials in the future.

1.6 Aims and structure of this thesis

The relationship between accurate descriptions of a material's structure and its properties ('structure–property relationships') has been crucial in the development of many materials central to 21st century life. However, the focus of structure property relationships has largely been on ordered crystalline solids, both because

crystallographic techniques make studying periodic systems easier and because the tools to understand the properties of non-periodic solids are less well developed. Is it possible that we have overlooked many 'disorder–property relationships' for this reason?

The central question of this thesis is how does spin and pseudospin disorder govern the strength and behaviour of the physical properties detailed in the previous section. I will examine the four crystalline framework materials detailed in Section 1.1.4, each of which exhibits either disordered magnetism or pseudospin disorder. Table 1.1 sets out the properties investigated in each system. I aim to answer three questions: (i) what (pseudo)spin disorder is present; (ii) what aspects of the composition of the system leads to these properties; and (iii) what implications does pseudospin disorder have for the properties of the materials studied? I aim to develop tools to aid the study of disorder-property relationships, which will have applicability beyond the four systems which concern this thesis. The ultimate hope with this approach is that by understanding the relationship between the structures of the systems and their properties, we should be able to develop new systems which outperform existing materials.

Chapter 3 investigates $NaMn(HCOO)_3$, in which the implications of geometric frustration for magnetic order are studied. The aim of this study was to develop a model to describe the magnetism in $NaMn(HCOO)_3$, understand the behaviour of this model and the material under field and therefore rationalise the strength of the magnetocaloric effect in this system. This allows for speculation about what types

Framework Material	Disorder of...	Property investigated
$NaMn(HCOO)_3$	Heisenberg spins	Magnetocaloric Effect
$Tb/Y(HCOO)_3$	Ising spins, composition	Heat Capacity
$(Gua)Mn/Fe(HCOO)_3$	Heisenberg spins, composition	Ferrimagnetism
$Cd(CN)_2$	Cyanide pseudospins	Thermal expansion

Table 1.1: An overview of the four systems studied in this thesis, indicating the degree(s) of freedom investigated and the subsequent property investigated.

of systems may show stronger magnetocaloric effects.

The second set of results [Chapter 4] combines the anomalous properties seen in one-dimensional, geometrically frustrated and dilute magnetic systems. The aim was to develop a theoretical approach to understand the behaviour of these systems and explain the heat capacity data measured for the $Tb_{1-x}Y_x(HCOO)_3$ series. The analysis in this section is intentionally broad, with applications in both spin and pseudospin physics. The hope is that, by understanding the behaviour of dilute q-1D systems, we can make predictions about the behaviour about a broad set of physical systems.

The solid solution (Gua)Mn/Fe$(HCOO)_3$ is the subject of study in Chapter 5. The implications of the B-site ordering noted by Boström and coworkers [104] for the magnetism is investigated both using magnetometery and MC simulations. The aim is to extend the percolation induced ferrimagnetism framework which has been well studied in the context of inorganic materials to hybrid inorganic-organic systems.

Chapter 6 comprises an investigation of lattice dynamics in $Cd(CN)_2$. The central aim is to understand the role of cyanide order (if any) in the lattice dynamics of the system. This would be useful to shed light on the mechanism of NTE in $Cd(CN)_2$, and also help to explain why it is such a successful NTE material. The first aim is to gain an experimental measure of the Grüneisen parameter of Equation (1.48). I also carry out a lattice dynamics measurement as a function of temperature and investigate the anomalous features of this experiment using a combination of MC and SCLD simulations. In order to compare with experiment a variation of SCLD to deal with polycrystalline systems was developed.

The thesis concludes with a discussion of the work as a whole which categorises the disorder-property relationships studied and how the results contained may inform future research.

Chapter 2

Methods

2.1 Neutron Scattering

2.1.1 Overview

For over 100 years, scattering has been a primary tool in understanding the structures of liquids, solids and cooperatively disordered states in between. Hot neutrons of the kind produced by reactor (§2.1.3) and spallation (§2.1.4) sources have wavelengths $\sim$ Å and energies $\sim$ meV. These length and time-scales ($\sim$fs) make neutrons ideal to probe the structure and dynamics in framework materials (§1.1). The magnetic moment of the neutron allows for the study of magnetic structure and dynamics [69]. In this section, I will give an overview of the theory and practice of neutron scattering as used in the thesis, largely following standard texts on the subject [273, 274].

The basic principle of the neutron scattering experiment is shown schematically in Figure 2.1. Neutrons are first generated with an appropriate distribution of momenta ($\mathbf{k}_\mathrm{i}$). These particles can be represented as wavepackets with wavevector $\mathbf{k}_\mathrm{i}$, this wave picture helps explain the interference which is central to the neutron scattering experiment. The neutrons are directed towards a sample and scattered with final momentum $\mathbf{k}_\mathrm{f}$. Finally, the beam hits a detector, which spans solid angle $\mathrm{d}\Omega$, and the final wavevector may be measured. Because the overall energy and momentum must be conserved, we can work out the energy E and momentum $\mathbf{Q}$ transferred to the sample in this scattering process using

$$E = E_\mathrm{i} - E_\mathrm{f} = \frac{\hbar^2}{2m_\mathrm{n}}\left(|\mathbf{k}_\mathrm{i}|^2 - |\mathbf{k}_\mathrm{f}|^2\right), \tag{2.1}$$

$$\mathbf{Q} = \mathbf{k}_\mathrm{i} - \mathbf{k}_\mathrm{f}. \tag{2.2}$$

Because the neutron scatters from the lattice planes coherently, the interference pattern that it makes on the detector contains information about the atomic structure and motion of the crystal.

The total intensity of scattering is measured as the 'neutron cross-section', $\sigma_{\rm tot}$, which is defined as the ratio of scattered neutrons to incoming neutrons per unit area. As such it has dimensions of area; a convenient unit being the barn $= 10^{-28}$ m^2. It is also convenient to define individual scattering b lengths for each element, which can be related to that element's total scattering via $\sigma_{\rm tot} = 4\pi b^2$. In order to resolve diffraction patterns, one needs to know the angular dependence of scattering. For this purpose, the differential scattering cross-section $\mathrm{d}\sigma/\mathrm{d}\Omega$ is defined as

$$\frac{\mathrm{d}\sigma}{\mathrm{d}\Omega} = \frac{\text{number of neutrons scattered per sec into solid angle } \mathrm{d}\Omega}{I_0 \mathrm{d}\Omega}. \tag{2.3}$$

The scattering per unit solid angle has units barns sr^{-1}. To resolve inelastic scattering, we must define a double differential cross section

$$\frac{\mathrm{d}^2\sigma}{\mathrm{d}\Omega \mathrm{d}E_{\rm f}} = \frac{\text{number of neutrons scattered per sec into solid angle } \mathrm{d}\Omega \text{ with final energy between } E_{\rm f} \text{ and } \mathrm{E_f}+\mathrm{d}E_{\rm f}}{I_0 \mathrm{d}\Omega \mathrm{d}E_{\rm f}}, \tag{2.4}$$

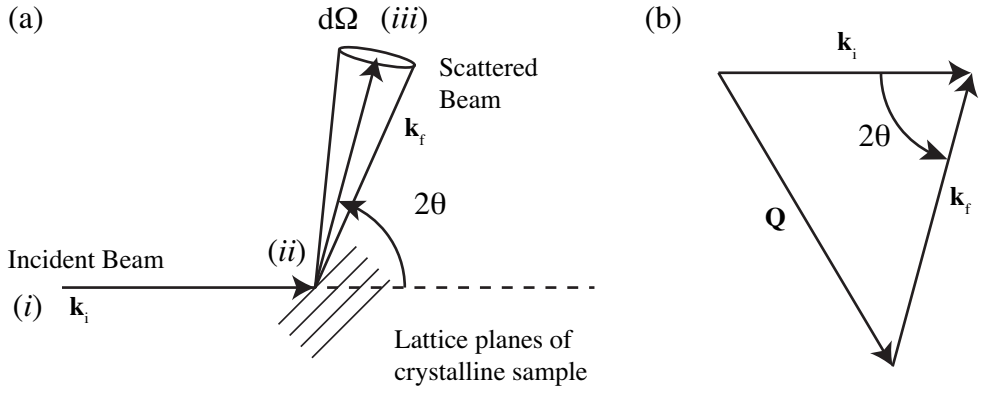

Figure 2.1: (a) Schematic overview of the neutron scattering process: neutron is generated with wavevector $\mathbf{k}_{\rm i}$ at (i), scattered by the lattice planes of a crystaine sample at (ii), emerge with wavevector $\mathbf{k}_{\rm f}$, and hit the detector with solid angle $\mathrm{d}\Omega$ at (iii). (b) A scattering triangle can be constructed from wave vectors $\mathbf{k}_{\rm i}$ and $\mathbf{k}_{\rm f}$.

which is related to the scattering function $S(\mathbf{Q}, E)$, which I will define for of a system of N atoms as

$$\frac{\mathrm{d}^2\sigma}{\mathrm{d}\Omega \mathrm{d}E_\mathrm{f}} = \frac{k_\mathrm{f}}{k_\mathrm{i}} N S(\mathbf{Q}, E). \tag{2.5}$$

There are three main classifications of neutron scattering event which concern this thesis: nuclear, magnetic and spin-incoherent. Nuclear scattering events involve the interaction of an atom's nucleus and the neutron via the Pauli exclusion force [275]. For this reason, the strength (and even phase) of such scattering, given by the scattering length b, has a complex relationship with the composition of the nucleus. The neutron is a spin–$\frac{1}{2}$ particle so it interacts with the magnetic field of both the nucleus and unpaired electrons. Nuclear spin-incoherent and magnetic scattering are the result of this interaction [218]. With a few exceptions [276], nuclear spins are completely disordered at the temperatures of interest so only contribute to the incoherent scattering. Magnetic scattering therefore refers to the contribution of unpaired electrons' spin correlations to the scattering.

Nuclear scattering arises from direct contact between the neutron and the nucleus of atoms. It requires direct contact of nucleus which occurs at ∼fm length-scales [275] so can be treated as effectively point-like scattering: this is the reason that the scattering lengths b_j are invariant to $\mathbf{Q}$. The corresponding component of the coherent scattering can be related to an important dynamic measure of the atomic structure called the Van Hove correlation function,

$$S(\mathbf{Q}, E) = \frac{1}{2\pi\hbar} \iint G(\mathbf{r}, t) \exp\left[\mathrm{i}\left(\mathbf{Q}\cdot\mathbf{r} - \frac{Et}{\hbar}\right)\right] \mathrm{d}\mathbf{r}\mathrm{d}t. \tag{2.6}$$

For a classical system, $G(\mathbf{r}, t)$ is the probability that, given that an atom is at the origin, the same or some other atom will be located at $\mathbf{r}$ at time t:

$$G(\mathbf{r}, t) = \left\langle \frac{1}{N} \int \sum_{i,j} b_i b_j \delta[\mathbf{r}' + \mathbf{r} - \mathbf{r}_j(t)] \delta[\mathbf{r}' - \mathbf{r}_i(0)] \mathrm{d}\mathbf{r}' \right\rangle. \tag{2.7}$$

For a static system, $G(\mathbf{r}, t)$ is invariant with t. In this situation, $S(Q, E)$ will only

be nonzero at $E = 0$. In this case the 'elastic scattering' is essentially the Fourier transform of $G(\mathbf{r}, 0)$,

$$S(\mathbf{Q}, E = 0) = \frac{1}{2\pi} \int G(\mathbf{r}, 0) \exp\left[\mathrm{i}\left(\mathbf{Q} \cdot \mathbf{r} - \frac{Et}{\hbar}\right)\right] \mathrm{d}\mathbf{r}, \tag{2.8}$$

which can be expanded as

$$S(\mathbf{Q}, E = 0) = S(\mathbf{Q}) = \frac{1}{N} \sum_{ij} b_i b_j \exp\left[\mathrm{i}\mathbf{Q} \cdot (\mathbf{r}_j - \mathbf{r}_i)\right] \tag{2.9}$$

or equivalently

$$S(\mathbf{Q}) = \frac{1}{N} \left| \sum_j b_j \exp \mathrm{i}\mathbf{Q} \cdot \mathbf{r}_j \right|^2 . \tag{2.10}$$

Magnetic scattering arises from the interaction of the neutron's magnetic moment with the magnetic moment of unpaired electrons. Anticipating $NaMn(HCOO)_3$ in Chapter 3, I will focus on a system where there is one magnetic scattering species (in this case, Mn^{2+}), which is fixed to occupy positions on the magnetic sublattice $\{\mathbf{r}_j\}$. In this case,

$$S(\mathbf{Q}) = \frac{p^2 \left[f(Q)\right]^2}{N} \left| \sum_j \mathbf{S}_j^{\perp} \exp \mathrm{i}\mathbf{Q} \cdot \mathbf{r}_j \right|^2 , \tag{2.11}$$

where $\mathbf{S}_j^{\perp}$ represents the projection of the spin-vector $\mathbf{S}_j$ into the plane perpendicular to $\mathbf{Q}$

This process differs from nuclear scattering in two important respects: (i) the scattering depends on the orientation of the spin vector relative to the scattering vector, making the corresponding scattering inhomogeneous in reciprocal space (and therefore containing information about the orientation of the interactions [277]); (ii) the neutron is scattered by the valence electrons rather than the nucleus, which means that the form factor $f(Q)$ is no longer flat in Q (as is the case for the scattering nuclear scattering lengths in Equation (2.11)). The form factors can be

calculated quantum mechanically but it is usually more effective to use analytical forms determined experimentally and tabulated for the elements [278].

2.1.2 Scattering from Powders

So far, I have considered the scattering from well-oriented crystals. Polycrystalline and powdered systems are made up of a statistical quantity of miniscule crystals. If it is assumed that the orientation of crystals is truly random, this powder scattering loses all dependence on the orientation of $\mathbf{Q}$:

$$S(Q) = \frac{1}{4\pi}\int_0^{2\pi}\int_0^{\pi} S\left(\begin{bmatrix} Q\sin\theta\cos\phi \\ Q\sin\theta\sin\phi \\ Q\cos\theta \end{bmatrix}\right)\mathrm{d}\theta\mathrm{d}\phi. \tag{2.12}$$

This integral can be performed analytically on Equations (2.10) and (2.11) to give the Debye scattering equation (2.13, Ref. 279) and its magnetic analogue (2.14, Ref. 280) respectively

$$S(Q) = \frac{1}{N}\sum_i b_i^2 + \frac{1}{N}\sum_{i\neq j} b_i b_j \frac{\sin Qr_{ij}}{Qr_{ij}}; \tag{2.13}$$

$$S(Q) = p(Q)^2\left[\frac{2}{3}|\mathbf{s}|^2 + \frac{1}{N}\sum_{i\neq j} A_{ij}\frac{\sin Qr_{ij}}{Qr_{ij}} + B_{ij}\left(\frac{\sin Qr_{ij}}{(Qr_{ij})^3} - \frac{\cos Qr_{ij}}{(Qr_{ij})^3}\right)\right], \tag{2.14}$$

where the spin correlation coefficients in the latter are given by

$$A_{ij} = \mathbf{s}_i\cdot\mathbf{s}_j - (\mathbf{s}_i\cdot\hat{\mathbf{z}}_{ij})(\mathbf{s}_j\cdot\hat{\mathbf{z}}_{ij}); \tag{2.15}$$

$$B_{ij} = 3(\mathbf{s}_i\cdot\hat{\mathbf{z}}_{ij})(\mathbf{s}_j\cdot\hat{\mathbf{z}}_{ij}) - \mathbf{s}_i\cdot\mathbf{s}_j, \tag{2.16}$$

where $\hat{\mathbf{z}}_{ij}$ represents the unit vector along the direction between atom i and atom j.

In practice, calculating the scattering from powders in this way works well when there is no long-range magnetic or structural order but in ordered systems, the equations converge very slowly and for finite approximations to the sum, ripples resulting from the termination of the sum dominate the signal. Instead, it is easier to calculate $F(\mathbf{G})$ at the magnetic Bragg peak positions according to Equation (2.11) and convolve with the experimental resolution function.

For ordered magnetic structures, I therefore calculate Bragg scattering in absolute units using the expression [152]

$$I_{\text{Bragg}}(Q) = C[gf(Q)]^2 \frac{2\pi^2}{nV} \sum_{\mathbf{G}} \frac{|\mathbf{F}(\mathbf{G})|^2}{G^2} \mathcal{R}(Q-G). \tag{2.17}$$

Here, C is a constant equal to 0.07265 barn, $f(Q)$ is the magnetic form factor, $\mathbf{G}$ is a reciprocal lattice vector, $\mathbf{F}(\mathbf{G})$ is the corresponding magnetic structure factor, and V is the volume of the magnetic unit cell. I used a Gaussian form for the instrumental resolution function:

$$\mathcal{R}(Q-G) = \sqrt{\frac{4\ln 2}{\pi}} \frac{1}{H(G)} \exp\left[-4\ln 2 \left(\frac{Q-G}{H(G)}\right)^2\right], \tag{2.18}$$

where $H(G)$ is the full width at half-maximum of a peak centred at $\mathbf{G}$, given by

$$H(G) = \frac{2\pi\cos\theta}{\lambda} \sqrt{U\tan^2\theta + V\tan\theta + W}, \tag{2.19}$$

with U, V, W the usual peak-width parameters obtained using conventional full-profile refinement.

2.1.3 Polarised Neutron Scattering

XYZ–polarisation analysis

Polarisation analysis allows for the separation of magnetic, spin incoherent and nuclear components of magnetic scattering. I will consider here the case of energy integrated scattering $S(\mathbf{Q})$, with no energy resolution, as calculated from Equation (2.11). The basic principle is that a magnetic scattering event may lead to a change in neutron spin while nuclear scattering never leads to this kind of change. The neutron beam may be polarised using polarising filters. By applying fields in controlled ways the orientation of spin polarisation may be rotated to some arbitrary orientation.

XYZ-analysis is an extension of this approach which allows for the separation of nuclear, magnetic and nuclear incoherent scattering [218]. This is done by comparing the intensity of spin-flip scattering when neutrons are polarised in three orthogonal directions, with geometry as shown in Figure 2.2(a). As such, the nuclear and magnetic component of $S(\mathbf{Q})$ can be calculated. The nuclear neutron scattering for $Na[Mn(HCOO)_3]$ was calculated from the XYZ-polarised neutron scattering cross-sections according to

$$S_{\mathrm{nuc}}(\mathbf{Q}) = \frac{1}{6}\left[2\left(\frac{\mathrm{d}\sigma}{\mathrm{d}\Omega}\right)_{\mathrm{nsf}}^{\mathrm{tot}} - \left(\frac{\mathrm{d}\sigma}{\mathrm{d}\Omega}\right)_{\mathrm{sf}}^{\mathrm{tot}}\right], \tag{2.20}$$

while the magnetic neutron scattering was calculated from an error-weighted average of

$$S_{\mathrm{mag}}(\mathbf{Q}) = 2\left(\frac{\mathrm{d}\sigma}{\mathrm{d}\Omega}\right)_{\mathrm{sf}}^{x} + 2\left(\frac{\mathrm{d}\sigma}{\mathrm{d}\Omega}\right)_{\mathrm{sf}}^{y} - 4\left(\frac{\mathrm{d}\sigma}{\mathrm{d}\Omega}\right)_{\mathrm{sf}}^{z} \tag{2.21}$$

and

$$S_{\mathrm{mag}}(\mathbf{Q}) = 4\left(\frac{\mathrm{d}\sigma}{\mathrm{d}\Omega}\right)_{\mathrm{nsf}}^{z} - 2\left(\frac{\mathrm{d}\sigma}{\mathrm{d}\Omega}\right)_{\mathrm{nsf}}^{x} - 4\left(\frac{\mathrm{d}\sigma}{\mathrm{d}\Omega}\right)_{\mathrm{nsf}}^{y}. \tag{2.22}$$

Here, the quantities have the same meaning as in Ref. 281 and 'sf' and 'nsf' denote spin-flip and non-spin-flip measurements, respectively.

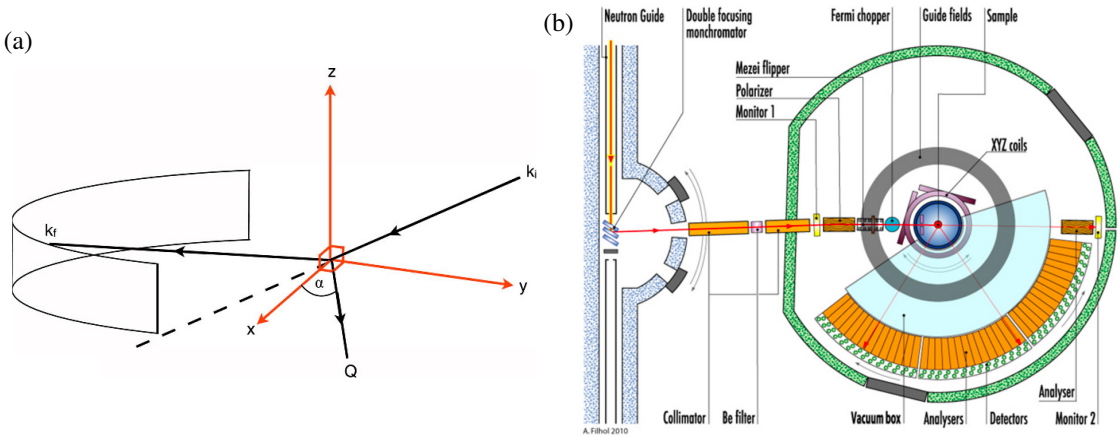

Figure 2.2: (a) Sample geometry for XYZ-analysis. (b) Schematic of the D7 diffractometer at the ILL. Reproduced from Ref. 218.

The D7 diffuse-scattering diffractometer at the ILL

In order to measure the correlations in the paramagnetic phase of $NaMn(HCOO)_3$ [Chapter 3], I required an instrument with high flux and low, well-characterised background. Thermal neutrons generated from a reactor source have a relatively stable flux. The D7 diffuse-scattering diffractometer at the Institut Laue-Langevin (ILL) was chosen for these reasons.

The design of the D7 instrument [218] is shown in Figure 2.2(b). Neutrons are first generated in the reactor of the ILL source and emerge as hot neutrons, which are passed along the neutron guide. A graphite monochromator allows an incident neutron wavelength of 3.1, 4.8, or 5.7 Å to be selected from the 'white beam', by moving the rest of the instrument to match the chosen scattering angle from the monochromator. The beam is then polarised along **z** using a supermirror of Co/Ti alloy which selects a single neutron spin state. The supermirror polariser uses a radially-focusing geometry which allows a wide (divergent) beam to be polarised efficiently [282]. The beam polarisation is preserved by applying a small magnetic 'guide field' (103 mT) along **z**. A Mezei flipper reverses the initial neutron polarisation so that both $(\mathrm{d}\sigma/\mathrm{d}\Omega)^z_{\mathrm{nsf}}$ (flipper off) and $(\mathrm{d}\sigma/\mathrm{d}\Omega)^z_{\mathrm{sf}}$ (flipper on) can be measured. Three orthogonal coils surrounding the sample apply a magnetic field which adiabatically rotates the neutron polarisation along x,y and z directions, allowing for the measurement of all six cross-sections of Equations (2.20), (2.21) and (2.22). Finally, after the incoming beam is scattered by the sample, the final neutron polarisation is analysed by a second large array of supermirrors, which are positioned in front of an array of neutron detectors covering a wide angular range. The detectors are tubes of ^{3}He, which generate energy via the nuclear reaction $^3\mathrm{He} + \mathrm{n} \rightarrow {}^3\mathrm{H} + \mathrm{p} + 0.8\,\mathrm{MeV}$ [273].

We carried out experiments—see Figures 3.3(c), 3.5, and 3.7—at two different wavelengths, $\lambda = 3.1565$ Å (at 20 K and 1.6 K) and 4.873 Å (at 1.6 K and 100 mK). Using the lower wavelength improves flux at the cost of Q resolution. This is ac-

ceptable for measuring the diffuse signals which emerge from magnetic short range order ar $T > T_{\mathrm{N}}$, since the signals were broad in Q. The later experiment, which was cooled to a temperature of 100 mK using an Orange Cryostat, required higher Q-resolution so $\lambda = 4.873$ Å was chosen. In each case an empty can was measured as well as a sample of vanadium with the same geometry, allowing for the subtraction of sample environment and approximate normalisation of scattering.

Data Treatment

Normalisation to vanadium standard, subtraction of the background signal and weighted sum of Equations (2.22) and (2.21) were carried out using the Large Array Manipulation Program software of the ILL [283]. In order to obtain quantities in absolute units, a scale-factor was fitted to the nuclear scattering via a Rietveld refinement using FullProf [284]. Since the Q-range available for refinement was small, the structure model (see Table B1) was fixed to that obtained in Ref. [89], although the cell parameter and various diffractometer constants were allowed to refine. The details of this refinement are given in Appendix B.1.

2.1.4 Inelastic Neutron Scattering

The Van Hove correlation function (2.7) contains information about the motion of atoms, as reflected in the frequency dependence of $S(Q, E)$. Since neutrons can easily be generated with similar frequencies to atomic motion ($\sim$meV), inelastic scattering is easily resolved. In this way, neutron scattering can be used to directly probe atomic motion as described in Equation (1.31) [35].

Theory

Using the approach of Section 1.3.1, we can write atomic positions as deviations from their average $\mathbf{u}_i(t) = \mathbf{r}_i(t) - \langle \mathbf{r}_i \rangle$. Substituting this expression into Equations

(2.6) and (2.7), we obtain

$$S(\mathbf{Q},E) = \sum_{ij} b_i b_j \exp(\mathrm{i}\mathbf{Q}\cdot[\langle\mathbf{r}_i\rangle - \langle\mathbf{r}_j\rangle]) \times \int \langle\exp(\mathrm{i}\mathbf{Q}\cdot[\mathbf{u}_i(t)-\mathbf{u}_j(0)])\rangle \exp\left(-\frac{\mathrm{i}Et}{\hbar}\right)\mathrm{d}t. \quad (2.23)$$

We can use a result for distributions which are characteristic of harmonic motions to write

$$\langle\exp(\mathrm{i}\mathbf{Q}\cdot[\mathbf{u}_i(t)-\mathbf{u}_j(0)])\rangle = \exp\left(-\left\langle(\mathbf{Q}\cdot\mathbf{u}_i)^2/2\right\rangle\right)\exp\left(-\left\langle(\mathbf{Q}\cdot\mathbf{u}_j)^2/2\right\rangle\right) \times \sum_{m=0}^{\infty}\frac{1}{m!}\langle[\mathbf{Q}\cdot\mathbf{u}_i(t)][\mathbf{Q}\cdot\mathbf{u}_j(t)]\rangle^m. \quad (2.24)$$

The first two terms can be subsumed as the 'Debye–Waller' (or 'temperature') factors $T_i(\mathbf{Q})$ and $T_i(\mathbf{Q})$. These functions vary with temperature and show a Gaussian dependence on the scattering vector. Combining these expressions, we can construct a general equation for scattering:

$$S(\mathbf{Q},E) = \sum_{ij} b_i b_j \exp(\mathrm{i}\mathbf{Q}\cdot[\langle\mathbf{r}_i\rangle - \langle\mathbf{r}_j\rangle])T_i(\mathbf{Q})T_j(\mathbf{Q}) \times \sum_{m=0}^{\infty}\frac{1}{m!}\int\langle[\mathbf{Q}\cdot\mathbf{u}_i(t)][\mathbf{Q}\cdot\mathbf{u}_j(t)]\rangle^m \exp\left(-\frac{\mathrm{i}Et}{\hbar}\right)\mathrm{d}t, \quad (2.25)$$

which can be expanded in m to give $S(\mathbf{Q},E) = S_0(\mathbf{Q},E)+S_1(\mathbf{Q},E)+\ldots$. The order of the term corresponds to the number of phonons exchanged in the process. The $m = 0$ term represents elastic (or zero-phonon) scattering processes. Consequently, the integral over time reduces to a delta-function in energy:

$$S_0(\mathbf{Q},E) = \sum_{ij} b_i b_j \exp(\mathrm{i}\mathbf{Q}\cdot[\langle\mathbf{r}_i\rangle - \langle\mathbf{r}_j\rangle])T_i(\mathbf{Q})T_j(\mathbf{Q}) \times \delta(E). \quad (2.26)$$

The next term in the sum (i.e. $m = 1$) arises from one-phonon processes: the neutron either creates or annihilates one phonon from the lattice. The scatter-

ing includes the contribution of various modes (with periodicity $\mathbf{k}$ and mode label ν), which—as in Section 1.3.1—have corresponding energies $\omega_\nu(\mathbf{k})$ and eigenvectors $\mathbf{e}^j_\nu(\mathbf{k})$. By combining the $m = 1$ term with the equations of motion in the harmonic approximation (Equation (1.31)), we obtain, after some work, the equation for the one-phonon scattering processes:

$$S_1(\mathbf{Q}, E) = \frac{N\hbar}{2} \sum_\nu \frac{1}{\omega_\nu} \left| \sum_j \frac{b_j}{m_j^{1/2}} \left[\mathbf{Q} \cdot \mathbf{e}^j_\nu(\mathbf{k}) \exp(i\mathbf{Q} \cdot \langle \mathbf{r} \rangle_j) T_j(q) \right] \right|^2 \times [n(\omega, T) + 1]\, \delta(E + \hbar\omega_\nu(\mathbf{k})) + n(\omega, T)\delta(E - \hbar\omega_\nu(\mathbf{k})). \quad (2.27)$$

There are two non-zero contributions of each mode ν to the scattering. These represent the intensities from 'phonon creation' (at $E = +\hbar\omega_\nu(\mathbf{k})$) and 'phonon annihilation' (at $E = -\hbar\omega_\nu(\mathbf{k})$). The probability of each event depends on the Bose factor,

$$n(E, T) = \frac{1}{\exp E/k_\mathrm{B}T - 1}, \quad (2.28)$$

which encodes the temperature dependence of the scattering: at a low temperature, a neutron annihilation event is more unlikely since fewer phonons are available to give their energies to the neutron.

The scattering given by Equation (2.27) allows for the direct experimental determination of the dispersion relations discussed in Section 1.3.1. This is demonstrated in Figure 2.3, which shows some measurements and simulations of $S(\mathbf{Q}, E)$ for silicon. The most information rich form of the experiment is performed on single crystals. Because the $S(\mathbf{Q}, E)$ is only non-zero when E corresponds to a phonon energy, measurement directly produces the form of the phonon dispersion curves $\omega_\nu(\mathbf{k})$ [Fig. 2.3(a)]. When not limited by the resolution of the instrument, the phonon linewidth can provide a direct measure of the lifetime of phonons in crystalline materials [285].

In principle, the same information is present in a powder measurement of INS but it is more difficult to analyse because of the spherical integration described by Equa-

tion (2.12). For example in the case of silicon, we can relate a few of the features of the dispersion curves of Figure 2.3(a) to the polycrystaline measurement [Fig. 2.3(b–c)]: (i) The acoustic phonons near Bragg peaks are realised as 'cones' emerging from these positions, the first of which appears as a triangle-like feature centred on the the 100 peak at $Q \approx 2\,\text{Å}^{-1}$. (ii) Regions of relatively 'flat' dispersion (such as that at $E \approx 20\,\text{meV}$) appear as strong flat features (iii) the highest intensities appear at lower energy transfers. Since $S(Q, E)$ tends to scale with Q^2, the higher intensities are resolved at higher Q but for the polycrystalline measurement, it is the low Q region, where fewer signals are superimposed which is easiest to interpret. Because of the greater difficulty in interpreting polycrystalline inelastic neutron scattering, a large amount of the analysis focuses on simulating $S(Q, E)$ from ab. initio calculations [Fig. 2.3(c)] or forcefield simulations and directly comparing to observations [287]. Recent implementations include the AbINS and Euphonic packages [288, 289].

The LET and MARI time-of-flight spectrometers at ISIS

Two inelastic neutron scattering studies on a polycrystalline sample of $^{114}Cd(CN)_2$ are reported in this thesis [Chapter 6]. The isotopic enrichment is crucial for these experiments to illuminate the high absorbance cross-section (20600 barns) for which

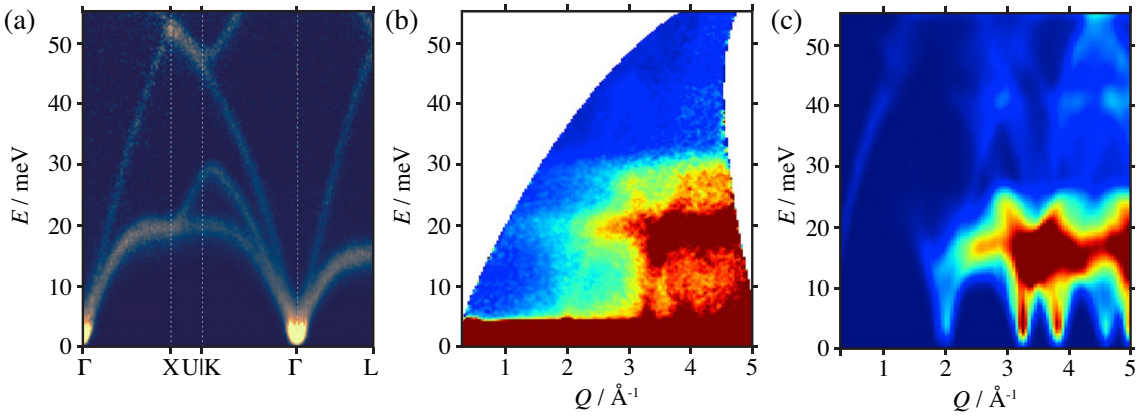

Figure 2.3: (a) $S(\mathbf{Q}, E)$ for a single crystal sample of Si at 300 K shown along some selected lines of low symmetry measured on the ARCS time-of-flight spectrometer. Adapted from Ref. 285. (b) The corresponding measurement of polycrystalline Si, performed on SEQUOIA time-of-flight spectrometer. (c) $S(\mathbf{Q}, E)$ simulated from an ab. initio calculation. Adapted from Ref. 286.

^{113}Cd is famous. For these studies, the powder samples were well suited to a time of flight scattering experiment. We chose to perform the experiments at the nearby ISIS neutron source. The facility operates by generating neutrons from pulses of protons, travelling at 84 % of the speed of light which are collided with a heavy-metal target in order to produce short pulses of neutrons by spallation. The path of the pulsed proton beam, shown in Figure 2.4(a), is split between two target stations before spallation.

A schematic of the instrument is shown in Figure 2.4(b). First a pulse of neutrons arrives at the instrument, which are passed through a moderator, which produces an approximately black-body distribution of wavelengths. The white beam spreads out from the moderator and a set of choppers select a number (three, in the case of LET and MARI) of incident energies by blocking out all of the neutrons not travelling

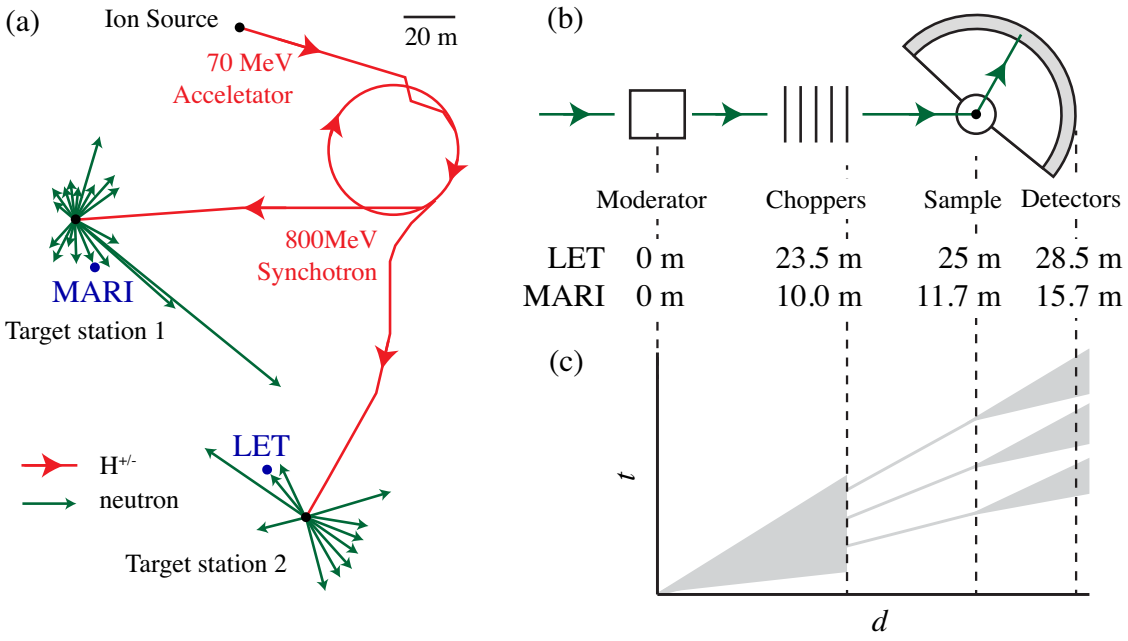

Figure 2.4: (a) Schematic overview of the ISIS pulsed neutron source, showing the H^- path from ion source through a linear accelerator and synchrotron to the two target stations in red and the neutron paths to each instrument in green. The two instruments of interest to the thesis are shown in blue. (b) A schematic of a direct geometry time of flight spectrometer, showing the path from moderator–choppers–sample–detectors. The path distance from moderator to each component is compared for LET and MARI. (c) A schematic distance-time diagram showing the possible paths of neutrons in grey, with the choppers selecting three incident energies and their corresponding trajectories to the detector.

at a certain speed. The neutrons (now of known incident energy E_i) impact on the sample and scatter, either losing or gaining energy. This gives them a new distribution of speeds which can be measured on the detectors by monitoring their intensity as a function of time of flight t. As long as the windows which correspond to each incident energy pulse do not overlap, it is possible to fit multiple incident energies into the same experiment but one needs to monitor the overlap of these signals carefully to avoid cross-contamination of separate neutron pulses.

Although the MARI and LET spectrometers operate in the same geometry, there are a few important differences between their operation. Firstly, LET is a much larger instrument. The longer path-lengths [Fig. 2.4(b)], better angular resolution, and more recent detector technology make the energy-resolution on LET ($\Delta E/E \geq 0.8\,\%$) much better than that on MARI ($\Delta E/E \geq 1.5\,\%$). Additionally, the neutron flux at LET ($5 \times 10^4\,\mathrm{n\,cm^{-2}\,s^{-1}}$) is also considerably higher than at MARI ($1.4 \times 10^4\,\mathrm{n\,cm^{-2}\,s^{-1}}$). Consequently, the amount of detail obtained in the LET experiment was greater, which allows for the resolution of more subtle signals in $S(Q, E)$, which would be overlooked in the corresponding MARI experiment.

For the variable pressure experiment a pressure can was required to obtain hydrostatic pressures up to 2 kbar at ambient temperature. Due to covid restrictions, we could not access ISIS and the experiments were carried out remotely by Dr. Helen Walker. The TAV-6 alloy was used to minimise coherent neutron scattering background and thus its cans exhibit a less structured inelastic signal. Measurements were performed at ambient temperature on a ~ 1 g of $^{114}Cd(CN)_2$ using the MARI instrument at ISIS. The incident neutron energy was 10 meV (400 Hz choppers), which gave an energy resolution of about 0.175 meV at an energy transfer of 2 meV. Pressure was applied using He as pressure-transmitting medium. Each measurement corresponded to a neutron beam exposure of approximately 1000 µA h and was corrected for background scattering from the sample environment. We carried out measurements at five pressure values: 0, 0.6, 1.0, 1.3, and 2 kbar.

The variable temperature experiment on LET was carried out remotely by instrument responsible, Dr. Ross Stewart, using the same $\sim 1\,\mathrm{g}$ sample of $^{114}\mathrm{Cd(CN)_2}$ in an annular aluminium can. To cool across the temperature range, we required a closed cycle refrigerator.

Data Treatment

For both experiments, I used a Mantid [290] workstation to perform reconstruction, background subtraction and normalisation to a Vanadium standard. The Mslice tool was used to generate planes and cuts through $S(Q, E)$.

2.2 Magnetometery

The measurement of magnetisation in this project was carried out using superconducting quantum interference device (SQUID) magnetometry. These devices work by passing a known mass of sample though a 'weak-link' in a superconducting loop, such that any magnetisation in the sample leads to a persistent current proportional to the sample magnetisation in the superconducting circuit.

Applying an external magnetic field adds an experimental complication: there is an experimental magnetisation induced in the space around the sample by the magnetic field. The quantity measured by the SQUID is the magnetic flux density, proportional to the sum of the internal magnetic field $\mathbf{H}_\mathrm{i}$ and magnetisation $\mathbf{M}$,

$$\mathbf{B} = \mu_0(\mathbf{H}_\mathrm{i} + \mathbf{M}). \tag{2.29}$$

This internal magnetic field may depend on the position in the sample. However, for ellipsoidal sample geometries the induced magnetic field strength and flux density in the sample can be calculated directly as

$$\mathbf{H}_\mathrm{i} = \mathbf{H}_\mathrm{a} - N\mathbf{M}, \tag{2.30}$$

$$\mathbf{B}_\mathrm{i} = \mathbf{B}_\mathrm{a} + \mu_0(1 - N)\mathbf{M}, \tag{2.31}$$

where $\mathbf{H}_\mathrm{a}$ and $\mathbf{B}_\mathrm{a}$ represent the external magnetic field and flux, respectively, and N is a geometric constant which equals $\frac{1}{3}$ for spherical samples. In this way, solving Equations (2.30) and (2.31) simultaneously allows for the direct calculation of $\mathbf{M}(\mathbf{H}_\mathrm{i})$. Similar expressions can be derived for arbitrary sample geometries. In practice, the correction term $\mathbf{H}_\mathrm{d} = \mathbf{H}_\mathrm{a} - \mathbf{H}_\mathrm{i} = f(\mathbf{M})$, called the demagnetising field, can be generated for a given instrument and sample geometry so that an equivalent correction can be applied to obtain $\mathbf{M}(\mathbf{H}_\mathrm{i})$. We have seen how performing the polycrystalline average in Equation (1.15), smooths out sharp features [§1.2.2].

Samples are cooled using liquid nitrogen, and isotopes of helium. For the work detailed in Chapter 5, liquid helium cooling was used to cool samples to $\sim 2\,\mathrm{K}$, while liquid nitrogen was used to cooler the outer jacket of the refrigerator. For the work carried out in Chapter 3, magnetometry down to $\sim 130\,\mathrm{mK}$. was required, which was achieved using a ^{3}He-^{4}He dilution refrigerator isotopes. In this way, magnetometry allows the scientist to direct measure the $M(H,T)$ state function.

The key experimental approaches used in this thesis involve probing the $M(H,T)$ space in three different ways: (i) field cooled (FC) and (ii) zero field cooled measurements (ZFC) probe $M(T)$, with fixed (and small) magnetisation and (iii) 'magnetisation curves' are constant temperature slices, giving $M(H)$.

2.2.1 Field-Cooled and Zero-Field-Cooled Measurements

We saw in Equation (1.4) how χ_0 gave direct information about the time-averaged fluctuations in the magnetisation. For small magnetisations, $\chi_0 = M/H$ and so by applying a small field (typically $\sim 100\,\mathrm{Oe}$), measurement of $\chi_0(T)$ can be achieved.

Applying the fluctuation–dissipation relation to the ferromagnetic model (which has two degenerate states with $M = \pm N$) predicts $\chi_0(T \to 0) = \infty$. However, if a ferromagnet is cooled to low temperature and a $\sim 100\,\mathrm{Oe}$ field is applied, no change will occur. This is because the time-frame required to flip between the two states is very long compared to the experiment. (At absolute zero this is much longer than the age of the universe [145].) This highlights a flaw in our experimental method

for probing magnetometry for non equilibrium states, which cannot be overcome.

A common solution is to acknowledge this history dependence and measure an approximate upper and lower bound on $\chi_0(T \to 0)$, given by the field-cooled (FC) and zero-field-cooled measurements (ZFC), respectively. These parameters agree when the experiment is probing equilibrium magnetisation and deviate when kinetics slower than the experiment are present. In such a procedure, the sample is cooled with or without field, respectively. The field is applied and the sample is heated at a steady state, allowing the magnetisation to equilibrate on the $\sim 5\,\mathrm{s}$ timescale between temperature steps. At low temperatures, when the magnetisation is kinetically trapped either at a relatively high value (in the FC case) or at a low value (in the ZFC case), measuring $\chi_0(T)$ on heating should approach its equilibrium value from above or below, respectively.

By contrast, the magnetisation of an antiferromagnet is small at low temperatures, and so its fluctuations are small too. For this type of system, we expect a maximum in its susceptibility curve. The field cooled measurements can still measure higher values for this parameter though if the magnetisation is kinetically trapped during the field cooling process. This difference in ZFC/FC response seen between ferro and antiferromagnets is highlighted schematically in Figure 2.5 and allows for a simple experimental determination of whether remanent magnetisation is present.

2.2.2 Magnetisation Curves

By applying a magnetic field, we are also gaining information about the linear response (and therefore fluctuations) in the material as a function of temperature. We can see this most clearly by plotting $\chi = \mathrm{d}M/\mathrm{d}H$. Minima in this parameter correspond to stable states with relatively low fluctuations in the magnetisation and peaks to fluctional states between these islands of stability. This is the reason that in Figure 1.8(c), we saw peaks corresponding to the spin flop transition and a minimum related to the antiferromagnetic state. In general, when there are transitions as a

function of field, one can expect to see plateaux of low magnetisation gradient around stable states.

In order to measure the entropy change on the application of field—so key to quantifying the magnetocaloric effect—one can apply the integrated Maxwell relation,

$$\Delta S_{\mathrm{mag}}\left(H_{\mathrm{i}} \rightarrow H_{\mathrm{f}}\right) = \int_{H_{\mathrm{i}}}^{H_{\mathrm{f}}} \left(\frac{\partial M}{\partial T}\right)_{H} \mathrm{d}H. \tag{2.32}$$

2.2.3 $\mathbf{NaMn(HCOO)_3}$

Magnetisation and AC susceptibility measurements were performed on a SQUID magnetometer developed at the Institut Néel - CNRS [291] and equipped with a dilution refrigerator. Measurements were performed on a powder sample of about 10 mg, mixed with Apiezon N grease to ensure a good thermalisation, and packed in a copper pouch.

Variable-temperature magnetisation measurements—see Figures 3.3(b) and 3.5—were performed in a 100 Oe applied field. Measurements were first performed in a ZFC–FC procedure. The sample was first zero-field cooled, the field being applied at

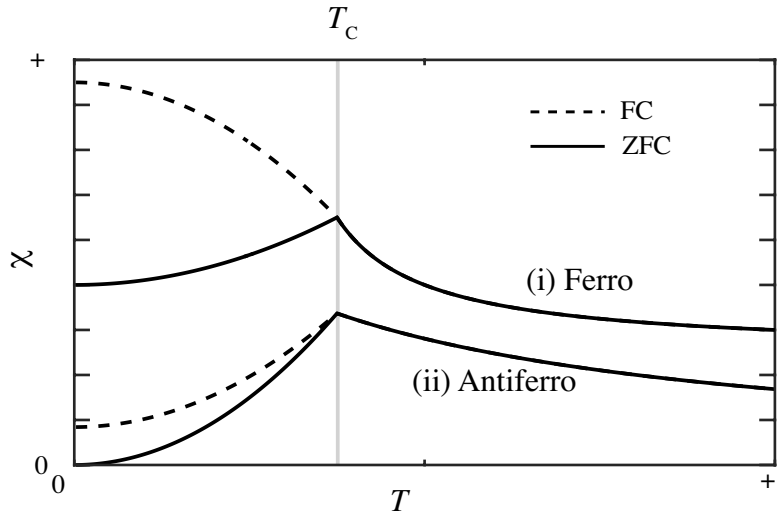

Figure 2.5: Schematic showing characteristic ZFC-FC magnetometry for ferro- and antiferromagnetic samples. At high temperatures these measurements give the same results but at lower temperatures, deviations are due to sample history.

low temperature (100 mK). The magnetisation was then measured whilst warming the to sample 1.1 K, followed by cooling (under applied field), and subsequent re-warming. A small hysteresis was observed below the transition between the cooling and warming curves, independently of the ZFC or FC procedure. Several temperature ramps were used—between about 4.5 mK min^{-1} and 7.2 mK min^{-1}—but the hysteresis width was invariant to rate.

Isothermal field-dependent magnetisation curves—used in Figures 3.8, 3.9, and 3.10—were measured at several temperatures between 100 mK and 4.2 K, using fields up to 8 T. At these low temperatures, the magnetisation is essentially saturated under an applied field of 2 T. No hysteresis was observed.

2.3 Magnetic Heat Capacity

2.3.1 Theory

While we cannot measure the Hamiltonians of Equations (1.7), (1.10), (1.11), (1.12), heat capacity measurements can allow for measurement of the fluctuations in the total energy. This point is demonstrated by the corresponding fluctuation-dissipation relation,

$$C_{\mathrm{mag}} = \frac{1}{k_{\mathrm{B}}T^2}\left[\left\langle E^2\right\rangle - \left\langle E\right\rangle^2\right]. \tag{2.33}$$

The basic experiment is simple: one applies a known amount of heat ΔQ to a sample (via a heating coil or similar) in equilibrium with a heat-bath (of know heat capacity C_{bath}) that is thermally isolated from its environment, and then measures the associated temperature increase ΔT. Conservation of energy dictates that

$$\Delta T\left(C_{\mathrm{sample}} + C_{\mathrm{bath}}\right) + \Delta Q = 0, \tag{2.34}$$

which allows for the determination of C_{sample}. This calculation assumes a constant heat capacity over the temperature range, so requires an incremental addition of heat $\Delta Q \to 0$. In practice, to ensure normalisation, this experiment is done in

parallel between a sample and a reference of known heat capacity. Calibration against known standards corrects for deviations from ideality, such as due to heat loss to the environment.

The sample heat capacity contains contributions from lattice vibrations, defects, nuclear spin disorder and other factors. If we are certain that the degrees of freedom associated with these contributions are not correlated, the heat capacity can be partitioned as a sum over these contributions,

$$C_{\text{sample}} = C_{\text{elec}} + C_{\text{lat}} + C_{\text{nuc}} + C_{\text{mag}} + \dots . \tag{2.35}$$

This approximation will break down when degrees of freedom correlate, for example in systems with magnetoelectric or maganetoelastic coupling [292]. In order to resolve C_{mag}, which contains information about the magnetic Hamiltonians which concern the thesis, it is important to subtract the nuclear component and lattice components.

There are two main approaches for estimating the lattice component. An empirical correction can be achieved if there is an appropriate non-magnetic analogue of the material studied [293–295]. The approach taken for systems where a nonmagnetic measurement is not practical is to carry out a fit to the Debye expression for the heat capacity given in Equation (1.35). The Debye temperature Θ_D is a free parameter of the model which depends on the energy scale of the softest phonon branch.

In order to remove the contribution from nuclear spins, one must have an idea of the nuclear structure, the details of which are beyond the scope of the thesis. For a nucleus with *nuclear* spin quantum number I, the magnetic field induced by the electronic spin splits the nuclear level into $2I + 1$ equally spaced levels [145, 296]. The associated partition function can therefore be parametrised by the variable Δ,

and is given by

$$Z_{\mathrm{nuc}} = \sum_{I_z=-I}^{I} \exp -\frac{\Delta I_z}{2Ik_{\mathrm{B}}T}. \tag{2.36}$$

One can calculate the Schottky anomaly associated with nuclear scattering [297].

After subtracting the appropriate terms, one is left with the magnetic heat capacity, which contains fluctuation information. Peaks in this quantity correspond to ordering process and the energy associated with a particular ordering transition can be calculated from Kirchov's Law:

$$\Delta E_{\mathrm{mag}} = \int_{T_{\mathrm{i}}}^{T_{\mathrm{f}}} C_{\mathrm{mag}}(T)\mathrm{d}T. \tag{2.37}$$

In this way one can get an estimate for the strength of interactions in the magnetic Hamiltonian.

2.3.2 Entropy Changes

The number of microstates W is a measure of the disorder of a system. Boltzmann gave us a more direct way to measure this with his relation to entropy:

$$S = k_{\mathrm{B}} \log W. \tag{2.38}$$

While it is not possible to measure S directly, changes in its value as a function of temperature and/or magnetic field can be extracted from magnetometry and heat capacity measurements respectively. The latter is especially important when it comes to measuring the magnetocaloric effect. If one has a good estimate of the entropy in the high or low temperature limit of a feature, it is possible to obtain entropies on an absolute scale.

Changes in entropy with temperature can be extracted using an expression related to Equation (2.37):

$$\Delta S_{\mathrm{mag}}\left(T_{\mathrm{i}} \rightarrow T_{\mathrm{f}}\right) = \int_{T_{\mathrm{i}}}^{T_{\mathrm{f}}} \frac{C_{\mathrm{mag}}(T)}{T}\mathrm{d}T. \tag{2.39}$$

In this way it is possible to measure directly the number of microstates associated with an specific state.

At this stage it is important to highlight a fundamental limitation of the vector model of spins. Consider a spin at low temperature fluctuating around its equilibrium orientation. In the low temperature limit, the energy of the spin varies with the square of the angular displacement because the size of the fluctuations is small. In this limit, we can apply the equipartition theorem to the two angular degrees of freedom giving the heat capacity $C(T = 0) = k_{\mathrm{B}}$. Applying Equation (2.39), we predict an infinite entropy change for $\Delta S_{\mathrm{mag}}\,(T_{\mathrm{i}} \rightarrow T_{\mathrm{f}} = 0)$. The same problem is present in applying Equation (2.32): as $H \rightarrow \infty$ an essentially infinite supply of entropy can be absorbed because fluctations around the field direction are not quantised. This problem is resolved by spin wave theory, which provides a more accurate description of the entropy at very low temperatures [298]. For estimating the entropy as a function of temperature, models which respect the quantisation are important. However, these problems only become significant when the temperature is very low and the fields are very strong. For this reason it is important to use quantised models to model low temperature behaviour [Chapter 4] while vector models are sufficient to model disordered properties [Chapters 3 and 5].

2.3.3 $\mathbf{Tb}_{1-x}\mathbf{Y}_x\mathbf{(HCOO)}_3$

Heat capacity $C(T)$ data were measured for $\mathrm{Tb(HCOO)_3}$ and $\mathrm{Tb_{1-\mathit{x}}Y_{\mathit{x}}(HCOO)_3}$ with $x = 0.05$, 0.10, 0.20 and 0.40 in zero-field conditions. Here, the electronic term C_{elec} in Equation (2.35) can safely be ignored since these materials are insulators. The corresponding lattice contribution C_{lat} were estimated and subtracted by taking a Debye fit [Eq. 1.35] to the heat capacity data for $\mathrm{Tb(HCOO)_3}$ between 8 to 14 K, where phonon population is the dominant process at play. We obtained a common Debye temperature of 156.2(1.8) K. The value of C_{lat} is very small at the temperatures of relevance to magnetic ordering.

Finally, the nuclear contribution due to a Schottky anomaly was estimated by fitting to the low-temperature data $0.4 < T < 0.8\,\mathrm{K}$ using the expression:

$$C_{\mathrm{nuc}}(T) = \frac{\Delta^2 R}{9k_{\mathrm{B}}^2 T^2} \frac{e^{-\Delta/3k_{\mathrm{B}}T}[1 + e^{-\Delta/3k_{\mathrm{B}}T}]^4 + 4e^{-\Delta/k_{\mathrm{B}}T}}{[1 + e^{-\Delta/3k_{\mathrm{B}}T} + e^{-2\Delta/3k_{\mathrm{B}}T} + e^{-\Delta/k_{\mathrm{B}}T}]^2}, \tag{2.40}$$

which is derived from Equation (2.36) with the $I = 3/2$ of the terbium nucleus. Because the nuclear Zeeman effect is $\sim 10^3$ times weaker than electronic coupling to field [145], this term is mostly unaffected by the developing nuclear order so its contribution to the heat capacity can be partitioned from the magnetic contribution. Here the single adjustable parameter Δ captures the hyperfine splitting [297]. We found $\Delta = 0.437(2)\,\mathrm{K}$ for $\mathrm{Tb(HCOO)_3}$, which is consistent with many other systems, including Tb metal (see Table 2.1) [299–301], suggesting this value solely depends on the internal electronic structure of Tb and is insignificantly affected by the local chemical environment. Therefore, this parameter is here assumed to be constant with respect to stoichiometry and subtracted from the measured heat capacity for all samples. Doing so leads to the curious result that this hyperfine coupling contribution does not account for the entirety of the observed low-temperature heat capacity of those members with higher concentrations of Y^{3+} (see Figure 4.12). The resulting $C_{\mathrm{mag}}(T)$ data, obtained following subtraction of lattice and nuclear contributions, shows that $\mathrm{Tb(HCOO)_3}$ has the highest strongest magnetic contribution to the heat capacity, with this contribution decreasing with higher Y^{3+} concentration in the other samples, as would be expected.

2.4 Mean-Field Theory

A simple, phenomenological approximation to solving magnetic models is to assume that a spin's surrounding interactions constitute a 'molecular field'. This simplification evolves naturally for a vector model if each spin is written as a deviation from its average $S_i = \langle \mathbf{S} \rangle + \delta \mathbf{S}_i$. In this way, we can rewrite the Heisenberg Hamiltonian

Eq. 1.10 as

$$\mathcal{H} = \frac{J}{N}\sum_{\langle i,j\rangle}(\langle \mathbf{S}\rangle^2 + \langle \mathbf{S}\rangle \cdot (\delta\mathbf{S}_j + \delta\mathbf{S}_i) + \delta\mathbf{S}_i \cdot \delta\mathbf{S}_j. \tag{2.41}$$

For a starting example, I will consider a ferromagnetic ($J < 0$) model, similar to that discussed in the previous section, with the ground-state shown in Figure 1.7(a).

In mean-field theory (MFT), we neglect the term $\delta\mathbf{S}_i \cdot \delta\mathbf{S}_j$, which encodes correlations between the fluctuations in the system. This approximation is successful if the fluctuations are small e.g. at low temperatures. Likewise, at high temperatures the correlation functions [e.g. Figure 1.9] decay quickly, hence $\delta\mathbf{S}_i \cdot \delta\mathbf{S}_j$ is on average small. Near the transition, where short range order persists this term may be important, which leads to the failure of MFT in this regime.

In the mean-field approximation, the Hamiltonian reduces to a simple, separable expression,

$$\mathcal{H}_{\mathrm{MF}} = \frac{Z\mathbf{M}J}{2} \cdot \sum_i \mathbf{S}_i, \tag{2.42}$$

where Z represents the coordination number and the magnetisation $\mathbf{M}$ is subject to the self consistency equation

$$\mathbf{M}(T) = \frac{1}{N}\sum_i \mathbf{S}_i. \tag{2.43}$$

Because Equation 2.42 is now separable, we can use molecular statistical dynamics to solve this equation. In the simpler case of Ising spins S_i—which take two values with

Table 2.1: Comparison of values for the hyperfine splitting parameter in terbium, highlighting that the value I obtain for analysis in Chapter 4 is consistent with literature values.

System (Tb ox. state)	Δ / K	Method	Ref.
Tb–metal (0)	0.45	Empirical fit to heat capacity	[297]
Tb @ SrF_2 (3+)	0.476	Simulation from field-gradient	[299]
$Tb(CF_3SO_3).4H_2O$ (3+)	0.470	Simulation from field-gradient	[300]
$Tb(HCOO)_3$ (3+)	0.437(2)	Empirical fit to heat capacity	This thesis

probabilities $P^+ = \exp -\frac{ZMJ}{2k_\mathrm{B}T}$ and $P^- = \exp +\frac{ZMJ}{2k_\mathrm{B}T}$—this self consistency equation reduces to

$$M = \tanh \frac{zJM}{k_\mathrm{B}T}, \tag{2.44}$$

with non-zero solutions if $T > \frac{ZJ}{K}$. A numerical solution to this equation is plotted in Figure 2.6(a). When compared with the exact 2D Ising result [130], the behaviour is phenomenologically similar. As in the 2D Ising model, a singularity is predicted at T_C, and the magnetisation tends to its maximum value below this point. However, it is clear that neglecting correlations between disorder causes significant problems around the transition. The transition temperature itself is significantly overestimated. This is because the stabilisation of the high temperature phase which results from short range order is neglected.

A similar approach can be taken for antiferromagnets, where it is useful to divide the lattice into two sublattices, as shown schematically in Figure 2.6(b). We borrow language from graph theory to describe how many sublattices are required for such a decomposition. We say that the ferromagnetic model is 'monopartite' because we only need one sublattice to represent its ground state properly while the square antiferromagnetic model is 'bipartite' because two sites are required, with sublattice magnetisation $M^{(1)}$ and $M^{(2)}$. These two sublattices have a pair of coupled self consistency equations

$$M^{(1)} = \tanh \frac{zJM^{(2)}}{k_\mathrm{B}T} \quad \text{and} \tag{2.45}$$

$$M^{(2)} = \tanh \frac{zJM^{(1)}}{k_\mathrm{B}T}, \tag{2.46}$$

which have a solution of the same form as before but where $M^{(1)} = -M^{(2)} = M$ [Fig. (2.6)(c)]. As discussed in Section 1.2.4, geometrically frustrated systems have increased complexity, represented by lattices which are tripartite and beyond. I extend the theories presented here to tripartite lattices in Section 4.5.1.

The mean-field approximation also provides insight in the disordered phase. To

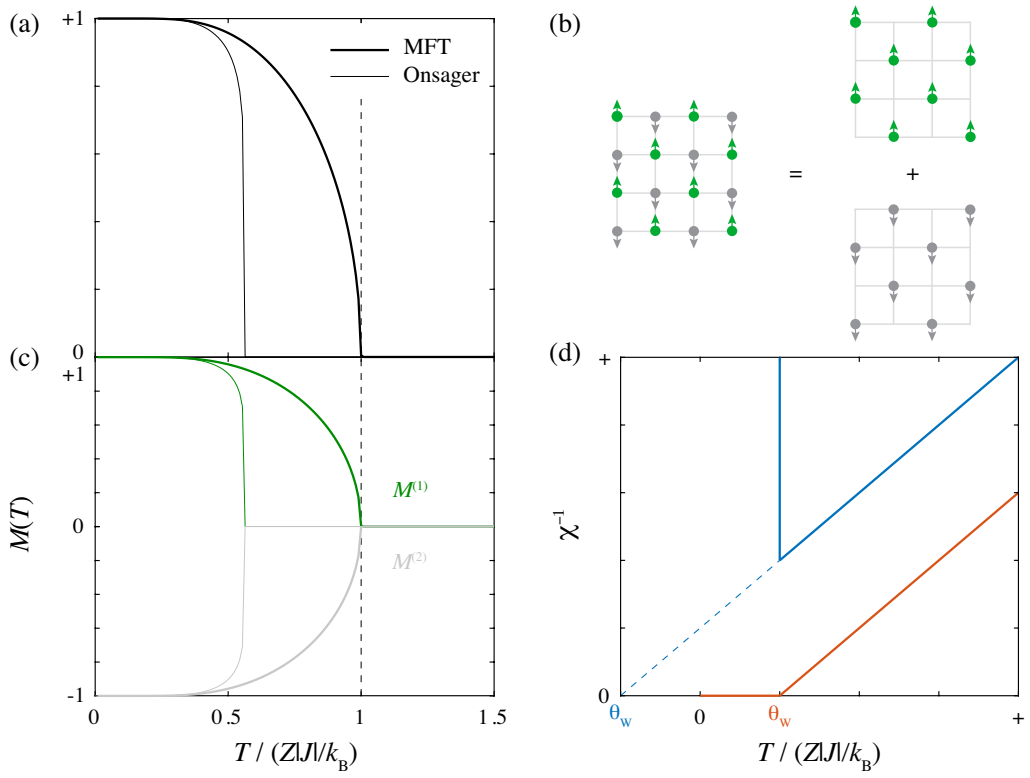

Figure 2.6: (a) Magnetisation of the nearest neighbour mean-field model [Eq. (2.42)] calculated as an iterative solution to Equation (2.44). This is compared with the exact result for a square lattice ($Z = 4$) calculated as the square root of Equation (1.21). (b) The groundstate of a square lattice antiferromagnet can be decomposed into two interpenetrated sublattices on which the spins are coaligned. (c) The magnetisation of those two sublattices as a function of temperature. (d) The susceptibility of the mean-field model, showing the Weiss temperature Θ_{W} as the x-intercept.

explore this point we must include a small perturbing field H to the Hamiltonian. In the Heisenberg case, we have

$$\chi_0 = \lim_{H\to 0} \frac{M(H)}{H} = \frac{C}{T - \Theta_{\mathrm{W}}}, \tag{2.47}$$

where

$$C = \frac{\mu_0 \mu^2}{3k_{\mathrm{B}}}, \tag{2.48}$$

$$\Theta_{\mathrm{W}} = \frac{ZJ}{3k_{\mathrm{B}}}, \tag{2.49}$$

for the Heisenberg model and

$$C = \frac{\mu_0 \mu^2}{2k_\mathrm{B}}, \tag{2.50}$$

$$\Theta_\mathrm{W} = \frac{ZJ}{2k_\mathrm{B}}, \tag{2.51}$$

for the Ising model. In general $\Theta_\mathrm{W} \propto J$ so its value is negative for antiferromagnets and positive for ferromagnets. These results offer an experimental approach to characterising the strength and sign of interactions in magnetic materials. The approach is shown in Figure 2.6(d) where χ_0^{-1} is plotted against T. The intersect with the T-axis gives the value of Θ_W and therefore an indication of whether interactions are ferro- or antiferromagnetic. In ferrimagnets, even though remanent polarisation exists, we observe $\Theta_\mathrm{W} < 0$ because the interactions are antiferromagnetic.

The Curie–Weiss law of Equation (2.47) is followed well in a large range of systems experimentally at high temperatures (i.e. within the paramagnetic regime), but when T_C is approached, the assumptions of mean-field theory break down and we require a more involved theory. A number of more complex theories improve on the techniques detailed here, such as cluster expansions and renormalisation approaches [204].

2.5 Monte Carlo Simulations

2.5.1 Background

The analytical approaches taken so far [§1.2.2, §1.2.3, §2.4] shed light on the origin of the structures seen in materials. A complementary strategy is to build large-scale simulations of the system which are representative of snapshots (μ) of the structure over time, with associated weights w_μ representing how likely they are to occur in the true system. If we can be sure that such snapshots are *decorrelated* from each other, then

$$\langle Q \rangle = \sum_\mu w_\mu Q_\mu \tag{2.52}$$

should represent the thermal average of some measurable quantity Q (the magnetisation, energy etc.), allowing insights about the relationship between disordered structures and bulk properties. My overview of these numerical techniques follows standard texts [292, 302].

Other than for small nanoparticles [303], it is impractical to generate models of whole crystals. Instead, it is common to work with the assumption that the system is homogenous across its volume and it is sufficient to simulate some smaller volume, defining an $[L_x, L_y, L_z]$ supercell of the parent unit cell, which should reproduce the bulk behaviour of the system as $L_\alpha \to \infty$ [304]. Because we want the structure to be representative of the internal bulk of the sample, it would not be representative if the atoms at the edge of the simulation volume could see the edge of the simulation. The typical approach taken is to employ periodic boundary conditions to model the edge [304].

There are a few approaches to generate the configurations and their associated weights. One strategy—spin dynamics—is to evolve the spin vectors in time according to the time-dependant Schrodinger equation [305, 306]. The computation time required for this approach scales very quickly with the size of the system. An empirical approach to generating w_μ—reverse Monte Carlo (RMC)—generates representative configurations which are maximally disordered whilst fitting to an experimental determination of the spin correlation function [307]. The Hamiltonians described in Section 1.2.2 give us a direct way to access the weights. This is to calculate E directly, then we should expect *equilibrium* states of real magnets to sample the Boltzmann distribution,

$$w_\mu = \frac{1}{Z} \exp \frac{-E_\mu}{k_B T}, \tag{2.53}$$

where Z is the partition function. This is the approach taken throughout this thesis. I will give a brief overview here, following Ref. 292.

The numerical strategy taken in this thesis—Monte Carlo simulation—involves

sampling μ using random number generation. It is routinely possible by these methods to simulate $\simeq 10^3$ spins, which recovers in some detail the emergent properties of large ensembles. Sampling Equation (2.52) directly using random number generation is inefficient because the Boltzmann weights of most samples will be very close to zero. Instead, it is necessary to use importance sampling so that the probability of a state μ appearing in the simulation is given by $P(\mu) = w_\mu$. In this way, we can simply run our algorithm through t steps and sample according to

$$\langle Q \rangle = \frac{1}{t} \sum_{\mu=1}^{t} Q_\mu. \tag{2.54}$$

The list $\{\mu\}$ of states meets the condition required if they form a 'Markov Chain' [308]. This requires two conditions on the steps: (i) *ergodicity*: there must be a non-zero possibility of moving from any state μ to any other state ν, (ii) *detailed balance*: there is a condition on the probability of moving between these states:

$$\frac{P(\mu \to \nu)}{P(\nu \to \mu)} = \frac{w_\nu}{w_\mu}. \tag{2.55}$$

The Metropolis algorithm [309] which is used throughout this work ensures detailed balance by sampling the probabilities

$$P(\mu \to \nu) = \min \left\{ \exp \left[- \left(E_\nu - E_\mu \right) / k_B T \right], 1 \right\}. \tag{2.56}$$

While it is convincing that Equation (2.55) is obeyed by this algorithm, the key difficulty for these algorithms is that of ensuring ergodicity. It is clear that this condition is not met by a single spin move: how would you flip the whole lattice in one go? In principle by chaining a sufficient number of moves together ($\mu_1 \to \mu_2 \to \cdots \to \nu_1$), the step from $\mu_1 \to \nu_1$ should represent a link in our Markov chain. Commonly, it is sufficient to use many times ($\sim 10^3$) more moves than spins in the simulation, but the number of moves required varies depending

on the problem. A common approach [90, 310] is to define the spin autocorrelation function,

$$\langle \mathbf{S}(0) \cdot \mathbf{S}(t) \rangle = \frac{1}{N} \sum_i \mathbf{S}_i(0) \cdot \mathbf{S}_i(t). \tag{2.57}$$

The number of moves required for the autocorrelation function to reach zero is t_0, so this should represent complete decorrelation. If the simulations continue for a little longer than this time (e.g. $\sim 5t_0$), one can be reasonably confident that the system is properly decorrelated.

Collective moves are an effective means of spanning a large space. One example is the Wolff algorithm, which flips whole domains of spins together [311]. When there is one interaction which dominates the Hamiltonian, it is sometimes effective to propose collective moves which leave this interaction unchanged but may affect smaller interactions. This is the basis of the loop moves used in modelling the spin ices for example [312]; such algorithms have allowed for a much more efficient spanning of configurational space.

Monte Carlo simulations are powerful because the snapshots generated encode the fluctuations in the system. It is therefore possible to use fluctuation-dissipation approaches to extract linear-response properties such as the susceptibility [Eq. (1.4)] or heat capacity [Eq. (2.33)].

More importantly, because Monte Carlo configurations constitute explicit descriptions of the structure, it is possible to interrogate these configurations directly, in a way which is impossible to do using exact or mean-field methods. This allows us to gain insights about which particular structural feature is leading to the disorder. Because they don't require an exactly solvable model or a unique ground state, MC simulations—alongside exact and MF simulations—have been central to the development of theories of disordered magnets [90, 312, 313].

2.5.2 Overview of implementation in this thesis

Monte Carlo modelling is the most prevalent from of modelling employed in this thesis. In each of the results chapters, I develop an approach to model the effects of temperature on the structure of solids, based on the Metropolis algorithm. I will give an overview of the methods employed in each chapter here but detailed methodology for each is given in their respective chapters.

In Chapter 3, a MC approach is used to probe the influence of temperature and the dipolar interaction on my models of $NaMn(HCOO)_3$. To model the long-range dipolar interaction, Ewald summation was employed in the same manner as Wang [314]. In Chapter 4, I develop an approach which includes collective 'Chain–moves', related to the loop moves of Ref. 312. In Chapter 5, a dual-MC approach is employed to model the joint occupational pseudospin disorder, in which strong anticlustering drives order, and magnetic disorder. In Chapter 6, I use the MC approach developed by Coates and coworkers for orientational pseudospin disorder in $Cd(CN)_2$ to build disordered supercells, which are then used for lattice dynamical calculations [§2.6.4].

2.6 Empirical lattice dynamics

2.6.1 Overview

Monte Carlo simulation captures a snapshot of a system but does not capture the dynamical evolution of the system. To model the dynamical properties (such as phonon-driven NTE), it is useful to have a method which can describe the time-dependence of the structure. One suitable approach is that of classical lattice dynamics, in which the time-dependence of the structure is modelled using Newton's equations of motion.

We have seen already [§1.3.1] that equations of motion become much easier to solve in the harmonic approximation, where they can be described as sinusoidal oscillations [Equation (1.31)]. First it is necessary to find a local minimum in the

energy in order to determine the 'static' structure. Typically this is done via some form of 'hill climbing' algorithm. Once a minimum energy structure has been found (such that $\partial E/\partial u_i^{(\alpha)} = 0 \quad : \quad \forall i, \alpha = x, y, z$), the energy can be described as a truncated form of Equation (1.30). The next step is to calculate the dynamical matrix according to Equation (1.33). The diagonalisation of the dynamical matrix gives the phonon frequencies and eigenvectors, from which one can calculate elastic and one-phonon scattering according to Equations (2.26) and (2.27).

This strategy requires an accurate estimate of the dependence of the internal energy $E(\{u_i^{(\alpha)}\})$ on the lattice coordinates. For simple systems with small unit cells it is sometimes effective to use quantum mechanical calculations to directly access these coordinates. Methods such as density functional theory, which is based on the principle that the ground-state properties of a system can be determined by the electron density, is the dominant numerical approach [108, 315]. However, this approach is prohibitively slow for large, unit cells with the calculation scaling with the number of atoms as N^6.

Instead, the approach I take for $Cd(CN)_2$ [§6.3.1] is the parametrisation of a semi-empirical potential to DFT simulations of small molecules and molecular ions involving Cd^{2+} and CN^-. By distorting the molecular geometry of these species away from their equilibrium positions, the force field can be chosen to approximate the dynamical behaviour present in $Cd(CN)_2$ itself.

2.6.2 General Utility Lattice Program

The molecular dynamics calculations detailed in this thesis are implemented using the General Utility Lattice Program (GULP) [316]. This software package is commonly used for lattice energy minimisation, the calculation and diagonalisation of the dynamical matrix, and calculation of physical properties. My discussion of the program GULP follows Refs. 316 and 317.

The forcefield approach is centred around finding an effective ansatz for the function $E(\{u_i^{(\alpha)}\})$. The most important terms in this equation are pairwise interactions.

The most simple stretch term is the harmonic bond (essentially a spring between atoms X and Y) which is defined by the deviation away from an ideal length r_0 and a force constant k:

$$E_{\mathrm{XY}}^{\mathrm{harm}} = \frac{1}{2}k\left(r_{\mathrm{XY}} - r_0\right)^2. \tag{2.58}$$

A more accurate form is given by the Morse potential, which encodes anharmonicity:

$$E_{\mathrm{XY}}^{\mathrm{Morse}} = D[1 - \exp(-\alpha(r - r0))]^2 - 1. \tag{2.59}$$

Three-body terms are also important to constrain molecular geometries. These include the harmonic three-body

$$E_{\mathrm{XYZ}}^{\mathrm{harm}} = \frac{1}{2}K(\theta_{\mathrm{XYZ}} - \theta_0)^2 \tag{2.60}$$

and linear three-body term

$$E_{\mathrm{XYZ}}^{\mathrm{harm}} = \frac{1}{2}K(1 - \cos\varphi_{\mathrm{XYZ}}). \tag{2.61}$$

For the longer range 'dispersion' interaction a Buckingham potential is used:

$$E_{\mathrm{XY}}^{\mathrm{Buck}} = A\exp(-r_{\mathrm{XY}}/\rho) - (C/r_{\mathrm{XY}}^6). \tag{2.62}$$

The related Lennard-Jones potential (also known as the 12/6 potential) plays on a similar role:

$$E_{\mathrm{XY}}^{\mathrm{LJ}} = (A/r_{\mathrm{XY}}^{12}) - (C/r_{\mathrm{XY}}^6). \tag{2.63}$$

Longer range electrostatic interactions,

$$E^{\mathrm{electrostatic}} = \frac{1}{8\pi\varepsilon_0}\sum_{ij}\frac{q_i q_j}{r_{ij}}, \tag{2.64}$$

are little more difficult to implement. This is because, as the cutoff radius is expanded, the overall strength of the interactions seems to diverge: the number of atoms in each shell at radius r from a central atom is proportional to r^2 and the electrostatic interaction scales with $\frac{1}{r}$ so the overall sum diverges unless constructed carefully. The most commonly used method for three-dimensional materials to address this issue, and that used in GULP, is the Ewald method [318]. This approach enforces charge neutrality and zero dipole moment conditions, resulting in a convergent series with a well-defined limit. To speed up the evaluation process, the Coulomb term undergoes a Laplace transformation and is then separated into two components. One of these components converges rapidly in real space, while the other decays quickly in reciprocal space:

$$E^{\text{real}} = \frac{1}{8\pi\varepsilon_0} \sum_{ij} \frac{q_i q_j}{r_{ij}} \operatorname{erfc}\left(\eta^{\frac{1}{2}} r_{ij}\right) \tag{2.65}$$

$$E^{\text{recip}} = \frac{1}{2\varepsilon_0 V} \sum_{ij} \sum_{\mathbf{G}} q_i q_j \exp\left(i\mathbf{G}\cdot\mathbf{r}_{ij}\right) \frac{\exp\left(-\frac{G^2}{4\eta}\right)}{G^2} \tag{2.66}$$

$$E^{\text{self}} = -\frac{1}{4\pi\varepsilon_0} \sum_{i=1}^{N} q_i^2 \left(\frac{\eta}{\pi}\right)^{\frac{1}{2}} \tag{2.67}$$

$$E^{\text{electrostatic}} = E^{\text{real}} + E^{\text{recip}} + E^{\text{self}} \tag{2.68}$$

The parameter η and cutoffs $r_{\max}$ and $G_{\max}$ must be chosen carefully to ensure a sufficient accuracy as detailed in Ref. 319.

One of the main roles of GULP is to perform a geometry optimisation. GULP makes use of the Newton-Raphson optimisation method [320], which updates the positions each cycle by the displacement vector

$$\Delta\mathbf{x} = -\alpha\mathbf{H}^{-1}\mathbf{g}, \tag{2.69}$$

where the gradient vector $\mathbf{g}$ and Hessian matrix $\mathbf{H}$ are defined as the first and second derivatives (respectively) of the free energy taken with respect to the atomic

coordinates. The value of α is chosen to minimise the energy. Efficient updating of the Hessian is made via Broyden-Fletcher-Goldfarb-Shanno algorithm [321]. The most important criterion for optimisation is the final value of $|\mathbf{g}|$.

The other important role of GULP for this thesis is to perform lattice dynamical calculations—that is to determine the mode eigenvalues $\omega_\nu(\mathbf{k})$ and eigenvectors $\mathbf{e}_\nu(\mathbf{k})$. This is achieved by calculation of the dynamical matrix $\mathbf{D}$ according to Equation (1.33) and diagonalisation. In GULP it is possible to specify a set of $\mathbf{k}$ points to be sampled.

2.6.3 Empirical potential fitting

In the previous section, I detailed the terms which describe the forcefields in this thesis. There are a number of approaches to parametrising the ansatz: a fully empirical method can be employed, fitting to the phonon energies $\omega_\nu(\mathbf{k})$ measured by inelastic neutron scattering [322, 323]. Another approach—common in the description of organic molecules—is fitting to quantum mechanical calculations [324]. This is the approach used Fang and co-workers for $Zn(CN)_2$ [325]. In this thesis, I will be developing a potential model for use in calculating inelastic neutron scattering and the dynamical behaviour of $Cd(CN)_2$. This work was overseen by Prof. Ben Slater and carried out in part in his group at UCL. I outline briefly the methodology here, but the full details of my own fitting and testing are provided in Chapter 6.

Quantum mechanical calculations must first be carried out to produce a set of molecular geometries, labelled with their energies. The quality of the potential of course relies on the energy calculations $E(\{r_i\})$ to which we fit. For this reason it is both important the method to generate $E(r)$ is accurate and that the set of bond geometries $\{r_i\}$ samples an appropriate space of atomic configurations (probing the appropriate force-constants, bending strengths, etc.). In the work detailed in Chapter 6, I use the DFT implementation ORCA [326], which allows for the generation of multiple configurations with related geometry. Because of the small size of molecules ('gas-phase' $Cd(CN)_2$ and $Cd(CN)_4{}^{2-}$), it was possible to use a relatively high level

of theory and so I employed the PBE-d^3 functional [327]. The calculations ran in a matter of minutes on a laptop.

In most force-field models, the charge of atoms is located at the nuclear position. This leads to considerable ambiguity in how these charges should be defined: Electron clouds are diffuse and there is no unique way to define where one atom starts and the other ends. Mulliken analysis is straightforwardly performed on DFT calculations [328], but it rarely provides an accurate representation of the electric field around a molecule. Bader's 'atoms in molecules' approach is more effective, partitioning the charge at turning points in the electron density [329]. Multipole analysis of clusters is an effective way to parametrise the charges, such that the surrounding electric field in the MD model resembles that predicted by DFT [330].

This multipole analysis approach was taken for the charges in $Zn(CN)_2$ by Fang and coworkers [325], who went on to use configurations which are energy-labelled by DFT to fit the forcefield described in Table 2.2. In order to eliminate variables we can fix some distances and vary angles or bond lengths. For example, to fit the Morse potential of the Zn–C bond, all other distances and angles are fixed and a scan is performed over this distance, with multiple 'snapshot' DFT calculations

Table 2.2: The potential model. E is energy, r is interatomic distance, r_0 is equilibrium interatomic distance, θ and ϕ are bond angles, and Θ_0 is equilibrium bond angle. Energies are in eV, distances are in A , and bond angles are in degrees. The prefactor of the harmonic bond-bending term is in eV/rad. Adapted from Ref. 325.

Potential	**Type of Bond**	**Values of parameters**
Morse	Zn–C	$D = 0.2432, \alpha = 2.917, r_0 = 2.109$
(Eq. (2.59))	Zn–N	$D = 0.1795, \alpha = 2.701, r_0 = 2.157$
Harmonic three-body	C–Zn–C	$K = 1.5157, \theta_0 = 109.47$
(Eq. (2.60))	C–Zn–N	$K = 1.2695, \theta_0 = 109.47$
	N–Zn–N	$K = 1.0233, \theta_0 = 109.47$
Linear three-body	Zn–C–N	$K = 1.196$
(Eq. (2.61))	Zn–N–C	$K = 1.1968$
Buckingham	C–C	$A = 2806.9, \rho = 0.2667, C = 17.67$
(Eq. (2.62))	C–N	$A = 2365.0, \rho = 0.2825, C = 20.88$
	N–N	$A = 1992.7, \rho = 0.2874, C = 24.67$

performed with varying energies. Because we care the most about capturing the energy landscape near the minimum, a geometry optimisation is performed before the scans. After the subtraction of the electrostatic component of the energy, the Morse potential of the bond [Equation (2.59)] can be fitted to the scan. In this way, it is possible to build up an accurate picture of all the interactions present in a system.

2.6.4 Supercell lattice dynamics

As for MC modelling [§5.3], understanding the dynamics of disordered systems involves the use of supercells. The extended 'supercell lattice dynamics' (SCLD) method is essentially equivalent to the lattice dynamics method described in Section 2.6.2 [214]. Conventional SCLD methods sample the Γ-point of an $L_x \times L_y \times L_z$ supercell. Accordingly, the allowable $\mathbf{k}$ points are

$$\mathbf{k} = \left(\frac{n_x}{L_x}, \frac{n_y}{L_y}, \frac{n_z}{L_z} \right) \quad : \quad n_\alpha \in \mathbb{Z}. \tag{2.70}$$

So a larger supercell allows for a finer $\mathbf{k}$ mesh and higher resolution in reciprocal space. More efficient approaches for the calculation for the special case of mass disorder are possible based on the T-matrix approximation [331], but for more general potentials the calculation remains quite slow.

SCLD calculations remain effective at highlighting the sensitivity of phonon band structure to 'hidden' order [332]. Figure 2.7 shows four different types of local order in a two dimensional system. All the simulations have the same average unit cell so have the same phonon dispersions according to the virtual crystal approximation. However the degree of localisation, phonon energies and line-widths, and even presence of a band-gap varies considerably between the models. One can see from Figure 2.7(e-h) that the measurement of the supercell phonon-density (closeley related to the $S(\mathbf{Q}, E)$ of Equation) is an appropriate probe of the effect of disorder on dynamics.

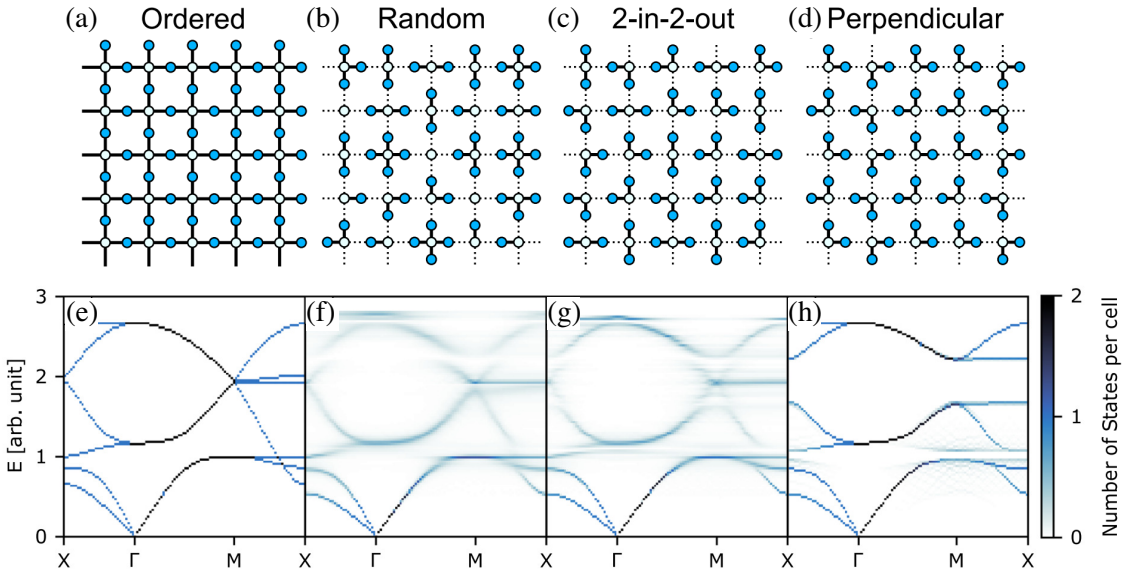

Figure 2.7: (a-d) Models for systems investigated by Roth and Goodwin, with varying degrees of order on the blue site [332] (a) shows long-range order, (b) complete disorder, (c) ice-like disorder (§1.2.4), (d) 'perpendicular-ice' rules. (e-h) The corresponding supercell phonon-density in the harmonic approximation. (e) The ordered model shows sharp dispersion relations as described in Section 1.3.1 while (f–h) show different degrees of broadening and band splitting. Reproduced from Ref. 332.

Chapter 3

Frustrated magnetism in $NaMn(HCOO)_3$

Summary

We have discussed (§1.2.4) how geometrically frustrated materials often exhibit magnetic ordering suppressed to temperatures much lower than the dominant magnetic interaction energy. A consequence of this is that making small changes to the Hamiltonian (*e.g.* by the application of magnetic field) often leads to a substantial change to the magnetic structure. In the case that this change in magnetic structure is accompanied by a change in magnetic entropy, there is a strong magnetocaloric effect. This makes frustrated magnets excellent candidates for magnetocaloric materials [258]. It is in this context that I set out to explore to a relatively understudied lattice—the trillium net—in the dense MOF $Na[Mn(HCOO)_3]$.

I begin the chapter by introducing magnetic framework materials. I then show that $Na[Mn(HCOO)_3]$ exhibits three hallmarks of geometric frustration: (i) the suppression of its Néel temperature T_N far below the characteristic energy scale of its magnetic interactions; (ii) the strongly-correlated disorder indicative of a classical spin liquid (CSL) phase; and (iii) a magnetisation 'pseudo-plateau' indicative of complex field-dependent behaviour. The magnetic ground-state is different to that expected for the trillium nnHAF model, but can be rationalised by accounting for the weaker but ever-present dipolar interactions ('nnHAF+D'). I demonstrate that the resulting nnHAF+D model: (i) accounts quantitatively for the magnetic susceptibility above T_N using an interaction strength J that is consistent with T_N; (ii) correctly predicts both the short-range magnetic correlations of the CSL phase and the magnetic ground-state, as observed in neutron-scattering measurements; and (iii) can be

used to rationalise the existence and temperature-dependence of the measured magnetisation pseudo-plateau. A characteristic magnetocaloric effect associated with this pseudo-plateau emerges. Using the theoretical background obtained for this system, the microscopic driving forces behind this effect are investigated.

Acknowledgements

This project was carried out under the supervision of Dr. Joe Paddison (Churchill College, Cambridge) and Dr. Andrew Wildes (ILL, Grenoble). I am grateful to Dr. Joe Paddison and Prof. Siân Dutton for their generosity at the Cavendish Laboratory, Cambridge and to Dr. Andrew Wildes for supervising me at the ILL. The sample was synthesised by Dr. Breogán Pato-Doldán and Dr. Lilián Claudia Gómez-Aguirre. I carried out magnetisation measurements at the Institut Neel in collaboration with Dr. Elsa Lhôtel, and supported by the European Union's Horizon 2020 Research and Innovation Programme, under Grant Agreement No. 824109.

3.1 Magnetic Framework Materials

The language used to describe framework materials, that of nodes and linkers, is already well suited to the spin/super-exchange description developed in §1.2 for ceramic materials. While there is an important class of framework materials with magnetic linkers [70, 333–335], spin-moments tend to reside in metal nodes with unpaired electrons and superexchange is mediated by the linkers [70]. The description of magnetism in these systems is essentially equivalent to the ceramic systems which have been our focus up to this point. There are some differences related to the greater topological diversity, flexibility and super-exchange types available, which will be the focus of this section.

The aforementioned topological diversity offered by framework materials gives an exciting possibility for the rational design of magnetic models. This allows the chemist to access a range of architectures that would not be imagainable via conventional inorganic magnets [336, 337]. Particular interest has been sparked in the

search for spin liquid candidates with frustrated lattices [338]. The recent discovery of the exactly solvable Kitaev model [339] has led people to look for realisations in layered mixed oxalates $MM'(ox)_3$ [Fig. 3.1(a,d,e)] [338, 340–343]. Most excitingly though, the diversity offered allows chemists to visit other, more complex lattice models too numerous to mention here. Fruitful linkers appear to be 1,2,3-triazolate [344–347], oxalate [340, 348, 349] and formate [350, 351]. One approach to generating new lattices involves augmenting an unfrustrated net with geometrically frustrated nodes [352]. This can be extended to frustrated decorations of frustrated lattices like in $Cr(tri)_2(CF_3SO_3)_{0.33}$ [Fig. 3.1(b)], the pyrochlore lattice is decorrelated with a frustrated node which leads to unusual (itinerant) ordering patterns and electron transport [344, 345, 353]. Where our ability to gain good understanding of metal-oxide magnetism results from these systems' structural simplicity, the future will require accurate prediction of the magnetic properties of increasingly complex structures.

Exchange interactions in framework materials are far more variable than in conventional oxides; in general increasing the size of the link decreases the strength of the interaction [355]. This can be seen as a weakness when compared with ceramic magnets: the ordering temperature in framework materials is typically much lower than room temperature [350]. However, the capability to host a wide range of superexchange parameters within one material (depending on linker length) makes these materials world leading in the design of low dimensional magnets [116, 356]. This approach targeted the pseudo-2D oxalates required for the Kitaev model as highlighted in Figure 3.1(e) [343]. Anticipating Chapter 4, I will focus on the quasi-one dimensional (or single chain) magnets. In these systems, many of the unusual properties discussed in §1.2.3 are found. The structure of a typical low dimensional magnet—$[Co(L)(H_2O)(DMF)]_n$ (NKUMOM-3)—is shown in Figure 3.1(f–g). A long organic linker separates chains by $\sim$ 20 Å and exchange along the chains is kept strong by water bridging [354]. These spin-chain compounds are

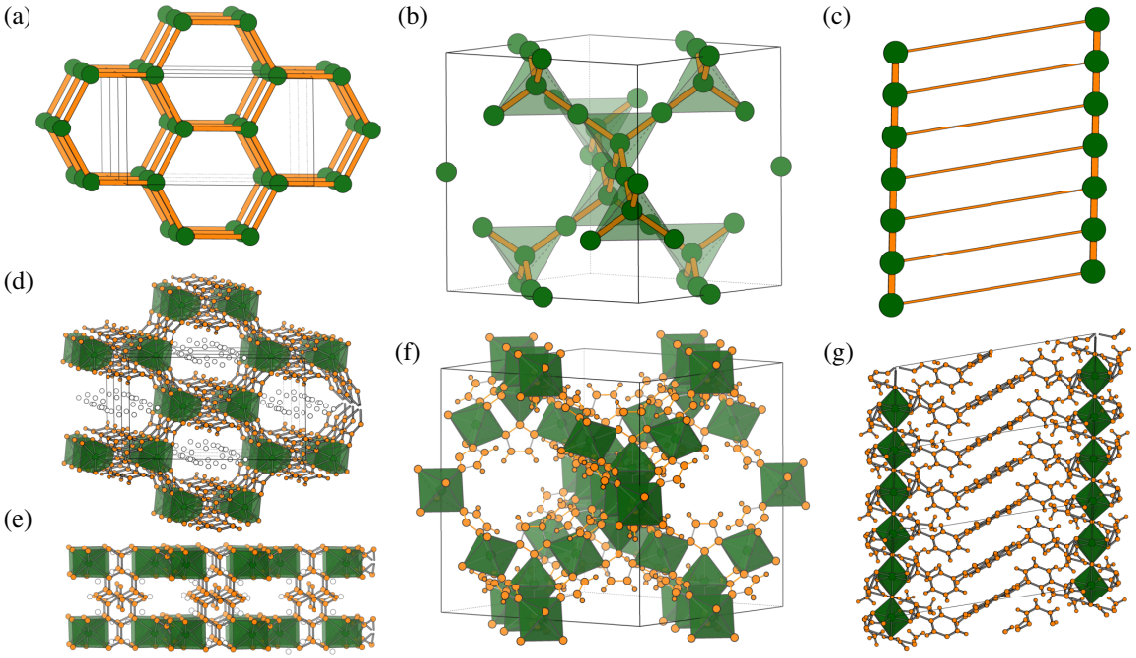

Figure 3.1: (a–c) Underlying node-linker topologies which are of fundamental interest due to their geometric frustration and/or low dimensionality: (a) hexagonal, (b) augemented pyrochlore (see text), and (c) q-1D nets. (d–g) Those topogies' realisation in: (d–e) the layered mixed oxalate $RuMn'(ox)_3$ [344], (f) $Cr(tri)_2(CF_3SO_3)_{0.33}$ [343], and (g) $[Co(L)(H_2O)(DMF)]_n$ [354].

well-established as host materials for distinctively quantum behaviour, from spin fractionalization in $Cu(C_6H_5COO)_2{\cdot}3H_2O$ to the quantum sine-Gordon physics of $Cu(pym)(NO_3)(H_2O)_2$ (pym = pyrimidine) and $[Cu(pym)(H2O)_4]SiF_6{\cdot}H_2O$ [134, 135, 357].

Superexchange interactions exhibit a large range of values depending on the bonding geometry from which they arise. This is true of single atom and molecular species. In the oxides, the Goodenough– Kanamori–Anderson (GKA) rules use the overlap between the orbitals to explain the angle dependence of the superexchange interactions along this line. For example, in octahedral oxides with coupling between two partially filled electron shells superexchange varies from strongly antiferromagnetic to weakly ferromagnetic as the M–O–M angle is changed from 180° to 90° [Fig. 3.2(a–b)] [358, 359]. The situation is more complex for metal formates where the variable topologies seen in Figure 1.1(a) lead to different pos-

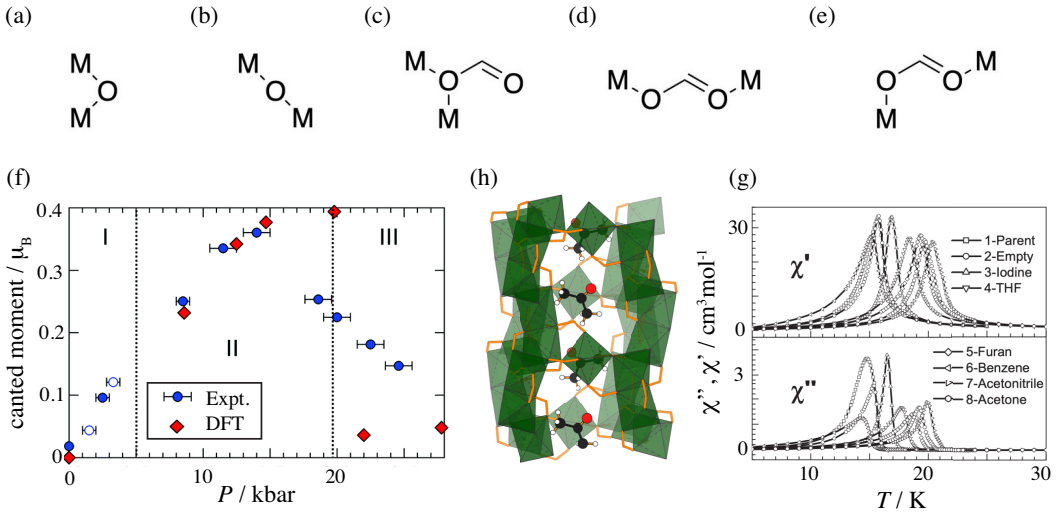

Figure 3.2: (a–e) Super exchange geometries discussed in the text for oxides (a, b) and formates (c,d). From left to right: (a) 90° and (b) 180° oxide superexchange, (c) single atom formate superexchange, and (d) syn–anti, (e) anti–anti [M]–O–C–O–[M] super exchange. (f) The dependence of canted moment on pressure in $[NH_4]Fe(HCOO)_3$, reproduced from Ref. 360. (g) A channel of the host guest structure for acetone@$[Fe_3(HCOO)_6]$ and (h) the guest dependence of the real and imaginary components of the susceptibility. Reproduced from Ref. 361.

sibilities for binding modes, as shown in Figure 3.2(c-e). The binding mode in frame (c) gives the strongest superexchange due to the shared atom but distinguishing between the binding strength of the M–O–C–O–M link is more difficult. Recent work has indicated that GKA rules extend to the formates, based on a joint DFT, magnetometery and quantum crystallography study on the formate perovskite $[(CH_3)_2NH_2]Cu(HCOO)_3$, where extreme octahedral tilting leads to vastly different coupling constants ($J/J' \sim 10$) despite the same bonding mode [86].

The strength of exchange constants seems to be different depending on topology. The value is much stronger in perovskite and chiral hexagonal topologies, which involves anti–anti binding of formate [Fig.3.2(h)], than the chiral cubic family, where binding is syn–anti [Fig.3.2(g)]. This can be seen throughout the family but anticipating §3 and 5, I will focus this analysis on Manganese containing formates, AMn(HCOO)$_3$. In the perovskite series, namely for $A = [H_3CNH_2]^+$, $[H_2C(CH_3)NH_2]^+$, $[HC(CH_3)_2NH]^+$, $[c\text{-}(CH_2)_3NH]^+$, $[NH_2NH_2]^+$ and $[HONH_3]^+$,

this family shows consistent behaviour [87, 362, 363]. All of these systems show antiferromagnetism, characterised by a maximum in the ZFC magnetisation at T_N. The antiferromagnetic interaction strength has been estimated for four members of the series by fitting to the susceptibility data and is apparently fairly indifferent to the cation: values range from $J = 5.7$ to 6.5 K for the various formate perovskites [87]. A similar coupling constant (5.68 K) is obtained by fitting to the magnetic component of the heat capacity in $Mn(HCOO)_2{\cdot}2H_2O$ [364].

A less significant factor which make the magnetism of the family more rich is that all of the systems cited show a canting transition [87, 362, 363, 365], characterised by a maximum in magnetic susceptibility as a function of field. The form of the maximum stays the same but it changes in position depending on the identity of A. For the same four formate perovskites discussed in the last paragraph, the position of this maximum varied considerably between $H \simeq 0.2$ and 1.1 T, depending on the identity of A [87]. Although we do not expect a large anisotropy in these systems, this canting transition is likely due to a small magnetic anisotropy which may arise effectively from the dipolar or some other anisotropic interaction(s) [366]. This similarity of behaviour is in spite of the two different topologies that these structures exhibit, suggesting that it relates to the composition and local environments involved and not the large scale structure.

The observation of moment canting, leading to very weak remnant magnetisation, is probably the best studied observation about the magnetism in this series [87, 362, 363]. The canting likely arises due to the antisymmetric exchange [103, 367]. In the case of the materials examined in this study, weak ferromagnetism is expected to arise from the Dzyaloshinski-Moriya interaction, which is the result of the lack of a centre of symmetry between the isotropic Mn^{2+} ions that are bridged by $HCOO^-$, and the different orientation of each coordination octahedron of the metal ion compared to its six neighbors. The design principles needed to induce ferroelectricity into Formate Perovskites are known and well studied [28]. The coupling of this very

weak ferromagnetism to ferroelectricity makes $[(CH_3)_2NH_2]Mn(HCOO)_3$ a multiferroic compound [95]. Moreover, this coexistence has been demonstrated to lead to magneto-electric coupling [368]. However, the small magnitude of the permanent magnetisation makes this coupling weak.

The coexistence of magnetic order and mechanical softness leads to strongly pressure dependant super-exchange in the formates. This has been the subject of a recent study on the $[NH_4]M(HCOO)_3$ (M=Mn, Fe, Ni) channel formates by Collings *et al.* [360]. These systems undergo a cascade of phase transitions related to formate rearrangements and have a small change in direct exchange, indicated by an $\sim 20\,\%$ change in the Néel temperature, and explained by DFT simulations. The more significant change is in the canted moment [Fig. 3.2] which changes in a way which is well predicted by DFT across the 3 phases. A relevent example is $[Fe_3(HCOO)_6]$, where the channel structure allows for the intercalation of host solvent molecules such as acetone [Fig. 3.2(g)]. This is highly consequential for the magnetic interactions, leading to a considerable change in the magnetic susceptibility as a function of guest absorption [Fig. 3.2(h)] [361]. This strong guest dependant magnetism may be exploited for sensing in framework materials [70, 333].

There are relatively few systems which crystallise in the polar $P2_13$ space group of $NaMn(HCOO)_3$. The coupling in these systems seems to be much weaker ($J \sim 1\,\mathrm{K}$) obtained for $NaMn(HCOO)_3$ by Aston and coworkers from a Curie–Wiess fit to magnetometery data [89]. This is because of the differing superexchange pathways for the anti-anti binding mode seen for formate perovskites compared with the syn-anti mode seen in $NaMn(HCOO)_3$ [89, 369]. It is this system which will be the focus of my first investigation, due to the frustration inherent to its trillium lattice (§1.2.4).

3.2 Observation of Magnetic Ordering

I begin by reporting the low-field magnetic behaviour of $NaMn(HCOO)_3$, expanding on the earlier measurements of Ref. 89, which are plotted in Figure 3.3(a). A $\sim 0.4\,\mathrm{g}$

polycrystalline sample of $NaMn(HCOO)_3$ was prepared by Breogán Pato-Doldán and L. Claudia Gómez-Aguirre using a slow diffusion method related to that reported in Refs. 84, 89 and described in Ref. 370. I used powder X-ray diffraction to check that the purity of this sample has not degraded since its original synthesis. The limitations on the existing magnetisation measurement can be seen in varying the minimum temperature of this fit. Varying this value sees the estimate of the value span $-1.5 \lesssim \Theta_{\mathrm{CW}} \lesssim 2.5\,\mathrm{K}$, indicating that this estimate of the interaction strength is not robust.

To obtain a better estimate of the interaction type present in this system and to understand the low-temperature limit of the magnetic behaviour magnetisation measurements were performed down to 80 mK. The low-field magnetic susceptibility, measured for a 10 mg fraction of this sample, allowed for another estimate of Θ_{CW}. For $T \gtrsim 2\,\mathrm{K}$, the magnetic behaviour is Curie-Weiss-like and antiferromagnetic; the corresponding fit over the range $2.0 < T < 4.5\,\mathrm{K}$, (which is shown in Figure 3.6) gives another estimate $\Theta_{\mathrm{CW}} = -2.3(3)\,\mathrm{K}$, which is consistent with the value obtained in [89]. Again, the uncertainty on this value reflects the variation of our fit with the minimum of the fitting range T_{min}. A better estimate of the interactions will be found in §3.4 based on fitting of our model but this value confirms the presence of antiferromagnetic interactions required for geometric frustration.

The low temperature behaviour of the inverse magnetic susceptibility [Fig. 3.3(b)] reveals a Néel transition—seen here for the first time for this system—at $T_{\mathrm{N}} = 0.223(18)\,\mathrm{K}$. The uncertainty in this value is a consequence of the small amount of thermal hysteresis shown in the value of χ^{-1}. The corresponding frustration parameter $f = |\Theta_{\mathrm{CW}}|/T_{\mathrm{N}} \sim 10$ indicates that $NaMn(HCOO)_3$ is a strongly frustrated magnet [§1.2.4] [371]. This value is consistent with theoretical estimates for the nnHAF model [168].

In order to understand the structure of this ground–state and the correlated paramagnetic regime above, I performed magnetic neutron scattering measurements in

collaboration with Andrew Wildes, based at the ILL, and Joe Paddison, then based at Churchill College, Cambridge. We used the D7 instrument at the ILL [281], operating in XYZ polarisation mode, to separate the magnetic scattering for a powder sample of $Na[Mn(HCOO)_3]$ from the nuclear and spin-incoherent components. These were performed at two different wavelengths, $\lambda = 3.1565$ and $4.873\,\text{Å}$, the lower wavelength at 20 K and 1.5 K and the higher wavelength at 1.5 K and 100 mK. The lower wavelength was used at 100 mK to ensure the highest q-resolution to resolve Bragg peaks.

Our measurements at 100 mK ($T < T_N \ll J$) are shown in Fig. 3.3(c), where I have placed the scattering intensities on an absolute scale by Rietveld refinement of the nuclear scattering. Below T_N, magnetic Bragg peaks do indeed appear and the magnetic diffuse scattering is suppressed, consistent with long-range magnetic order. From the theory of the nnHAF, model, the magnetic ground state is predicted to have the $k_{ord} = [1/3, 0, 0]$ ordering vector and each of the three sublattices is predicted to have spins coaligned but pointing at 120° to each-other [372]. However,

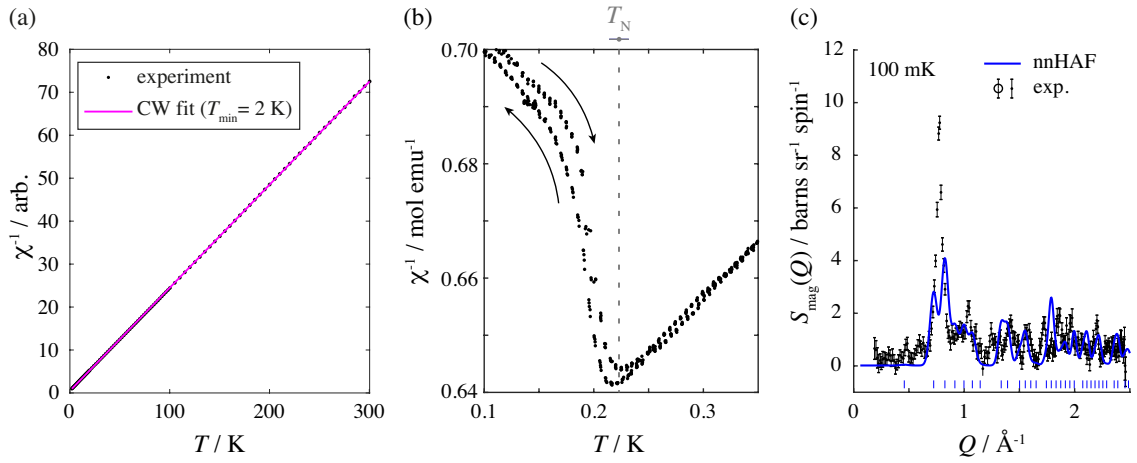

Figure 3.3: (a) High temperature inverse magnetic susceptibility, data reproduced from reference [89] compared with its Curie–Weiss fit. *Inset*: the variation of Θ_{CW}, fitted over the temperature range $T_{min} \leq T \leq 300$ K, with T_{min}. Our estimate based on the low temperature data (shown with errors in green) overestimates the magnitude of Θ_{CW}. (b) Low temperature inverse magnetic susceptibility with an indication of T_N and its errors. (c) The magnetic component of the low temperature (100 mK) neutron scattering measured on D7, compared with the simulated pattern expected for the nnHAF groundstate described in Ref. 89.

the magnetic scattering calculated from the known magnetic structure *via* Equation (2.17) is completely inconsistent with that measured experimentally. It is not even possible to index the Bragg peaks in terms of the $\mathbf{k}_{\mathrm{ord}} = [\frac{1}{3}, 0, 0]$ ordering vector expected from the nnHAF ground-state. For this reason it is clear that the simple level of theory studied on this lattice so far (the nnHAF model) is insufficient to explain the physics of this system.

3.3 Behaviour of the nnHAF+D model

An obvious omission of this model is consideration of the always-present magnetic dipolar interactions; note that no significant single-ion anisotropy is expected for the high-spin Mn^{2+} (d^5) configuration in an octahedral crystal field. Using the crystallographic Mn...Mn separation and taking $S = \frac{5}{2}$ for Mn^{2+}, the relevant dipolar energy scale in $Na[Mn(HCOO)_3]$ is $D = 0.118\,\mathrm{K}$. Since $D \ll J$, one might ordinarily have expected the nnHAF ground-state to be robust to this additional interaction. Yet, in the absence of the corresponding theory (to the best of our knowledge), it fell to me to test this assertion by introducing dipolar interactions into the nnHAF model.

Mean-field calculations were carried out to ascertain whether a dipolar term would be sufficient to change the ordered state. A previous mean-field study of the nnHAF model found a degenerate sphere of ground-states at $|\mathbf{k}| = 1/3$ [164]. Figure 3.4(a) shows that the addition of a dipolar term of similar magnitude to that considered in our study is sufficient to move the maximum eigenvalue along the $[h, 0, 0]$ direction from $[1/3, 0, 0]$ to close to $[1/2, 0, 0]$. While the magnitude of the ordering wave-vector remains well-defined, its direction in $\mathbf{k}$-space is again relatively unconstrained. The global maximum eigenvalue in fact lies along the [110] direction, although its eigenvalue ($3.22J$) is almost exactly degenerate with the value at the $[1/2, 0, 0]$ position ($3.19J$). Consequently, our main conclusion from these mean–field calculations is that, within the mean–field approximation, the dipolar interactions of the relative strength predicted for $Na[Mn(HCOO)_3]$ is sufficient to account for a

change in ordering from $\mathbf{q}_{\text{ord}} = [1/3, 0, 0]$ to $[1/2, 0, 0]$.

In previous studies of the the nnHAF model, MF was insufficient to ascertain the nature of the ground state and it was necessary to turn to Monte Carlo simulations. For this reason I carried out a series of classical Monte Carlo (MC) simulations related to those of Ref. 168 but with MC energies now calculated using the nnHAF+D expression

$$E_{\text{MC}} = J \sum_{\langle i>j \rangle} \mathbf{S}_i \cdot \mathbf{S}_j + D \sum_{i>j} \frac{\mathbf{S}_i \cdot \mathbf{S}_j + 3(\mathbf{S}_i \cdot \hat{\mathbf{r}}_{ij})(\mathbf{S}_j \cdot \hat{\mathbf{r}}_{ij})}{(r_{ij}/r_1)^3}. \tag{3.1}$$

Here, $\mathbf{S}_i$ represents the vector spin orientation at site i, $\hat{\mathbf{r}}_{ij}$ is the unit-vector pointing from spin i to spin j, and r_1 is the nearest-neighbour separation. The first sum is taken over distinct nearest-neighbour pairs i, j. Here, as elsewhere, the spin magnitudes are subsumed within the constants J and D. For all our simulations, we generated spin configurations representing a $6 \times 6 \times 6$ supercell of the $P2_13$ unit-cell ($N = 864$ spins each), initially assigning spin orientations randomly. Each MC move corresponded to a random reorientation of a randomly-chosen spin. Proposed moves were accepted or rejected according to the Metropolis-Hastings criterion [313]. I used Ewald summation as implemented in Ref. 90 to treat the long-range dipolar interactions when present.

For the MC simulations used to calculate low-field susceptibility there were two regimes explored: a sparser temperature grid was required at high temperatures, and a finer grid at low temperatures. In the 'high temperature' regime, the effective MC simulation temperature T/J was varied between 0.4301 and 2.1505, with intervals $\Delta T/J = 0.0215$. This gave a total of 81 temperature points. In the low temperature regime $0.2056 < T/J < 0.5376$, with $\Delta T/J = 0.0108$; this gave 32 temperature points.

For each run, at each temperature, there were 100 independent measurements. Each simulation was allowed to completely decorrelate between successive measure-

ments. This was ensured by tracking the self-correlation function:

$$\langle \mathbf{S}(0) \cdot \mathbf{S}(t) \rangle = \frac{1}{N} \sum_i \mathbf{S}_i(0) \cdot \mathbf{S}_i(t). \tag{3.2}$$

Between samples, the simulation was run for twice as many steps as was required for this quantity to reach zero. Between temperatures, the simulation was run for three times this same step-count. Below the ordering temperature, the amount of simulation time required for this strict criterion to be met meant that only four temperature-points below T_{N} could be simulated. Magnetic susceptibilities were calculated from the isothermal fluctuations using

$$\chi_{\mathrm{m}} = \frac{\mu_0}{N k_{\mathrm{B}} T} \left[\langle M^2 \rangle - \langle M \rangle^2 \right], \tag{3.3}$$

where M is the configurational magnetisation [292]. The whole procedure was repeated 1600 times (*i.e.* cooling from T_{max} to T_{min} 1600 times) and the susceptibility calculated as an average over all 1600 runs.

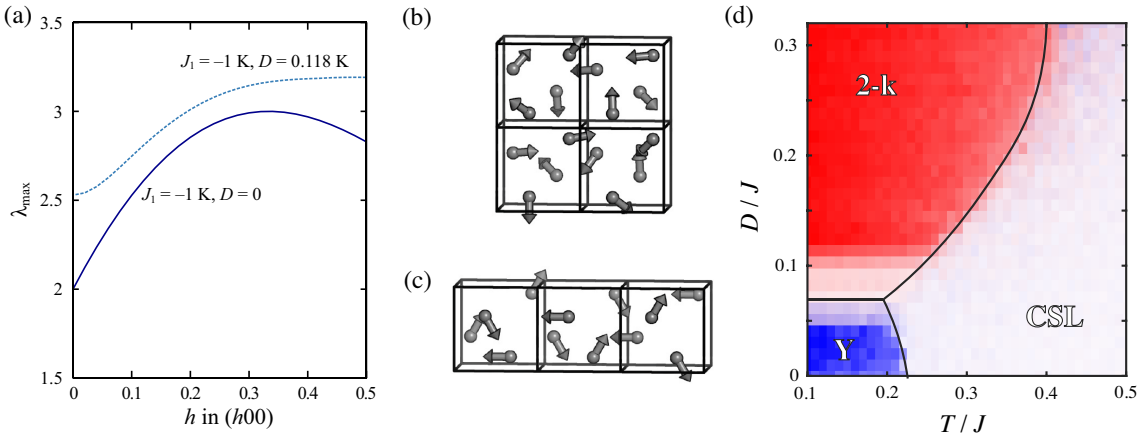

Figure 3.4: (a) Maximum eigenvalue of a mean–field simulation for the nnHAF and nnHAF+D model, with a similar ratio of J/D as in the refined model. Note that the energy landscape is shallow enough that the addition of the much smaller $D = 0.118\,\mathrm{K}$ term is enough to move the maximum eigenvalue along the $h00$ line from $[1/3, 0, 0]$ to close to $[1/2, 0, 0]$. (b–c) Ground states of the nnHAF and nnHAF+D models respectively. (d) Phase diagram for the nnHAF+D model with the structure parameter associated with $\mathbf{k} = [1/3, 0, 0]$ in blue and the $\mathbf{k} = [1/2, 0, 0]$ in red.

Consistent with the mean–field simulations, the type of magnetic order driven by Eq. (3.1) at low temperatures turns out to be surprisingly sensitive to the value of D/J [Fig. 3.4(d)]. For $D \gtrsim 0.08J$, the magnetic ground-state switches from the helical $\mathbf{k}_{\rm ord} = [\frac{1}{3}, 0, 0]$ [Fig. 3.4(c)] order of the nnHAF model to a 2-$\mathbf{k}$ state with $\mathbf{k}_{\rm ord} \in \langle \frac{1}{2}, 0, 0 \rangle$ [Fig. 3.4(b)].

Spin orientations in a representative solution to the magnetic ground-state of the nnHAF+D model are given in Appendix B.2. In this particular case, the ordering wave-vectors are $\mathbf{k}_{\rm ord} = [\frac{1}{2}, 0, 0]$ and $[0, 0, \frac{1}{2}]$. For these particular wave-vectors, all spin decorations of the trillium lattice are described by the same totally-symmetric irreducible representation Γ_1. For the specific spin orientations given in Table B4, the corresponding basis vectors have real components

$$\mathrm{Re}[\psi(\tfrac{1}{2}, 0, 0)] = (0.78, -0.10, 0.38); \tag{3.4}$$

$$\mathrm{Re}[\psi(0, 0, \tfrac{1}{2})] = (0.19, 0.39, -0.32). \tag{3.5}$$

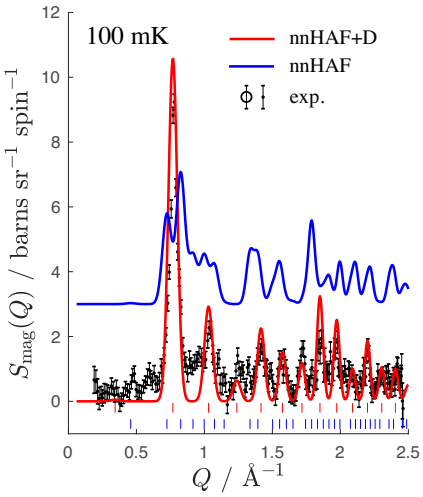

Figure 3.5: The low temperature magnetic neutron scattering shows a much better agreement with theoretic predictions for the ground state of the nnHAF+D model [Fig. 3.5(b)], shown in red, data than that of the nnHAF model [Fig. 3.4(c)], shown in blue and offset by 3 units for clarity.

The magnetic Bragg diffraction pattern of this new 2-**k** ground-state shows a remarkable similarity to our 100 mK measurement for $Na[Mn(HCOO)_3]$ [Fig. 3.5], which suggests that the nnHAF+D model may indeed capture the key physics at play in this magnetic MOF.

3.4 Parametrisation and Validation

In order to test the effectiveness of the model against all our experimental measurements, we required an accurate estimate of the Heisenberg exchange strength J. Fig. 3.6 compares the inverse susceptibilities calculated for both nnHAF and nnHAF+D models over the same temperature range used for parametrisation. For $D \ll J$, the behaviour of Eq. (3.1) at $T \geq J/2$ was essentially indistinguishable to the nnHAF model ($D = 0$). Consequently, we estimated J by determining the $T \geq J/2$ susceptibility for the $D = 0$ case, and then carrying out a least-squares fit of J to best match experiment.

From the MC configurations, χ_m was calculated at each temperature from the fluctuations in z-magnetisation M *via* Equation (3.3). In order to parameterise the nnHAF model—*i.e.* determine an appropriate J and mass-scale-factor—it was necessary to fit to the experimental magnetisation. From the Curie–Weiss law, one might expect inverse susceptibility to be approximately linear locally. For this reason, linear interpolation was used between the discrete simulation points on the grids described above in order to map the experimental temperature points onto the simulated ones.

We define an error function, $\Xi(\mathbf{P})$, for a given parametrisation $\mathbf{P}$ (with $P = 2$ parameters and $N = 1268$ measurements) as a sum over our *experimental* data points:

$$\Xi(\mathbf{P}) = \frac{1}{N} \sum_i \left\{ \left[\chi_m^{\mathrm{exp}}(T_i)\right]^{-1} - \left[\chi_m^{\mathrm{MC}}(\mathbf{P}, T_i)\right]^{-1} \right\}^2 . \tag{3.6}$$

A grid-search can then be carried out in order to identify the minimum value of $\Xi(\mathbf{P})$. The resulting figure-of-merit is shown in Figure 3.6 alongside the corresponding best

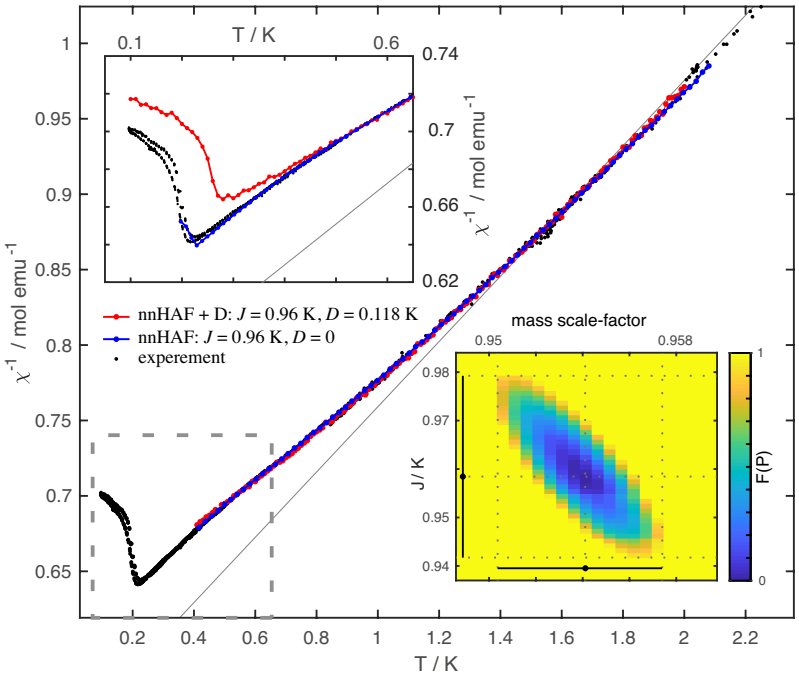

Figure 3.6: Low-field (100 Oe) magnetic susceptibility of Na[Mn(HCOO)$_3$], shown as its inverse (black data points). A Curie–Weiss (CW) fit over the range $2 < T < 4.5$ K is shown as a thin black line. The experimental data were first fitted using the nnHAF model, for which there are two free parameters: the magnitude of J and a mass scale-factor to align experiment and calculation. *Top-left insert* showing that the model in the absence of a dipolar interaction predicts the Neel temperature slightly better, but both models well reproduce the observed deviation from linearity. *Bottom right insert* shows the figure-of-merit for this fitting process. Error bars demarcate confidence intervals on the two fit parameters bounding the region where $F(P) \leq 1$. Refined values are $J = 0.96(2)$ K and a mass scale factor of 0.954(3). The resulting fit of the nnHAF model is shown in blue in the main figure. This fit is compared to the inverse susceptibility calculated for the nnHAF+D model, now using the refined value of J (0.96 K) together with $D = 0.118$ K as discussed in the main text. A slightly different mass–scale factor (1.0306) was used to scale this calculation so as best to match experiment. Note that both scale factors are within a few percent of unity. Both nnHAF and nnHAF+D models give accurate descriptions of the susceptibility—including the deviation from Curie-Weiss behaviour—over the temperature range discussed here.

fit. Since our fit is sufficiently good, we make the assumption that deviations from our best fit give an estimate of the errors present in the measurement. As such the error in the parameters can be estimated via the F-test by defining

$$F(\mathbf{P}) = (N - P)\left[\frac{\Xi(\mathbf{P})}{\Xi(\mathbf{P}_{\text{best}})} - 1\right]. \tag{3.7}$$

The fit is considered significantly worse than our best fit if $F(\mathbf{P}) > 1$ [Fig. 3.6]. The range over which $F(\mathbf{P}) \leq 1$ defines the size of our error in each parameter.

In this way, I obtain $J = 0.96(2)\,\mathrm{K}$, a value which is consistent with the estimate given in Ref. 89, from a Curie–Wiess fit to high temperature data. Moreover, the resulting relative energy scale $D/J = 0.119$ locates $Na[Mn(HCOO)_3]$ within the regime for which 2-**k** order is expected [Fig. 3.4(d)]. The results of the nnHAF+D MC simulations carried out using this combination of J and D are shown as the red lines in Fig. 3.7. The nnHAF+D model captures at once the Curie-Weiss behaviour for $T \gtrsim 2\,\mathrm{K}$, the departure from Curie-Weiss behaviour for $T \lesssim 2\,\mathrm{K}$, and the Néel transition itself. We find $T_\mathrm{N} = 0.27(1)\,\mathrm{K}$, in good agreement with experiment, although slightly worse than the pure nnHAF model.

Given this parameterised value of J, two additional MC simulations were run at $T = 1.5\,\mathrm{K}$ and $20\,\mathrm{K}$—the two temperatures for which we measured $S_\mathrm{mag}(Q)$. For these configurations, spin–spin correlation functions were calculated, using the SPINCORREL code [373]. These functions are shown in Fig. 3.7(a–b) and the corresponding scattering functions in Fig. 3.7(c). The magnetic diffuse scattering was calculated using the SPINVERT code [307, 373] using Equation (2.14).

So the nnHAF+D Hamiltonian provides a good representation of the spin physics at play in $Na[Mn(HCOO)_3]$. Perhaps the largest discrepancy between experiment and calculation is the small difference in T_N [see inset to Fig. 3.6]. This discrepancy may reflect the relevance of yet weaker interactions, such as single-ion anisotropy (usually safely ignored for high-spin Mn^{2+}) and/or antisymmetric exchange interactions, as allowed by the chiral crystal structure. We have not explored either case here further. We do note, however, that the dipolar interactions of our nnHAF+D model induce an Ising-like spin anisotropy consistent with the crystallographic point symmetry of the Mn site (*cf.* [90]). Consequently, an easy-plane single-ion term in an extended Hamiltonian may compete with the dipolar interactions, in turn reducing T_N.

3.5 Behaviour under Higher Fields

Given the sensitivity of the nnHAF model to perturbations in the zero-field limit, we might expect $Na[Mn(HCOO)_3]$ to be especially sensitive to an applied magnetic field. To explore this point we carried out a series of high-field magnetisation measurements at finely-spaced temperatures within the ordered and correlated paramagnetic regimes ($200 < T < 350\,\mathrm{mK}$) using applied fields $0 < \mu_0 H < 1.5\,\mathrm{T}$. Isothermal field-dependent magnetisation curves were measured at several temperatures between 100 mK and 4.2 K, using fields up to 8 T. Fig. 3.8 shows these data for $T \leq 500\,\mathrm{mK}$. At these low temperatures, the magnetisation is essentially saturated under an applied field of 2 T. No hysteresis was observed.

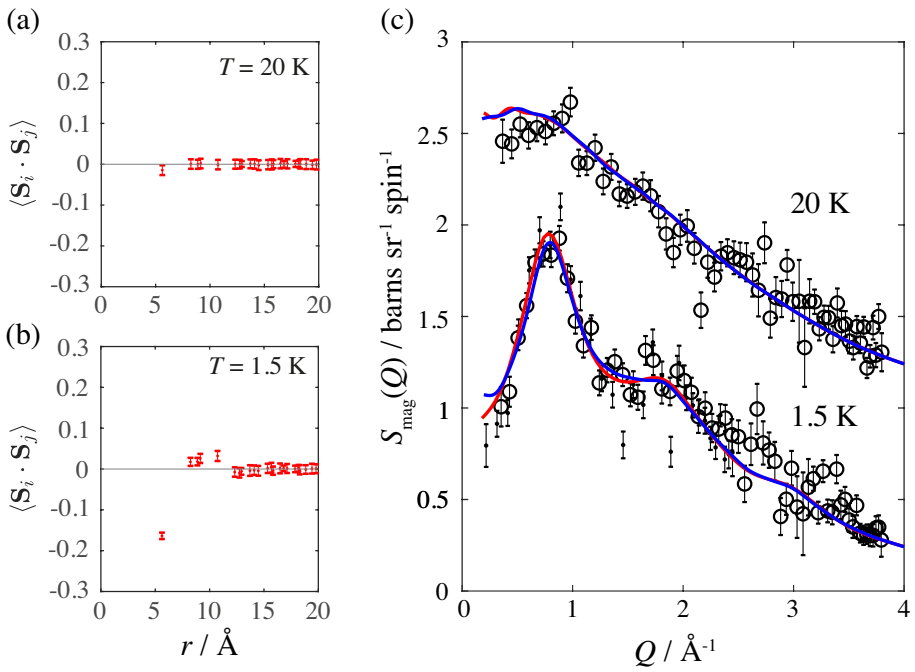

Figure 3.7: (a–b) Spin–spin correlation functions calculated from Monte-Carlo simulations at the two temperatures investigated experimentally. (a) At 20 K there are no significant correlations present in the nnHAF+D model; hence $S(Q)$ is well represented by the magnetic form-factor. (b) By contrast, at 1.5 K nearest neighbour pairs have a negative spin correlation, meaning that they are more likely to be aligned anti-parallel to one another. Correlations beyond nearest-neighbour are very weak. (c) The corresponding magnetic neutron scattering and calculated neutron scattering for the nnHAF and nnHAF+D models at 20 and 1.4 K, the latter offset by one unit for clarity.

The most obvious feature we observe is a valley in $\mathrm{d}M/\mathrm{d}H$ centred on $\mu_0 H \sim 0.6\,\mathrm{T}$ that corresponds to a pseudo-plateau in the field-dependence of the magnetisation at $M/M_{\mathrm{sat}} = \frac{1}{3}$. This feature is strongest at low temperatures, but persists with varying prominence throughout the temperature range of our measurements. I proceed to show that the origin of this feature is the suppression of magnetic fluctuations within a new ordered phase that is stabilised at finite field. Additionally at lower temperatures, another feature develops with at least 3 peaks in the susceptibility as a function of field.

This behaviour is reminiscent of a pseudoplateau predicted theoretically by Moliner and collaborators [374] for a Heisenberg nearest neighbour model on the related and better studied Shastry Sutherland lattice (SSL). This is unlikely to be coincidence: Fig. 3.8(c–d) illustrates the mapping between trillium and SSL lattices: when

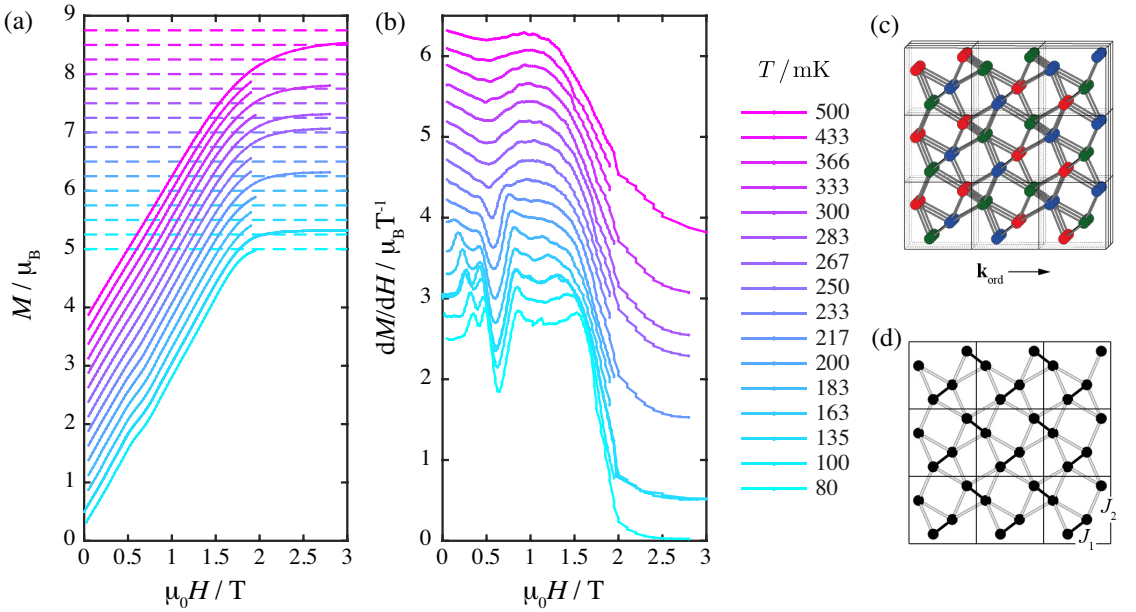

Figure 3.8: (a) Experimental magnetisation measurements for $Na[Mn(HCOO)_3]$ performed at 11 different temperatures. For clarity, successive curves are offset vertically by 0.25 units. The dashed horizontal lines show the theoretical saturation magnetisation of 5.0 μ_B ($S = 5/2$). (b) The gradient of magnetisation with respect to field. (c) A $3\times3\times3$ supercell of the trillium lattice, with nodes coloured red green and blue according to the unique tripartite colouring, with the $\mathbf{k} = [1/3, 0, 0]$ ordering vector horizontal. (d) A $3 \times 3 \times 3$ supercell of the Shastry Sutherland lattice (SSL) showing the nearest (J_1) and next-nearest (J_2) neighbours as black and white bonds, respectively. The SSL is the projection of the trillium lattice into the plane.

the trillium lattice is projected down $\langle 100 \rangle$, one recovers the SSL with the parameterisation $J_2/J_1 = 0.5$ (here, J_1 and J_2 are the 'short' and 'long' interactions of the SSL model, and twice as many links of the trillium lattice project onto the short interactions as the long). In this projection, the two lattices have the same tripartite colouring. Crucially, a MC study of the SSL model at precisely this J_2/J_1 ratio uncovered the same type of magnetisation pseudo-plateau and phase field as those observed here [374].

Inspired by these observations on the related SSL lattice, and to help understand this field-dependent behaviour, we explored the effect of introducing a Zeeman term into the original nnHAF model:

$$E = J \sum_{\langle i>j \rangle} \mathbf{S}_i \cdot \mathbf{S}_j + \mu_0 \mathbf{H} \cdot \sum_i \mathbf{S}_i. \tag{3.8}$$

Here I intentionally neglect dipolar interactions for two key reasons: (i) the corresponding energy scale in this system is an order of magnitude smaller than that of Heisenberg exchange, and (ii) our powder measurements represent an average over crystallite orientations, the effect of which is computationally difficult to take into account when including anisotropic interactions. We will discuss in due course the most important consequences of this approximation. Nevertheless we carried out a new set of MC simulations driven by the modified Hamiltonian (3.8), focusing on the same range of $\mu_0 H$ and T values explored experimentally.

The simulation results reflect both similarities and differences to experiment [Fig. 3.9]. Perhaps most importantly, the susceptibility minimum near $M/M_{\mathrm{sat}} \sim \frac{1}{3}$ appears strongly for temperatures below 290 mK, which indicates that a magnetisation pseudo-plateau is intrinsic to the Hamiltonian (3.8). In the simulations, this susceptibility 'valley' is flanked by two sharp maxima that demarcate a new phase region centred at finite field. This phase is stable for temperatures beyond T_{N} to a critical value $T^* \sim 290$ mK. The susceptibility maxima marking the phase boundary are not resolved in our experimental data, but may have been washed out as a re-

sult of orientational averaging. The zero-field nnHAF Hamiltonian (3.8) is isotropic, which means the system's response is invariant to the direction of applied field and hence there is no need to take into account crystallite orientation; the presence of anisotropic dipolar interactions in practice introduces an orientational dependence over which our experimental measurements are integrated.

Inspection of our MC simulations shows the new field-stabilised phase to be an 'up–up–down' (UUD) state in which the moments of two thirds of the Mn^{2+} ions align parallel to the applied field, and that of the other third opposes the field. Complete UUD order gives $M/M_{\text{sat}} = \frac{1}{3}$, which is why the susceptibility drops around this value. We note that the field-dependent behaviour of Heisenberg antiferromagnets on other tripartite lattices (*e.g.* triangular [375, 376] and Shastry-Sutherland (SSL) [374]) are also known to involve a transition from their zero-field ground-state to an 'UUD' phase, such as we see here [374–376]. The SSL physics likely reflects the similarities between the two lattices' nets, as discussed above.

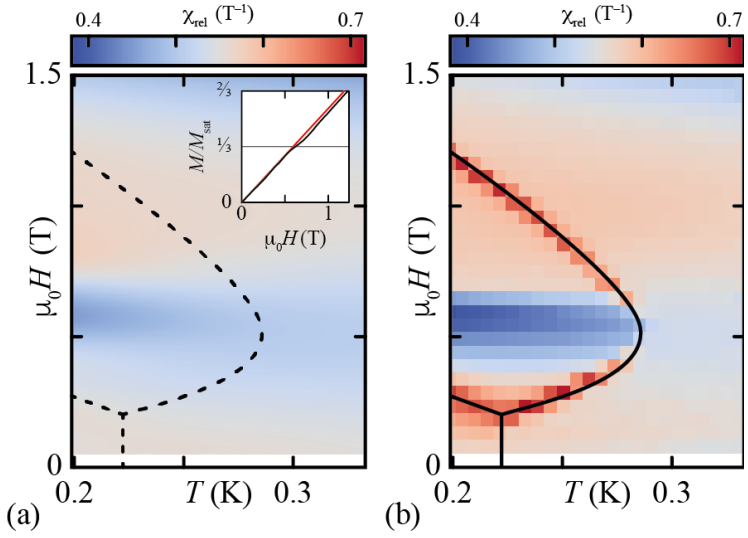

Figure 3.9: (a) Experimental field and temperature dependence of the magnetic susceptibility of Na[Mn(HCOO)$_3$]. The inset shows the field-dependent magnetisation at 100 mK; experimental data in black and low-field linear fit in red. Note the pseudo-plateau at $M/M_{\text{sat}} \simeq \frac{1}{3}$. This feature corresponds to the horizontal blue region at ∼0.6 T in the main plot. (b) Magnetic susceptibility from MC simulations, with phase boundaries shown as solid lines. Within the regime $T_{\text{N}} < T < T^*$, it is possible to cycle between disordered and ordered states under the application and removal of a low magnetic field (white circles).

There is a special significance of the proximity of (disordered) CSL and (ordered) UUD phases for $T_{\mathrm{N}} < T < T^{*}$. Within this regime, an applied field drives a disorder/order transition, resulting in a sudden loss of entropy to be expelled as heat—*i.e.* a magnetocaloric effect [377]. Moreover, since the UUD state has $M/M_{\mathrm{sat}} \sim \frac{1}{3}$, the field required to generate this entropy change is small by comparison to that required to induce transitions in conventional antiferromagnets. As such we expect an attractive low-field magnetocaloric entropy change in $\mathrm{Na[Mn(HCOO)_3]}$.

The magnitude of this magnetocaloric response was calculated from both experiment and simulation according to the relation [377]

$$\Delta S_{\mathrm{mag}}(H,T) = \mu_0 \int_0^H \frac{\partial M_{\parallel}(H',T)}{\partial T} \mathrm{d}H'. \tag{3.9}$$

Here $M_{\parallel}$ is the magnetisation parallel to the direction of applied field. Our results are shown in Figure 3.10. For temperatures $T > T^{*}$, the magnetic entropy change behaves essentially as one expects for a paramagnet: field increasingly reduces the magnetic degrees of freedom, such that entropy reduces smoothly and monotoni-

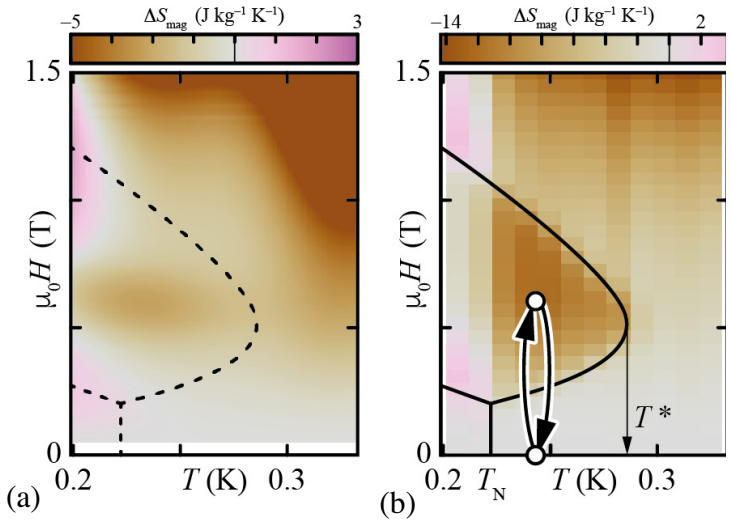

Figure 3.10: The corresponding field-induced change in magnetic entropy from (a) experiment and (b) MC simulations, which has a local maximum within the UUD phase. Hence the cycling regime illustrated in panel (b) offers a magnetocaloric cooling strategy.

cally. For $T < T^*$, however, there is a local maximum in magnetic entropy change that coincides with UUD order. In our simulations, the most negative value of ΔS_{mag} we obtain (*viz.* $-12\,\mathrm{J\,kg^{-1}\,K^{-1}}$) is actually competitive with that of systems used commercially for magnetocaloric cooling [378, 379]. The experimental value is less extreme by a factor of about four because orientational averaging over crystallite orientations makes the CSL→UUD transition smooth. One expects a sharper transition in single-crystal measurements that no longer integrate over crystallite orientation, which in turn would amplify the magnetocaloric entropy change attainable in this system. One way or the other, the basic principle would be to cycle between CSL and UUD states by applying and removing field, dumping the heat generated as entropy during the CSL→UUD transition, then forcing the system to cool its environment on recovery of the higher-entropy CSL phase [Fig. 3.10(b)].

3.6 Conclusion

This study has demonstrated that $\mathrm{Na[Mn(HCOO)_3]}$ exhibits strong magnetic frustration, characterized by the suppression of the Néel transition at temperatures well below the expected magnetic interaction strength, the presence of short-range magnetic order at high temperatures, and a pseudo-plateau in the magnetic susceptibility at $\frac{1}{3}$-saturation magnetisation. These observations can be quantitatively explained by a model involving Heisenberg antiferromagnetic and dipolar interactions between nearest-neighbors, leading to an unusual 2-$\mathbf{k}$ magnetic ground-state. The relative strength of dipolar interactions plays a key role in determining this ground-state. Additionally, the system exhibits a large magnetocaloric response in the classical spin liquid regime at low applied fields, which is reduced in powder samples due to the anisotropy of dipolar interactions.

From a materials design perspective, avenues for optimising trillium magnetocalorics are straightforwardly identified—after all, the phase behaviour we identify here depends only on the magnitudes of S and J, and the trillium edge length, which in turn influences D. Because a large D/J washes out the magnetocaloric effect in

powder samples, optimising the isotropic coupling J is likely better than optimising S. One possibility for doing so is to use an alternative bridging ion (*e.g.* azide) with stronger superexchange.

Geometric frustration is clearly the driving force for the strong magnetocaloric effect at relatively low applied fields within the CSL phase. The analysis detailed here as provides a robust link between frustration and this useful physical property. A corollary is that non-magnetic frustration in pseudospin systems may favour strong barocaloric responses at low pressures, offering a new design strategy for efficient solid-state cooling devices [80, 380, 381].

Chapter 4

Spin-chain segmentation in diluted quasi-one-dimensional Ising materials

Summary

In the previous chapter, we saw that by designing structural features of the magnetic lattice—namely geometric frustration—it is possible to induce complex thermodynamic responses, both to temperature and external stimuli (e.g. magnetic field). Alongside geometric frustration, this chapter considers another structural feature of the magnetic lattice alongside geometric frustration. First, I introduce background on the theory of unfrustrated and frustrated lattices which are 'quasi-one-dimensional' and the specific heat as a useful probe of low-dimensionality. Little is currently known about the impact of nonmagnetic doping on such materials. I introduce the solid solution $Tb_{1-\rho}Y_{\rho}(HCOO)_3$ ($0 \leq \rho \leq 1$) where an anomalous evolution of the magnetocaloric effect is observed. In the chapter, I set out to study the effect of nonmagnetic doping on the magnetic thermodynamics of quasi-one-dimensional Ising materials such as $Tb_{1-\rho}Y_{\rho}(HCOO)_3$.

Using Monte Carlo simulations, I show that, on dilution by non-interacting sites, q-1D Ising models display a low-temperature signature not present in conventional three-dimensional models. Frustrated embeddings of 1D chains show similar features to unfrustrated embeddings, which arises from chain segmentation. I introduce a mean-field formulation which captures the low-temperature behaviour of the model. This theoretical framework is applied to the interpretation of experimental heat-capacity measurements of the $Tb_{1-\rho}Y_{\rho}(HCOO)_3$ family of magnetocalorics. I find

good correspondence between simulation and experiment, establishing this system as a canonical example of dilute q-1D magnets. The experimental and theoretical results of this chapter can be found in the publications Ref. 94 and 382, respectively.

Acknowledgements

This project was carried out as a collaboration between the University of Oxford and University of Kent. The synthesis, structural characterisation, and many of the measurements were carried out in the competent hands of Dr. Mario Falseperna, supervised by Prof. Paul Saines, to both of whom I am very grateful for fruitful conversation and hard work in Kent. I am grateful to Dr. Richard Dixey (Queen Mary's University) and Dr. Joe Paddison (Oak Ridge National Lab) for useful conversations about the system. The sub-Kelvin heat capacity measurements were performed by Dr. Gavin Stenning at ISIS.

4.1 Introduction

The existence of partial order has been well characterised in a range of quasi-one dimensional (q-1D) systems—materials containing one dimensional (1D) motifs embedded in a weakly interacting three dimensional (3D) lattice; examples include urea clathrates [76, 383], charge-density wave phases [384], organic conductors [385], and ferroelectrics [386, 387].

A key signature of q-1D physics, applicable to magnetic and pseudospin materials, can be found in the temperature dependence of the heat capacity $C(T)$: the function contains a broad feature associated with the development of order within 1D motifs, and a lower-temperature peak signifying the onset of long-range 3D order [Fig. 4.1]. Small changes in the strength of inter-chain coupling give rise to large changes in $C(T)$, as seen in Onsager's analytical solution to the heat capacity of the anisotropic rectangular lattice [Fig. 4.1]. This sensitivity is why heat capacity measurements are such an effective tool for model parameterisation of q-1D systems [146].

This chapter is concerned with the role of defects in modifying q-1D and geometrically frustrated physics. Because the 1D lattice is unique in having no percolation threshold—a single vacancy divides the lattice in two—q-1D systems have been found to be surprisingly sensitive to small defect concentrations [142]. For example, defect pinning and incommensurations play an accidental role in the physics of 1D charge density wave (CDW) materials [388, 389]. Likewise, the deliberate inclusion of nonmagnetic defects is emerging as an effective strategy both to tune magnetocaloric effects [94, 390] and to develop unconventional ferromagnets [391]. In chain magnets, as the magnetic correlation length becomes large, even the presence of a small number of nonmagnetic defects can have a drastic effect [142]. Given the importance of thermodynamic measurements in understanding q-1D materials, an obvious outstanding question is how the incorporation of defects affects $C(T)$.

To address this question, I focus on the well-studied problem of nonmagnetic doping (dilution) of Ising models [186, 191, 392, 393]. To quantify the roles of dimensionality and geometric frustration, and to allow direct comparison against

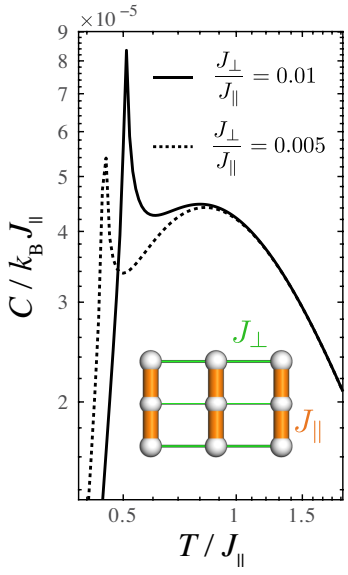

Figure 4.1: Onsager's exact solution [130] for the heat capacity of an anisotropic rectangular lattice, shown for $J_\perp/J_\parallel = 0.01$ and 0.005. A fragment of the lattice is shown as an inset, with intra-chain ($J_\parallel$) and inter-chain ($J_\perp$) interactions represented by (thick) orange and (thin) green rods respectively.

experiment in due course, four simple models are considered [Fig. 4.2]. We are chiefly interested in the family of q-1D models involving chains of ferromagnetically coupled Ising (pseudo-)spins, which interact via a much weaker antiferromagnetic inter-chain coupling. Such models have the Hamiltonian

$$\mathcal{H} = -J_{\parallel} \sum_{\langle i,j \rangle_{\parallel}} o_i o_j S_i S_j + J_{\perp} \sum_{\langle i,j \rangle_{\perp}} o_i o_j S_i S_j, \tag{4.1}$$

where $J_{\parallel} \gg J_{\perp} > 0$ are the intra- and inter-chain coupling strengths and the corresponding sums are taken over nearest-neighbour intra- and inter-chain pairs, respectively. The pseudospin variables $S_i = \pm 1$ represent a general Ising state and the corresponding occupancies o_i denote whether the site either has a degree of freedom ($o_i = 1$) or is a non-interacting defect ($o_i = 0$). The o_i are distributed randomly amongst all sites i subject to an overall defect density $\rho = 1 - \langle o \rangle$ and are considered immobile—the so-called quenched limit [142]. For each of the models studied, it is already well established that dilution leads to a 'Griffiths' phase, where statistically-rare regions of complete order make such models impossible to solve analytically [186, 191, 392].

In this chapter, I study the effects of dilution on q-1D Ising systems. Chain move Monte Carlo (MC) simulations are used to identify a dimensional crossover spanning three temperature regimes, and mean-field theory is used to study the low- and

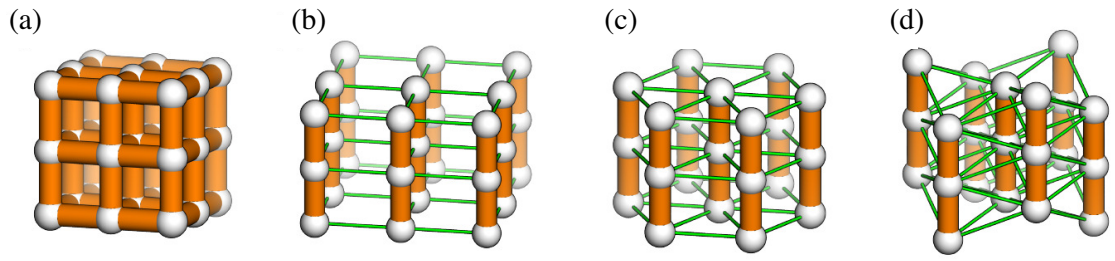

Figure 4.2: Lattices considered in this chapter: (a) the 3D cubic lattice, (b) the q-1D square lattice, (c) the q-1D triangular lattice, and (d) the staggered triangular terbium sublattice of the $R3m$ $Tb(HCOO)_3$ crystal structure [94].

medium-temperature regimes further. We identify three thermodynamic signatures of dilute q-1D physics which distinguish it from the behaviour of higher-dimensional systems: (i) the entropy associated with the high-temperature transition decreases linearly with defect concentration; (ii) a maximum emerges at low temperature in the specific heat, which grows in intensity and decreases in temperature with increasing defect concentration; and (iii) below this maximum, the heat capacity decays slowly, with a range where $C(T) \propto T$ emerging at low levels of dilution. We demonstrate that magnetic frustration leads to a broadening of these features and a zero-point-entropy that varies linearly with ρ. The theoretical framework is then applied to interpret recent experimental heat capacity measurements of the q-1D magnetocalorics $Tb_{1-\rho}Y_{\rho}(HCOO)_3$. I conclude by reporting the magnetocaloric effect across this series and discuss the potential applicability of the theory discussed to explaining these trends.

4.2 Background: the $Tb_{1-\rho}Y_{\rho}(HCOO)_3$ series

In the previous chapter, we saw that framework materials provides a versatile playground for studying magnetic physics. Of course, the importance of the magnetocaloric entropy change in these materials extends beyond just $NaMn(HCOO)_3$. A topical quasi-one-dimension magnetic framework material is $Tb(HCOO)_3$, as has already been touched on in the introduction. The key experimental result of this chapter involves studying the effect of non-magnetic doping in $Tb(HCOO)_3$. Since it has a similar atomic radius to Tb^{3+} and the same formal charge, Y^{3+} made a good candidate for nonmagnetic doping.

$Tb(HCOO)_3$ itself has a competitive magnetecaloric effect (MCE) over the $2 < T < 4\,\mathrm{K}$ range. The maximal value of $\Delta S = 6\,\mathrm{JK^{-1}kg^{-1}}$ at 4 K, makes this compound one of the most strongest Tb-based MCE materials [93]. As we have already seen in $NaMn(HCOO)_3$, geometric frustration leads to an enhancement of the MCE [394]. $Tb(HCOO)_3$ sits on a geometrically frustrated lattice and the spin hamiltonian has already been studied and this has been used to explain the strong MCE

in this system [162]. The Hamiltonian was parametrised using diffuse neutron scattering to obtain a measure of spin correlations as a function of temperature. The values obtained ($J_1 = 1.5(5)\,\mathrm{K} \gg J_2 = J_3 = -0.03(1)\,\mathrm{K}$) place $Tb(HCOO)_3$ as a strongly one-dimensional system with relatively weak antiferromagnetic interchain coupling [116].

The synthesis of polycrystaline samples of $Tb_{1-\rho}Y_\rho(HCOO)_3$ (with nominal stoichiometry $\rho = 0, 0.05, 0.1, 0.2, 0.4$) was carried out by Dr. Mario Falseperna and Prof. Paul Saines in the University of Kent using a previously reported procedure [161]. Combinations of $Y(NO_3)_3.6H_2O$, $Tb(NO_3)_3.6H_2O$, and formic acid were mixed in ethanol before being extracted as powders by filtering and drying [94]. Stoichiometry was verified by X-ray fluorescence measurements, which allowed for a direct measurement of the stoichiometric coefficient ρ. The values obtained from this method were homogenous across the powder sample and within the experimental bounds of the anticipated stoichiometry [94]. SEM imaging displayed a homogenous distribution of Y within samples [94] whilst Lebail fits to the powder diffraction patterns revealed a continuous alteration of lattice parameters, deviating only slightly from Vegard's law [94]. Both experiments indicate the formation of a homogenous solid solution.

Magnetisation curves were measured on all members of the series in collaboration between myself and Mario Falseperna (Univ. Kent). The resulting $M(H)$ measurements were used to derive the magnetocaloric entropy change on each member of the series as a function of field and temperature. The maximal values of this magnetocaloric entropy change are shown in Figure 4.3 at for two different applied magnetic fields. In general, diluting $Tb(HCOO)_3$ has the effect of decreasing the mass-normalised entropy (blue symbols) change for both applied fields. This is unsurprising: by doping with non-magnetic impurities, the contribution of magnetism to the entropy will decrease.

A more indicative measure is the entropy normalised by mole of Tb: this is the

contribution of each terbium spin to the magnetic entropy. This function (shown in red) has a nonmonotonic variation with ρ: at first it decreases and then increases.

When compared to other magnetically-dilute MCE materials, such as the Ga-doped $La_{0.7}(Ba,Sr)_{0.3}Mn_{1-x}Ga_xO_3$ ($x = 0, 0.1, 0.2$) [301] and the Sn-substituted RCo_2 (R = Gd, Tb, Dy) alloys [395], the $Tb_{1-\rho}Y_\rho(HCOO)_3$ series follows similar trends with respect to its initial decrease in $-\Delta S_{\max}$ with Y^{3+} doping—i.e. lower transition temperatures and lower values of $-\Delta S_{\max}$ when higher concentrations of non-magnetic impurities are present. This has also been observed in the geometrically frustrated $Tm_{1-x}Lu_xB_4$, which features a Shastry-Sutherland lattice, for $x < 0.06$ [390]. However, for $Tm_{0.7}Lu_{0.3}B_4$ the trend is reversed. Monte Carlo modelling suggested that in $Tm_{1-x}Lu_xB_4$ small concentrations of non-magnetic ions relieve the degeneracy of the ground state for this magnetic system, which results in a decrease in ground-state entropy and, therefore, of the MCE. Conversely, higher concentrations of non-magnetic dopant result in the formation of nearly independent clusters which are responsible for a significant degeneracy of the ground-state, leading to a higher zero-field entropy change and, ultimately, in an improvement of the MCE [390]. This observation is compatible with the putative role of fragmented chains discussed in Ref. 390. Indeed, theoretical studies of selective doping of the

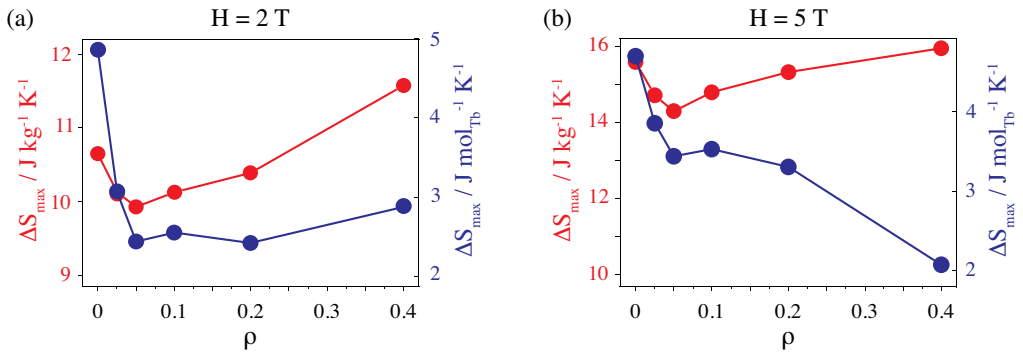

Figure 4.3: Maximal values of the magnetocaloric entropy change as a function of dilution (ρ in the stoichiometry $Tb_{1-\rho}Y_\rho(HCOO)_3$) when ramping the magnetic field from (a) $H = 0 \rightarrow 2\,\mathrm{T}$ and (b) $H = 0 \rightarrow 5\,\mathrm{T}$. In both plots, blue symbols represent mass normalised ΔS (left axis) and red symbols represent the quantity normalised to the molar spin concentration (right axis).

sublattices of a Triangular Ising Antiferromagnet have shown that it is possible to achieve a similar effect, i.e. an increase in the maxima of entropy change when higher concentration of non-magnetic dopants are present in such a system [390].

Given this interesting observation, there is interest in studying the thermodynamics of this system in more general. While the magnetocaloric effect—that is the effect of applying a magnetic field on the entropy of a system—is not studied explicitly in this chapter, it does provide a full framework for studying the *z*ero-field thermodynamics of dilute q1D Ising materials, of which the $Tb_{1-\rho}Y_{\rho}(HCOO)_3$ series is an important example. An accurate description of these zero-field dynamics are an important prerequisite to properly describing the anomalous evolution of the magnetocaloric entropy shown in Figure 4.3.

4.3 Chain move Monte Carlo simulation

MC simulation of q-1D systems is made difficult by the range of energy scales involved. Conventional algorithms are easily trapped in local minima, since traversing the energy landscape involves overcoming strong intra-chain interactions. One workaround, used *e.g.* to model the frustrated q-1D magnet $Ca_3Co_2O_6$, is the Wang–Landau algorithm [314, 396, 397]; a second is the application of non-local moves, such as the 'loop moves' of spin-ice simulations [310, 398, 399]. We employ a similar non-local approach here, allowing occasional collective 'chain moves' of any spin-chain segment (a set of spins in the same chain, uninterrupted by a vacancy).

We used a classical Metropolis algorithm [313] to carry out MC simulations on large supercells. A spin configuration is first generated at random, with a vacancy distribution which is fixed for each subsequent cooling cycle. Move types were selected randomly from either a single spin flip or a collective chain segment move (or chain move), in which we flipped the spin of an entire chain segment. We used a 10 % probability of selecting chain moves. A random spin or chain was selected from the supercell. Both spin moves and chain moves were either accepted or rejected according to the Hastings–Metropolis criterion [313]. Simulations were

annealed from high temperature according to a logarithmically distributed grid of 167 temperature points between $10^2/J_{\|}$ and $10^{-3}/J_{\|}$. A total of 5×10^4 moves were proposed per spin for each temperature step, with an equilibration period of of 10^3 moves between successive temperature steps. The cooling cycle was repeated 60 times for each vacancy concentration sample, using different vacancy configurations on each repeat.

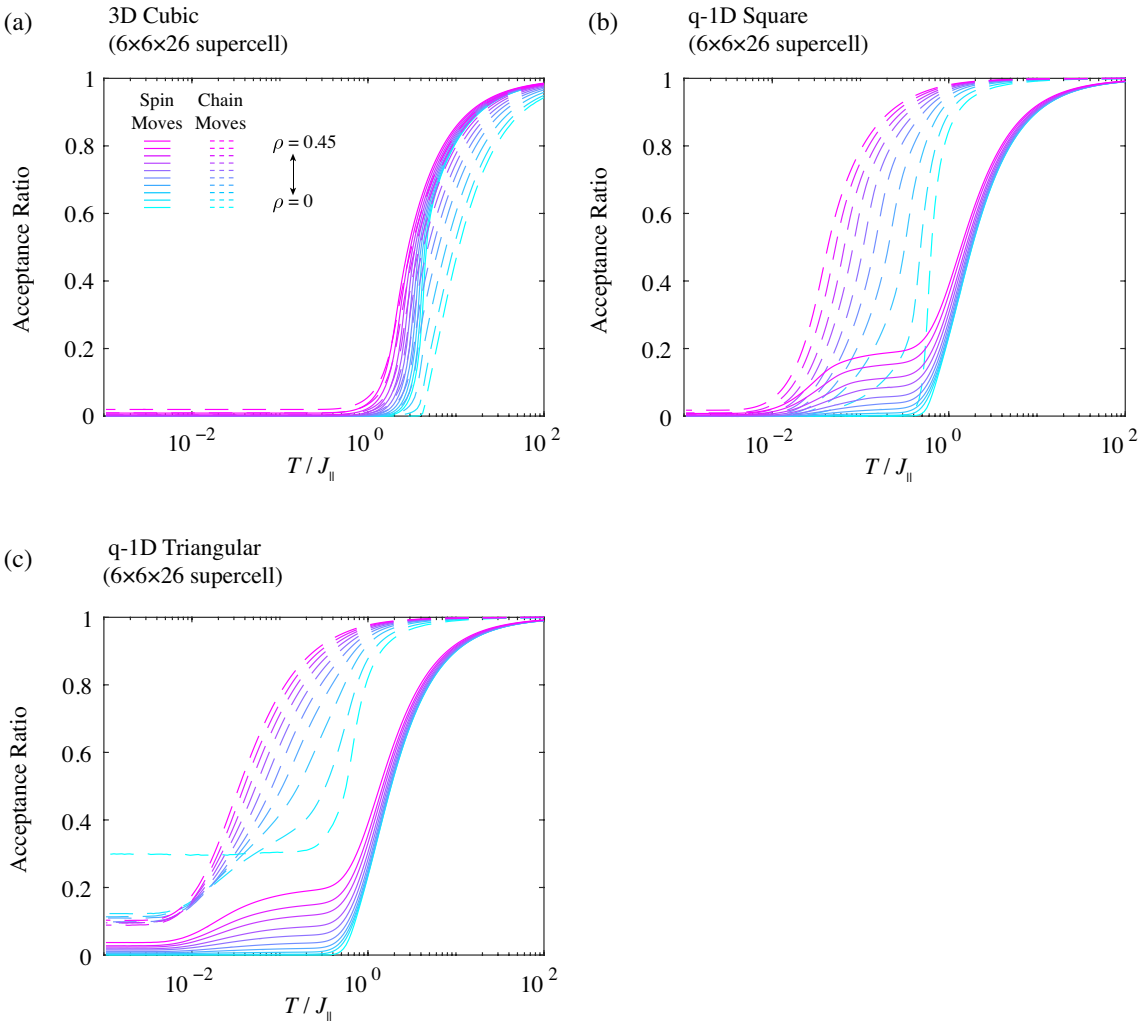

Figure 4.4: Ratio of moves accepted to proposed as a function of temperature, shown for 10 equally-spaced vacancy concentrations between 0 and 0.45 for Monte Carlo simulations in the three models considered. (a) The 3D cubic model sees chain moves freeze at higher temperatures than spin moves since they involve stronger interactions. (b) In the q-1D square model, the chain moves generally freeze at lower temperature than single spin moves. (c) The same is true of the q-1D triangular model, but in this case chain moves never fully freeze and are always present to zero temperature. The low-temperature limit of this ratio tends to $P^\star$ in the undoped case, and a lower value close to 10 % in all other cases.

The acceptance ratio for both types of moves is compared as a function of temperature and vacancy concentration in Figure 4.4. Chain moves were accepted less often in the cubic case at all temperatures; however, at low temperature in the q-1D models, chain moves make up the majority of accepted moves. In the triangular lattice models, the low-temperature limit sees chain moves accepted whenever chains are in environments with no net interaction. For the $\rho = 0$ limit, this is the same $P^\star$ as defined in section A above. Interestingly, on the incorporation of any vacancies, this low temperature limit drops to a value close to 10 % and stays quite constant as a function of doping. This limiting fraction represents the proportion of chain segments for which there is no energetic cost for changing their collective spin.

In all cases, the average energy, normalised per spin, decreases monotonically on cooling. Since $J_\parallel \gg J_\perp$, the internal energy is dominated by the stronger interactions, so we only clearly see the high temperature transition. For $\rho = 0$, the low-T limit of $\langle E \rangle$ approaches $-J_\parallel Z_\parallel/2$. This value is $-3J_\parallel$ in the 3D cubic case and $\sim -J_\parallel$ in the q-1D cases. As dopant concentration increases, the effective coordination number decreases linearly as $(1 - \rho)$.

We use two different methods to calculate heat capacity: the first is from the gradient of the internal energy,

$$C = \frac{\partial \langle E \rangle}{\partial T}, \tag{4.2}$$

and the second method is from the fluctuations in the internal energy [292],

$$C = \frac{1}{k_\mathrm{B} T^2} \left(\left\langle E^2 \right\rangle - \langle E \rangle^2 \right). \tag{4.3}$$

Over the temperature range studied, these methods give similar values, with the gradient method showing more statistical noise at low temperatures in the q-1D triangular case, likely due to the sensitivity in magnetic ground state to the exact distribution of vacancies. However, the fluctuation method showed an error at low temperatures, which is caused by rounding effects. This issue only arises when both

the heat capacity and temperature are very low, so was safely ignored in the analysis.

The entropy was calculated by integrating over the heat capacity,

$$S(T) = k_{\mathrm{B}} \log 2 - \int_{T}^{T_{\max}} \frac{C(T')}{T'} \, \mathrm{d}T', \tag{4.4}$$

where $T_{\max}$ is sufficiently high that the system is fully disordered and $S = k_{\mathrm{B}} \log 2$. Because of the rounding issue with the fluctuations method, we use Equation (4.2) to estimate C.

4.4 Effect of dilution on heat capacity

Our results [Fig. 4.5] show that dilution impacts the specific-heat of the 3D simple-cubic model very differently to the two q-1D models investigated. In the cubic

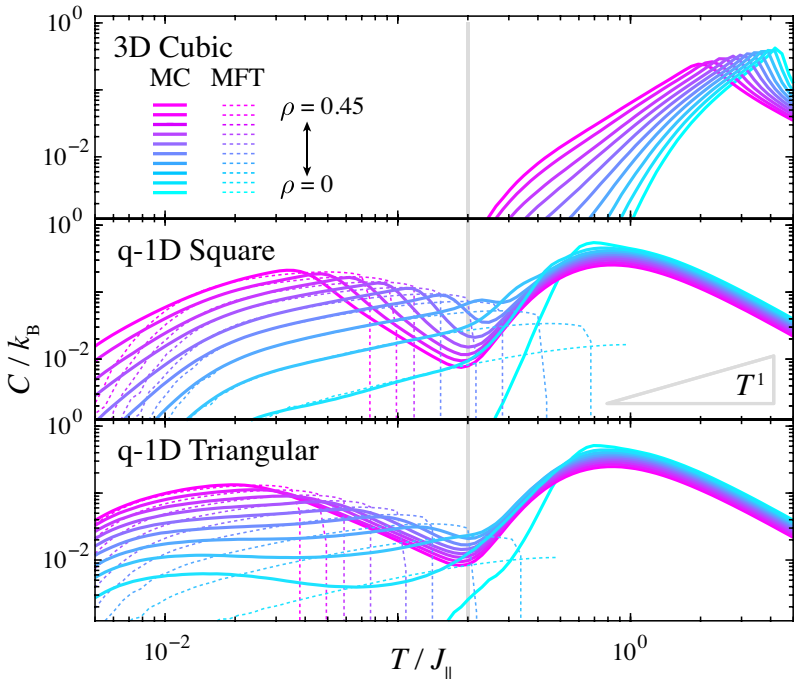

Figure 4.5: Comparison of heat capacity per spin in the 3D cubic, q-1D square and q-1D triangular models at ten evenly-spaced vacancy concentrations between $\rho = 0$ and $\rho = 0.45$. In each of the q-1D models, $J_{\perp}/J_{\parallel} = 10^{-2}$. Solid lines display MC results, and the mean-field theory results are shown as dashed lines. Linear scaling corresponds to the slope of the gray triangle. In the 3D cubic case, there is only one feature, while in the other two cases, both high and low temperature heat-capacity features are present. The low temperature feature is strongly temperature dependant.

model, we see a similar result to that noted in previous studies: namely, that doping acts both to suppress the peak in $C(T)$ associated with 3D ordering to lower temperature and at the same time to broaden this feature [186, 393]. This behaviour is straightforwardly explained: dilution decreases the average number of interacting neighbour-pairs and also makes the distribution of interacting pairs more varied.

By contrast, the effect of dilution on the $C(T)$ functions of q-1D models is more complex. The broad high-temperature feature associated with 1D order is surprisingly resilient to doping, varying only in intensity but always resembling the behaviour expected for isolated 1D chains. More obviously, a low temperature feature appears, which grows in size and is suppressed to lower temperature with dilution. This feature is qualitatively similar in both square and triangular q-1D models, but appears at lower temperature in the frustrated case. We denote the temperature maxima associated with these two features T_{1D} and T_{3D}, respectively.

Examination of the individual spin-configurations of the simulation [Fig. 4.6(a–f)] and spin–spin correlation functions [Fig. 4.6(g–l)] reveal the origin of this signature. The two heat capacity features demarcate three temperature regimes: (i) at high temperature only short-range correlations exist along the chains, and the system is disordered; (ii) at temperatures between the two $C(T)$ maxima, spins order within individual chain segments but inter-chain order is short-range (iii) at low temperatures, full 3D order of the spins is observed.

In the intermediate temperature regime, I expect a q-1D system to act as weakly interacting, ordered chains. Consequently, understanding the distribution of segment lengths will be central to explaining to the underlying physics. If the vacancies are randomly arranged, this distribution can be expressed as the probability of a randomly selected site falling into a chain segment of length ℓ:

$$P(\ell) = \ell\rho^2(1-\rho)^\ell. \tag{4.5}$$

The average chain length $\langle\ell\rangle = 1/\rho$: as vacancy concentration is increased, the

chains become shorter on average. Since the effective interactions between two segmented chains increases with the segment length, it makes sense that the strength of interactions, and therefore the 3D ordering temperature, decreases with increasing vacancy concentration.

Similar behaviour emerges as a finite-size effect in undoped q-1D models [400]. In our simulations of the $\rho = 0$ q-1D square model, varying the size of the system in the chain direction (L_z) leads to a substantial change in the heat-capacity [Fig. 4.7]. With decreasing L_z, a new feature emerges on the low-temperature side of the main $C(T)$ peak, growing in intensity and decreasing in temperature in a way that mirrors the behaviour observed on doping. The two effects are similar because increasing dopant concentration and reducing model size both decrease the average segment length. The main difference between these responses is that the low-temperature

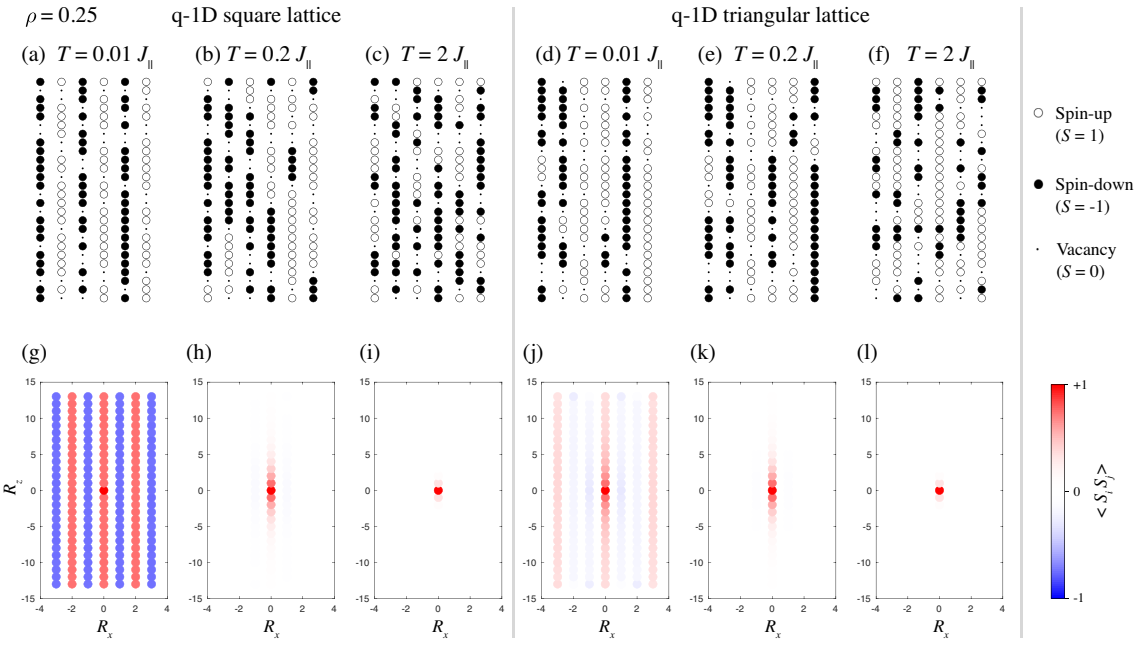

Figure 4.6: (a–f) A representative xz plane taken from our $\rho = 0.25$ MC simulation of the (a–c) q-1D square model and (d–f) the q-1D triangular model at three different temperatures: (a, d) $T = 0.01J_{\|}$, (b, e) $T = 0.2J_{\|}$, and (c, f) $T = 2J_{\|}$. For both lattices, the low temperature structure contains order along chains and in the square lattice case, there is complete in-plane order at low temperature. At $T = 0.2J_{\|}$, both lattice types show order along chain segments but not between segments. At $T = 2J_{\|}$, order along chains is not complete. (g–l) Spin–spin correlation functions calculated from configurations at the same temperatures.

feature in Fig. 4.5 is much broader than that in Fig. 4.7 because there is a distribution of segment lengths in the randomly-doped samples, whereas varying the box size leaves all chain lengths the same.

4.5 Mean–Field Theory

This mapping between dilution and finite size effects suggested an approximate formulation for the doped q-1D case. In this section, I introduce a mean–field model. I will start by introducing the basic mean–field theory as a justifying example and extend this to the theory of the segmented phase studied in the text. The properties of the model are examined and the presence of a linear regime below T_{3D} follow from this theory.

4.5.1 Derivation

Basic theory

The theories developed here are an extension of the mean-field theory developed for a simple monopartite ferromagnet and bipartite antiferromagnet which were described in section 2.4. We saw how the Hamiltonian of a simple ferromagnet [Eq. (2.41)] could be approximated as the interaction of separable spins with an effective magnetisation [Eq. (2.42)] subject to a self consistency equation [Eq. (2.43)]. Further-

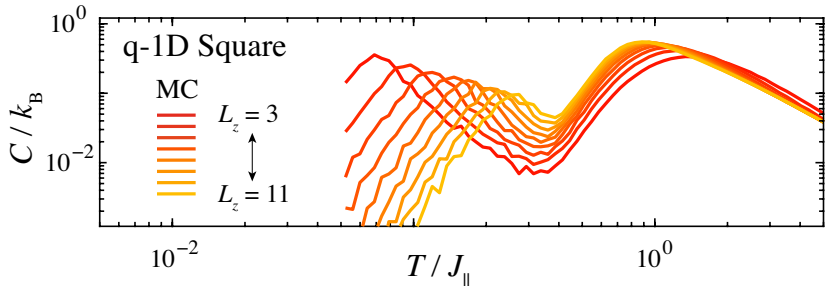

Figure 4.7: The effect of finite size on the simulated magnetic heat capacity of an $8 \times 8 \times L_z$ supercell of the undoped q-1D square lattice, showing two features: the high temperature feature, associated with order along the chains is reasonably insensitive to the finite size of the lattice while the low temperature feature, associated with interchain order falls in intensity and rised in temperature as the simulation size is increased along the chain direction.

more, we saw how a bipartite system like an antiferromagnet could be formulated as two interacting sublattices, with a system of two self consistency equations constraining the magnetisation of each sublattice [Eqs. (2.45), (2.46)]. Here, I present an extension of this approach for a system of segmented chains with lengths distrubuted according to Equation (4.5). This treatment is developed for systems of chains sitting on monopartite, bipartite and tripartite lattices and limiting cases of the equations are presented.

Extension to segmented phase

In the segmented phase, we assume that chain segments (of length ℓ) are coaligned, represented by the collective pseudospin $S_j^{(\ell)} = \pm 1$. We can recast Eq. (4.1) as

$$\mathcal{H} = J_\perp \sum_{\langle ij \rangle_\perp} n_{ij} S_i S_j, \tag{4.6}$$

where n_{ij} is the number of neighbours between chain segment i and chain segment j. Using a similar mean–field approximation to that exploited in Equation (2.42), we obtain

$$\mathcal{H}_{\mathrm{MF}} = \frac{J_\perp M}{2} \sum_j \left[\frac{1}{N} \sum_i n_{ij} \right] S_j = \frac{J_\perp M}{2} \sum_j S_j \left\langle n_{ij} \right\rangle . \tag{4.7}$$

Since each site on a chain is connected the surrounding lattice via $Z_\perp$ links, we have $\langle n_{ij} \rangle = \ell Z_\perp$. This Hamiltonian is once again separable—as in Equation (2.42)—but now depends on chain length. It will prove useful to partition this sum by chain length:

$$\mathcal{H}_{\mathrm{MF}} = \frac{J_\perp M}{2} \sum_j \ell S_j = \frac{J_\perp M}{2} \sum_\ell \ell \sum_{j \in (\ell)} S_j \tag{4.8}$$

Thus the self-consistency equation must now be an average over the magnetisation of different segment lengths, multiplied by their contribution to the total magnetisation:

$$M = \sum_\ell P(\ell) \tanh \left(\frac{J_\perp \ell Z_\perp M}{T} \right), \tag{4.9}$$

where $P(\ell)$ represents the probability of a given spin falling in a chain segment of length ℓ. Note that the low temperature limit of this equation is $M = \sum_\ell P(\ell) = (1-\rho)$.

Extension to Multiple Sublattices

The model detailed in the previous section works well for a ferromagnetic system, where the order develops on one magnetic sublattice. In general, the extension the mean–field Hamiltonian to N sublattices leads to a system of N self consistency equations. This is certainly the case for the equivalent mean–field Hamiltonian,

$$\mathcal{H}^{\alpha}_{\mathrm{MF}} = \left[\frac{J_\perp}{2}\sum_\beta Z_{\alpha\beta}M_\beta\right]\left[\sum_{\ell=1}^{\infty}\ell\sum_{j\in(\ell,\alpha)}S_j\right]. \tag{4.10}$$

which leads to a self consistency equation for each sublattice α,

$$M_\alpha = \sum_{\ell=1}^{\infty}P(\ell)\tanh\left[\frac{\ell J_\perp}{T}\left(\sum_\beta Z_{\alpha\beta}M_\beta\right)\right], \tag{4.11}$$

A schematic of this set of interactions and self consistency equations is shown in Figure 4.8.

Numerical Calculation

We solve the system of equations given in (4.11) by minimising the function

$$\Phi(\{M_n\}) = \sum_n\left\{M_n - \sum_{\ell=1}^{\infty}P(\ell)\tanh\left[\ell J_\perp\beta\left(\sum_{n\neq m}Z_{nm}M_m\right)\right]\right\}^2. \tag{4.12}$$

The sum over ℓ converges for all values of ρ, and we find a maximum value of $\ell = 1000$ ensures numerical accuracy.

Unsurprisingly, we find a solution for the bipartite lattice when $M_1 = -M_2$ and a solution for the tripartite lattice when $M_1 = -M_2$ and $M_3 = 0$. Defining $\mu = M_1 = -M_2$ both cases, we can see that all of these equations map onto the single sublattice Hamiltonian, with rescaled energies and temperatures. In the bipartite

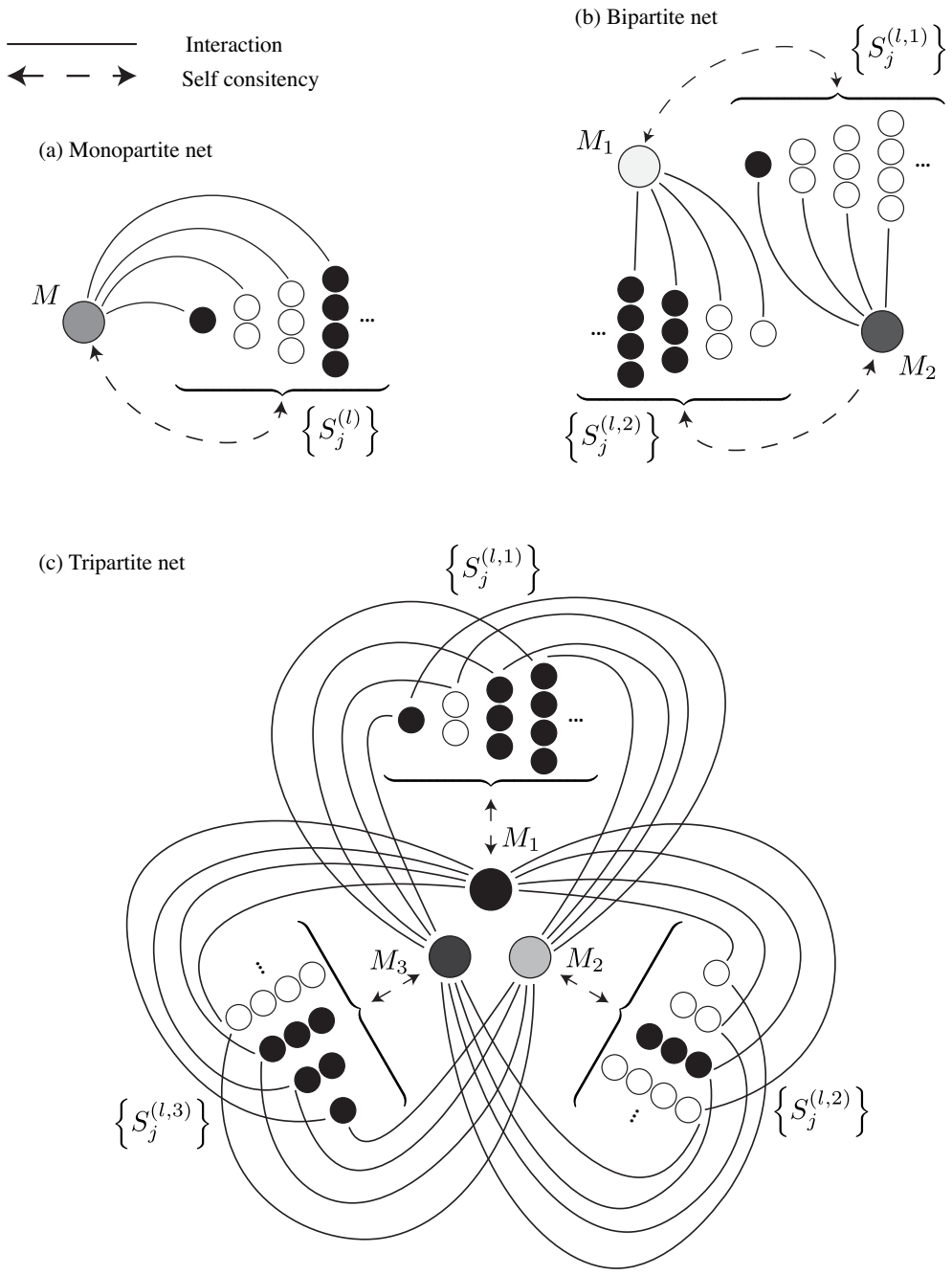

Figure 4.8: Three schema for the mean-field theory developed in this thesis for (a) monopartite (b) bipartite (e.g. square q-1D) and (c) tripartite (e.g. triangular q-1D) lattices. (a) Spin chains are shown as black or white chains, which interact with their mean-field, indicated with a larger circle. Self consistency ensures that the magnetisation is the thermal average of the spin chains. In (b) this is extended to a two-sublattice model for bipartite lattices where each sublattice has a magnetisation (M_1 and M_2), and the spins on each sublattice interact only with the magnetisation of the other sublattice. (c) shows the extension of this concept to three sublattices.

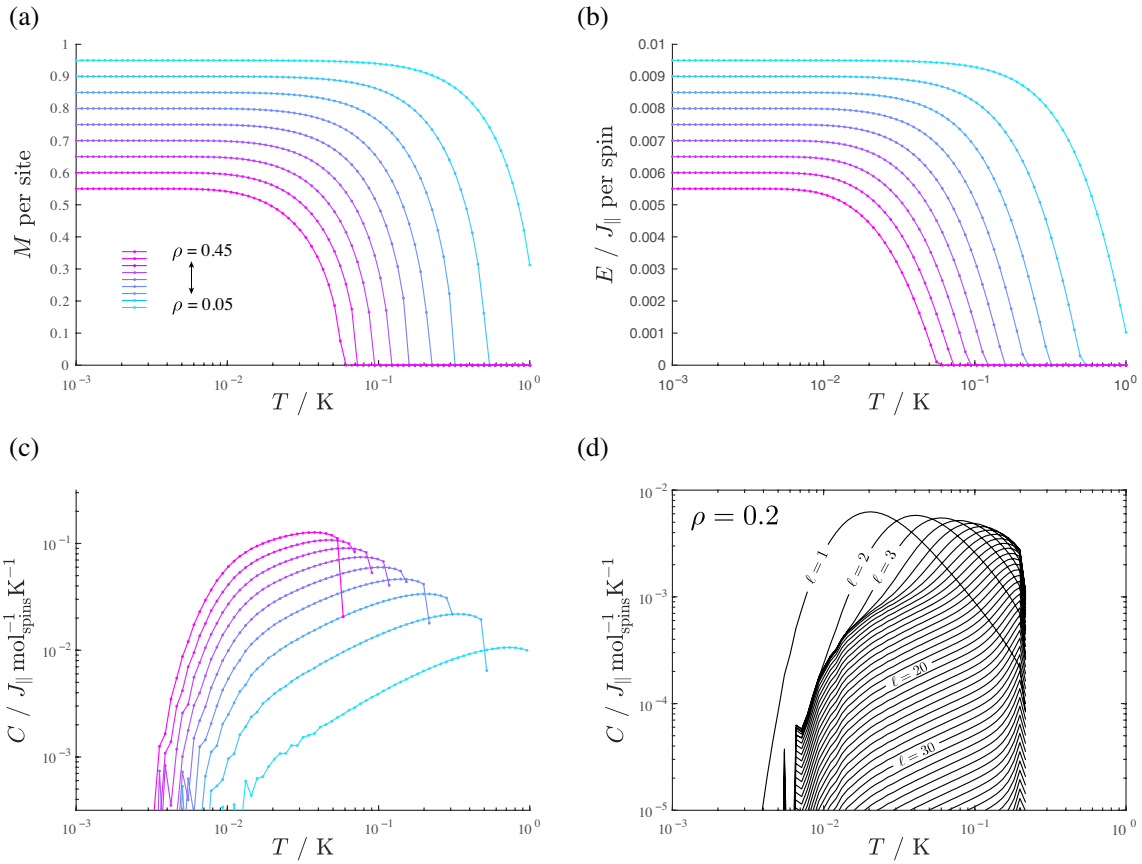

Figure 4.9: Thermodynamic variables calculated from our mean-field theory as a function of temperature: (a) magnetisation per site, from the numerical solution of Eq. (4.9), (b) energy per spin, calculated from Eq. (4.10), (c) $C(T)$, calculated as the gradient of the panel (b), and (d) a breakdown of this quantity for $\rho = 0.2$ by in terms of the contributions from various chain-lengths ℓ.

case,

$$\mathcal{H}_{\text{MF}} = \frac{1}{2}\left(\mathcal{H}^{(1)}_{\text{MF}} + \mathcal{H}^{(2)}_{\text{MF}}\right) = \frac{J_\perp Z_\perp \mu}{2} \sum_{\ell=1}^{\infty} \ell \sum_{j\in(\ell)} S_j. \tag{4.13}$$

and in the tripartite case,

$$\mathcal{H}_{\text{MF}} = \frac{1}{3}\left(\mathcal{H}^{(1)}_{\text{MF}} + \mathcal{H}^{(2)}_{\text{MF}} + \mathcal{H}^{(3)}_{\text{MF}}\right) = \frac{J_\perp Z_\perp \mu}{3} \sum_{\ell=1}^{\infty} \ell \sum_{j\in(\ell,\alpha\neq 3)} S_j. \tag{4.14}$$

In Equation (4.14), there is a smaller proportion of spins contributing to the total heat capacity (by a factor of $2/3$ since the $\alpha = 3$ sublattice is not involved in bonding) and those spins contribute less strongly (by a factor of $1/2$ since only two of

the nearest neighbours are involved in bonding) than in Equation (4.13). Thus when we solve Equation (4.9) numerically, we can use these results for the heat capacity—obtaining $C_{\text{bipartite}}(T) = C_{\text{monopartite}}(T)$ and $C_{\text{tripartite}}(T) = 2/3C_{\text{monopartite}}(T/2)$ for the bipartite and tripartite cases, respectively.

The results of the calculation for the monopartite lattice are shown in Figure 4.9. Broadly speaking, the ordering temperatures (i.e. the temperature at which $M \to 0$ in Fig. 4.9(a)) displays the same trends as in the MC simulations of sections 4.4: as the doping is increased, the ordering temperature decreases. The mean-field model makes clear why this is the case, since the distribution $P(\ell)$ moves more towards lower values of ℓ as ρ increases, the effective interaction becomes weaker. Naturally, this same trend is seen in panels Fig. 4.9(b-c).

Figure 4.9 shows a breakdown of the contributions from each chain for $\rho = 0.2$. This demonstrates that showing that throughout the heat capacity feature T_{3D}, there are contributions from many different chain lengths: it is not the case that one chain-length dominates the signal.

Approximations and Linear Regime

The objective of this section is to obtain an expression for the temperature regime over which one expects the mean–field treatment to be relevant. This behaviour is appropriate only in the low-ρ limit.

First we consider the monopartite case. In the low-temperature limit of Equation (4.9), we can approximate that all spins are aligned $M \to (1 - \rho)$. In this case, the equation reduces to

$$\mathcal{H}_{\text{MF}} = J_{\perp} Z_{\perp} (1 - \rho) \sum_{\ell=1}^{\infty} P(\ell) \ell \sum_{j \in n} S_j^{(\ell)}, \tag{4.15}$$

which is a collection of two-level systems, so the heat-capacity should be given as a sum over Schottky anomalies,

$$C = k_{\rm B} \sum_{\ell=1}^{\infty} \rho^2 (1-\rho)^{\ell-1} \frac{{\rm e}^{-\Delta\ell/T}}{\left[1+{\rm e}^{-\Delta\ell/T}\right]^2}, \tag{4.16}$$

where $\Delta = 2J_\perp Z_\perp(1-\rho)$. Since in the temperature range considered $|\exp -\Delta\ell/T| < 1$, we can use the expansion

$$\begin{aligned} C &= \frac{\Delta^2 k_{\rm B}\rho^2}{(1-\rho)T^2} \sum_{\ell=1}^{\infty}\sum_{k=0}^{\infty} (-1)^k (k+1)\ell^2 \left[(1-\rho){\rm e}^{-\Delta(1+k)/T}\right]^\ell & (4.17)\\ &= \frac{\Delta^2 k_{\rm B}\rho^2}{T^2} \sum_{k=0}^{\infty} (-1)^k (k+1) \frac{{\rm e}^{-\Delta(1+k)/T}\left[(1-\rho){\rm e}^{-\Delta(1+k)/T}+1\right]}{\left[1-(1-\rho){\rm e}^{-\Delta(1+k)/T}\right]^3}. & (4.18) \end{aligned}$$

This series converges much more quickly than the sum over ℓ, such that for all the values of the parameters concerned, it is dominated by the $k = 0$ term.

Up to this point we have been taking the low-T approximation. In order to capture the medium temperature behaviour, let us now take a high-T approximation where $\Delta(1+k)/T \ll 1$. Since this sum is dominated by the $k = 0$ term, this approximation is valid when $\Delta/T \ll 1$. Applying the approximation simplifies the expression considerably:

$$C \simeq \frac{\Delta^2 k_{\rm B}\rho^2}{T^2} \sum_{k=0}^{\infty} (-1)^k (k+1) \frac{(2-\rho)}{\left\{1-(1-\rho)[1-\Delta(1+k)/T]\right\}^3}. \tag{4.19}$$

The final approximation to this expression involves taking the $\rho \ll \Delta/T$ limit. When taken with our earlier approximation, this implies that $\rho \ll 1$ and hence

$$C \simeq \frac{2k_{\rm B}T\rho^2}{\Delta} \sum_{k=0}^{\infty} \frac{(-1)^k}{(k+1)^2} = \frac{\pi^2 k_{\rm B} T\rho^2}{6\Delta} = \frac{\pi^2\rho^2 k_{\rm B}}{12 J_\perp Z_\perp} T. \tag{4.20}$$

Putting the two approximations together, we see that the mean-field result is valid over a temperature range spanned by $\Delta \ll T \ll \frac{\Delta}{\rho}$. This range spans a large tem-

perature range only when $\rho \ll 1$—as is is clear from Figure 4.10, which demonstrates that the agreement between Equation s(4.16) and (4.20) is good for a wide range of values when ρ is small, whereas for larger values of $\rho \gtrsim 0.05$ the range over which these approximations are simultaneously valid disappears.

Applying the rescaling discussed in the previous section, we can introduce a geometric factor γ to Equation (4.20), which is equal to 1, 1 or $\frac{4}{3}$ for monopartite, bipartite or tripartite lattices, respectively, to arrive at

$$C(T) = \frac{\gamma \pi^2 \rho^2 k_{\mathrm{B}}}{12 J_{\perp} Z_{\perp}} T. \tag{4.21}$$

4.5.2 Discussion

The theory reproduces well the low-temperature behaviour of the square q-1D system, particularly at low vacancy concentrations [Fig. 4.5]. It is prone to many of the shortfalls of mean-field theories: the transition temperature is overestimated and the behaviour near the ordering transition is less well captured. The behaviour

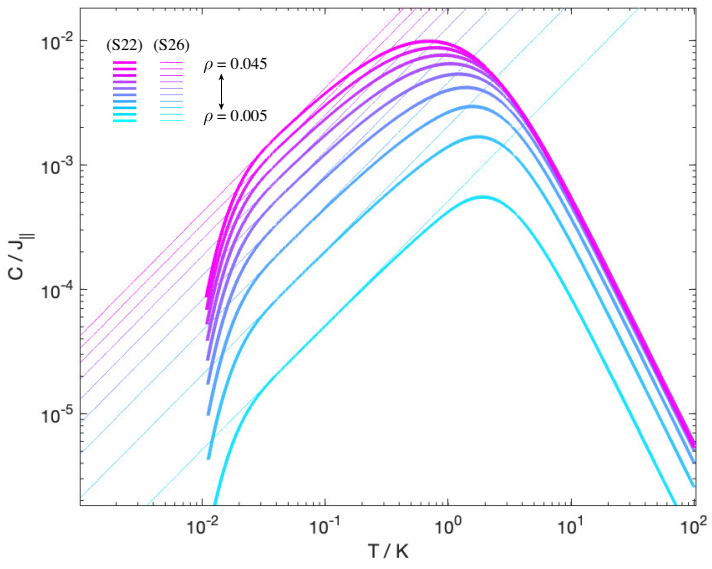

Figure 4.10: Comparison of the approximations (4.16), shown with bold lines and (4.20), shown with faint lines for low values of ρ.

of the q-1D triangular case is less well captured because geometric frustration leads to a distribution of local spin environments at the lowest temperatures, making the tripartite approximation of this lattice less effective than the bipartite approximation in the square case. Nevertheless, the important point is that the mean-field model captures the dependence of the low-T feature on ρ: the transition temperature decreases as ρ increases and the feature at T_{3D} becomes more pronounced.

It is apparent from the MC results that for low dilution, the square q-1D lattice has a regime where $C(T)$ varies linearly with T. This regime spans the largest temperature range for low vacancy concentrations and occurs at a lower temperatures with increased values of ρ. In this limit, we can use the mean-field framework developed in the previous section to show that there is a regime below T_{3D} (specifically, $1 \ll T/2J_{\perp}Z_{\perp} \ll 1/\rho$) for which the heat capacity follows Equation (4.21) Although this approximation is valid only within a small window of the function, Eq. (4.21) illustrates a more general point: namely, that the decay of the heat capacity below the anomaly maximum is very slow. This is because of the broad distribution of segment lengths—and therefore inter-chain interaction strengths—that are involved in developing full 3D order.

4.6 Effect of dilution on Entropy

In the high-temperature limit of the mean-field theory, chain segments are internally ordered but there exist no correlations between segments. The associated per-spin entropy ($S = \rho k_{B} \log 2$) is shown in Fig. 4.11(a) alongside the values calculated from the MC simulations an intermediate temperature, $T = 0.2J_{\parallel}$, chosen between T_{3D} and T_{1D}. The relation matches closely for all but the lowest values of ρ, where correlations between segments lead to a suppression of entropy. By contrast, the 3D cubic model is completely ordered for all values of ρ.

When evaluated to the low-temperature limit, the entropies of the undoped q-1D models join that of the cubic model, with only minor deviations from complete order [Fig. 4.11(b)]. The low-temperature entropy of the triangular model shows a com-

plex evolution as a function of doping. S varies approximately linearly with ρ for all nonzero values of ρ, but jumps at $\rho = 0$ because of a subextensive entropy contribution that is a finite-size effect. The value of this contribution is given by theory as $S = 0.3231 k_{\mathrm{B}}/L_z$, which matches well the simulated value [156]. A small addition of vacancies breaks this degeneracy by creating an imbalance in the geometrically-frustrated interactions between chain segments of varying lengths, which is the reason for the initial decrease in entropy on doping. By contrast, the linear entropy increase with further doping is robust to changes in the simulation size. The empirical relation $S \simeq 0.128\,\rho k_{\mathrm{B}} \log 2$ implies a $\sim$12.8% chance of a vacancy doubling the ground-state degeneracy. This result contrasts that of higher-dimensional systems such as the spin ices, where doping leads to a non-monotonic variation of residual entropy with dilution [401, 402].

Why does residual entropy scale linearly with defect density? To explain this trend, we consider environments such as that shown in Fig. 4.11(c,d), where the spins in the central column could take either state with minimum energy. Taken in isolation, the addition of a vacancy of this kind would double the ground-state

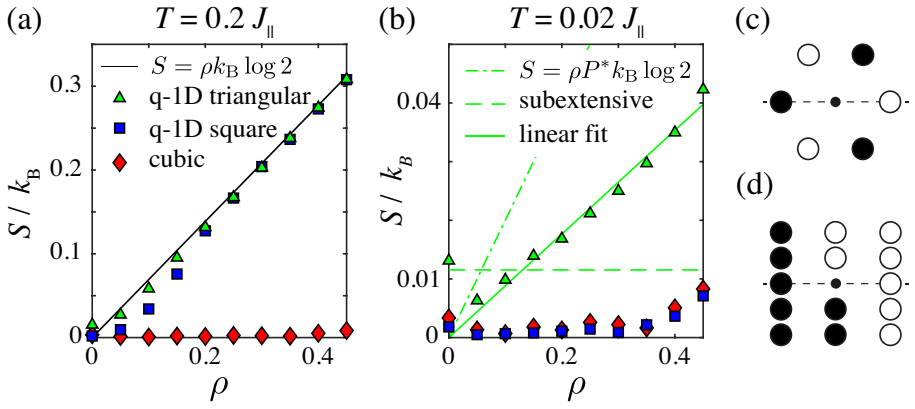

Figure 4.11: (a) The intermediate-temperature ($T_{3\mathrm{D}} < T = 0.2J_{\|} < T_{1\mathrm{D}}$) MC entropy per spin of the three models as a function of dilution. (b) The low-temperature ($T = 0.01J_{\|}$) entropy, with a linear fit to the q-1D triangular results shown as a solid line and the finite-size limit shown as a dashed line. The upper-bound trend discussed in the text is shown as a dot-dashed line. (c,d) A local state that gives rise to a ρ-dependant ground-state entropy, viewed (c) along and (d) perpendicular to the chain axis.

degeneracy. Using a MC method, we calculate the probability of selecting such an environment in the two-dimensional triangular Ising antiferromagnet as $P^* = 0.289(3)$. This value is derived from an MC simulation on the 2D triangular lattice model as detailed in Appendix A. The corresponding entropy [shown as a dot-dashed line in Fig. 4.11(b)] is a severe overestimate because it neglects the entropy-suppressing effect already noted: vacancies not only create environments like (d) but also make the surrounding chain-segments more unequal. Environments like this are unique to geometrically-frustrated lattices, which explains why this effect is not seen in the square or cubic models.

4.7 Application to experiment

So how successful are these theoretical and computational results at explaining the experimental behaviour of the q-1D magnets $Tb_{1-\rho}Y_{\rho}(HCOO)_3$? In §1.1.4, we saw how in this family magnetic Tb^{3+} and non-magnetic Y^{3+} ions are arranged on a triangular lattice. Intra-chain interactions are ferromagnetic; inter-chain interactions are weaker and antiferromagnetic. The experimental heat-capacity curves, measured as detailed in §2.3.3, are shown in Fig. 4.12(a) [94]. The data shows a clear evolution as a function of doping.

To determine whether the theories developed in this chapter can capture the key physics of this system, we use an Ising variant of the Hamiltonian of Ref. 116 to drive MC simulations. The chain-move MC algorithm described in section 5.3 was used on the supercell considered in Ref. 116, with a supercell of the parent $R3m$ unit cell given by the transformation matrix

$$\mathbf{M} = \begin{bmatrix} 3 & -3 & 0 \\ 5 & 5 & 0 \\ 0 & 0 & 13 \end{bmatrix}. \tag{4.22}$$

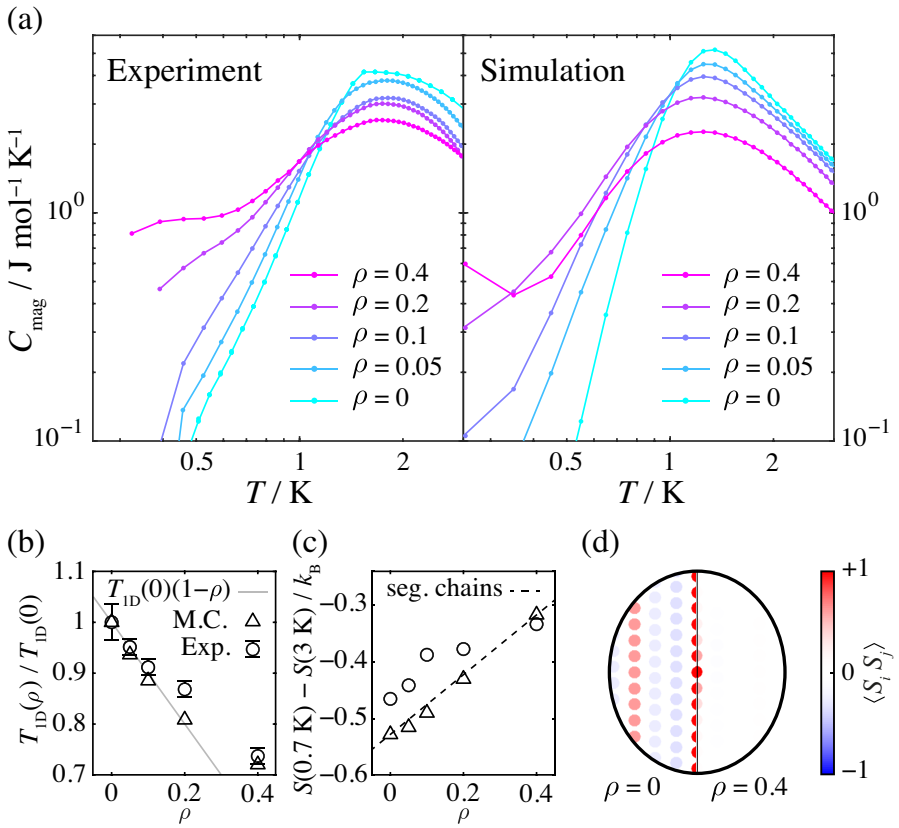

Figure 4.12: (a) Experimental and simulated magnetic heat capacity of the $Tb_{1-\rho}Y_\rho(HCOO)_3$ series. (b) The variation in T_{1D} with degree of dilution for simulation (triangles) and experiment (circles), compared with the mean-field result (line). (c) Entropy change over the 1D ordering transition as a function of dilution. Markers have the same meanings as in (a), but the solid gray line is now the simple relation $\Delta S(\rho) = \Delta S(\rho = 0)(1-\rho)$, expected for complete in-chain order. (d) Spin–spin correlation functions generated from the $T = 0.4\,K$ MC simulations with $\rho = 0, 0.4$.

The simulation was annealed to from 5 K to 0.4 K in steps of 0.1 K. Otherwise, the procedure was identical to that described in Section 4.3.

The results of the simulation are shown in the right-hand panel of Fig. 4.12(a): the two specific heat functions display a clear separation between a high temperature ordering transition and an upturn at low temperature that increases in intensity as ρ increases. The very low temperatures involved mean that we were unable to access the full 3D ordering transition experimentally, but we interpret our results nonetheless as consistent with theory. Moreover, there is good quantitative agreement between the defect-dependence of the position of the maximum in $C(T)$

[Fig. 4.12(b)], and also of the entropy change associated with 1D order [Fig. 4.12(c)]. In both simulation and experiment, the entropy change follows the relation

$$\Delta S(\rho) = \Delta S(\rho = 0)(1 - \rho). \tag{4.23}$$

This rule is consistent with the linear trend in Fig. 4.11(a), and based on the understanding that at 0.7 K interchain correlations are largely weak while intra-chain correlations are strong [§4.6]. This demonstrates that nonmagnetic doping has led to a residual entropy at 0.7 K, in a manner consistent with theory.

On examining the spin correlations of our simulation [Fig. 4.7(d)], we see that inter-chain correlations are disordered in the $\rho = 0.4$ segmented phase to the lowest experimentally-accessible temperature. This is evident too in the direct inspection of the spin configurations in Figure 4.13. What is going on here is more interesting than in the unfrustrated case since the starting model does not host long-range order, but rather algebraically decaying correlations. Polarised neutron scattering techniques like those used in the previous chapter could be used to gain an experimental measure of the dopant-dependence of magnetic correlations.

4.8 Conclusion

In this chapter, I have developed Monte Carlo and mean-field methods based on the collective action of chain segments. In the intermediate temperature range, these chains are internally ordered and while correlations exist between nearby chains,

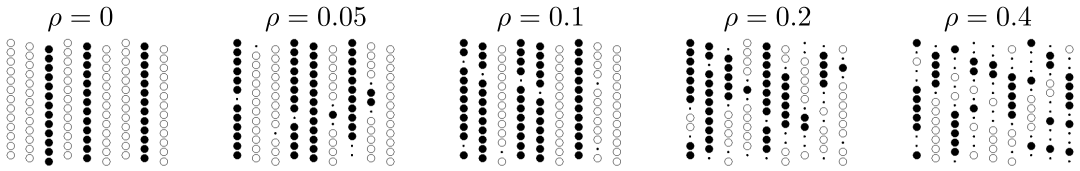

Figure 4.13: Representative spin configurations for the $T = 0.4$ K MC simulations of $Tb_{1-\rho}Y_{\rho}(HCOO)_3$, showing the loss of interchain order as a result of doping.

these correlations are short range. Since the measurement of $C(T)$ is acutely sensitive to the distribution of chain lengths $P(\rho)$, it may even be possible to gain information about this distribution directly from $C(T)$. In this way, the heat capacity measurement itself contains information about occupational pseudospin correlations. We have been assuming that the nonmagnetic Y is distributed randomly in the $Tb_{1-\rho}Y_{\rho}(HCOO)_3$ solid solution, which implies that $P(\rho)$ is given by Equation (4.5) but this equation could be corrected for short-range order. Further local experiments (e.g. diffuse neutron scattering, PDF, NMR) could also be used to determine whether this atomic distribution contains short-range order.

If the magnetism in $Tb_{1-\rho}Y_{\rho}(HCOO)_3$ is so acutely dependant on low levels of doping, an interesting question is raised: could these approaches be used to shed light on accidental impurities in 'undoped' $Tb(HCOO)_3$ and other q-1D systems? If we assume that such impurities (stacking defects, impurities etc.) behave similarly to non-magnetic defects, we may anticipate the same characteristic $C \propto T$ signature predicted here. It is unclear from this study whether—for small defect-concentrations—this signal could be resolved over other contributions to the heat capacity or whether a general defect behaves in the same way to those studied here.

The concept is interesting in light of the recent proposal of an 'eminuscent phase' in frustrated magnets [195]: a claim that the glass-transition temperature actually grows with decreasing impurity concentration up to a finite value in the 'impurity-free' limit. If this were the case, then a careful characterisation of the low level impurity distribution would be useful. In principle, this work flags that this information may be present in $C(T)$, assuming sufficient understanding of the system's Hamiltonian. However, this also flags a potential deficiency of this work, which assumes a thermodynamic equilibrium is reached at all experimentally accessed temperatures. The freezing of spin chains presents a challenge for these models. The extension of these theories to systems out of thermal equilibrium—via Glauber dynamics or similar [143]—would help address such claims. The simplicity of the theories in q-1D

systems make them an excellent test case to look for an 'eminuscent phase'.

The two 'transitions' seen on doping with Y emerge due to a dimensional crossover: at high temperature the correlations in the system are exclusively one dimensional and at low temperatures three-dimensional correlations emerge. The separation of these temperature scales can be understood as an effect of the chain segments' finite size: increasing vacancy concentration decreases the size of chains, which in turn exacerbates the finite size effects and increases the separation between the two energy scales. Fundamentally, this works because the percolation threshold of a 1D chain is zero, so it requires only one vacancy to segment the chain. Beyond the percolation threshold of a 2D lattice, the magnetic ground-state consists of a distributions of segmented clusters which can not interact via nearest neighbour links. A theory similar to that described here would therefore be applicable to the quasi-two-dimensional models also.

A key advantage of exploiting heat capacity measurements as a probe of unconventional order is that there is no fundamental constraint on the type of degree of freedom involved. While the focus of this chapter has been on magnetic dipoles (i.e. spins), it could be equally well applied to electric dipole pseusospins, for example the orientation of ammonium molecules in $[NH_4]Zn(HCOO)_3$ [403]. In the intermediate temperature range of such models, chain segments with large effective dipole moment would be freely fluctuating. Would these have the potential to host large dielectric susceptibility, as do the polar nanoregions of relaxor ferroelectrics [234, 404]? This could have applications in energy storage and capacitor technology.

The scope of our study has been limited to the Ising model. Nevertheless, our analysis might in future be extended straightforwardly to XY or Heisenberg degrees of freedom, and/or to include long-range interactions (*e.g.* dipolar)—so long as these additional interactions are much weaker than the intra-chain coupling. The prediction that $C \propto T$ at low temperature for low concentrations of impurities may be of interest to in quantum magnetism, where linear heat capacities are used as a

hallmark of fermionic excitations [268] but the presence of defects is not considered. Such studies may also be relevant to the behaviour of a variety of q-1D CDW systems, for example, where chemical or microstructural defects are thought to play an important role [389].

Chapter 5

Ferrimagnetism from partial vacancy order

Summary

In the previous chapter, I discussed how doping by nonmagnetic sites affected the magnetic properties of a formate coordination polymer in complex ways. In the series, $Tb_{1-\rho}Y_{\rho}(HCOO)_3$, it proved sufficient to neglect correlations between vacancy positions. In this chapter, the series $[C(NH_2)_3]Mn_{(1-x)}$ $[Fe_{2x/3}\square_{x/3}](HCOO)_3$ is investigated, in which the B–site of the perovskite structure is occupied by Mn^{2+}, Fe^{3+}, and vacancies (denoted $\square$). Unlike the systems studied in the previous chapter, the distribution of these vacancies is not random, but rather highly correlated.

I start by summarising the percolation induced ferrimagnetism mechanism and the reasons why it may be applied to the magnetic hybrid perovskites. I then present the magnetometry data central to the study: an effect of the vacancy order is the onset of ferrimagnetism at a critical percolation threshold $x = 0.6$, which leads to a significant enhancement of the magnetic moment. A Monte Carlo simulation is developed to describe the dual disorder of vacancies and spins based on a simple ansatz Hamiltonian. Only at intermediate compositions $0.6 < x < 1.2$—all involving a degree of compositional disorder—is long-range ferrimagnetic order possible.

Acknowledgments

This project was carried out in collaboration with a Part II student, Alex Willis. She carried out some of the magnetisation measurements and Monte Carlo simulations. The samples were synthesised and characterised by Jonas Bruckmoser and Hannah Böstrom in a the previous study, Ref. 104.

5.1 Background

5.1.1 Percolation Induced Ferrimagnetism

The approach taken in this chapter to enhance magnetisation is based on the Percolation Induced Ferrimagnetism (PIF) mechanism discussed by Timonin [405–407] and investigated in the context of inorganic materials. I start here by describing the principle of this mechanism and then explain the importance of its applicability to the magnetic hybrid perovskites.

In the case of the previous chapter non-magnetic ions were distributed approximately randomly on the magnetic lattice. Percolation induced ferrimagnetism is a phenomenon observed in certain magnetic materials where an imbalance between the occupation of two sublattices leads to a net magnetisation [405]. This occurs because magnetic atoms tend to anti-cluster. A few 'imbalanced graphs' are shown in Figure 5.1(a–d), when antiferromagnetic interactions are introduced to these models, the A sites and B sites develop opposing magnetisations.

The behaviour of these models depends on the concentration of vacancies, as illustrated in Figure 5.1(e). At low concentrations of vacancies, the model is not imbalanced so behaves as an antiferromagnet. Introducing a magnetic field can flip some clusters of spins at a certain magnetic field, leading the the improper ferrimag-

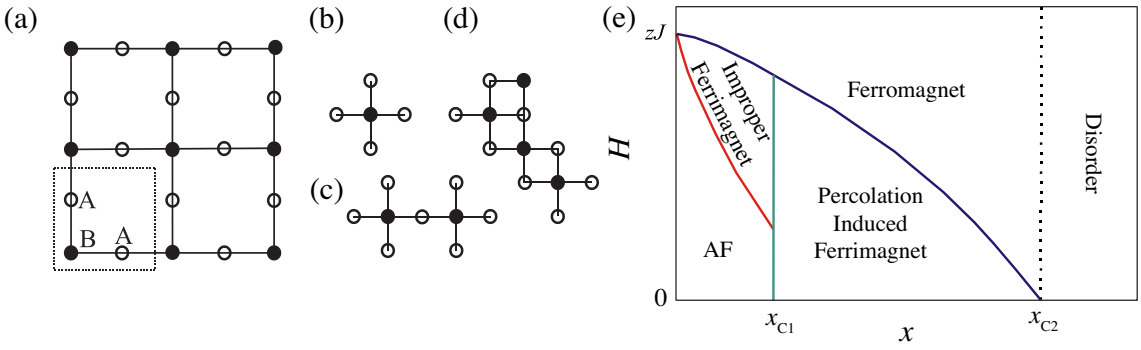

Figure 5.1: (a-d) Examples of imbalanced bipartite graphs with different numbers of sites in sublattices A (open circles) and B (filled circles). (a) The Lieb lattice, (b–d) fragments of a 2D lattice, (e) (x, H) phase diagram. Reproduced from Ref. 405.

net phase. However, when one gets to a critical concentration of vacancies (x_{C1}), there will always be an imbalanced cluster which percolates the whole crystal. This is the so-called Percolation Induced Ferrimagnet (PIF) phase, which is predicted to behave much like a ferrimagnet.

These theories have been applied in the metal fluorides, such as to the series $Fe_{1-x}Zn_xF_2$ and $KNi_xZn_{1-x}F_3$, where imbalanced magnetisation arises due to anticlustering of magnetic Fe/Ni and non-magnetic Zn [405–407]. This is a useful design strategy to introduce bulk magnetisation into antiferromagnets which will be the subject of Chapter 5.

5.1.2 Magnetic Hybrid Perovskites

The hybrid perovskites are interesting places to look for inducing interesting magnetic properties. The weak ferrimagnetism observed in many of the $AMn(HCOO)_3$ hybrid perovskites as been discussed in Section 3.1 [87, 95, 362, 363, 368]. This likely arises because of spin canting induced by antisymmetric exchange [103, 367]. Additionally, a peak in dM/dH associated with a spin-flop transition was observed in a number of systems [87, 362, 363, 365]. In light of the percolation induced magnetism approach discussed above, introducing nonmagnetic sites onto the magnetic sublattice may be a way to introduce ferrimagnetism into the system and enhance the residual magnetisation.

This approach was taken (perhaps fortuitously) in Ref. 408, which investigated the $[(CH_3)_2NH_2]Mn_{1-x}Zn_x(HCOO)_3$ series ($0 \leq x \leq 1$). In this series, they observed some complex changes as a function of nonmagnetic doping: the spin canting transition was suppressed and there was some increase in the zero field cooled magnetic susceptibility at low temperature however there was no critical concentration at which magnetisation was enhanced, in the way that would be expected for PIF [405]. The first and second requirements for PIF are met: the interactions are antiferromagnetic and the system is forms a homogeneous solid solution. However, because of there is no long-range structural transition associated with Mn-Zn anticlustering

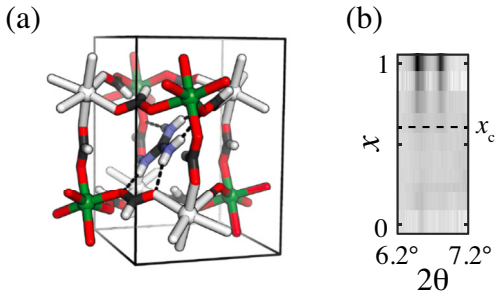

Figure 5.2: (a) The vacancy ordered structure of [Gua]$Mn_{1-x}Fe_{2x/3}\square_{x/3}(HCOO)_3$, with the metal definientia site shown in white and the vacancy rich site in green. (b) A film plot showing the onset of superlattice reflections associated with vacancy order at the critical concentration. Both are reproduced from Ref. 104.

for any value of x (single crystal XRD sees no such superlattice reflections), PIF cannot arise.

The recent discovery that anticlustering of vacancies induces the long-range B-site order as shown in Figure 5.2(a) means that one sublattice (shown with white atoms) is more vacancy rich and other is metal rich (green atoms). Long-range order of this kind develops at a percolation threshold $x_c = 0.6$, characterised by sharp superlattice reflections [Fig. 5.2(b)] and with the appropriate symmetry lowering. While other aliovalent solid solutions of formate perovskites investigated [409, 410], it is the stability of Guanadinium hydrogen bonds which allows for a sufficient vacancy content to be reached without the collapse of the structure [104, 411]. In this chapter, I study the implications of this B-site order for the series' magnetic properties.

This observation contrasts with the series of interest to this chapter, which as highlighted in section 1.1.4, does show B-site magnetic order resulting from vacancy anticlustering. This chapter will investigate how this long range B-site order changes the behaviour of the system.

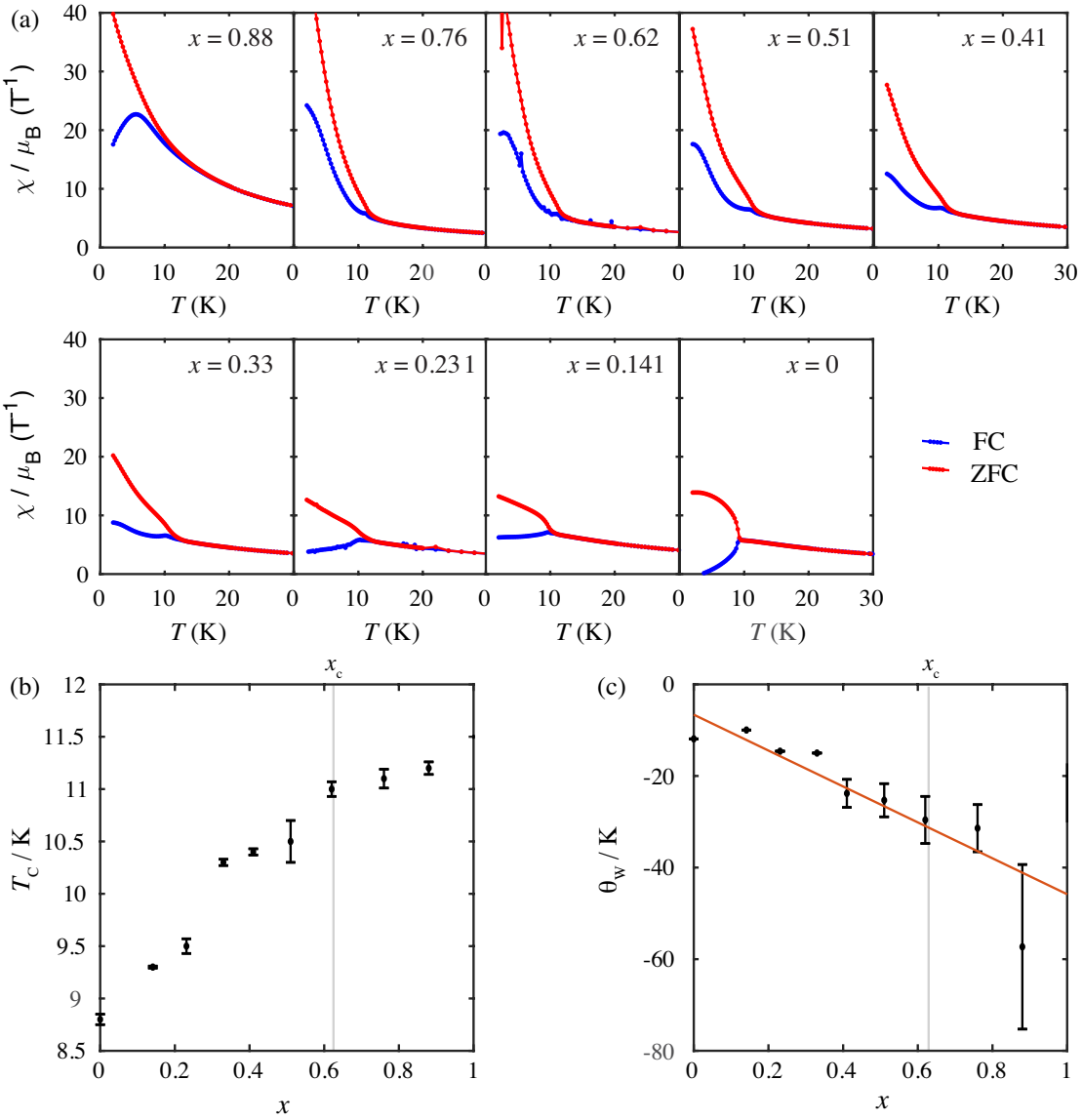

Figure 5.3: (a) Zero field cooled (red) and field cooled (blue) measurements, plotted across the series, showing their bifurcation at T_C and the change of the behaviour around the maximum at $x \sim x_c$. (b) The variation of T_C with x, marked by the divergence of FC and ZFC measurements in pane (a). (c) The dependence of $\theta_{\mathrm{W}}(x)$ on T. The error bars in this plot are estimated from the change in fitted value as the minimum fitting temperature is varied between 50 and 150 K.

5.2 Magnetometery

5.2.1 Low field measurements

I start this chapter by detailing the magnetic measurements across the series. We measured the field-cooled (FC) and zero-field-cooled (ZFC) magnetometry between

300 and 2 K on an MPMS-3 magnetometer on ~ 10 mg portions of all 9 members of the series in investigated in Ref. 104.

The resulting curves [Fig. 5.3(a)] show a complex evolution as a function of x and temperature. At low x, the curves are as expected for a canted antiferromagnet: a bifurcation occurs at the transition temperature below which the ZFC susceptibility decreases and FC increases. As x is increased, the behaviour changes, with a particular change for values of $x > x_c \simeq 0.6$. The low temperature susceptibility increases for both FC and ZFC traces. The transition temperature [Fig. 5.3(b)], shows some small variation as a function of x. This trend is investigated quantitatively in section 5.3.

There is also a large increase in the magnitude of θ_{W} [Fig. 5.3(c)], although the origin of this increase is less clear. The large increase in the errors of this value is also notable. These errors are calculated from the change in the value as a function of the fitting range, so this trend may arise from the presence an impurity with much more significant magnetic interactions (although this would have to be in a small enough proportion not to show up in the previous X-ray scattering experiment). Alternatively crystal field effects may explain the increase in coupling strength going from Mn^{2+} to Fe^{3+}. This could either result from an increase in charge (and therefore shorter M–O distance) or a rearrangement of bonding geometry.

On doping with Fe^{3+}, the magnetic behaviour changes considerably. The $x = 0$ end-member shows a similar antiferromagnetism to other Mn^{2+} formate perovskites. The FC and ZFC susceptibility diverge at the transition temperature (T_C), with the former showing the maximum at T_C expected for an antiferromagnet. As x is increased, the FC susceptibility below T_C changes from increasing with temperature to decreasing, and the maximum at T_C disappears. These observations are qualitatively consistent with a significant increase in the static magnetic moment. A switch from canted antiferromagnetism to ferrimagnetism, with the most extreme change occurring at x_{c}.

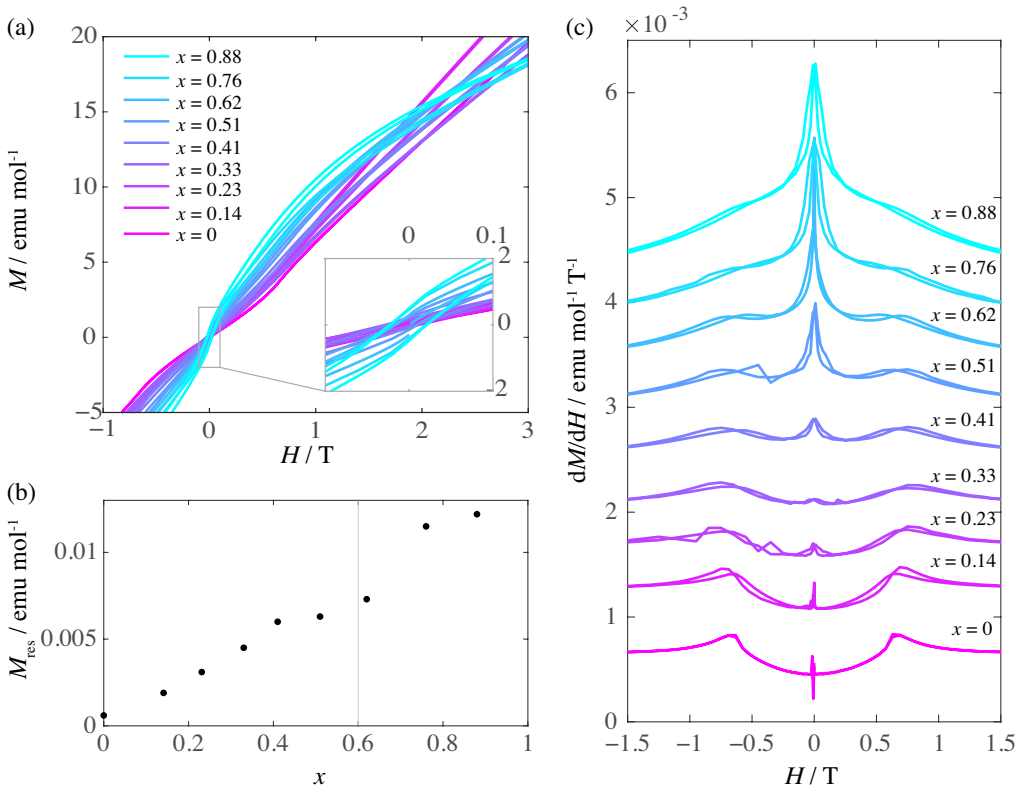

Figure 5.4: (a) Applied field measurements measured with the magnetisation cycle described in the text. The hysteresis loop, which opens for larger values of x is highlighted in the inset. (b) The dependence of remanent magnetisation on x. (c) The gradient of the magnetisation. For clarity, each successive curve is offset by 0.5 units.

5.2.2 Variable Field Measurements and Hysteresis

Variable field magnetometry measurements were measured on the same device for each member of the series, showing a marked change in the magnetic behaviour across the series. Magnetic field was cycled though an $H = 0 \rightarrow 5 \rightarrow -5 \rightarrow 0$ loop in order to understand the degree of magnetic hysteresis. The results are plotted in Figure 5.4(a), and shown as their gradient in Figure 5.4(c). The residual magnetisation [Fig 5.4(b)] is extracted as the average of residual magnetisation on the first and second demagnetisations i.e. the y-intercept of the magnetisation on the application and deapplication of field.

On doping with Fe^{3+}, a magnetic hysteresis loop is opened at low field. At $x = 0$, there is a very small residual magnetisation of $M_{\text{res}} = 6 \times 10^{-4}$ emu mol^{-1}, consistent

with the values seen in manganese formate perovskites [87, 362, 363], but this value is enhanced by more than an order of magnitude to a maximum value of 1.5×10^{-2} emu mol^{-1} for the $x = 0.88$ member of the series.

The magnetisation curves [Fig. 5.4(a)] also evolve considerably with x. This is most visible in their gradients [Fig. 5.4(c)], which shows the susceptibility changing from exhibiting a characteristic spin flop behaviour, with a maximum in $\mathrm{d}M/\mathrm{d}H$ at 0.66(3) T. The position and form of the maximum in the $x = 0$ sample is consistent with behaviour attributed to an antisymmetric exchange interaction for different A-site cations [87, 95, 362, 363, 368]. The maximum remains but becomes more broad as x is increased. This same behaviour is observed in the $[(CH_3)_2NH_2]Mn_{1-x}Zn_x(HCOO)_3$ series ($0 \leq x \leq 1$) [408], suggesting that it is related to the broadening of the distribution of local environments associated with doping. As x is increased, a central feature appears in $\mathrm{d}M/\mathrm{d}H$ at $H = 0$, consistent with the increased spin fluctuations at zero-field associated with ferrimagnetism. This behaviour seems to change most abruptly for the $x > x_c$ members of the series.

5.3 Monte Carlo Model and Parametrisation

In order to better understand the changes to the magnetisation at finite temperature and intermediate vacancy concentration, building on the previous Monte Carlo simulations which explained the vacancy structure of the system [28]. These simulations were able to reproduce the ordering transition at the correct percolations threshold. The general simulation approach is shown schematically in Figure 5.5(a). First, vacancies are randomly distributed in a supercell; then the first MC procedure redistributes the vacancies such that there are no nearest neighbour contacts. In the next series of Monte Carlo simulations, magnetic moments are allocated to the sites and evolved according to the spin Hamiltonian at finite temperature. In this section, I will detail these steps and describe the procedure used to parametrise the Hamiltonian.

The bulk of the MC simulations analysed in section 5.4 were performed on $6 \times 6 \times 6$

supercells, consistent with the work of Ref. 104. Subsequent simulations detailed in section 5.4.2 to analyse the domain structure were carried out on larger $20 \times 20 \times 20$ cells—large enough to potentially host multiple domains.

In previous work on the system [104], the ordering of vacancies was demonstrated using a simplified cubic model (which neglects the differences between the three crystallographically-inequivalent directions). In this way, the vacancy distribution of the system can be described as arising from vacancy anticlustering (i.e. the tendency for vacancies to avoid nearest-neighbour contacts). The first step of our simulation reproduces these established results. Vacancies are randomly distributed in the unit cell and simulated annealing is used to produce a set of maximum entropy configurations which minimise the number of vacancy–vacancy nearest-neighbours. This process is repeated for many values in the range $0 \leq x \leq 1$, chosen to correspond to the experimental values of x discussed above. Further simulations were subsequently carried out on finer x grids and over a larger range.

By tracking an order parameter Böstrom and coworkers the onset of anticlustering at $x \approx 0.6$. The order parameter for the chequerboard ordering at the vector $\mathbf{k} = \left[\frac{1}{2}, \frac{1}{2}, \frac{1}{2}\right]$ is defined as

$$\alpha(x) = \frac{1}{N_{\text{vac}}} \left| \sum_{i \in \text{sites}} o_i \exp 2\pi \mathrm{i} \mathbf{r}_i \cdot \mathbf{k} \right|, \tag{5.1}$$

where N_{vac} is the number of nearest neighbours. This equation is normalised such that the value of $\alpha = 1$ would be produced by a chequerboard arrangement which involves the maximum possible order for a given concentration. Using this MC approach, we have reproduced the x dependence of the order parameter [Fig. 5.5(bi)] in Ref. 104: the order parameter is low when $x < x_c = 0.6$ but increases rapidly at this percolation threshold. Although no long range order exists in the model for $x < x_c$, a statistically fluctuating imbalance between the occupation of sublattice I and II leads to some non-zero values for α. This finite size effect would disappear if the simulation was scaled up since the size of the fluctuations grows slower than

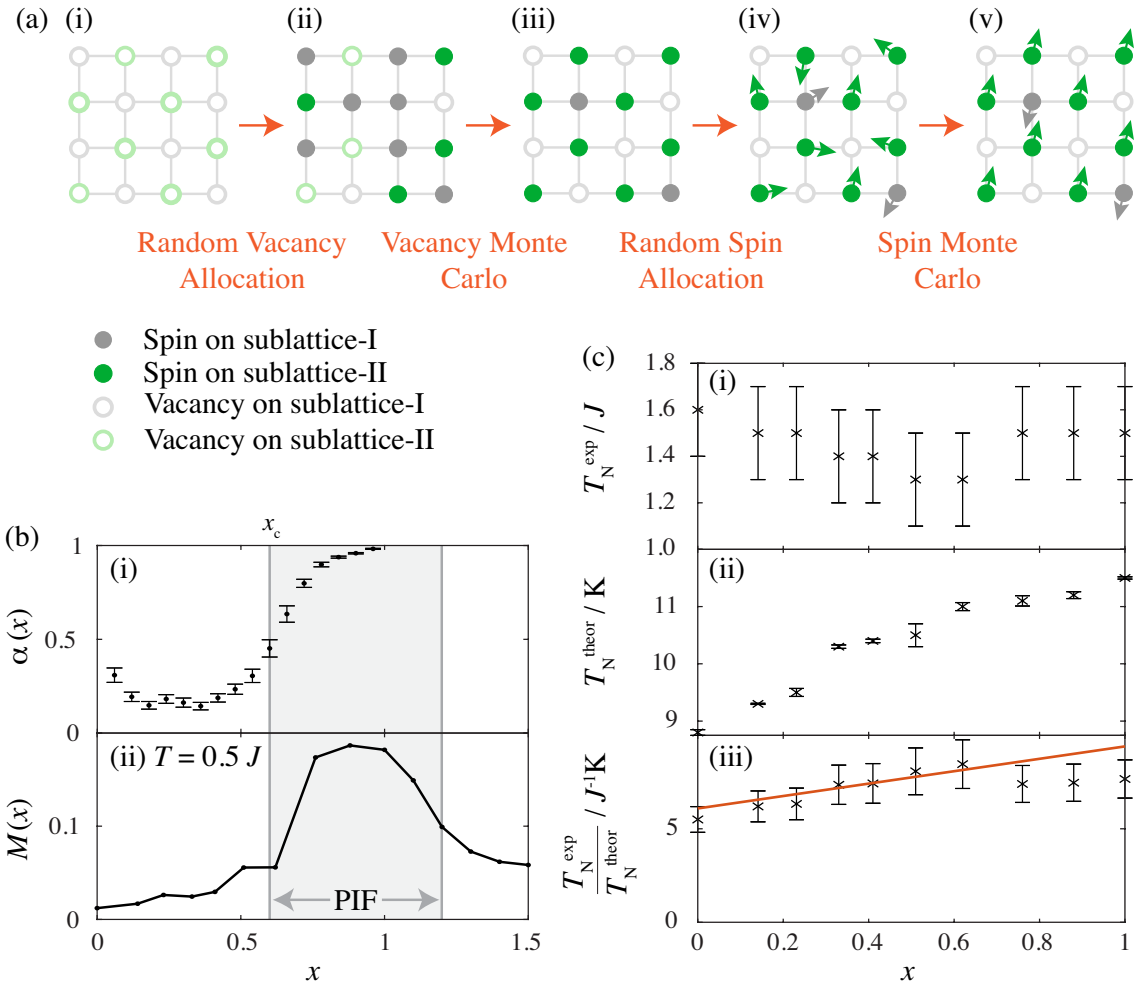

Figure 5.5: (a) Schematic showing the approach to MC simulations in these systems: (ai) the bare lattice partitioned into an I and II sublattice, (aii) the system after randomly assigning the number of vacancies corresponding the stoichiometry x, (aiii) the vacancy MC step minimises the number of nearest neighbour vacancy contacts, (aiv) the system after decoration with Heisenberg spins, and (av) by the end of the spin Monte Carlo step at a low temperature, the system has ordered into a near-groundstate configuration. (bi) The variation of vacancy order parameter with stoichiometry, as determined theoretically from Equation (5.1). (cii) The variation with total magnetisation of the Monte Carlo simulations, normalised to the magnetic moment. (c) The approach taken to parametrising $J(x)$ in Equation (5.2): (i) the theoretically determined transition temperature, (ii) the value experimentally derived from the divergence of ZFC and FC susceptibility, and (iii) their ration, shown alongside a linear fit.

the size of the system.

The next step of the modelling approach is to decorate the magnetic atoms in this model with spins. We have seen from the $x = 0$ end member that the biggest term in the magnetic Hamiltonian is antiferromagnetic Heisenberg exchange. Any terms in the Hamiltonian besides Heisenberg exchange are neglected in our treatment.

This approximation means that our model will be unable to reproduce the spin flop transition or residual magnetisation seen experimentally. However, I will go on to show that the model is able to capture the important PIF transition seen in this system. Based on these vacancy distributions ($o_i = 1, 0$ if occupied or unoccupied) we describe the dependence of the energy on the Heisenberg spin orientations $\mathbf{S}_j$ using the simplified ansatz Hamiltonian,

$$E_{\mathrm{MC}} = J(x) \sum_{\langle ij \rangle} o_i o_j \mathbf{S}_i \cdot \mathbf{S}_j, \tag{5.2}$$

which again treats the three pseudocubic neighbours $\langle ij \rangle$ equivalently. Due to tilting patterns lowering symmetry, in $GuaMn(HCOO)_3$ there are two inequivalent neighbours which are bridged by anti-anti Mn–O–C–O–Mn exchange pathways. However, our approach, inspired by Ref. 87 treats these pathways as equivalent.

The MC simulation itself is carried out using a custom code related to that used in Chapter 3. This simulation takes configurations with frozen vacancy distributions generated by the previous MC step. The first series of simulations was carried out on the $6 \times 6 \times 6$ supercells. Simulated annealing is used, cooling from $T = 3J$ in steps of 0.05 K, halting after 100 h, typically at $T \approx 0.5J$. At each temperature, the algorithm measures decorrelation time n_{d} (the number of moves required for Equation (2.57) to reach zero), equilibrates for $10n_{\mathrm{d}}$, and progresses to measure 80 samples with $2n_{\mathrm{d}}$ moves per sample. In this way, we ensure ergodicity in the simulations.

The net magnetisation of simulations at low temperature ($T = 0.5\,J$) is shown in Figure 5.5(bii). This value tracks the order parameter quite well: increasing most significantly for $x \sim x_c$ and staying quite low in the antiferromagnetic regime. An interesting observation is that the value increases with x even below x_c which may be consistent with the observation of some small ferrimagnetism below T_{C}. This may also be due to the same finite size effect noted earlier. Despite this, the result is clearly consistent with previous simulations of the PIF mechanism [405] for this

Ising model and extends these theories to the Heisenberg model.

Extending the simulation range into the chemically unfeasible $1 \leq x \leq 1.5$ range reveals that there is an upper limit to this behaviour when too many vacancies are introduced, the magnetic structure fragments into domains which cannot communicate. This leads to a second percolation limit. This same observation was made by Timonin [405], studying similarly diluted Ising models. He predicted this percolation threshold, which corresponds in our system to $x = 1.2$, beyond which PIF cannot contribute to a net magnetisation. This same argument applies in the Heisenberg system, which explains the eventual decrease in magnetisation at $x = 1.2$.

A common approach to parametrising such a Hamiltonian would be a fit to the low field magnetometry data. However, given the large errors in our values reported in Figure 5.3(b), this approach is not viable. Our approach (shown in Figure 5.5(b)) involves fitting to the value of the transition temperature, which has much smaller errors. The dependence of T_{N} on x is calculated from the model and experimentally, with a linear fit to their ratio taken as an estimate of $J(x)$. By this method, we obtain

$$J \,/\, \mathrm{K} = 3.32x + 6.09. \tag{5.3}$$

The $J = 6.09$ value for $x = 0$ falls within the range of values seen in other formate perovskites, e.g. between 5.7 and 6.5 K for the four systems studied in Ref. 87. The increase in J seen in its positive gradient could be for a variety of reasons. The increased charge from Mn^{2+} to Fe^{3+} could result in greater covalency interactions and therefore shorter bond lengths, both improving superexchange. Given the geometry-dependant magnetism seen as a function of pressure in related system [360] [§3.1], the changing structure would likely result from relaxation around vacancies which may play a role too.

5.4 Results and Discussion

5.4.1 Simulating $\chi(T)$

Susceptibility is calculated from Monte Carlo simulations via the fluctuation method. The resulting values are plotted in Figure 5.6(a). In order to normalise for errors in measuring the mass of samples noted in section 5.2.1, values are normalised to their value at 15 K. This allows for direct comparison between MC and FC/ZFC results.

Despite being based on a simplified ansatz, our model reproduces the trend at play across the series: for $x \leq 0.14$ the magnetisation shows a maximum at T_{N}, as expected for an antiferromagnet and at $x \geq 0.62$, there is a sharp upturn in the susceptibility at T_{N}, consistent with a ferrimagnet. Over the x range, our model reproduces the smooth increase in the low temperature susceptibility seen experimentally. While we only expect global PIF at values of $x > x_{\mathrm{c}}$, ferrimagnetism at lower values may be explained by short range vacancy order. For the most part, the simulated value of the susceptibility falls somewhere between the field–cooled and zero field cooled susceptibility, which is consistent with this being an equilibrium calculation.

The gradual increase in low temperature magnetic susceptibility with x outside of the range of values expected for PIF (namely $x \geq 0.6$) is surprising. In a macroscopic simulation this would not be possible as the number of domains aligned with field should entirely cancel those opposing it, given the lack of percolation at these concentrations. Indeed, this is almost certainly due to a finite size effect rather than any particular strength of the simulation: within the $6 \times 6 \times 6$ supercell, the exact cancelling of magnetisation which exists in an infinitely large simulation is not guaranteed.

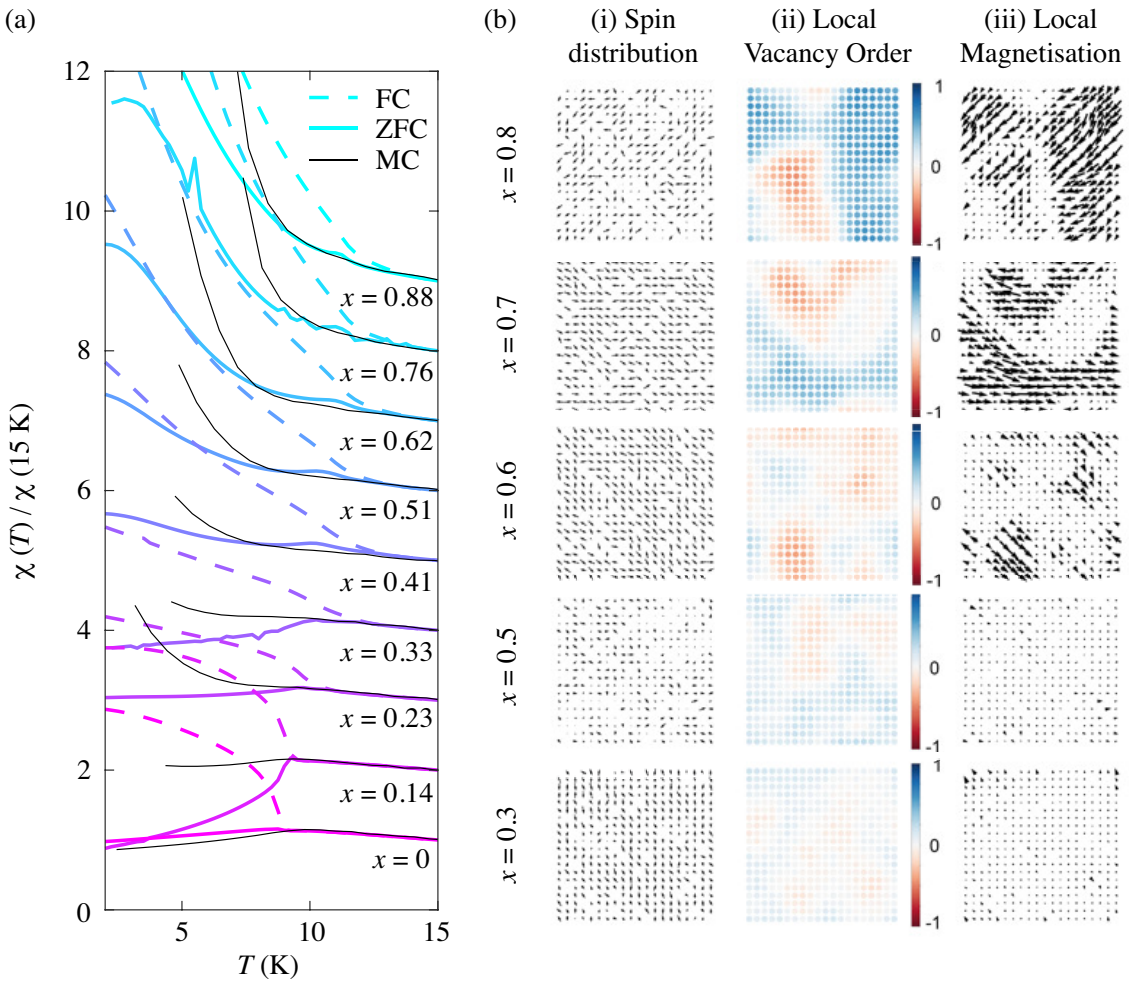

Figure 5.6: (a) Field cooled (dashed coloured lines) and zero–field cooled (solid coloured lines) magnetic susceptibility (H=100 Oe) as a function of temperature for nine members of the series [Gua][$Mn_{1-x}Fe_{2x/3}(HCOO)_3$ shown alongside the simulated values (solid black lines) generated from the MC procedure described in the text. To aid comparison, successive compositions are offset by one unit and each is normalised to its 15 K value. (bi) A slice through one configuration of a $20 \times 20 \times 20$ supercell at the lowest simulation temperature. (bii) The local vacancy order and (biii) magnetisation for the same supercell slices as defined in Equations (5.4) and (5.5), respectively. Regions of local magnetisation order and vacancy order correlate for $x > 0.6$.

5.4.2 Domain formation

In order to investigate the role of domains, we move to even larger supercells: $20 \times 20 \times 20$. The simulations are carried out with the same approach as for the smaller supercell. However, it was not always possible to ensure decorrelation at the lowest temperatures so it became necessary to allow the simulation to proceed

if not decorrelated within 10^4 moves per spin.

A single plane of the spin distribution at the lowest simulation temperature, $T = 0.5J$ is shown in Figure 5.6(bi). In order to gain a little more insight from these configurations, it is easier to view local variations of the order parameter (again, $\mathbf{k} = \left[\frac{1}{2}, \frac{1}{2}, \frac{1}{2}\right]$) and magnetisation are plotted in Figure 5.6(cii–iii) respectively. These quantities are defined as

$$\Phi_{\text{loc.}}(\mathbf{R}) = \left[\sum_{i \in \text{sites}} w(|\mathbf{r}_i - \mathbf{R}|) o_i \exp 2\pi \mathrm{i} \mathbf{r}_i \cdot \mathbf{k}\right] \Bigg/ \left[\sum_{i \in \text{sites}} w(|\mathbf{r}_i - \mathbf{R}|)\right] \tag{5.4}$$

and

$$\mathbf{M}_{\text{loc.}} = \left[\sum_{i \in \text{sites}} w(|\mathbf{r}_i - \mathbf{R}|) o_i \mathbf{S}_i\right] \Bigg/ \left[\sum_{i \in \text{sites}} w(|\mathbf{r}_i - \mathbf{R}|)\right] \tag{5.5}$$

respectively. In this case, $\mathbf{R}$ is the position within the supercell, normalised so that the Mn–Mn separation is unity. These quantities allow us to see the spatial variation of the local order parameter and magnetisation in the neighbourhood of the spin at $\mathbf{r}$, defined an exponential window function,

$$w(r) = \exp -\frac{r}{2\zeta}, \tag{5.6}$$

where we use $\zeta = 0.5$ unit cell distances.

Figure 5.6(bii) displays the plot generated from Equation (5.4), where the red regions indicate the placement of vacancies on one fcc sub-lattice and the blue regions indicate their placement on the other fcc sub-lattice. For $x > x_{\text{c}}$, we anticipated observing long-range order, which was confirmed by the macroscopic domains that spanned the entire structure. However, the domain size is similar to that of the supercell, indicating that finite size effects may still be present.

The corresponding local magnetisation plots are shown alongside in Figure 5.6(biii). A clear correlation between domains of local vacancy order and magnetisation arises: red regions have magnetisation aligned in one direction and blue regions tend to oppose this. The correspondence between domains of local order vacancy order

and magnetisation is perhaps unsurprising: the antiferromagnetic spins have the same ordering vector as the **k** vector used. A surprising observation is made in the $x = 0.5$ simulation, which falls slightly below the percolation threshold for the lattice. Despite this, local nano domains are clearly present in the simulation, with corresponding regions of local magnetisation.

5.5 Conclusion and Outlook

In this chapter, I have demonstrated that doping $GuaMn(HCOO)_3$ with Fe^{3+} leads to an enhancement of the residual magnetic moment. This behaviour is rationalised in terms of the percolation-induced ferrimagnetism mechanism. MC simulations were parametrised to the experimentally-determined transition temperature. These simulations reproduce the PIF behaviour, as is highlighted in the $\chi(T)$ function. While the qualitative predictions of the theory are correct, we do not predict the correct magnitude of remanent magnetisation.

In both the simulations and experiment, the trends are more gradual than expected, with systems below the critical concentration x_c exhibiting some enhanced susceptibility below T_N. This might be explained by the limitations in the size of our simulations and/or the simulation time for which they were allowed to equilibrate. For disordered magnetic systems, it is unclear whether simulation ergodicity is even possible (cf. spin glasses [§1.2.4] [194]) but finite size scaling could rule out size effects as a contributing factor [292]. The latter approach may help answer the question of whether a more local form of the PIF mechanism may be driving a residual magnetisation in these species, in a similar way to the weak domain-wall magnetisation which is important in antiferromagnets [412].

The Monte Carlo simulations used to describe the system are intentionally simple but we have seen a number of indications that the true Hamiltonian of the system is more complex than indicated here: experimental evidence for (i) anisotropy and (ii) antisymmetric interactions in the $GuaMn(HCOO)_3$ Hamiltonian come from the observation of (i) a spin flop transition and (ii) a residual magnetic moment. Future

work could investigate the role of these terms on PIF physics. The impact of antisymmetric exchange may induce to a rich behaviour due to the competition of the 'weak ferromagnetism' mechanism [103] with PIF. One particular system already discussed is $[(CH_3)_2]\,Mn_{1-x}Zn_x(HCOO)_3$, where a slight enhancement of residual magnetism is seen even in the absence of the long-range order required for PIF. Could some modification to the Hamiltonian explain this observation?

I see the key success of this study as extending the PIF physics previously investigated in inorganic systems to the hybrid perovskites, raising a number of possibilities for future studies. AC susceptibility measurements could investigate the role of kinetics in the PIF mechanism; might a dynamical version of our MC approach (e.g. the kinetic MC algorithms of Refs. 413 and 414) reveal something interesting about the kinetics?

This observation suggests a route to design a multiferroic framework material. Related formate perovskites $[C(NH_2)_3]Cu(HCOO)_3$, $[C(NH_2)_3]Cr(HCOO)_3$, $[NH_3NH_2]Mn(HCOO)_3$, and $[EtNH_3]Mn(HCOO)_3$ all exhibit improper ferroelectricity [28]. It is foreseeable that by using similar approaches in these systems as discussed here for $[C(NH_2)_3]Mn(HCOO)_3$, there is the possibility of achieving ferroelectricity and ferrimagnetism simultaneously, offering a novel approach to multiferroicity. Materials with this property are rare but promising for applications such as 4-state memory storage [100, 415].

Chapter 6

Correlated disorder and lattice dynamics in $Cd(CN)_2$

Summary

Cadmium cyanide [§1.1.4] has the largest isotropic negative thermal expansion (NTE) of any material. Its performance is greater than that predicted by DFT simulations and the quasi-harmonic approximation. Recent interest in the orientational CN pseudospins of the model comes from its mapping onto spin ice [§1.4.3] [65]. Figure 6.1—highlighting the change in thermal expansion with temperature—shows that the behaviour is sensitive to the onset of cyanide pseudospin order. An aim of this study is to shed light on the origins of the negative thermal expansion in $Cd(CN)_2$.

First, at room temperature, I report variable pressure powder inelastic scattering measurements to ascertain the dependence of the lattice dynamics on pressure. This gives an estimate for the Grüneisen parameter of the lowest frequency phonon

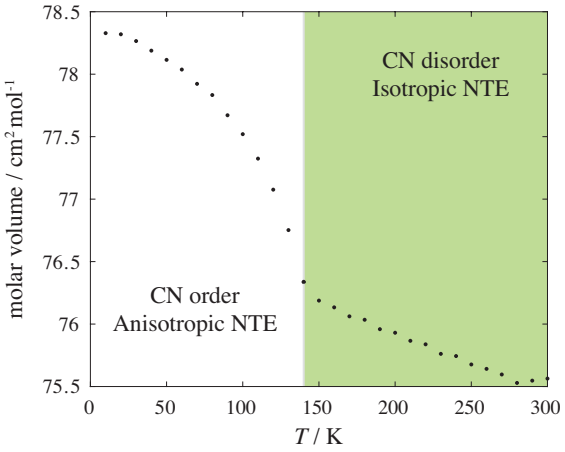

Figure 6.1: The thermal expansion of $Cd(CN)_2$, calculated from the lattice parameters reported in Ref. 65. Expansion is isotropic in the high temperature phase but anisotropic at low temperature.

branch.

The main result of this chapter is an understanding of the interplay between lattice dynamics and cyanide flipping dynamics. I have carried out inelastic neutron scattering (INS) as a function of temperature over the temperature range associated with cyanide order and discuss potential signatures of this static correlated disorder in the experimental data. The difference in timescales complicates simulation of these systems. In order to resolve these difficulties, a hybrid approach is taken, coupling an existing Monte Carlo simulation to a supercell lattice dynamics simulation within the harmonic approximation. These simulations required the fitting of a custom forcefield, which is detailed. The results of the simulation are compared to the INS experiment and understood in the context of the large isotropic NTE seen for $T > T_c$.

Acknowledgements

I have Chloe Coates to thank for much of the preceding work for this chapter: she measured all of the diffraction data used, characterised the phase diagram in Figure 6.2. Mia Baise carried out a number of DFT simulations on $Cd(CN)_2$ which lay the ground work for the results of this chapter, including the phonon dispersion curves used in Fig. 6.9(a). Ben Slater provided guidance in parametrising the DFT simulation. The instrument scientists Helen Walker and Ross Stewart carried out the INS experiments expertly during the time when in person attendance was impossible and Arianna Minelli was invaluable help during in person experiments.

6.1 Pressure dependence of lattice dynamics

6.1.1 Background

On the application of relatively small pressures, $Cd(CN)_2$ undergoes a cascade of phase transitions. Recent work has investigated these transitions by changes in the neutron diffraction pattern [416]. The phase behaviour is summarised in Figure

6.2(a), the system evolving though three phases (labelled I, II, and III) on the application of pressure. The characterisation of these phases is difficult; a decreased Q-range, increased background and introduction of additional reflections from the pressure cell all contribute to make the crystallographic information from this type of experiment less definitive. Phase II seems to be related to the cyanide ordered $I4_1/amd$ structure described in the introduction with the structure apparently consistent with a symmetry lowering of this phase to $C2/c$, although the allocation of this symmetry is tentative for the reasons mentioned. There is another high pressure phase at $p > 0.25\,\mathrm{GPa}$, but no progress has been made on solving its crystal structure [416] and it is beyond the scope of this study.

Ref. 416 is primarily concerned with the behaviour of the cyanide disordered Phase I. At 300 K, this phase is stable up to $p_\mathrm{C} \approx 1.4\,\mathrm{kbar}$, at which point it converts to Phase II. Fitting to an equation of state reveals that, aside from the negative thermal expansion already mentioned, two other unusual characteristics can be seen as a function of pressure and temperature. The compressibility of the material increases under pressure—termed 'pressure-induced softening'; the material also becomes less compressible on heating—termed 'warm hardening'. The second of these effects is a consequence of strong anharmonicity and sets cadmium cyanide apart from the isostructural zinc cyanide, indicating a stronger anharmonicity in this system. All of these behaviours shed light on the nature of anharmonicity in $Cd(CN)_2$, which is the origin of NTE in this material.

There are many questions raised by these experimental results. What is the mechanism for pressure-induced softening? Can we see direct evidence of the anharmonicity? Which phonons are most anharmonic and which are responsible for NTE? Does the cyanide pseudospin order evolve as a function of pressure?

6.1.2 Inelastic Neutron Scattering

In order to understand the mechanism for these structural observations more directly, I turn to a direct measurement of the lattice dynamics. These dynamics

have been investigated theoretically beforehand in the DFT study of Ref. [108], and should show similarities to the MD study on $Zn(CN)_2$ described Ref. [325], which was based on the forcefield described in §2.6.3. The dispersion curves calculated from DFT are shown in Figure 6.2(b). The form of pseudospin order used for these configurations—with each cadmium either surrounded by 4 carbons or 4 nitrogens—is actually the least favourable configuration energetically [65]. Nevertheless, calculations on this configuration—which has the same unit cell as disordered $Cd(CN)_2$—allow for a good first estimate of the high temperature behaviour. Although higher energy dynamics undoubtedly play a role in NTE, lower energy branches will have a stronger contribution [35, 39]. The intensity of INS also scales with $\frac{1}{E}$, which makes the lowest energy branch easier to probe. It is for this reason that I limit this study to the lowest energy branch, which disperses between 0 and 3 meV.

It is important at this stage to note the limitations of both DFT and MD in this system: the interpenetrated frameworks necessitate the use of dispersion corrections and the strong anharmonicity in these systems renders harmonic calculations insuf-

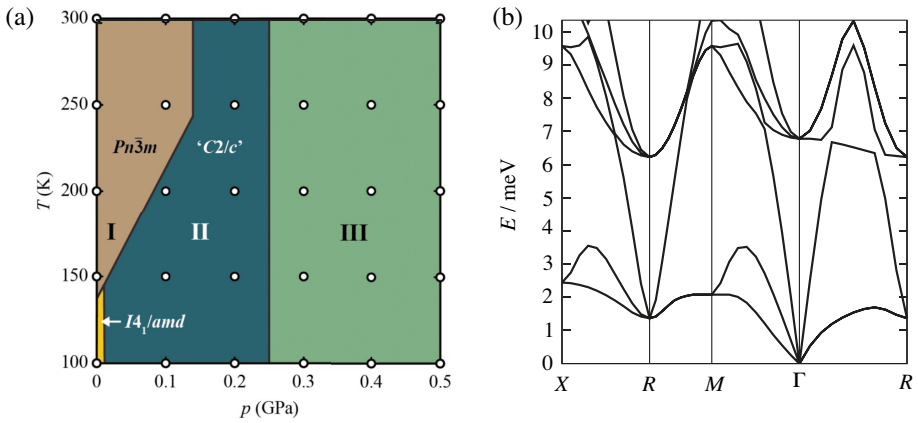

Figure 6.2: (a) Phase Diagram of $Cd(CN)_2$ elucidated by neutron diffraction experiments and reproduced with permission from Ref. [416]. On applying pressure the system transitions from the cyanide-disordered Phase I to Phase II, which is likely cyanide disordered, and then to Phase III (b) The low energy phonon dispersion relations calculated by DFT and adapted from Ref. [108] for the '4-in-4-out' cyanide ordered configuration of $Cd(CN)_2$.

ficient [417, 418]. Most importantly, all of the theoretical lattice dynamics studies to date [108, 109] neglect to include correlations between cadmium pseudospins. For these reasons, the outcome of simulations is highly dependent on the approximations made and models used.

By contrast, INS provides a direct measure the of dynamics of the system. In NTE materials such as ZrW_2O_8, INS measurement of polycrystalline samples allow for a direct observation of various pressure-dependent of lattice dynamical observables: line-width, density of states, and—most relevantly–the mode Grüneisen parameter [419]. Phonon density of states measurements are common in powder measurements. The recent development of low-background pressure cans for inelastic neutron scattering applications, such as the cylindrical pressure can used in both the diffraction experiments described and subsequent inelastic experiments, allows for investigation of the pressure dependence of INS in a more detailed way than previously possible [420]. The TAV-6 alloy is chosen to minimise to background scattering and improve the signal-to-noise in pressurised inelastic experiments [420].

The inelastic neutron scattering experiment was carried out on the MARI spectrometer at ISIS [421]. Details of the instrument and measurement are given in Section 2.1.4 for the five pressure values $p = 0$, 0.6, 1.0, 1.3 and 2 kbar. The background subtracted $S(Q, E)$ is shown in Figure 6.3(a) for the $p = 0$ and 2 kbar endmembers. The energy range includes the relatively dispersionless phonon branches understood to dominate NTE response [108]. The trace showing very similar behaviour for the four concentrations with $p < p_c = 1.4$ GPa [416] and a significant decrease in intensity for the final $p = 2$ kbar $> p_c$ trace. Despite the new sample can, the signal to noise in this experiment makes it difficult to directly extract information from $S(Q, E)$.

The small differences in scattering at $p < p_c$ can only be seen clearly in the neutron-weighted density of states (nDOS) which is defined as $S(E) = \int S(Q, E)dQ$, and plotted in Figure 6.3(b). Indeed, at all pressures, $S(E)$ is dominated by a

single feature centred at $E \simeq 1.2\,\mathrm{meV}$. For pressures below $p_c \simeq 1.4\,\mathrm{kbar}$, the $S(E)$ function is very similar, with the position of the main feature shifting to lower energy as pressure increases. By contrast, the $S(E)$ function measured for $Cd(CN)_2$-II at 0.2 GPa is very different: while there is still a single peak, it is much broader and centred at a higher E.

I have quantified these various observations by fitting the $S(E)$ functions using a double Gaussian

$$S(E) = c_1 \exp\left[-\frac{(E-E_0)^2}{w_1^2}\right] + c_2 \exp\left[-\frac{(E-E_0)^2}{w_2^2}\right], \tag{6.1}$$

to the data displayed in Figure 6.3(b). This double Gaussian is required to reproduce the centre and spread of the distribution. The fit parameters—c_1, w_1, c_2, w_2 and E_0—were determined by fitting to experimental data $0.5 \leq E \leq 4\,\mathrm{meV}$. The fitted values of E_{max} and their confidence intervals are shown in in the inset of Figure 6.3(b). The

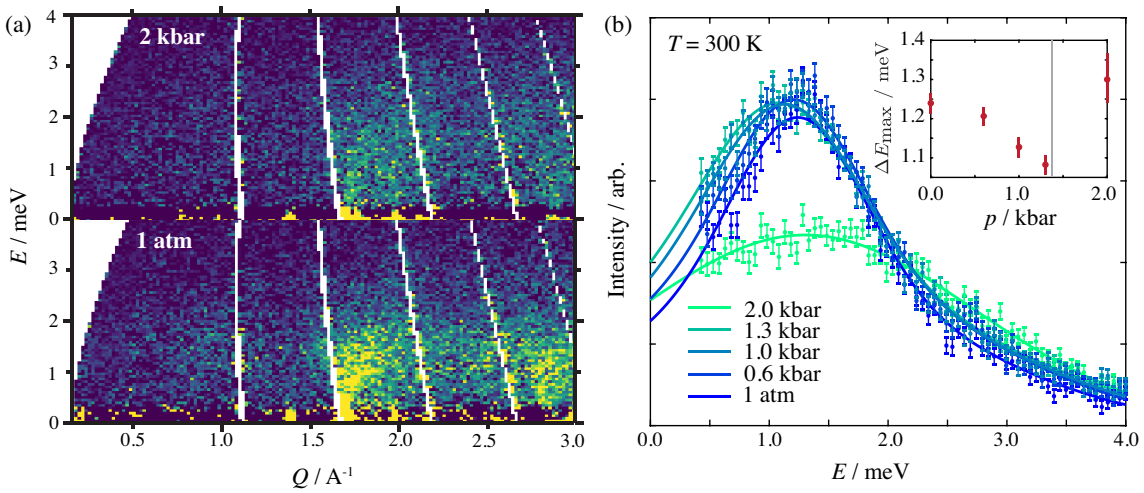

Figure 6.3: (a) $S(Q,E)$ plotted for the two extreme pressures 1 atm and 2 kbar after the subtraction of background. The plots for $p = 0.6$, 1.0, 1.3 appear essentially indistinguishable to $p = 1$ atm. (b) The energy integral of the Integrated trace for each pressure measurement, alongside the empirical fit to equation (6.1). Inset: the position of the maximum of the empirical fit (i.e. the E_0 variable) as a function of pressure, showing 95 % confidence intervals which are obtained from the fitting process.

mode softens whilst in Phase I but in Phase II, the phonon is markedly different: higher and more diffuse in energy, as well as less intense. This change is reminiscent of the change to the phonon spectrum on cooling described already, which may be an indication that the unknown Phase II is similar in nature to the cyanide–ordered $I4_1/amd$ phase.

From the pressure dependence of the average phonon energy, I obtain a coarse estimate of the Grüneisen parameter of the low energy mode investigated, $\langle\gamma\rangle$. Interpreting the value of E_0 as an approximation to the mean energy of the low-frequency phonon branches in Cd(CN)2-I, we can fit the equation

$$\log(\langle E\rangle) = -\frac{\langle\gamma\rangle}{B_0}p + \text{const.}, \tag{6.2}$$

which is derived from (1.48), assuming a constant modulus and Grüneisen parameter. B_0 represents the bulk modulus. In this way I obtain the estimate of $\gamma = -14(3)$. Such a large and negative Grüneisen parameter (cf. $\gamma \sim -1$ for ZrW_2O_8, Ref. 422) is similar to the value $\gamma \simeq -20$ determined for the lowest-energy NTE modes using density functional theory calculations [109]. We therefore see that the dynamical model within the quasi harmonic approximation is approximately consistent with the observed pressure induced softening at 300 K. This suggests that the majority of the NTE at this temperature can be attributed to the thermal population of phonons with a negative Grüneisen parameter.

More importantly, since the dynamical calculations neglect the correlated disorder of cyanide pseudospins, these correlations seem not to be crucially important to the NTE. Within the bounds of our experimental error, their inclusion in a model does not seem to be necessary at all at 300 K. However these errors are very large. This is not only true of the statistical error (seen in the confidence interval on $\gamma = -14(3)$), but on the underlying assumptions made by fitting the empirical potential (Eq. (6.1)), integrating across Q over a limited range ($0 < Q < 3$ Å), neglecting the experimental energy resolution, and assuming the linearity of Equation

(6.2). More favourable experimental errors could help resolve this problem.

6.2 Dependence of Lattice Dynamics on Cyanide Order

In an attempt to answer the questions raised in the previous section, we can turn to a more direct probe of the dependence of lattice dynamics on cyanide order. Noting that previous studies have observed the dependence of cyanide order with temperature (§1.1.4) [65, 113], varying temperature should give a more direct probe of this. These studies observed that cyanide orientations undergo an ordering transition at $\sim 140\,\mathrm{K}$, with evidence coming from NMR, scattering experiments and theoretically from a combined DFT and MC study [65]. These studies also found that there is a high degree of correlated disorder in the cyanide orientations over a range of temperatures above the transition. In this section, we will investigate the impact of changing cyanide (dis)order on the lattice dynamics through a combined neuron scattering and molecular dynamics study.

6.2.1 Experimental

Inelastic scattering data were measured using the LET spectrometer at ISIS [§2.1.4]. The same $\sim 1\,\mathrm{g}$ neutron sample was packed into a cylindrical aluminium can. Data were measured with an incident energy of $3.7\,\mathrm{meV}$ and subtracted from an empty can, measured at $180\,\mathrm{K}$. The system was first cooled to $130\,\mathrm{K}$ and measured on warming at $T = 130$, 140, 150, 160, 170, 180, 190, 200, 225, 250, 270 and $300\,\mathrm{K}$ using a CCR. At each temperature the scattering was binned by time-step and we did not observe any time-evolution of the elastic or inelastic scattering.

I show measurements on neutron energy loss in Figure 6.4(a). Compared with the data measured under pressure, the energy resolution of this experiment is much higher: both the resolution and flux of the LET is superior to MARI experiment detailed in the previous section. Additionally, the lack of pressure vessel decreases

the errors due to background subtraction.

6.2.2 Elastic Scattering

I start by plotting elastic scattering in the first pane of Figure 6.4(b). This is integrated between ± 0.2 meV, which corresponds to the resolution of the instrument. The Van Hove correlation function [Equation (2.7)] tells us that we can obtain a time averaged correlation function over a certain time-frame by integrating over time. The timescale of this average is given by the inverse of the energy width that is averaged over [423]. We can therefore understand that this scattering as coming from an average structure over the timescale 0.4 fs. Since the lowest phonon frequency (around 0.5 meV) is resonates with a higher frequency than this, I conclude that diffuse scattering contributions come from a 'quasistatic' (i.e. with dynamics on a much slower timescale than 0.4 fs) contribution. Given what we already know about the correlated cyanide disorder present, it is reasonable to assume that this is the dominating contribution to this signal.

We expect cyanide disorder to be correlated over all temperatures, and therefore show structured diffuse scattering over all temperatures. In the low temperature phase (*i.e.* at 130 K), the system orders with new Bragg peaks at $Q \approx 0.8$ and 1.1 Å^{-1}, corresponding to the R and M distortions from the parent cubic unit cell and $\left\langle \frac{1}{2}\frac{1}{2}\frac{1}{2} \right\rangle$ and $\left\langle 1\frac{1}{2}0 \right\rangle$ reflections respectively (indexed relative to the cubic cell). The distortion at R drives the transition so this peak is stronger. In the cubic phase, these peaks persist as diffuse elastic contributions to the elastic scattering. This provides evidence that diffuse scattering in $Cd(CN)_2$ arises from static contributions and not only from the dynamic contribution of the low energy phonon branch. The peak-width of this branch contains information about the cyanide orientational correlation length in $Cd(CN)_2$ and is analysed in more detail in Section 6.2.4.

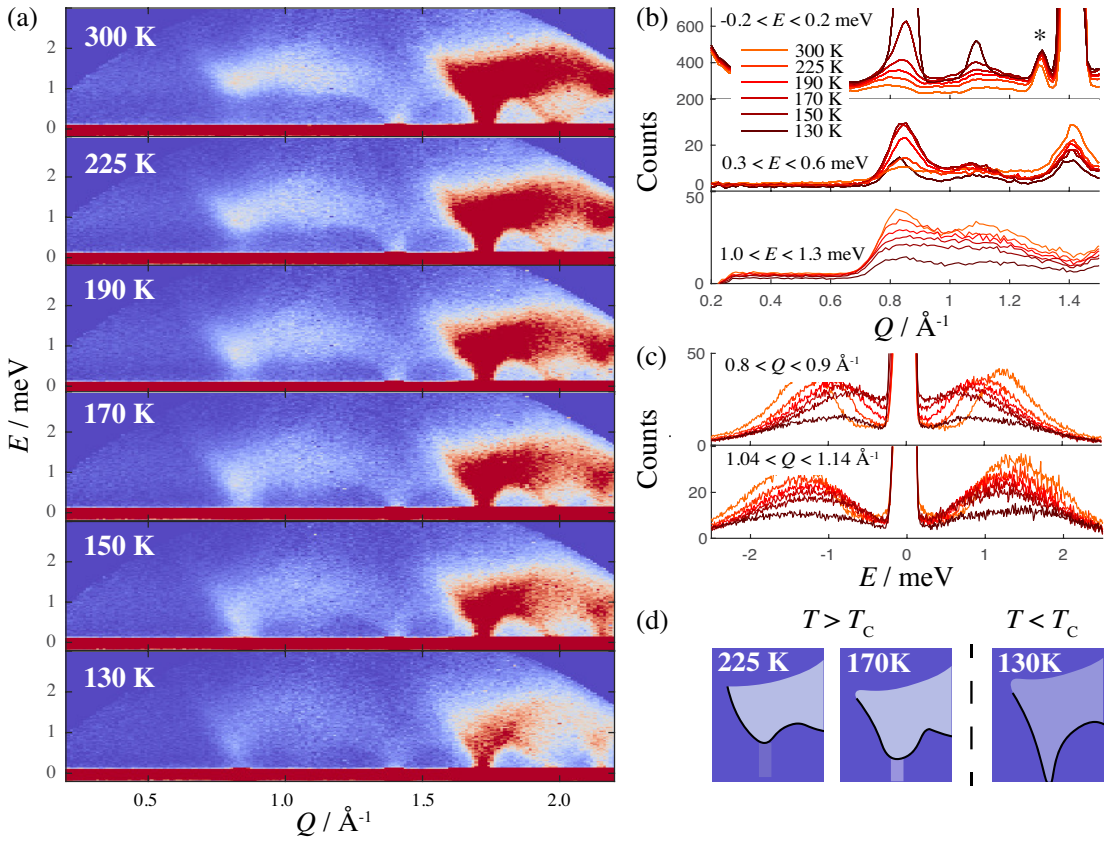

Figure 6.4: (a) Panes of background subtracted inelastic scattering $S(Q, E)$ at various temperatures, shown for neutron energy gain. (b) Energy integrated cuts for selected energy ranges, chosen to highlight the intensity corresponding to inelastic, intermediate and first phonon branches in order. An additional, starred Bragg peak seen at $\approx 1.3\,\text{Å}^{-1}$, arises from a minor $Hg(CN)_2$ impurity which is a consequence of the synthesis [65, 424]. (c) Q-integrated cuts at selected momentum transfers, chosen to include the R- and M-points in the top and bottom panes respectively. (d) Schematic of the temperature dependence of the low-Q region in pane (a).

6.2.3 Inelastic Scattering

The better quality of these data allows us to examine changes to the $S(Q, E)$, which contains information about the dynamics of the system. How should one understand these data? Compared to single crystal $S(\mathbf{Q}, E)$, the data are more complex because at any (Q, E) coordinate there is a contribution from many $\mathbf{Q}$ vectors. An example of this is found near the Γ-points (i.e. the Bragg peaks), where the linear dispersion in $(\mathbf{Q}, E)$ space are projected into (Q, E) space as the cone-like dispersions which emerge from the Bragg positions. In Figure 6.4(a), such

features are seen at $Q \approx 1.4, 1.7$ and $2\,\text{Å}^{-1}$, corresponding to the $\langle 110 \rangle$, $\langle 111 \rangle$, and $\langle 200 \rangle$ Bragg peaks, respectively.

The lowest energy band of $Cd(CN)_2$ in its cubic phase is predicted to show a relatively flat dispersion, with a minimum around the R–point [108]. The phonons are predicted to disperse quadratically around this R–point minimum. There are two R-points that fall within the Q-range ($0 \leq Q \leq 2.2\,\text{Å}^{-1}$) plotted in Fig. 6.4(a). These are at $Q \approx 0.8$ and $2.1\,\text{Å}^{-1}$, corresponding to the $\left\langle \frac{1}{2}\frac{1}{2}\frac{1}{2} \right\rangle$ and $\left\langle \frac{5}{2}\frac{1}{2}\frac{1}{2} \right\rangle$ reflection conditions. At both positions, we find evidence of the this dispersion curve minimum in $S(Q, E)$: the lower edge of the band reaches a minimum at both these values of Q at this temperature. Put another way, the spectrum is 'gapped' for this value of Q.

At high temperature (300 K) the scattering band is well defined. Figure 6.4(c) shows clearly that the maxima in $S(Q \sim 0.8, E)$ around 1.2 meV shows a clear cut gap at around 0.7 meV. In other words, the scattering from this band at this momentum transfer does not extend below this energy at 300 K. This is also the case in Fig. 6.4(c). There is evidence of central mode scattering at this temperature, seen as quasielastic scattering, particularly clear in the lower panel of Fig. 6.4(c). In disordered materials such as paraelectric KDP and high temperature perovskites [425, 426], similar scattering is observed from uncorrelated defects (§1.4.3). Despite the increase in incoherent elastic background scattering seen on decreasing temperature, this feature disappears as the temperature is decreased, indicating that it may be associated with higher energy cadmium environments (CdC_3N, CdN_3C, CdN_4 and CdC_4), which are more prevalent in this temperature range than at lower temperatures [65]. Other than this small deviation, the inelastic scattering is consistent with the VCA picture which described the pressure dependence of scattering in the previous section well: the cyanide orientational disorder appears to have a weak impact on the dynamics.

At low temperature (130 K), the behaviour is as expected for a long-range-ordered crystal. The R-point distortions have by this temperature evolved into strong Bragg peaks at $Q \approx 0.8$ and 2.1 Å^{-1} and corresponding cones of inelastic scattering that emerge from these positions. In the same way as with the behaviour under pressure, the inelastic scattering has moved to higher energy and dropped considerably in intensity. The similarity between the behaviour on the application of field and on compression reinforces the previous hypothesis that Phase II is cyanide ordered in the same way as the low temperature $I4_1/amd$ phase. At this temperature, diffraction indicates that there is some cyanide disorder at 130 K.

Between these extremes, the data show a complex temperature dependence. Firstly, as the temperature is decreased, the whole branch softens in energy. This change is not limited to the R-point, where new Bragg peaks will emerge [Fig. 6.4(a)] and is present also in the $1.04 < Q < 1.14$ Å^{-1} range [Fig. 6.4(c)]. While the energy renormalisation of the whole branch might be related to the changing cyanide orientations, a more likely explanation is that it arises from the anharmonicity of the phonon branch. Our pressure dependant study has given us reason to believe the band is highly anharmonic. The mode also becomes more dispersed and this could be for one or both of the following reasons: (i) the dispersion of the mode covers more energies as a function of $\mathbf{q}$, (ii) the energy width of the mode is increasing on cooling. It is hard to distinguish between these two scenarios using polycrystalline INS alone.

The most striking temperature evolution is found at and around the R-point ($Q \sim 0.8$ and 2.1 Å^{-1}), summarised graphically in Figure 6.4(d). On cooling, the peak softens far more than at other Q positions and there is evidence of the central peak at all temperatures. The feature softens and broadens much more extremely. This bares a similarity to the behaviour exhibited in other soft pseudospin systems discussed in §1.4, namely $K(CN)_{0.5}Cl_{0.5}$ [Fig. 1.21(d-e)].

6.2.4 Estimation of quasistatic correlation length

The prevalence of structured elastic scattering over such a large range of temperatures above the phase transition may be expected due to the frustration inherent to $Cd(CN)_2$. We can test the degree to which Coates and co-workers' model [65] can reproduce the cyanide correlations. Such a test has not been possible using energy integrated diffraction data because it contains a large lattice dynamical contribution. Instead, we use the full-width half maximum (FWHM) as an estimate of the correlation length. We can determine an estimate of the experimental correlation length, assuming a Lorentzian peak shape, with

$$\xi_{\text{exp}} \sim \frac{2}{w_{\text{FWHM}}}. \tag{6.3}$$

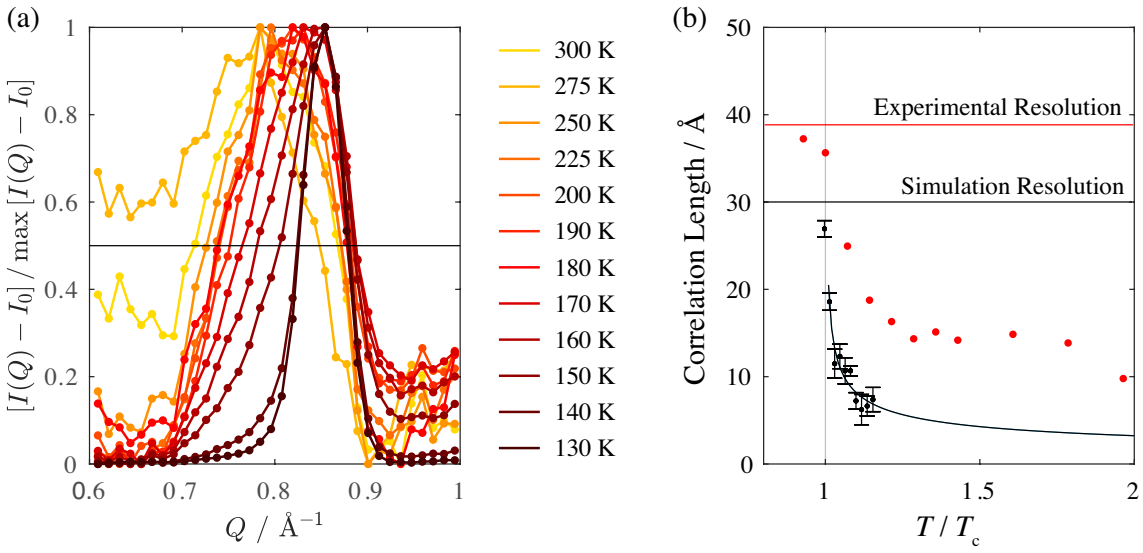

Figure 6.5: (a) Elastic scattering plotted near the emerging Bragg peak at $Q \sim 0.85\,\text{Å}^{-1}$, normalised and zeroed to adjust for incoherent scattering, for each of the temperatures measured. (b) The correlation length extracted from the model of Coates and collaborators [65], shown alongside a fit to Equation (6.4). This is compared with our experimental determination of the correlation length estimated using Equation (6.3). The resolution of the experiment is determined from the Q-width of the $\langle 110 \rangle$ Bragg peak and the resolution of the simulation is taken to be half of the supercell size.

The FWHM can be calculated from the elastic scattering described in section 6.2.2. This is extracted as the width of the feature in Figure 6.5(a). Coates's model correlation length is well fit with the critical relationship,

$$\xi = \xi_0 \left(\frac{T - T_c}{T_c} \right)^{-\nu}, \tag{6.4}$$

where we find that $\xi_0 = 3.32$ unit cell lengths and $\nu = 0.416$, close to the mean-field theory value of $\nu = 0.5$ for an Ising antiferromagnet [145].

These two measures of correlation length are plotted together in Figure 6.5(b). It is striking that the experimental correlation length stays consistently higher than the value simulated for the R-point order of the MC simulation. This seems to indicate that the geometrically frustrated model is not sufficient to explain the quasistatic correlations observed. The form of the behaviour is very different too: decreasing quickly near T_c and then remaining constant at $\xi_0 \sim 15$Å over a large range. This behaviour is reminiscent of the nanodomain correlation length seen in PMN, which remains constant, over a range of temperatures above T_c [See Figure 1.20(b), §1.4.2] [236]. The interpretation of this observation will be discussed in Section 6.5.1.

6.3 Simulating Lattice Dynamics

In order to simulate the lattice dynamics across the experimental temperature range, a technique is needed to describe the disorder in cyanide orientations. My approach

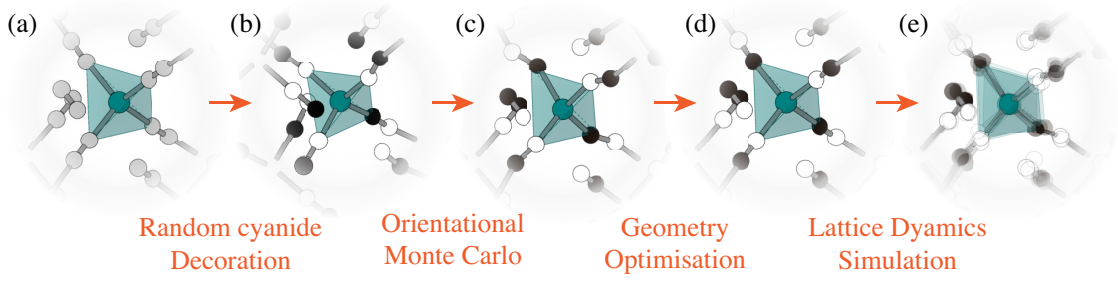

Figure 6.6: A schematic summarising the simulation approach employed, showing the evolution of a local Cd environment through the simulation procedure.

is summarised in Figure 6.6. The first step is to generate a realistic distribution of cyanide orientations. This is achieved in the same way as in Ref. 65: first, a supercell of the ideal cubic structure is generated [Fig. 6.6(a)] the random cyanide decoration is generated [Fig. 6.6(b)] and an orientational MC simulation is performed using the Hamiltonian (Eq. 1.40) to generate realistic distributions of cyanide orientations [Fig. 6.6(c)]. We know from Ref. 65 that the supercells generated at this stage will have local cadmium environments consistent with experiment across the high temperature phase.

To introduce lattice dynamics to this model, I follow the SCLD procedure laid out in the methodology (§2.6.4). From the starting models, I perform a geometry optimisation to generate a set of static structures [Fig. 6.6(d)] with varying degrees of cyanide order as a function of temperature. The dynamics in this system [Fig. 6.6(e)] can be probed in the harmonic approximation by calculating the phonon frequencies and eigenvectors, which can be directly examined. These phonons can then be projected out *via* Equation 2.27 to give $S(\mathbf{Q}, E)$ and applied a polycrystalline average. This can be compared with experiment and the phonons analysed directly.

In a supercell dynamics calculation, the $\mathbf{Q}$-resolution is inversely proportional to the supercell grid chosen so we need a large supercells (approximately $6 \times 6 \times 6$ of the parent cubic structure, i.e. 2160 atoms) which makes a dynamical DFT simulation prohibitively expensive. For this reason, I fit a molecular dynamics forcefield to make this approach computationally viable, rather than calculating within DFT directly.

6.3.1 Force-field fitting

The forcefield (FF) fitting process I have followed is based on that used for $Zn(CN)_2$ in Ref. 325 and summarised in Section 2.6.3. A few important modifications are made to the methodology to ensure that the forcefield reflects (i) the metal off-centring which is central to the physics of the system [113], (ii) our experimental

measurement of the vibrational energy-scale, and (iii) the cyanide dipole moment (which appears to be important for interframework slipping).

First, a DFT optimisation was carried out using the PBE functional with D3 dispersion corrections [327]. In Ref. 325, these optimisations are carried out on $[M(CN)_4]^{2-}$ and $[M(NC)_4]^{2-}$ clusters. Instead, I use a mixed-orientation cluster for this fitting procedure since the 2–in–2–out geometry of $[Cd(CN)_2(NC)_2]^{2-}$ is required to extract information about cadmium off-centring.

Charges

We want the charge in our model to reflect two key features of the DFT system: (i) charge separation between Cd-CN and (ii) the correct CN dipole moment. The two features are accessed *via* (i) an 'atoms in molecules' (Bader) approach—which uses a minimum charge density surface to partition charge [§2.6.3] [329]—and (ii) matching the dipole moment of an isolated CN anion, which is equal to 1.0 D. Bader analysis alone gives

$$q_{\mathrm{C}} = +0.708, +0.714, \quad q_{\mathrm{N}} = -1.428, -1.530, \quad q_{\mathrm{Cd}} = +1.07. \tag{6.5}$$

Two values of charges for C and N arise because of the different environment of the Cd-CN. These numbers give a similar metal–cyanide charge separation to that obtained by Fang and coworkers [325] for $Zn(CN)_2$, *viz.*

$$q_{\mathrm{C}} = -0.21, \quad q_{\mathrm{N}} = -0.36, \quad q_{\mathrm{Zn}} = +1.14. \tag{6.6}$$

The strength of the cyanide dipole moment calculated using the 'atoms in molecules' approach is unrealistic. It seems that this is because the highly covalent nature of the C≡N bond leads to a skewed charge distribution, which is poorly handled by the technique.

The solution used here is to use Bader analysis for the Cd/CN partition (which will be effective given the moderate covalency of the Cd–X bond) and choose the

C/N charge separation to reflect the known (1.0 D) dipole moment. This strategy gives

$$q_{\mathrm{C}} = -0.18, \quad q_{\mathrm{N}} = -0.35, \quad q_{\mathrm{Cd}} = +1.07. \tag{6.7}$$

In the following analysis, I use the numbers in Equation (6.7).

Cd–X stretch

In order to extract the forcefield associated with Cd–X stretching (X = C or N), we perform a scan which fixes all bond–lengths and angles apart from the Cd–X coordinate. The energy landscape is well described as an electrostatic term,

$$E_{\mathrm{el.}}(r_{\mathrm{CX}}) = \frac{1}{2 \times 4\pi\epsilon_0} \sum_{i>j} \frac{q_i q_j}{r_{ij}}, \tag{6.8}$$

involving the charges in (6.7) together with a Morse potential. The model thus involves the four parameters D_e, α, r_e, and E_0, which encode the dissociation energy of the bond, intrinsic length-scale, equilibrium length, and a zeropoint energy, respectively. The potential takes the form,

$$E(r_{\mathrm{CX}}) = D_e \left[1 - \exp -\alpha \left(r_{\mathrm{CX}} - r_e\right)\right]^2 + E_{\mathrm{el.}}(r_{\mathrm{CX}}) + E_0. \tag{6.9}$$

This procedure was carried out in turn for the Cd–C and Cd–N stretches, yielding values [Table 6.1], which are similar to those obtained in other simple inorganic systems [427]. The data and corresponding fits, which well reproduce the quantum mechanical calculations, are shown in Figure 6.7(a).

X	D_e / eV	α / Å^{-1}	r_e / Å
C	2.0145	1.5127	2.1546
N	1.8037	1.5862	2.1526

Table 6.1: Values obtained by a least squares fit to equation (6.9). The higher value of D_e for C reflects its stronger covalent nature.

Cd–X–Y bend

Similarly, we can flex the Cd–X–Y angle without affecting the other atomic coordinates. For simplicity, let us consider only flexing closest to the nearest cyanide. In general, the energy dependence of the DFT simulation will depend on the torsion angle of Z–Cd–X–Y. For simplicity, this dependence is ignored and the theta angle is defined as being towards the nearest cyanide group.

Fits of the form

$$E\left(\theta_{\mathrm{CdXY}}\right) = \frac{k_{\mathrm{CdXY}}}{2}\left(\theta_{\mathrm{CdXY}} - \pi\right)^2 + E_{\mathrm{el.}}\left(\theta_{\mathrm{CdXY}}\right) + E_0. \tag{6.10}$$

are shown in Figure 6.7(b) and the extracted values in Table 6.2.

X–Cd–Y bend

Unlike the previous coordinates, it is impossible to separately probe each of the three X–Cd–Y bending angles (X,Y = C or N), while fixing the others. For this

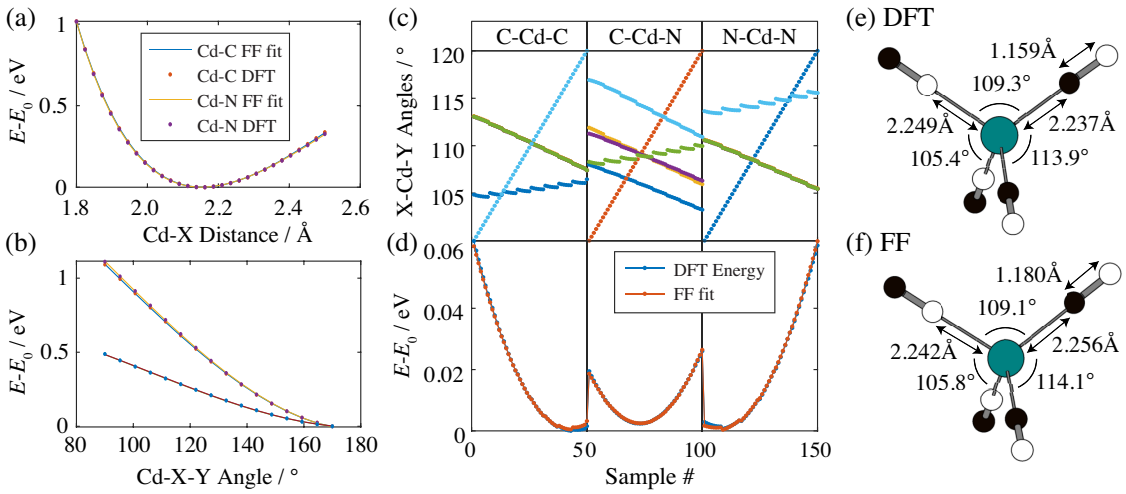

Figure 6.7: Fitting procedure for the molecular forcefield: (a): Fit of equation (6.9) to energy predicted by DFT after electrostatic subtraction. (b) Fit of equation (6.10) to energy predicted by DFT after electrostatic subtraction. (c) Each of the six X-Cd-X angles in constrained optimisation fixing the C-Cd-C angle (between sample 1 and 50), the C-Cd-N angle (#51–100) and the N-Cd-N angle (#101–150). (d): Fit of equation (6.11) to DFT energies which correspond to the angles in (c). (e) and (f): Comparison of DFT and MD geometry optimised structures.

X	Y	k_{XCdY} / eV rad^{-1}	Θ_{XCdY} / deg
C	N	1.0387	118.4907
N	C	1.0666	101.7548

Table 6.2: Values obtained by a least squares fit to equation (6.10).

reason a co-refinement of all three angle–forcefields is necessary. DFT simulations with varied values of the $\theta_{i\mathrm{Cd}j} \in \mathrm{X}_i\mathrm{CdY}_j$ bending angles are performed subject to fixing one of the angles and allowing the remaining six angles to vary in a geometry optimisation. This procedure is repeated, with the C–Cd–C, C–Cd–N, and N–Cd–N angles varied in turn to generate 150 configurations with changing geometry and energy, as summarised in Figure 6.7(c) and (d), respectively.

$$E\left(\{\theta_{i\mathrm{Cd}j}\}\right) = \sum_{i,j\in \mathrm{X}_i\mathrm{CdY}_j} \frac{k_{\mathrm{XCdY}}}{2}\left(\theta_{i\mathrm{Cd}j} - \Theta_{\mathrm{XCdY}}\right)^2 + E_{\mathrm{el.}}\left(\{\theta_{i\mathrm{Cd}j}\}\right) + E_0. \qquad (6.11)$$

This model has seven parameters: $k_{\mathrm{CCdC}}, k_{\mathrm{CCdN}}, k_{\mathrm{NCdN}}, \Theta_{\mathrm{CCdC}}, \Theta_{\mathrm{CCdN}}, \Theta_{\mathrm{NCdN}}, E_0$. By symmetry, it is clear that $\Theta_{\mathrm{CCdN}} = 109.47°$. Including this as a constraint reduces the number of free parameters to six. Equation (6.11) was fitted to the data and the final fit [Fig. 6.7(d)] shows good agreement to the data.

X	Y	k_{XCdY} / eV rad^{-1}	Θ_{XCdY} / deg
C	C	1.0387	118.4907
N	N	1.0666	101.7548
C	N	1.0016	109.47*

Table 6.3: Values obtained by a least squares fit to equation (6.11). The starred value is fixed by constraint.

Molecular models

Reassuringly, performing a geometry optimisation on the molecular $[\mathrm{Cd(CN)_2(NC)_2}]^{2-}$ anion gives an essentially similar geometry to that optimised by DFT. This point is made clear in Figure 6.7(e-f), which shows that the DFT-optimised anion has essen-

tially equivalent geometry to that of the anion optimised within the parametrised forcefield.

Interframework dispersion interaction

Ref. 325 also needed to include a dispersion interaction to simulate $Zn(CN)_2$: in that case the interaction took the form of a Buckingham potential between frameworks, extending up to 20 Å. This potential was parametrised from previous work on polypeptides. To reduce the number of parameters, I use a Lennard–Jones potential to achieve the same goal:

$$E = \sum_{r_{ij}<r_{\text{cut}}} A \left[\left(\frac{r_e}{r_{ij}} \right)^{12} - 2 \left(\frac{r_e}{r_{ij}} \right)^{6} \right], \tag{6.12}$$

with $r_{\text{cut}} = 30$ Å. Because the inter-framework interaction is more important in $Cd(CN)_2$ than in $Zn(CN)_2$ (the strength of this interaction governs the amount of inter-framework distortion), we take a semi-empirical approach to parametrising this equation.

This approach—detailed in Figure 6.8—uses two experimental measurements to fix the two parameters A and r_e, searching over their values using a grid search. These experimental measures are chosen to fix the phonon stability of the high temperature phase *via* the R–point energy and the extent of lattice distortion in the low temperature phase. The meaning of the second observable is clarified in Fig. 6.8(a). In the low temperature phase, the two frameworks slip against each other, in a $2 \times 2 \times 2$ supercell; this leads to a difference in the cadmium atoms' z position between each sublattice. At the lowest experimental temperature, this difference is 0.82 Å—as determined by powder neutron scattering [65], to which the values of A and r_e are sensitive [Fig. 6.8(b)]. This constraint on the parameters can be combined with a constraint on the energetics of the system to determine the pair of parameters which fits both observations [Fig. 6.8(c)]. The R–point energy is extracted to correspond to the lowest extent of the neutron scattering profile which

corresponds to $0.8 < Q < 0.9$ Å, which is 0.69 meV [Fig. 6.8(d)]. This will, by proxy include some of the effect of anharmonicity into rescaling the R-point energy and is certainly a significant approximation.

Combining equations (6.7)–(6.12), I obtain the forcefield model that I will use for the remainder of this chapter.

As a test of the quality of this parametrisation, I calculate the dispersion curves for a cyanide ordered model which has been previously investigated *via* DFT [110]. This model involves half of the cyanides having a CdC_4 environment and the other

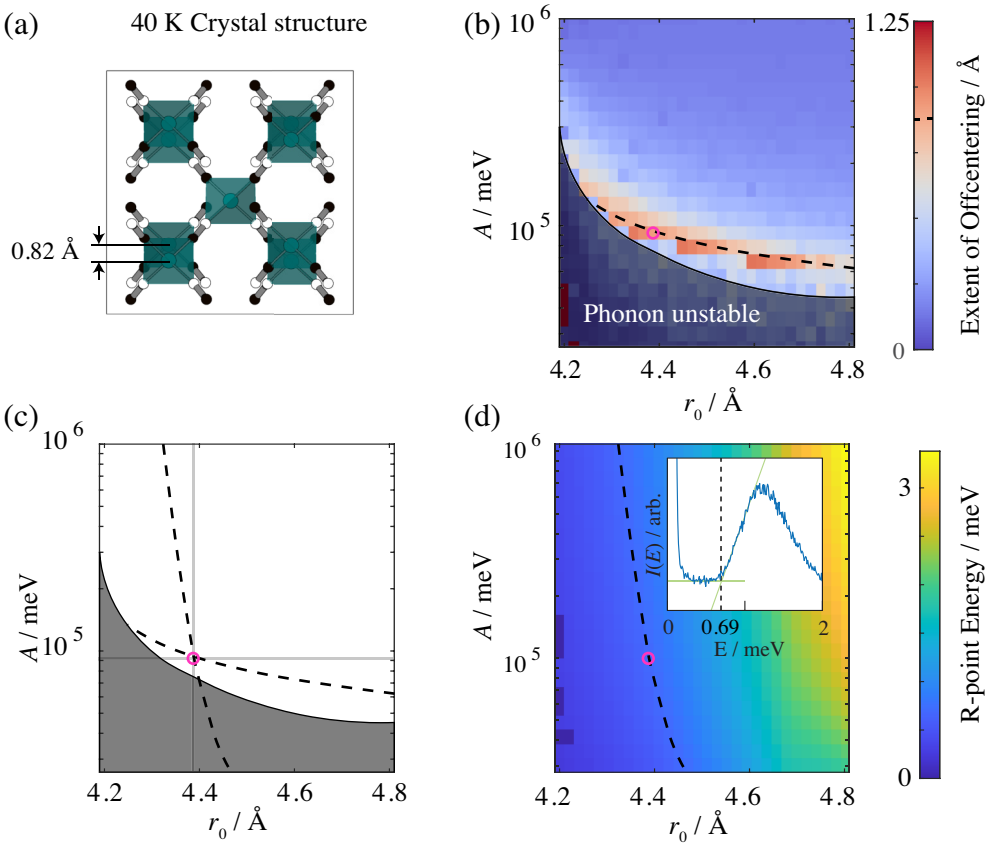

Figure 6.8: Figure detailing the parametrisation of equation (6.12). (a) A supercell of the refined 40 K crystal structure of $Cd(CN)_2$ from neutron diffraction [65]. C atoms are shown in black, N in white, and Cd in green. The extent of slipping between the frameworks is parameterised via the difference in z coordinate of the Cd in each framework. (b) The variation of simulated distortion extent with parameters. The region that is greyed hosts negative phonon frequencies so is ruled out. Dotted line corresponds to agreement with experiment. (c) A schematic showing the intersection between the two criteria. (d) The variation of VCA R-point energy with the two parameters. The inset shows the extraction of the parameters.

half having a CdN_4 environment ('4-in-4-out')—not a very physical model. Nevertheless, we can use this as a simple test case for the forcefield. I simulate dispersion curves using GULP to optimise the same unit cell investigated. A comparison between my results and the previous DFT study [110] are shown in Figure 6.9 and reveal that my model does a reasonably good job of reproducing the form of the dispersion in this ordered form of $Cd(CN)_2$. It is of note that the phonon energies are on different scales: the forcefield model seems to be considerably harder than DFT simulation. Given my approach to parametrisation, this is unsurprising. In a molecular anion the repulsion is likely to be much stronger than in the solid state so we do not expect to capture the energy of this band perfectly.

6.3.2 Monte Carlo

The Monte Carlo simulation described in Section 1.1.4 was used to generate supercell configurations as a function of temperature. Following the procedure described in Ref. [65], I generated 6×6×6 supercells decorated with Heisenberg pseudospins. The

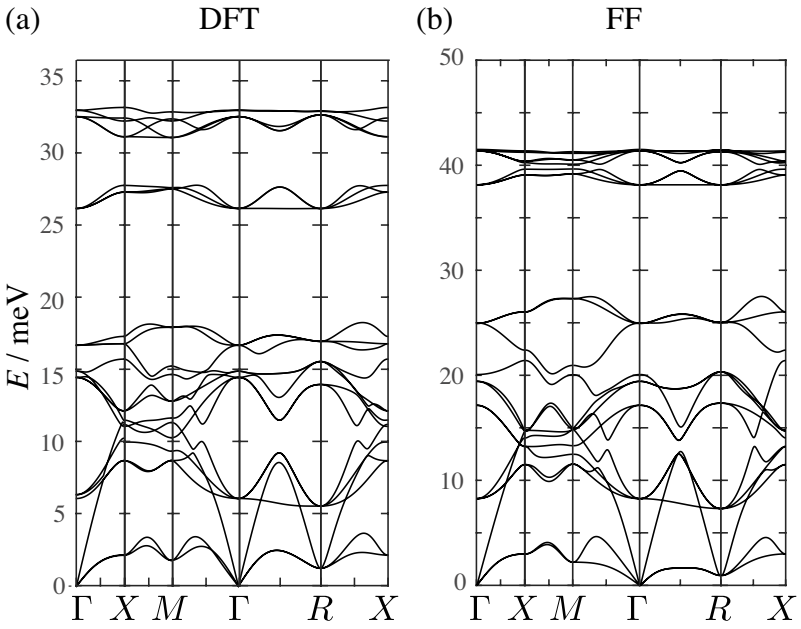

Figure 6.9: Comparison between 4-in-4-out ordered ground state when simulated via (a) DFT [110] and using (b) the forcefield described in the text.

configurations were evolved using a Metropolis Algorithm under the Hamiltonian of Equation (1.40). Simulations performed on cooling at 25 temperatures were distributed logarithmically between $T_{\mathrm{MC}} = 300$ and 80 K. At each temperature 20 samples were produced with 20,000 accepted moves between simulations.

In order to understand the role of nanodomain formation in these simulations, larger configurations were also needed. The procedure described was repeated for larger $4 \times 4 \times 24$ simulations, with a z-coordinate of ~ 150 Å, large enough to allow for multiple nanodomains of ~ 20 Å within a single configuration. This simulation was run with the same temperature grid as for the smaller configurations, but with another, finer temperature grid with 25 samples logarithmically distributed between 150 and 100 K to interrogate this regime further.

Heat capacity was calculated from the variance in the internal energy of the configurations, revealing a transition at $T_{\mathrm{c}}^{\mathrm{MC}} \simeq 130$ K, in agreement with the value reported by Coates *et al.* The exact temperature of this transition showed some size dependence, with a value of 127(1) K for the $4 \times 4 \times 24$ supercell and 132(4) K for the $6 \times 6 \times 6$ supercell. I calculate an order parameter at the R-point ($\mathbf{k} = \left[\frac{1}{2}, \frac{1}{2}, \frac{1}{2}\right]$), defined as

$$\Phi\left(T_{\mathrm{MC}}\right) = \frac{1}{N}\left|\sum_{j \in \mathrm{spins}} \mathbf{S}_j \exp\left(2\pi \mathrm{i} \mathbf{r}_j \cdot \mathbf{k}\right)\right|^2, \tag{6.13}$$

where N is the number of atoms. This parameter shows its greatest increase at T_{c} confirming that the phase transition has this ordering vector.

6.3.3 Geometry Optimisation

The spin vectors produced by the Monte Carlo simulations set the orientation of the cyanide ions in subsequent molecular dynamics simulations. This is done by projecting the spin vector along the anisotropy direction and positioning the cyanide in one of the two possible Ising pseudospin orientations for the local environment. This approach loses information about the orientation of the pseudospins but preserves their general orientation.

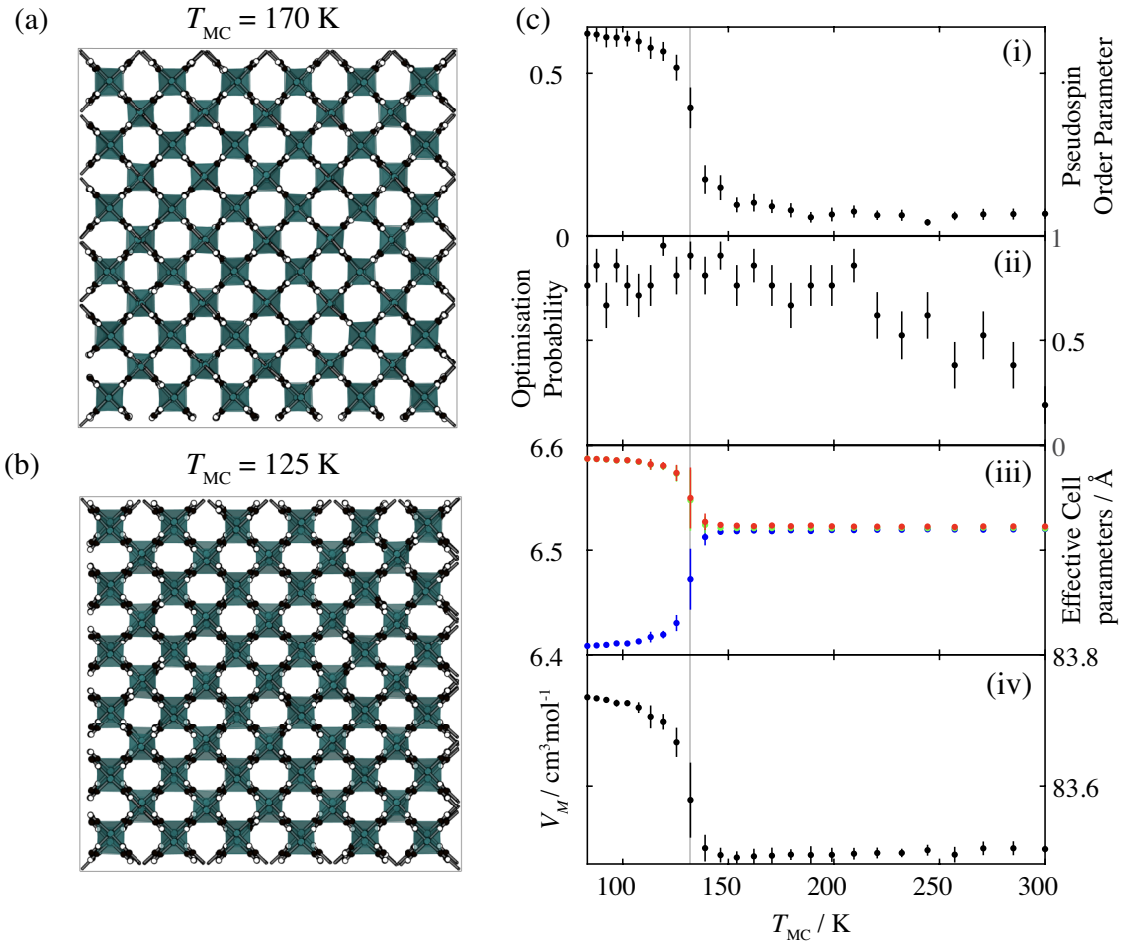

Figure 6.10: Relaxed $6 \times 6 \times 6$ supercells of $Cd(CN)_2$ generated as detailed in the text, and their variation as a function of MC temperature. View along the a direction in (a) the cubic and (b) the tetragonal phases. (c) Structural parameters plotted as a function of Monte Carlo temperature, averaged across 20 configurations per temperature. From top to bottom: (i) the order parameter defined in Eq. (6.13); (ii) the probability that a configuration will meet the $G_{\mathrm{norm}} < 5 \times 10^{-4}$ condition after 1000 cycles; (iii) the effective cubic cell parameter defined as one sixth of the supercell parameter and (iv) the corresponding molar volume. For the top two plots error bars indicate uncertainties in the value while for the bottom two they correspond to the spread of values.

Input files for GULP were generated for each of the 20 configurations at each of the 25 temperatures simulated for the $6 \times 6 \times 6$ supercell. Geometry optimisations were performed on these supercells using the forcefield detailed in Section 6.3.1. GULP uses an augmented Newton-Raphson approach to optimise unit cells [316]. A measure of the completeness of this optimisation is the final value of G_{norm}. It is especially important to ensure that this value is low for dynamical calculations as

these assume a local minimum in the internal energy landscape. Simulations were run in parallel on 20 cores and take ~ 80 hours on the Arcus supercomputer for a maximum of 1,000 optimisation cycles. By the end of this procedure, about 50 % of the simulations had optimised with low final forces. Some simulations fail to optimise after ~ 50 cycles and end with very low G_{norm} values.

A cutoff of $G_{\mathrm{norm}} < 5 \times 10^{-4}$ was chosen and configurations which optimised to higher than this value were rejected. It is possible that this approach introduces a bias into our results. If there is some property of pseudospin orientations which makes geometry optimisation more difficult, then this quality will be systematically excluded from our subsequent simulations (for example, highly strained local environments). There is some indication that this may play a role: although the optimisation probability is very high ($\sim 80\,\%$) around the phase transition it dips much lower as T increases above 200 K. This may indicate that the higher energy environments which do not obey ice rules cause some difficulties for the geometry optimisation. The relatively high acceptance ratio around the transition however, suggests that selection bias is not playing a major role in this temperature range.

The optimised structure shows a well defined evolution with T_{MC}, which largely follows the order parameter. Figure 6.10 shows that the optimised structure undergoes the same structural change as a function of Monte Carlo temperature as that seen experimentally. Pane (a) shows that in the absence of long-range cyanide order, while local distortions from the cubic structure exist, the average structure stays cubic. On cooling through the phase transition, the simulation undergoes the collective distortion seen in Pane (b) of the Figure, which is realised as a decrease in one lattice parameter and an increase in the other two. We have already parametrised the forcefield to ensure the correct extent of lattice slipping in the ordered state, but it should be reassuring that this extends to states of the system (e.g. at 125 K), where order is incomplete.

The same calculation was run for the $4 \times 4 \times 24$ supercells, now limited to four

temperatures, 80, 130, 140 and 200 K due to time constraints. The resulting geometry optimisation took a similar time ($\sim$ 100 hours) to complete 1000 optimisation cycles, but ended with a much lower chance of meeting good optimisation criteria. For the same $G_{\mathrm{norm}} < 5 \times 10^{-4}$ criterion used for the smaller supercells only a very few simulations would be viable. It was therefore optimal to loosen this criterion slightly to $G_{\mathrm{norm}} < 5 \times 10^{-3}$, yielding 2, 2, 3, and 5 successful optimisations out of 20 at 80, 130, 140 and 200 K, respectively. It is again important to note that discarding configurations which struggle to optimise may be adding a bias into our analysis.

The cell parameters vary with T_{MC} in the same way as the pseudospin order parameter. This can be seen in, Fig. 6.10(ciii), where the effective cubic cell length is calculated from the optimised cell parameters of the $6 \times 6 \times 6$ supercells. On passing through the transition the change in the shortest cell parameter is $-1.74\,\%$ while the other two lattice parameters increase by $1.0\,\%$. These changes almost exactly cancel out, resulting in a volume change of $+0.27\,\%$, going from the high to low temperature phase, indicating the cyanide disorder can account for some subtle NTE. The relevant experimental values show a qualitatively similar picture: the tetragonal distortion does indeed involve one lattice parameter shrinking and two expanding. The values are taken from Rietveld refined neutron scattering data [65], comparing the refined cell parameters at 140 K to that at 10 K, indicate $+1.58\,\%$ and $-0.56\,\%$ changes for a and c lattice parameters respectively, accounting appropriately for the change in unit cell orientation. The experimental volume change is $+2.05\,\%$, an order of magnitude more NTE than predicted from the equilibrium cell parameters. It is therefore clear that in order to properly account for NTE in this material, we must move to a dynamical calculation.

6.3.4 Correlated Pseudospin Disorder

Some insight has already been reached by Coates and coworkers about the nature of correlated disorder in the disordered phase of $Cd(CN)_2$ but our $4 \times 4 \times 24$ supercells

give a unique opportunity to understand the domain structure of such simulations. I take a similar approach to the local magnetisation calculated *via* Equation (5.5) in the previous chapter to define a local pseudospin order parameter, which encodes the directionality of the local order present.

$$\mathbf{N}_{\text{loc.}}(\mathbf{R}) = \left[\sum_{i\in\text{sites}} w(|\mathbf{r}_i - \mathbf{R}|)\mathbf{S}_i \exp 2\pi \mathrm{i}\mathbf{r}_i \cdot \mathbf{k}\right] \Big/ \left[\sum_{i\in\text{sites}} w(|\mathbf{r}_i - \mathbf{R}|)\right] \tag{6.14}$$

where the same weight function in (5.6) was used in order to reproduce local ordering.

The resulting pseudospin disorder is plotted in panes **A**, **D**, **G**, and **K** of Figure 6.11 and reveals that, unsurprisingly, complete order exists at low temperature, captured by co-aligned $\mathbf{N}_{\text{loc}}$ vectors. At intermediate temperatures this structure breaks into smaller ordered domains which sit in amongst regions of lower order. At $T = 200\,\text{K}$ any order largely becomes far weaker, although since the vectors in Figure 6.11 are normalised to their maximum value, we still see some pockets of local order.

The structures of frame **D** and **G** exhibit hierarchical order on multiple length-scales. On the smallest length-scale one can understand the structure relatively simply: most environments consist of local 'two-in-two-out' environments, which are geometrically similar to the gas phase model used in parametrisation [Fig. 6.7(f)]. When one zooms out however, a larger structure emerges simulations, as shown in Figure 6.11**D** and **G**: multiple domains exist with local order in different directions. A similar observation can be made about the relaxor ferroelectrics [428], where polar nanodomains are central to understanding the behaviour of systems in a way overlooked by conventional crystallographic analysis [429]. This raises a central question of the study: how does this changing nanostructure interplay with the dynamics?

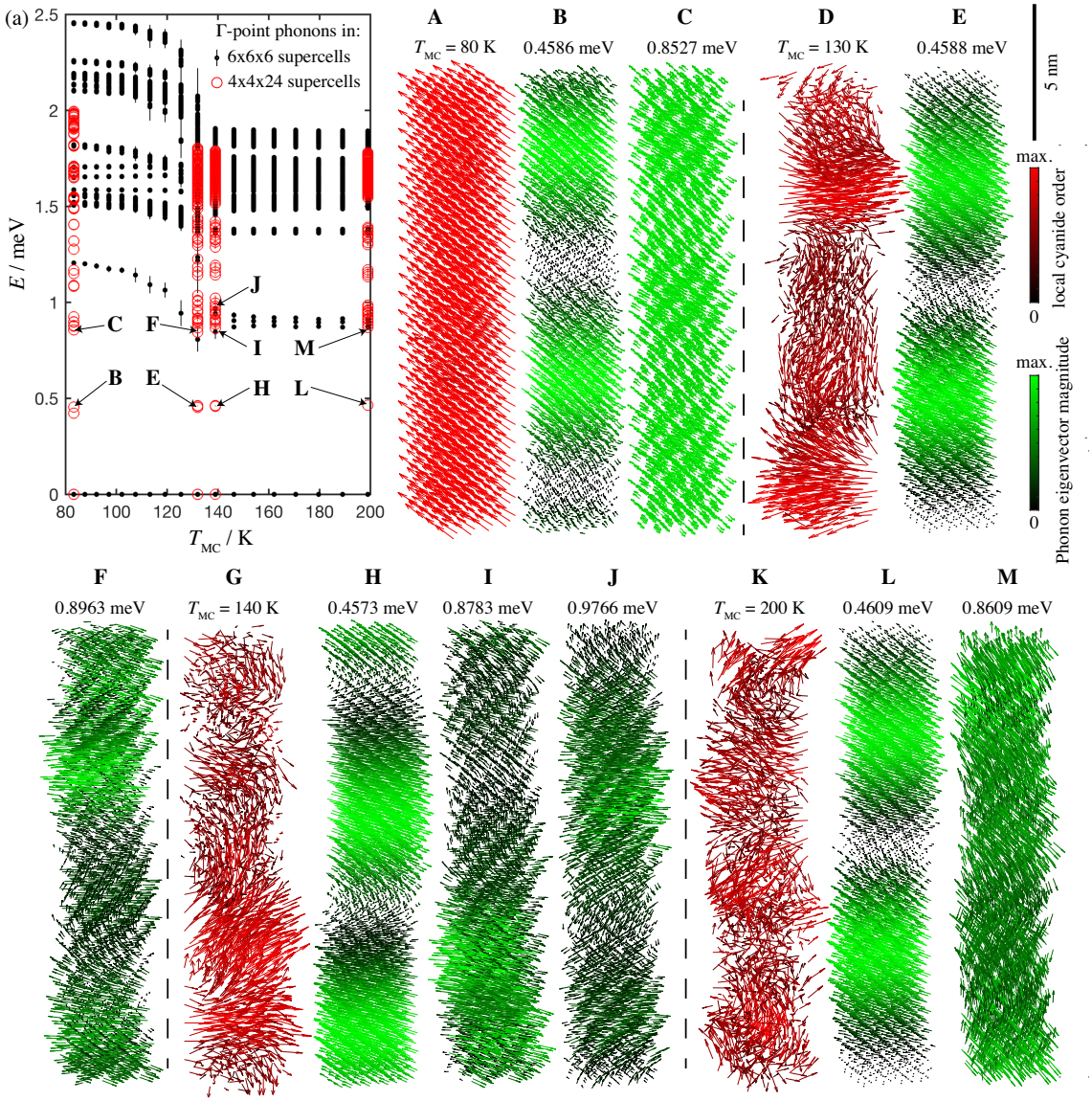

Figure 6.11: Direct examination of Γ-point phonon eigenvalues and eigenvectors, compared with local correlation functions. Top-left: plot of the first 300 phonon eigenvalues as a function of MC temperature. For $6 \times 6 \times 6$ supercells, eigenvalues are plotted in black, with dots representing the average value and bars representing the spread of values across simulations. For the larger $4 \times 4 \times 24$ simulations, for which far fewer meet our optimisation requirement, all phonon energies from each configuration are plotted with red circles. We go on to examine some selected eigenvalues for the $4 \times 4 \times 24$ simulations (shown in green plots **B**, **C**, **E**, **F**, **H**, **I**, **J**, and **M**) at all four temperatures investigated, comparing them with the local structure factor (shown in the red plots **A**, **D**, **G**, and **K**).

6.3.5 Supercell Γ-point Dynamics

In order to understand this relationship, I turn to the the supercell lattice dynamics method outlined in Section 2.6.4. This allows us to understand the dynamical

behaviour of the model within the harmonic approximation. To start, I used GULP to calculate the phonon eigenvectors and eigenvalues at the Γ-point of geometry-optimised supercells. This calculation is faster than the geometry optimisation, taking ~ 40 mins and 1 hour for the $6 \times 6 \times 6$ and $4 \times 4 \times 24$ supercells, respectively, with the same computational resources.

The changes in phonon frequency are plotted in Figure 6.11(a) for the first 300 modes in both supercell types and shows a clear dependence on cyanide order. The phonon energies renormalise with a clear dependence on the cyanide order parameter. While this is generally the case, some modes vary more than others with cyanide long-range order. This result is perhaps unsurprising given the large structural distortion seen in Figure 6.10. Most dramatically, the lowest energy R-point frequency increases from $E \simeq 0.8$ to $\simeq 1.3\,\mathrm{meV}$. We will see how this large renormalisation of phonon energies has significant implications for the thermodynamics in this model of $Cd(CN)_2$. The mode energies seem to change remarkably little at $T > T_c$ but appear to become more spread out as $T \to T_c$. This could reflect a growing variety of local environments within the crystal as nanodomains form.

Figure 6.11 also demonstrates that the phonon eigenvectors are acutely sensitive not only to the long-range order but also the type of short-range order that is present in configurations. In order to understand the relationship between the short-range order described in section 6.3.4, I have plotted some low energy modes of the $4 \times 4 \times 24$ supercell simulation alongside the local order parameter shown in frames **A**, **D**, **G**, and **K**. I have chosen modes which are representative of two important categories of low–frequency modes: **B**, **E**, **H** and **L** are near-Γ modes which are responsible for acoustic transport, as well as the R–point modes plotted in frames **C**, **F**, **I**, **J**, and **M** which are intrinsically tied to the observed phase transition. In frame **A**, at the lowest temperature, the structure is fully periodic, and the modes shown in frames **B** and **C** are delocalised. In the intermediate temperature regime shown in **D** and **G** where the temperature is only slightly above

T_c, domains form in the simulation. The lowest energy modes at $E \sim 0.4\,\text{meV}$ are largely indifferent to the short-range order. By contrast, the R-point modes at $E \sim 0.8\,\text{meV}$ seem to localise within the nanodomains at intermediate temperature (**F**, **I** and **J**). For $T_{\text{MC}} = 200\,\text{K}$ ($T \gg T_c$), short-range order is weak and the modes have apparently returned to being delocalised as is shown in frame **M**. This changing nature of phonon eigenvectors has implications for the negative thermal expansion of the system—"How do the mode Grüneisen parameter change with T_{MC}?"—and also effects the type of inelastic scattering measured—"how does the localisation effect $S(Q, E)$?".

The observation of phonon localisation within antipolar nanodomains at far larger scale than the unit cell is reminiscent of phonon localisation within the polar nanodomains of relaxor ferroelectrics [242]. Domain-wall localised phonons have been directly observed *via* multimode microscopy [430] and simulated in understanding the behaviour of domain walls in $BiFeO_3$ [430, 431]. Localisation has been studied at heterojunctions [432]. Looking beyond the atomistic scale, phonons have been observed localising at large scale defects such as dislocations [433, 434] and disinclinations [435] in mechanical model systems and materials. In all of these systems, a picture emerges of localisation changing the phonon transport processes from acoustic to balistic type transport but the understanding of the impact of this type of behaviour for thermal expansion is still in its infancy.

6.4 Simulation of INS

In this section I will attempt to find signatures of the R–point phonon localisation noticed theoretically in the previous section in the INS simulations. In order to do this I will use the supercell unfolding technique of simulating inelastic scattering discussed in Section 2.6.4. I will start by simulating single crystal inelastic scattering because (a) the simulation of this quantity is easier, each point only requiring one Q vector rather than a polycrystaline average, and (b) the analysis is easier: at any given coordinate in $(\mathbf{Q}, E)$ space, only one $\mathbf{Q}$ vector is contributing.

6.4.1 Single Crystal Simulations

We are interested in the behaviour of phonons around the $\mathbf{Q} = \frac{2\pi}{a}\left[\frac{1}{2}, \frac{1}{2}, \frac{1}{2}\right]$ point around which the anomalous behaviour reported in section 6.2.3 emerged. I start by investigating signatures of this phenomenon in the phonons at the supercell Γ-point by calculating $S(\mathbf{Q}, E)$. The best $\mathbf{Q}$ resolution is offered by the $4 \times 4 \times 24$ simulations. We are particularly interested in the behaviour around the cubic unit cell's R-point. The best resolution which intersects this point is along the R–M line, along which we can sample 12 points.

The Bose normalised inelastic neutron scattering is calculated from equation (2.27) and is shown in Figure 6.12. My first observation is the form of the scattering stays for the most part constant in the high temperature phase. On passing into the low temperature phase $S(\mathbf{Q}, E)$ changes considerably in form, with a new Γ-point at the previous R-point leading to the new low frequency scattering.

While the most significant change in Figure 6.12 is seen between the high and low temperature phases and a consequence of long-range cyanide order, there are some important changes present which relate to changing cyanide *disorder*. The most obvious, and perhaps relevant to our experimental observations is the emergence of additional scattering intensity at the R-point and $E \simeq 0.4\,\text{meV}$. The separation of this feature from the band is a finite size artefact resulting from the fact that spacing of low frequency being larger than the energy bin size chosen for plotting $S(\mathbf{Q}, E)$ maps. In a larger simulations, the feature seen here would likely resembles a waterfall of continuous scattering from the R-point at $E \simeq 0.4\,\text{meV}$ down to the elastic line. A more subtle change can be seen in the slight $\mathbf{Q}$-broadening of the R-point feature at $E \simeq 0.8\,\text{meV}$. Indeed, at 130 K this feature splits into two maxima, although given the very poor statistics in this simulation (we only have two simulations to probe), it is hard to say whether this is real or an artefact of the specific configuration present.

I investigate this feature further in the bottom two panes of Figure 6.12, which

plots the intensity at the frequency corresponding to these modes. I test the strategy employed by Manley and co-workers [242] for understanding phonon localisation in polar domains. Following the approach taken in this paper, I fit the localisation formula, based on the observation by Anderson and others that phonons are localised with exponentially decaying eigenvalues [203, 243], to the simulated $S(\mathbf{Q}, E)$ at these two energies.

$$S_{\text{loc}}(\mathbf{q}, E_0) = \frac{I_0}{1 + (2\pi\zeta_{\text{loc}})^2 \left|\mathbf{q} - \mathbf{q}_0\right|^2}, \tag{6.15}$$

where I_0 encodes the strength of scattering and ζ_{loc} is the localisation length. If we make the assumption that the only signal contributing to $S_{\text{loc}}(\mathbf{q}, E_0)$ $\mathbf{q}_0$ is localised with the vector $\mathbf{q} = \frac{2\pi}{a}\left[\frac{1}{2}, \frac{1}{2}, \frac{1}{2}\right]$, the fits and values found in the Figure 6.12 can be obtained. The approximation clearly breaks down at $T < T_c$, since it is clear that as a result of long range symmetry breaking, multiple $\mathbf{q}$ vectors are contributing to the scattering function. In the high temperature phase fitting this formula yields

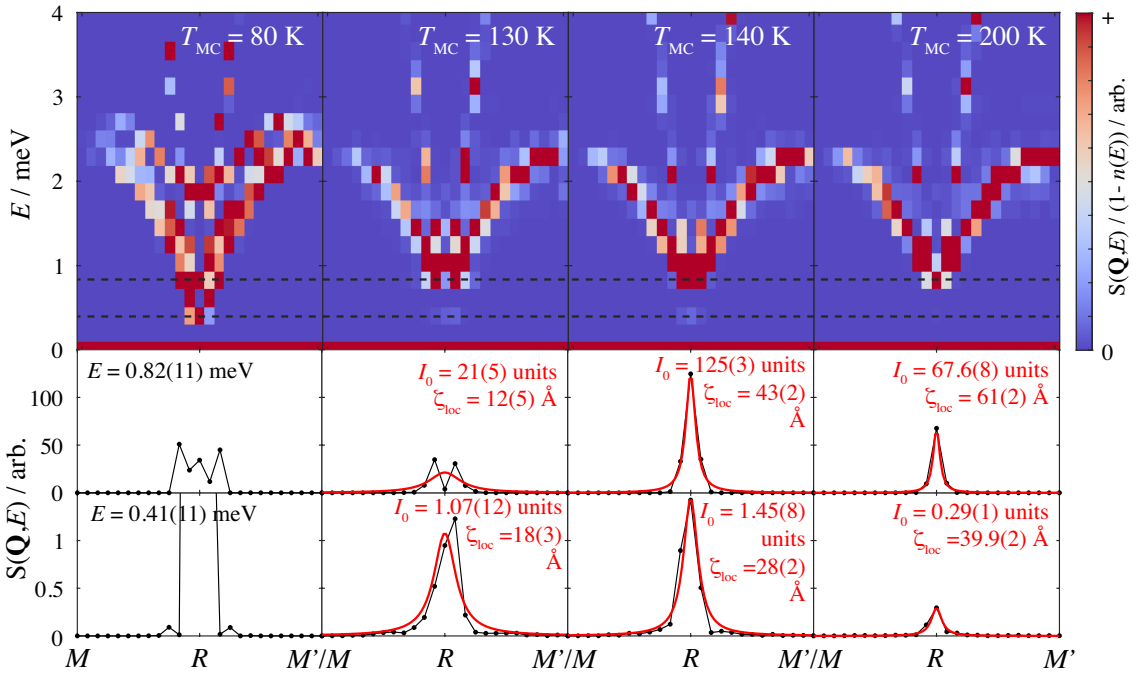

Figure 6.12: Single crystal inelastic neutron scattering at four temperatures simulated from the $4 \times 4 \times 24$ supercells as detailed in the text calculated from $M[0.5, 0.5, 0]$ to $R[0.5, 0.5, 0.5]$ to $M'[0.5, 0.5, 1.5]$. Top: Bose normalised scattering. Middle: cut at $E \sim 0.8$ meV highlights the scattering arising from R-point phonon modes, displayed on a log scale. Bottom: $S(Q, E)$ at $E \sim 0.4$ meV involves scattering from long wavelength acoustic modes.

reasonable fits, especially given the poor statistics of the simulation. The results are consistent with the counter-intuitive conclusions taken about R-point phonons at $E \simeq 0.8\,\mathrm{meV}$: namely, phonons become more delocalised with decreasing T_{MC}.

Single crystals of $Cd(CN)_2$ of the size needed for INS are not yet synthetically available and the difficulties with beam damage [114] make direct measurement of $S(\mathbf{Q}, E)$ impossible at present. However, the next generation of time of flight instruments, for example MUSHROOM at ISIS and BIFROST at the long-anticipated European Spallation Source will have the capabilities for measurements on much smaller samples, opening the door for direct examination of these quantities [436, 437].

6.4.2 Polycrystaline simulation strategy

In this section I look for signatures of cyanide disorder in the phonon scattering. How can we compare our simulations to the experiments of Figure 6.4? The simulation of the polycrystalline simulation requires a $\mathbf{Q}$-grid which is (a) finer than that offered by the $6 \times 6 \times 6$ simulation and (b) more isotropically distributed than that offered by the $4 \times 4 \times 24$ simulation. This higher resolution will answer one of the limitations of the previous simulation. Calculating Γ-phonons for a $\sim 30 \times 30 \times 30$ supercell is computationally unviable so we must take a different approach.

To increase the amount of $\mathbf{Q}$-points for sampling, I sample away from the supercell Γ-point. This is a key difference from the strategy of Overy and coworkers [214], who limited the $\mathbf{Q}$-resolution of their SCLD simulations to $a/2\pi L_x$ in the Q_x direction (with unit cell parameter a and supercell size L_x in that direction). As demonstrated in Figure 6.13, we can improve the energy resolution compared to with this strategy by sampling away from the Γ-point of the supercell. This is most important for modelling the very low energy phonons of interest to this study since they disperse sharply.

We use the $6 \times 6 \times 6$ supercells (i.e. $L = 6$) which pass the optimisation criteria to calculate matrix eigenvectors on a $5 \times 5 \times 5$ grid of points (i.e. $N_k = 5$) from

$0 \leq k_x, k_y, k_z < \frac{2\pi}{aLN_k}$, which together allows $S(\mathbf{Q}, E)$ to be sampled on a $30 \times 30 \times 30$ $\mathbf{Q}$ grid. This is done by interlacing $6 \times 6 \times 6$ grids with $\mathbf{k}$ displacements: a calculation done in GULP with vector $\mathbf{k}$ allows us to access the points corresponding to $\mathbf{H}_{\text{sc}} + \mathbf{k}$ where $\mathbf{H}_{\text{sc}} = \frac{2\pi}{aL}[n_x, n_y, n_z] : n_\alpha \in \mathbb{Z}$. This approach is shown schematically in Figure 6.13. Although it does not improve Q-resolution, the energy resolution can be improved using this strategy. The resulting $S(\mathbf{Q}, E)$ is then binned as $S(|\mathbf{Q}|, E)$ with Q and E bins of size $0.05\,\text{Å}^{-1}$ and $0.25\,\text{meV}$ respectively.

One difficulty in these simulations is the size of eigenvector files that are generated by GULP, which uses the relatively inefficient ascii format, as well as the amount of time taken to read such files. The size of output files is 526.4 MB, almost all of which is used to store matrix eigenvalues. If GULP were to simply be given the $5 \times 5 \times 5$ grid of $\mathbf{k}$ points simulated, the amount of storage would increase to $\sim 60\,\text{GB}$. Instead, I repeatedly call GULP, read the eigenvector files, store them in a more efficient binary (.mat) format and proceed to delete the large ascii files and move to a new $\mathbf{k}$ point. Accordingly the size storage required to run multiple instances of the algorithm in parallel is reduced by three orders of magnitude, allowing

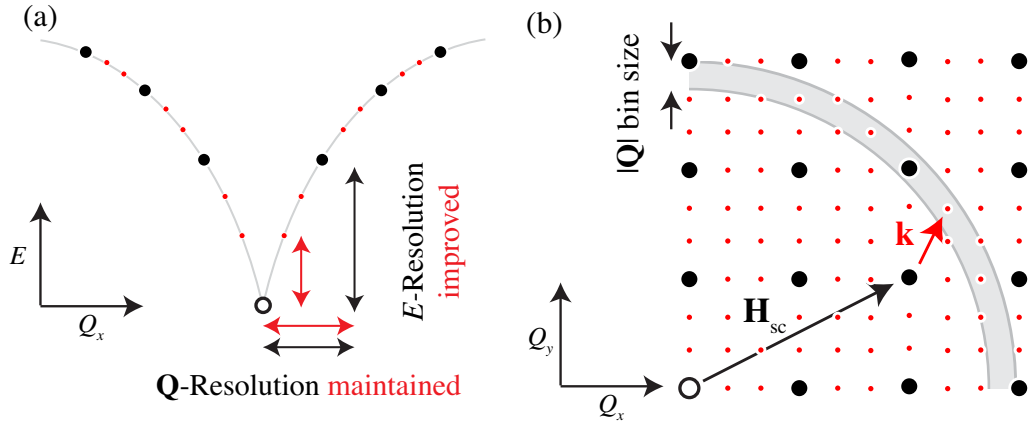

Figure 6.13: Schematic explaining the need for k–grid sampling to improve E-resolution. (a) A dispersion around a parent Γ-point, shown with an empty circle, showing that while Q-resolution is not improved by sampling off of the supercell Γ-points (solid black dots),using a use a $3 \times 3 \times 3$ $\mathbf{k}$-grid (red points) improves the energy resolution. (b) The subsequent grids of sampleable $\mathbf{Q}$-space, with arrows showing a possible construction of $\mathbf{Q} = \mathbf{H}_{\text{sc}} + \mathbf{k}$ and a ring showing an example bin which the scattering falls into.

for the parallelisation of multiple jobs.

Elastic scattering is calculated using a related method. Zero-phonon scattering is calculated according to equation (2.26) and resampled using a Gaussian of linewidth 0.03 Å. This approach neglects the contribution of inelastic scattering to the $S(Q, E = 0)$ data, which given the good energy resolution of the experiment is justified everywhere apart from very close to the Bragg peaks where the phonon energy falls below the instrumental resolution.

6.4.3 Polycrystalline results

$S(Q, E)$ was calculated as described in the previous section and is shown—alongside various cuts though (Q, E) space—in Figure 6.14. The cuts chosen aid comparison with experiment [Fig. 6.4]. Because of the superimposed signal from multiple **Q**-points, the powder INS experiment is harder to analyse. In light of this, I will look for features of our simulated data which resemble those related to short-range order and discussed in the previous section and so attempt to relate them to experimentally observed features.

At 300 K, the simulated $S(Q, E)$ [Fig. 6.14(a)] has a remarkably similar form to that measured experimentally [Fig. 6.4(a)]. Near-zone-centre phonons emerge as cones from each Bragg peak with intensities roughly corresponding to experiment and the form of the feature around $0.6 < Q < 1.3$ Å is approximately reproduced. Features are broader in experiment than in simulation. This is for a few reasons: (a) the simulation lacks resolution function convolution; (b) there is no lifetime broadening in our simulation, since the simulation is entirely harmonic; and (c) the resolution of the simulation is broader than the features plotted. The Q-resolution in our simulation is not reflected in the calculation. This implies that the phonon eigenvalues are similar in reality to those experimentally measured, which should give us faith in the ability of the forcefield parametrised in Section 6.3.1 to reproduce important features of the dynamics in this $Cd(CN)_2$.

While the form of the INS is similar between experiment and simulation at

300 K, its energetics is not. The most significant reason for this is that our forcefield overestimates phonon energies when compared to DFT. As discussed in Section 6.3.1, this is a consequence of fitting to a molecular anion rather than in the solid state. Additionally, DFT itself seems to overestimate the maximum frequency of this band when compared to the experimental distribution of frequencies. While it is hard to say why this may be true, it is unsurprising given the clear importance of dispersion interactions in this system where the two interpenetrating sublattices feature no inter-framework bonding. If (as we have observed) the model can reproduce the form of $S(Q, E)$ at 300 K, and therefore some key information about the dispersion curves, one might expect the model to representative of the most important behaviour shown by the system. However, if as we have observed, the energetics is off, the magnitude of scattering associated with such features may not be accurately reproduced.

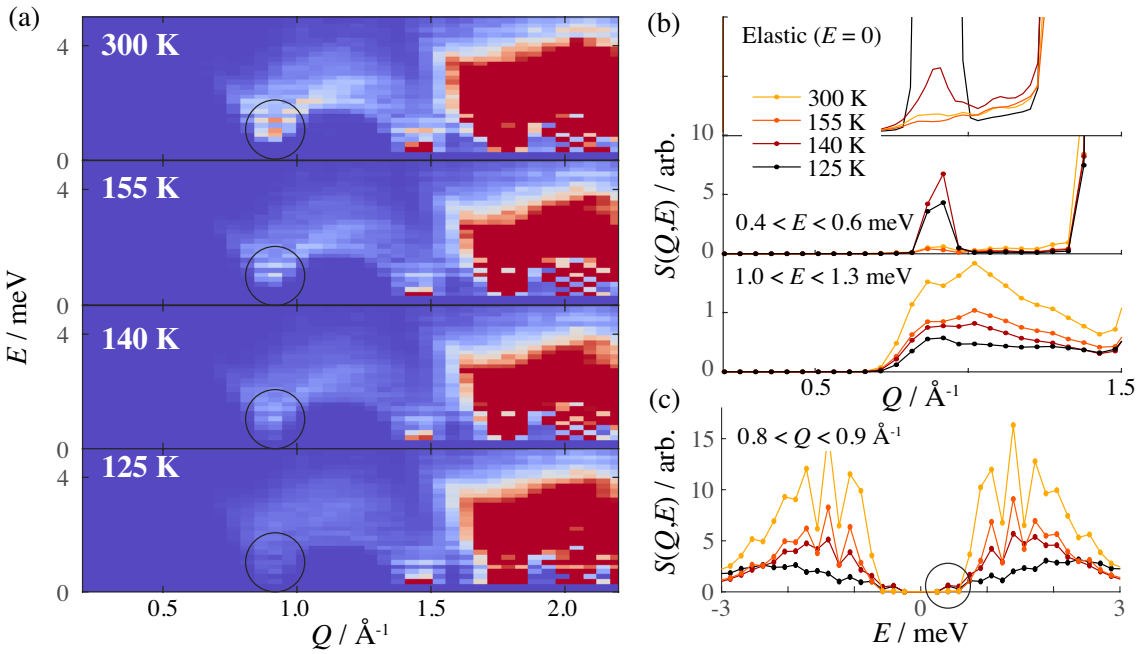

Figure 6.14: Simulated INS results simulated at $T = T_{\mathrm{MC}} = 300, 155, 140$ and 125 K. (a) $S(Q, E)$ plotted for various values. A circle at 140 K highlights the presence of scattering extending down to 0 meV arising from short-range order. (b) Constant energy cuts through the $S(Q, E)$ data. The elastic scattering is simulated from zero-phonon scattering as described in the text (c) Constant Q cut through the $S(Q, E)$ data at the position associated with R-point order.

Between 300 and 155 K there is a considerable change in the measured INS energies, particularity at $Q \simeq 0.8\,\text{Å}^{-1}$ which is not reproduced by our model. Instead, between 300 K and 155 K the model predicts constant frequencies (as can also be seen in Fig. 6.11). This deficiency is unsurprising as the behaviour likely arises from the anharmonicity neglected in the approximations of the model. Such anharmonicity leads to a renormalisation of phonon energies as a function of temperature due to phonon–phonon scattering, and could be incorporated in more accurate iterations of the model [35].

The model does succeed in capturing the collapse in phonon intensity and renormalisation of frequencies seen experimentally below the transition temperature. As we saw in Figure 6.11, most phonon branches sharpen as a result of the transition. This is the most likely cause of the substantial fall in phonon intensities seen in Figure 6.14(c) between 140 and 125 K as well as their corresponding experimental traces in Figure 6.4(c).

Perhaps a more exciting result of the model is its ability to reproduce the waterfall-type feature at 140 K despite the lack of long-range static order in this phase. The elastic scattering shown in the top pane of Figure 6.4(b) demonstrates that the feature is associated with R–point short-range order. The feature associated with static short-range order is broad at this temperature (140 K), but still shows some intensity. This is broadness emerges because $T_\text{c} > 140\,\text{K}$, and long-range order has not yet precipitated. Nevertheless, we see the contribution of the same weak and low energy scattering feature seen at the R-point in Figure 6.12, realised as a 'central mode' feature similar to that seen experimentally.

Since this feature emerges from the diffuse maximum which is to become a Bragg peak at $T < T_\text{c}$, we should understand it as arising from the presence of nanodomains. The inelastic neutron scattering essentially acts as a convolution of the phonon dispersion curves with the static structure, such that any static diffuse maximum should have an acoustic signature emerging from it—in some way similar to

the profile of the static diffuse scattering. This is a similar concept to the central scattering peak seen in Raman scattering as an indicator of locally polar fluctuations [438–440], particularly in the relaxor ferroelectrics, where these constitute the 'polar nanodomains' already discussed [234] [§1.4.2]. The features seen in Raman scattering occur at the Γ-point of reciprocal space. By contrast the scattering feature here seems to be associated with the R–ordering vector from which antiferroelectric order condenses. Hence this structure could be described as arising from antipolar nanodomains.

We have seen evidence of this continuum of scattering down to $E = 0$ both experimentally and theoretically. However, the temperature range over which the 'central-mode' scattering is seen at $Q \sim 0.8\,\text{Å}^{-1}$ is wider experimentally ($140 < T < 225\,\text{K}$) than theoretically ($130 < T_{\text{MC}} < 140\,\text{K}$). This is consistent with our earlier observation [§6.2.4] that antipolar correlations exist more strongly over a larger temperature range experimentally than according to the spin-ice Hamiltonian [Eq. (1.40)].

6.5 Outlook

6.5.1 The origin of antipolar nanodomains

We have seen a number of important deviations between the temperature scales associated with the pseudospin model developed by Coates and coworkers [65] and our experimental observations. The latter point to the stabilisation of antipolar nanodomains with a correlation length of $\sim 1.5\,\text{nm}$ over a larger temperature range $140 < T \lesssim 225\,\text{K}$ [§6.2.4] than predicted by the model.

Further evidence for antipolar nanodomains comes from the large amount of experimental quasielastic scattering particularly centred around $Q \sim 0.8\,\text{Å}$. This is somewhat reminiscent of the nanodomain structure in cyanide glasses, which was attributed to nanostructure in these systems [§1.4.3]. Simulations have shown that at temperature with large nanodomains, low energy phonons tend to localise around

or within the domains [§6.3.5], which presumably play an important role in NTE. Does the role of phonons change with localisation?

An equally puzzling question is what stabilises this nanodomain structure in the first place? We have seen in section 6.2.4 that the experimental correlation length seems to be much larger than that simulated in the model of Coates and coworkers. What is the origin of this dependency? I consider a few possibility:

There is no particular reason to assume that the correlation length of the relaxed system is the same as that of our Monte Carlo simulations. It may be the case that rare regions occur in the system where the order parameter is strong. In these regions, the lattice would relax with R–point order. However the order within these regions may 'drag' the lattice with it leading to correlations in the atomic positions extending over a larger range than the underlying pseudospin correlation length. Some evidence against this comes from the elastic scattering, which does not seem to show any signature of this relaxation above the phase transition (i.e. at $T = 155\,\mathrm{K}$ in Pane 1 of Figure 6.14(b)). It is not however clear whether this $6\times6\times6$ simulation would be large enough to resolve such effects. We could investigate this possibility further using larger simulations.

A second possibility is that phonon anharmonicity is broadening the R-point phonon so dramatically that it overlaps with the elastic line. This has been seen both experimentally in Raman spectroscopy of antiferroelectric $CsPbBr_3$ [438], attributed to the anharmonicity of the crystal. We know that $Cd(CN)_2$ is a highly anharmonic system, while the simulation strategy used here is within the harmonic approximation.

A third explanation comes from the observation of changing phonon energies seen in Figure 6.11 in the proximity of the phase transition. These increasing phonon energies in the low temperature phase presumably have an impact on the free energy of the system and are thus able to stablise the disordered phase in the proximity of the phase transition. To assess whether the energy scale of the phonon renor-

malisation is appropriate for this effect to occur, I take an approach similar to the quasi-harmonic approach [§1.5.4], constructing the free energy F function as a function of true temperature and Monte Carlo temperature. We then assume that the true state of the system exists at some Monte Carlo temperature T_{MC} and in which we must compare the free energy arising from cyanide orientations and lattice vibrations. The former can be calculated via the heat capacity of the Monte Carlo simulations detailed in section 6.3.2. From $F = U - TS$, one obtains

$$F_{\mathrm{MC}}(T, T_{\mathrm{MC}}) = \int_{T_{\mathrm{MC}}}^{T_{\mathrm{ref}}} C_{\mathrm{MC}}(\tau)\mathrm{d}\tau - T\left(\log 2 + \int_{T_{\mathrm{MC}}}^{T_{\mathrm{ref}}} \frac{C_{\mathrm{MC}}(\tau)}{\tau}\mathrm{d}\tau\right). \tag{6.16}$$

This function has a minimum at $T = T_{\mathrm{MC}}$ with respect to T_{MC}, showing that the most stable MC temperature is the true temperature without the influence of phonons. This quantity, subtracted from its minimum value, is plotted in Figure 6.15(a). In practice, I use $T_{\mathrm{ref}} = 300\,\mathrm{K}$, although it can be shown that the results are invariant to this quantity.

We can obtain an estimate of the phonon contribution from the phonon frequencies at the Γ-point of the $6 \times 6 \times 6$ supercells (for this it is likely important to get

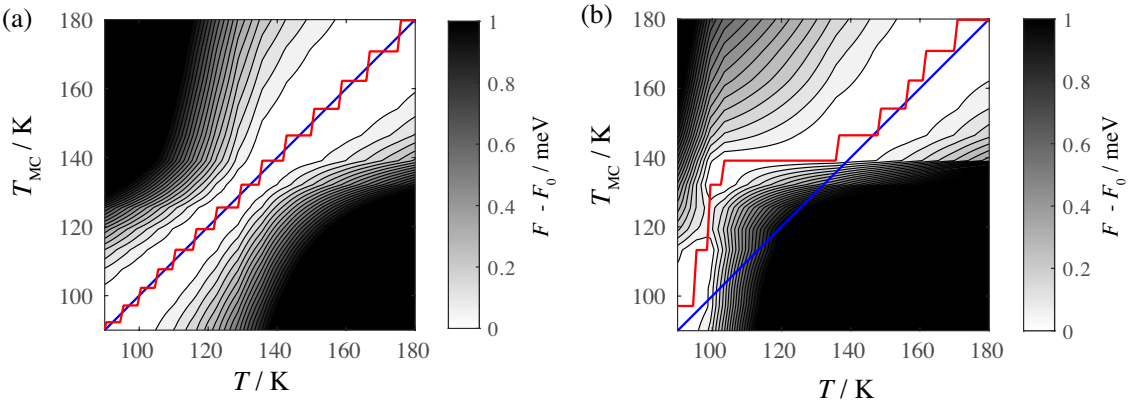

Figure 6.15: The dependence of the modelled free energy on Monte carlo temperature (T_{MC}) and true temperature (T). (a) omitting and (b) including the phonon contribution to the free energy . Contours are spaced on 0.05 meV intervals and the minimum is indicated with a red line, which tracks $T = T_{\mathrm{MC}}$ (blue) in (a) but deviated over the range $100 \lesssim T \lesssim 140\,\mathrm{K}$ in (b)

a homogenous sampling of reciprocal space):

$$F_{\text{phon}}(T, T_{\text{MC}}) = \frac{1}{N}\sum_{\nu}\frac{1}{2}\hbar\omega_{\nu}(T_{\text{MC}}) + k_{\text{B}}T\log\left[1 - \exp\left(-\frac{\hbar\omega_{\nu}(T_{\text{MC}})}{k_{\text{B}}T}\right)\right]. \quad (6.17)$$

Here it is important to normalise the two quantities correctly, so that their contributions can be compared. For this reason, we use N as the number of formula units in the supercell (i.e. since there are two formula units per cell, $N = 6^3 \times 2$).

The combined phonon free energy $F = F_{\text{MC}} + F_{\text{phon}}$ is subtracted from its minimum value (for a given value of T) and plotted in Figure 6.15(b). Now instead of tracing $T = T_{\text{MC}}$, the minimum deviates around T_{c}. There is now a range of temperatures in our model between $100 \lesssim T \lesssim 140\,\text{K}$ where the simulation is stuck near criticality. This observation may help explain the presence of nanodomains over a large temperature range. Over this temperature range, the Monte Carlo temperature is fixed slightly above the phase transition temperature. Our simulation now incorrectly predicts the ordering temperature: 100 K rather than $\sim 130\,K$ as seen experimentally. However, it does predict a large temperature range exhibiting antipolar nano domains that short-range order should persist over an extended temperature range, as seen experimentally.

This possibility—while appealing—requires more evidence. The arguments and methods of this section may be more broadly applicable than in $Cd(CN)_2$, as all they require is an order-disorder phase transition over which phonons harden. The mechanism bares some similarity to the apparent localisation-driven nanodomain structure of PMN [242] [§1.4.2].

6.5.2 Mechanism of NTE in $Cd(CN)_2$

The measurement of the Grüneisen parameter at 300 K is consistent with a quasi-harmonic phonon-driven picture of the negative thermal expansion in $Cd(CN)_2$ [§6.1.2]. This constituted the first measurements of pressure induced softening using the new, low-background TAV-6 cell at ISIS. These data may be better interpreted,

including behaviour on transition to the high pressure Phase-II, with a model incorporating cyanide disorder. To reproduce the approximate value of the Grüneisen parameter, a virtual crystal approximation approach seems to be sufficient. In this experiment, we were limited by the experimental energy resolution and counting statistics, so were unable to resolve the full $S(Q, E)$. Even after averaging over E, the counting statistics remained poor. Accordingly the errors on our estimate of the mode Grüneisen parameter remain large. Future experiments could remeasure on a different instrument (e.g. LET) to improve this estimate and perhaps reveal anomalous features in $S(Q, E)$. Nevertheless, our conclusion should be that the isotropic NTE seen at 300 K is well explained within the virtual crystal approximation of the cubic $Cd(CN)_2$ structure [Fig. 6.16(c)].

Such anomalous features were seen as a function of cyanide order on cooling and they have been interpreted here as resulting from antipolar nanodomains. The observation that these nanodomains are present over a much larger temperature range ($140 < T \lesssim 225$ K) than predicted by our model raises some questions about their stabilisation.

Regardless of their origin, we may speculate on what the antipolar nanodomain structure might mean for the world-leading isotropic NTE in $Cd(CN)_2$. Nanodomain

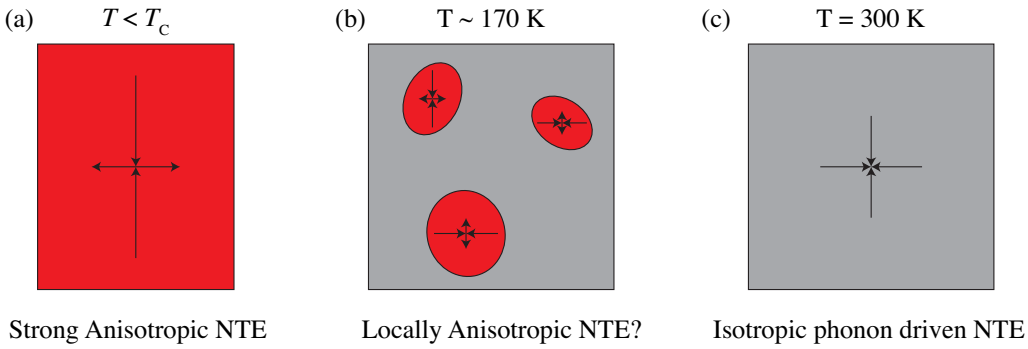

Figure 6.16: A somewhat-speculative schematic of a crystal of $Cd(CN)_2$: (a) at low temperature, NTE is anisotropic (red): one crystal axis shrinks and the other grows with temperature, (c) at high temperature, NTE is weak but occurs the same in all directions and is phonon driven (grey). (b) Could nanodomian structure lead to locally anisotropic NTE?

structure can be responsible for high values of the thermodynamic response variable. This has been seen in PZT, where polar nanodomains are responsible for 50–80 % of the piezoelectric response [231]. In Figure 6.1 it is made clear that the anisotropic NTE seen below T_c is much stronger than the isotropic NTE seen at high temperature [Fig. 6.16(a)]. However, if small nanodomains exhibiting strong NTE sat in a medium showing isotropic NTE—as is shown in Figure 6.16(b)—could this enhance the NTE overall? We have already seen that the phonons which drive NTE have a tendency to localise in and around nanodomain structures. Could this in part be responsible for the anomalously high NTE seen in $Cd(CN)_2$ [§1.1.4]?

The study detailed in this chapter highlights the rich physics which arises from the interplay of soft lattice dynamics and pseudospin (dis)order. While it is not yet clear exactly the role that pseudospin (dis)order plays in NTE, it is clear the conventional VCA or CN-ordered approach taken in previous studies is insufficient. Given the recent interest in disorder in framework materials [14, 441], the question of how it might effect the flexibility and expansion behaviour that defines this family of materials is an exciting and highly topical one.

Chapter 7

Concluding Remarks

I set out to investigate the relationship between disordered structures in framework materials and their properties. To conclude, I will summarise the key disorder–property relationships which have emerged in the research. Broadly, they fall into three categories.

Firstly, there are the relationships which essentially follow from the fluctuation-dissipation theorem: more disorder implies greater fluctuations which implies a stronger response to stimulus (*i.e.* properties). Some such relationships may be stated as follows:

- Greater magnetic disorder in the absence of magnetic field (*e.g.* that which is enhanced by geometric frustration) can be related to a large entropy change on the application of field, via the fluctuation-dissipation theorem [258]. This is the origin of the large magnetocaloric effect seen in many geometrically frustrated materials.

- The disorder seen in spin chain fragments leads to the emergence of a low temperature ($T \sim 0.3\,\mathrm{K}$) feature in the heat capacity in $Tb_{1-x}Y_x(HCOO)_3$ at the temperatures in which the fluctuations of these chains are at a maximum [§4.7].

- The vibrational disorder induced by the thermal occupation of low energy, negative Grüneisen modes is linked to pressure-induced softening of these modes, which can be measured [§6.1.2]. This pressure-induced softening is directly related to NTE.

The fluctuation-dissipation relation describes linear responses to stimulus. When stronger stimuli are applied we pass beyond the linear regime. This is particularly apparent with disorder-property relationships which relate to an order-disorder tran-

sition that is induced by a stimulus (pressure, field, etc.). Because of the discontinuities associated with such phase transitions, the properties will have a nonlinear dependence on their stimuli. Such relationships include:

- The field-induced order-disorder phase transition in $NaMn(HCOO)_3$ has an associated strong magnetocaloric entropy change on the application of field. We saw that fields required to induce this phase transition are particularly low due to geometric frustration [§3.5].

- A similar effect has been seen in barrocaloric framework materials, where a pressure-induced order-disorder transition drives a large entropy release [22],

- The pressure-induced softening in $Cd(CN)_2$ reverses after sufficient field because of a phase transition, which is likely a pseudospin order/disorder transition [§6.1.2]. (Could this have an associated barrocaloric effect too?)

So far, I have categorised the dependence of a type of disorder on properties into linear or non-linear relationships. More complex behaviour emerges when more than one degree of freedom is disordered. In the case of 'multiple disorder', the complex interplay between more than one degree of freedom leads to unusual properties. Examples in this thesis include:

- B-site pseudospin (dis)order and magnetic (dis)order couple to leads to percolation induced ferrimagnetism [§5].

- The disorder in chain lengths in $Tb_{1-x}Y_x(HCOO)_3$ and the disorder in the ising spins of these chains couple to give the form, and associated entropy of the heat-capacity anomaly studied in §4.5.2.

- In powder samples of $NaMn(HCOO)_3$, disorder in crystallite orientation couples the disorder of the magnetic spins in a way which leads to polycrystalline averaging—and therefore suppression—of the magnetocaloric effect [§3.5].

- Finally, I speculate that the combination of antipolar nanodomains and soft negative Grüneisen phonons (*i.e.* pseudospin and vibrational disorder) leads to an enhancement of NTE in $Cd(CN)_2$ [§6.5.2].

Because these multiple disorder effects are more complex, it is more difficult to find patterns in them. This means that the identification of universal design rules in these systems is less straightforward.

However, it is in this final class of disorder–property relation, partly because of their complexity, where we find the most exiting challenges for the future. Some of the most important examples include: high-temperature superconductors, where the correlated disorder in atomic positions couples with electron (dis)order to enhance superconductivity [442, 443]; solid-state energy devices (battery cathodes, thermoelectrics) where heat transport (which interplays with pseudospin-like cation disorder) is often a limiting factor in improving device performance [444]; atomic disorder may have the ability to suppress spin-liquid behaviour even at the lowest concentrations [195]. Real materials have multiple kinds of disorder and it will be essential to the design of new materials that our theoretical and experimental methods can reflect this.

Understanding these relationships is especially difficult when the two degrees of freedom show interplay in both directions, as appears to be the case in $Cd(CN)_2$: pseudospin disorder affects lattice dynamics and lattice dynamics affect pseudospin disorder. It is clear that neutron scattering experiments will be at the forefront of such studies because of their ability to separate the signatures of disorder of multiple degrees of freedom. The most important examples of this are the separation of structural from magnetic degrees of freedom via polarisation analysis [§2.1.3] and separation of dynamic from static disorder via INS [§2.1.4]. New instrumentation—such as the Mushroom and BIFROST [436, 437] spectrometers—as well as new computational methods—such as machine-learned potentials [445] and T-matrix SCLD methods [331]—will make the measurement and analysis of multiple disorder more

tractable.

Framework materials proved a fruitful choice of system for these studies, due to their topological diversity and compositional flexibility. It seems that these materials are perhaps overlooked as sources of unusual spin and pseudospin models, compared to the denser inorganic ceramic materials. One possible reason for this is that magnetic interactions in inorganic materials tend to be stronger, so magnetic order emerges at near-room temperature rather than $\sim 1\,\mathrm{K}$, which does cause experimental limitations as well as limiting practical applicability. On the other hand pseudospin interactions like those in $Cd(CN)_2$ do emerge on the room temperature scale [65], making pseudospin disorder central to studying framework materials.

Understanding structure–property relations is a faster, and more insightful, route to new functional materials than stabbing in the dark. While the study of disorder–property relationships is more involved that the 'order–property' relations traditional crystallography, it represents a central challenge for structural science in the 21st century. For now, what is needed is further case-by-case study in order to illuminate any broader patterns that emerge.

Bibliography

[1] B. F. Hoskins, R. Robson, *J. Am. Chem. Soc.* **112**, 1546 (1990).

[2] R. Robson, *J. Chem. Soc., Dalton Trans.* pp. 3735–3744 (2000).

[3] O. M. Yaghi, M. O'Keeffe, N. W. Ockwig, H. K. Chae, M. Eddaoudi, J. Kim, *Nature* **423**, 705 (2003).

[4] S. L. James, *Chem. Soc. Rev.* **32**, 276 (2003).

[5] O. Delgado-Friedrichs, M. O'Keeffe, O. M. Yaghi, *Phys. Chem. Chem. Phys.* **9**, 1035 (2007).

[6] E. V. Alexandrov, V. A. Blatov, A. V. Kochetkov, D. M. Proserpio, *CrystEngComm* **13**, 3947 (2011).

[7] J. D. Evans, F.-X. Coudert, *Chem. Mater.* **29**, 7833 (2017).

[8] T. C. Nicholas, A. L. Goodwin, V. L. Deringer, *Chem. Sci.* **11**, 12580 (2020).

[9] S. Chibani, F.-X. Coudert, *APL Mater.* **8** (2020). 080701.

[10] N. Castel, F.-X. Coudert, Computation of finite temperature mechanical properties of zif glasses by molecular dynamics (2023).

[11] G. Kieslich, S. Sun, A. K. Cheetham, *Chem. Sci.* **5**, 4712 (2014).

[12] S. M. Bovill, P. J. Saines, *Cryst. Eng. Comm.* **17**, 8319 (2015).

[13] N. L. Rosi, J. Eckert, M. Eddaoudi, D. T. Vodak, J. Kim, M. O'Keeffe, O. M. Yaghi, *Science* **300**, 1127 (2003).

[14] E. G. Meekel, E. M. Schmidt, L. J. Cameron, A. D. Dharma, H. J. Windsor, S. G. Duyker, A. Minelli, T. Pope, G. O. Lepore, B. Slater, C. J. Kepert, A. L. Goodwin, *Science* **379**, 357 (2023).

[15] M. Maczka, A. Gagor, K. Hermanowicz, A. Sieradzki, L. Macalik, A. Pikul, *J. Solid State Chem.* **237**, 150 (2016).

[16] A. K. Cheetham, G. Férey, T. Loiseau, *Angew. Chem., Int. Ed. Engl.* **38**, 3268 (1999).

[17] S. Kitagawa, R. Kitaura, S.-i. Noro, *Angew. Chem., Int. Ed. Engl.* **43**, 2334 (2004).

[18] H. Furukawa, K. E. Cordova, M. O'Keeffe, O. M. Yaghi, *Science* **341**, 1230444 (2013).

[19] K. Hurlbutt, S. Wheeler, I. Capone, M. Pasta, *Joule* **2**, 1950 (2018).

[20] Z. Gao, Q. Liu, G. Zhao, Y. Sun, H. Guo, *J. Mater. Chem. A* **10**, 7497 (2022).

[21] D. Boldrin, *Appl. Phys. Lett.* **118** (2021). 170502.

[22] J. M. Bermúdez-García, M. Sánchez-Andújar, S. Castro-García, J. López-Beceiro, R. Artiaga, M. A. Señarís-Rodríguez, *Nat. Commun* **8**, 15715 (2017).

[23] W.-J. Xu, P.-F. Li, Y.-Y. Tang, W.-X. Zhang, R.-G. Xiong, X.-M. Chen, *J. Am. Chem. Soc.* **139**, 6369 (2017).

[24] J. Salgado-Beceiro, A. Nonato, R. X. Silva, A. García-Fernández, M. Sánchez-Andújar, S. Castro-García, E. Stern-Taulats, M. A. Señarís-Rodríguez, X. Moya, J. M. Bermúdez-García, *Mater. Adv.* **1**, 3167 (2020).

[25] H. Li, L. Li, R.-B. Lin, W. Zhou, Z. Zhang, S. Xiang, B. Chen, *EnergyChem* **1**, 100006 (2019).

[26] D. Britt, D. Tranchemontagne, O. M. Yaghi, *Proc. Natl. Acad. Sci. U.S.A.* **105**, 11623 (2008).

[27] M. Das, S. Roy, N. Khan, P. Mandal, *Phys. Rev. B* **98**, 104420 (2018).

[28] H. L. B. Boström, M. S. Senn, A. L. Goodwin, *Nat. Commun* **9**, 2380 (2018).

[29] J.-P. Zhang, H.-L. Zhou, D.-D. Zhou, P.-Q. Liao, X.-M. Chen, *Natl. Sci. Rev.* **5**, 907 (2017).

[30] R. Kitaura, K. Fujimoto, S.-i. Noro, M. Kondo, S. Kitagawa, *Angew. Chem., Int. Ed. Engl.* **41**, 133 (2002).

[31] C. Serre, F. Millange, C. Thouvenot, M. Noguès, G. Marsolier, D. Louër, G. Férey, *J. Am. Chem. Soc.* **124**, 13519 (2002).

[32] K. Uemura, R. Matsuda, S. Kitagawa, *J. Solid State Chem.* **178**, 2420 (2005).

[33] G. Férey, C. Serre, *Chem. Soc. Rev.* **38**, 1380 (2009).

[34] S. Horike, S. Shimomura, S. Kitagawa, *Nat. Chem* **1**, 695 (2009).

[35] M. T. Dove, *Structure and Dynamics: An Atomic View of Materials* (Oxford University Press, Oxford, 2003).

[36] M. T. Dove, *Philos. Trans. R. Soc. A* **377**, 20180222 (2019).

[37] G. D. Gatta, S. A. Wells, *Phys. Chem. Miner* **31**, 465 (2004).

[38] J. S. O. Evans, T. A. Mary, T. Vogt, M. A. Subramanian, A. W. Sleight, *Chem. Mater.* **8**, 2809 (1996).

[39] A. L. Goodwin, C. J. Kepert, *Phys. Rev. B* **71**, 140301 (2005).

[40] A. L. Goodwin, D. A. Keen, M. G. Tucker, *Proc. Natl. Acad. Sci. U.S.A.* **105**, 18708 (2008).

[41] A. B. Cairns, A. L. Goodwin, *Phys. Chem. Chem. Phys.* **17**, 20449 (2015).

[42] A. U. Ortiz, A. Boutin, A. H. Fuchs, F.-X. Coudert, *J. Chem. Phys.* **138** (2013). 174703.

[43] P. G. Yot, Q. Ma, J. Haines, Q. Yang, A. Ghoufi, T. Devic, C. Serre, V. Dmitriev, G. Férey, C. Zhong, G. Maurin, *Chem. Sci.* **3**, 1100 (2012).

[44] D. Jiang, T. Wen, Y. Guo, J. Liang, Z. Jiang, C. Li, K. Liu, W. Yang, Y. Wang, *Chem. Mater.* **34**, 2764 (2022).

[45] A. V. Neimark, F.-X. Coudert, C. Triguero, A. Boutin, A. H. Fuchs, I. Beurroies, R. Denoyel, *Langmuir* **27**, 4734 (2011).

[46] W. Li, M. R. Probert, M. Kosa, T. D. Bennett, A. Thirumurugan, R. P. Burwood, M. Parinello, J. A. K. Howard, A. K. Cheetham, *J. Am. Chem. Soc.* **134**, 11940 (2012).

[47] C. S. Coates, M. R. Ryder, J. A. Hill, J.-C. Tan, A. L. Goodwin, *APL Mater.* **5** (2017). 066107.

[48] V. M. Goldschmidt, *Sci. Nat.* **14**, 477 (1926).

[49] C. J. Howard, H. T. Stokes, *Acta Crystallogr. B* **54**, 782 (1998).

[50] A. M. Glazer, *Acta Crystallogr. B* **28**, 3384 (1972).

[51] A. M. Glazer, *Acta Crystallogr. A* **31**, 756 (1975).

[52] L. C. Gómez-Aguirre, B. Pato-Doldán, A. Stroppa, S. Yáñez-Vilar, L. Bayarjargal, B. Winkler, S. Castro-García, J. Mira, M. Sánchez-Andújar, M. A. Señarís-Rodríguez, *Inorg. Chem.* **54**, 2109 (2015).

[53] K.-L. Hu, M. Kurmoo, Z. Wang, S. Gao, *Chem. Eur. J.* **15**, 12050 (2009).

[54] A. Stroppa, P. Barone, P. Jain, J. M. Perez-Mato, S. Picozzi, *Adv. Mater.* **25**, 2284 (2013).

[55] S. Vandenhaute, S. M. J. Rogge, V. Van Speybroeck, *Front. Chem.* **9** (2021).

[56] A. E. Hoffman, J. Wieme, S. M. Rogge, L. Vanduyfhuys, V. V. Speybroeck, *Z. fur Krist. - Cryst. Mater.* **234**, 529 (2019).

[57] R. Kitaura, K. Seki, G. Akiyama, S. Kitagawa, *Angew. Chem., Int. Ed. Engl.* **42**, 428 (2003).

[58] S. Horike, D. Tanaka, K. Nakagawa, S. Kitagawa, *Chem. Commun.* pp. 3395–3397 (2007).

[59] B. Chen, C. Liang, J. Yang, D. S. Contreras, Y. L. Clancy, E. B. Lobkovsky, O. M. Yaghi, S. Dai, *Angew. Chem., Int. Ed. Engl.* **45**, 1390 (2006).

[60] T. K. Maji, R. Matsuda, S. Kitagawa, *Nat. Mater* **6**, 142 (2007).

[61] C. Nanthamathee, S. Ling, B. Slater, M. P. Attfield, *Chem. Mater.* **27**, 85 (2015).

[62] L. Petters, S. Burger, S. Kronawitter, M. Drees, G. Kieslich, *CrystEngComm* **23**, 5425 (2021).

[63] Y. Liu, J.-H. Her, A. Dailly, A. J. Ramirez-Cuesta, D. A. Neumann, C. M. Brown, *J. Am. Chem. Soc.* **130**, 11813 (2008).

[64] W. Miller, C. W. Smith, D. S. Mackenzie, K. E. Evans, *J. Mater. Sci.* **44**, 5441 (2009).

[65] C. S. Coates, M. Baise, A. Schmutzler, A. Simonov, J. W. Makepeace, A. G. Seel, R. I. Smith, H. Y. Playford, D. A. Keen, R. Siegel, J. Senker, B. Slater, A. L. Goodwin, *Nat. Commun* **12**, 2272 (2021).

[66] K. Takenaka, D. Asai, R. Kaizu, Y. Mizuno, Y. Yokoyama, Y. Okamoto, N. Katayama, H. S. Suzuki, Y. Imanaka, *Sci. Rep.* **9**, 122 (2019).

[67] N. Lock, Y. Wu, M. Christensen, L. J. Cameron, V. K. Peterson, A. J. Bridgeman, C. J. Kepert, B. B. Iversen, *J. Phys. Chem. C* **114**, 16181 (2010).

[68] L. Pauling, *J. Am. Chem. Soc.* **57**, 2680 (1935).

[69] S. T. Bramwell, M. J. Gingras, *Science* **294**, 1495 (2001).

[70] G. Mínguez Espallargas, E. Coronado, *Chem. Soc. Rev.* **47**, 533 (2018).

[71] S. Ehrling, E. M. Reynolds, V. Bon, I. Senkovska, T. E. Gorelik, J. D. Evans, M. Rauche, M. Mendt, M. S. Weiss, A. Pöppl, E. Brunner, U. Kaiser, A. L. Goodwin, S. Kaskel, *Nat. Chem* **13**, 568 (2021).

[72] D. Umeyama, S. Horike, M. Inukai, T. Itakura, S. Kitagawa, *J. Am. Chem. Soc.* **137**, 864 (2015).

[73] X. Kong, H. Deng, F. Yan, J. Kim, J. A. Swisher, B. Smit, O. M. Yaghi, J. A. Reimer, *Science* **341**, 882 (2013).

[74] A. F. Sapnik, H. S. Geddes, E. M. Reynolds, H. H.-M. Yeung, A. L. Goodwin, *Chem. Commun.* **54**, 9651 (2018).

[75] K. W. P. Orr, S. M. Collins, E. M. Reynolds, F. Nightingale, H. L. B. Boström, S. J. Cassidy, D. M. Dawson, S. E. Ashbrook, O. V. Magdysyuk, P. A. Midgley, A. L. Goodwin, H. H.-M. Yeung, *Chem. Sci.* **12**, 4494 (2021).

[76] A. Simonov, T. De Baerdemaeker, H. L. B. Boström, M. L. Ríos Gómez, H. J. Gray, D. Chernyshov, A. Bosak, H.-B. Bürgi, A. L. Goodwin, *Nature* **578**, 256 (2020).

[77] M. J. Cliffe, W. Wan, X. Zou, P. A. Chater, A. K. Kleppe, M. G. Tucker, H. Wilhelm, N. P. Funnell, F.-X. Coudert, A. L. Goodwin, *Nat. Commun* **5**, 4176 (2014).

[78] L. Shen, S.-W. Yang, S. Xiang, T. Liu, B. Zhao, M.-F. Ng, J. Göettlicher, J. Yi, S. Li, L. Wang, J. Ding, B. Chen, S.-H. Wei, Y. P. Feng, *J. Am. Chem. Soc.* **134**, 17286 (2012).

[79] X.-K. Wei, N. Domingo, Y. Sun, N. Balke, R. E. Dunin-Borkowski, J. Mayer, *Adv. Energy Mater.* **12**, 2201199 (2022).

[80] P. Lloveras, A. Aznar, M. Barrio, P. Negrier, C. Popescu, A. Planes, L. Mañosa, E. Stern-Taulats, A. Avramenko, N. D. Mathur, X. Moya, J.-L. Tamarit, *Nat. Commun.* **10** (2019).

[81] P. J. Saines, P. T. Barton, M. Jura, K. S. Knight, A. K. Cheetham, *Mater. Horiz.* **1**, 332 (2014).

[82] J. M. Hopkinson, H.-Y. Kee, *Phys. Rev. B* **74**, 224441 (2005).

[83] M. O'Keeffe, S. Andersson, *Acta Crystallogr. A* **33**, 914 (1977).

[84] V. Paredes-García, A. Vega, M. A. Novak, M. G. F. Vaz, D. A. Souza, D. Venegas-Yazigi, E. Spodine, *Inorg. Chem.* **48** (2009).

[85] M. Inoue, M. Kubo, *Inorg. Chem.* **9** (1970).

[86] R. Scatena, R. D. Johnson, P. Manuel, P. Macchi, *J. Mater. Chem. C* **8** (2020).

[87] X.-Y. Wang, L. Gan, S.-W. Zhang, S. Gao, *Inorg. Chem.* **43**, 4615 (2004).

[88] H. C. Walker, H. D. Duncan, M. D. Le, D. A. Keen, D. J. Voneshen, A. E. Phillips, *Phys. Rev. B* **96** (2017).

[89] J. C. Aston, P. J. Saines, *Anorg. Allg. Chem.* **643**, 287.

[90] J. A. M. Paddison, H. Jacobsen, O. A. Petrenko, M. T. Fernández-Díaz, P. P. Deen, A. L. Goodwin, *Science* **350** (2015).

[91] E.-Q. Gao, N. Liu, A.-L. Cheng, S. Gao, *Chem. Commun.* **24** (2007).

[92] H. Kikuchi, K. Kunieda, T. Asano, Y. Fujii, Y. Inagaki, A. Matsuo, K. Kindo, *Phys. Proc.* **75** (2015).

[93] P. J. Saines, J. A. M. Paddison, P. M. M. Thygesen, M. G. Tucker, *Mater. Horiz.* **2** (2015).

[94] M. Falsaperna, J. M. Bulled, G. B. G. Stenning, A. L. Goodwin, P. J. Saines, *Phys. Rev. Mater.* **6**, 124410 (2022).

[95] P. Jain, V. Ramachandran, R. J. Clark, H. D. Zhou, B. H. Toby, N. S. Dalal, H. W. Kroto, A. K. Cheetham, *J. Am. Chem. Soc.* **131**, 13625 (2009).

[96] M. Sánchez-Andújar, L. C. Gómez-Aguirre, B. Pato Doldán, S. Yáñez-Vilar, R. Artiaga, A. L. Llamas-Saiz, R. S. Manna, F. Schnelle, M. Lang, F. Ritter, A. A. Haghighirad, M. A. Señarís-Rodríguez, *CrystEngComm* **16**, 3558 (2014).

[97] D.-W. Fu, W. Zhang, H.-L. Cai, Y. Zhang, J.-Z. Ge, R.-G. Xiong, S. D. Huang, T. Nakamura, *Angew. Chem., Int. Ed. Engl.* **50**, 11947 (2011).

[98] Y.-H. Chu, L. W. Martin, M. B. Holcomb, M. Gajek, S.-J. Han, Q. He, N. Balke, C.-H. Yang, D. Lee, W. Hu, Q. Zhan, P.-L. Yang, A. Fraile-Rodríguez, A. Scholl, S. X. Wang, R. Ramesh, *Nat. Mater* **7**, 478 (2008).

[99] R. Ramesh, N. A. Spaldin, *Nat. Mater* **6**, 21 (2007).

[100] N. A. Hill, *J. Phys. Chem. B* **104**, 6694 (2000).

[101] A. Stroppa, P. Jain, P. Barone, M. Marsman, J. M. Perez-Mato, A. K. Cheetham, H. W. Kroto, S. Picozzi, *Angew. Chem., Int. Ed. Engl.* **50**, 5847 (2011).

[102] L. C. Gómez-Aguirre, B. Pato-Doldán, A. Stroppa, S. Yáñez-Vilar, L. Bayarjargal, B. Winkler, S. Castro-García, J. Mira, M. Sánchez-Andújar, M. A. Señarís-Rodríguez, *Inorg. Chem.* **54**, 2109 (2015).

[103] I. Dzyaloshinsky, *J. Phys. Chem. Solids* **4**, 241 (1958).

[104] H. L. B. Boström, J. Bruckmoser, A. L. Goodwin, *J. Am. Chem. Soc.* **141**, 17978 (2019).

[105] A. L. Goodwin, M. T. Dove, M. G. Tucker, D. A. Keen, *Phys. Rev. B* **75**, 075423 (2007).

[106] T. A. Mary, J. S. O. Evans, T. Vogt, A. W. Sleight, *Science* **272**, 90 (1996).

[107] E. Shugam, H. Zhdanov, *Acta Physiochim. URSS* **20**, 247 (1945).

[108] J. W. Zwanziger, *Phys. Rev. B* **76**, 052102 (2007).

[109] P. Ding, E. J. Liang, Y. Jia, Z. Y. Du, *J. Condens. Matter Phys* **20**, 275224 (2008).

[110] M. Baise, Correlated disorder in coordination polymers, Ph.D. thesis, University College London (2020).

[111] A. P. Ramirez, A. Hayashi, R. J. Cava, R. Siddharthan, B. S. Shastry, *Nature* **399**, 333 (1999).

[112] S. Nishikiori, C. I. Ratcliffe, J. A. Ripmeester, *Can. J. Chem.* **68**, 2270 (1990).

[113] V. E. Fairbank, A. L. Thompson, R. I. Cooper, A. L. Goodwin, *Phys. Rev. B* **86**, 104113 (2012).

[114] C. S. Coates, C. A. Murray, H. L. B. Boström, E. M. Reynolds, A. L. Goodwin, *Mater. Horiz.* **8**, 1446 (2021).

[115] K. Yosida, *Theory of Magnetism: Edition en anglais*, Solid-State Sciences Series (Springer, 1996).

[116] D. R. Harcombe, P. G. Welch, P. Manuel, P. J. Saines, A. L. Goodwin, *Phys. Rev. B* **94**, 174429 (2016).

[117] L. Clark, G. Sala, D. D. Maharaj, M. B. Stone, K. S. Knight, M. T. F. Telling, X. Wang, X. Xu, J. Kim, Y. Li, S.-W. Cheong, B. D. Gaulin, *Nat. Phys.* **15**, 262 (2019).

[118] D. Bravo, F. J. López, *Phys. Rev. B* **58**, 39 (1998).

[119] Y. Xu, G.-L. Yang, D.-P. Chu, H.-R. Zhai, *Phys. Status Solidi B* **157**, 685 (1990).

[120] W. J. A. Blackmore, *et al.*, *New J. Phys.* **21**, 093025 (2019).

[121] A. Landart-Gereka, M. M. Quesada-Moreno, M. A. Palacios, I. F. Díaz-Ortega, H. Nojiri, M. Ozerov, J. Krzystek, E. Colacio, *Chem. Commun.* **59**, 952 (2023).

[122] D. A. Keen, R. L. McGreevy, *J. Condens. Matter Phys* **3**, 7383 (1991).

[123] S. Bhagavantam, P. V. Pantulu, *Proc. Natl. Acad. Sci. India A* **59**, 1 (1964).

[124] M. A. Ruderman, C. Kittel, *Phys. Rev.* **96**, 99 (1954).

[125] C. Kittel, *Phys. Rev.* **82**, 729 (1951).

[126] T. Kasuya, *Prog. Theor. Phys* **16**, 45 (1956).

[127] F. Bloch, *Z. Phys.* **61**, 206 (1930).

[128] A. N. Bogdanov, A. V. Zhuravlev, U. K. Rößler, *Phys. Rev. B* **75**, 094425 (2007).

[129] R. Carlin, *Magnetochemistry* (Springer Berlin Heidelberg, 1986).

[130] L. Onsager, *Phys. Rev.* **65**, 117 (1944).

[131] B. Kaufman, L. Onsager, *Phys. Rev.* **76**, 1244 (1949).

[132] E. W. Montroll, R. B. Potts, J. C. Ward, *J. Math. Phys.* **4**, 308 (1963).

[133] L. P. Kadanoff, *Il Nuovo Cimento B (1965-1970)* **44**, 276 (1966).

[134] D. C. Dender, P. R. Hammar, D. H. Reich, C. Broholm, G. Aeppli, *Phys. Rev. Lett.* **79**, 1750 (1997).

[135] S. A. Zvyagin, A. K. Kolezhuk, J. Krzystek, R. Feyerherm, *Phys. Rev. Lett.* **93**, 027201 (2004).

[136] L. Liu, Z. Chen, J. Wang, D. Zhang, Y. Zhu, S. Ling, K.-W. Huang, Y. Belmabkhout, K. Adil, Y. Zhang, B. Slater, M. Eddaoudi, Y. Han, *Nat. Chem* **11**, 622 (2019).

[137] A. Roy, D. Schuricht, J. Hauschild, F. Pollmann, H. Saleur, *Nucl. Phys. B.* **968**, 115445 (2021).

[138] F. D. M. Haldane, *Phys. Rev. Lett.* **50**, 1153 (1983).

[139] F. D. M. Haldane, *Phys. Lett. A* **93**, 464 (1983).

[140] H. Miyasaka, M. Julve, M. Yamashita, R. Clérac, *Inorg. Chem.* **48**, 3420 (2009).

[141] L. M. Toma, R. Lescouëzec, J. Pasán, C. Ruiz-Pérez, J. Vaissermann, J. Cano, R. Carrasco, W. Wernsdorfer, F. Lloret, M. Julve, *J. Am. Chem. Soc.* **128**, 4842 (2006).

[142] C. Coulon, H. Miyasaka, , R. Cl'erac, S.-C. M. T. Approach, E. S. I. R. Winpenny, *Single-Molecule Magnets and Related Phenomena. Structure and Bonding* **122** (Springer, Berlin, Heidelberg, 2006).

[143] R. J. Glauber, *J. Math. Phys.* **4** (1963).

[144] R. Cordery, S. Sarker, J. Tobochnik, *Phys. Rev. B* **24**, 5402 (1981).

[145] S. J. Blundell, *Magnetism in Condensed Matter* (Oxford University Press, Oxford, 2001).

[146] C. P. Landee, R. Kuentzler, , J. J. M. Williams, *J. Appl. Phys.* **67** (1990).

[147] N. D. Mermin, H. Wagner, *Phys. Rev. Lett.* **17**, 1133 (1966).

[148] S. S. P. Parkin, M. Hayashi, L. Thomas, *Science* **320**, 190 (2008).

[149] J. Li, A. Tan, K. W. Moon, A. Doran, M. A. Marcus, A. T. Young, E. Arenholz, S. Ma, R. F. Yang, C. Hwang, Z. Q. Qiu, *Appl. Phys. Lett.* **104**, 262409 (2014).

[150] F. Estellés-Duart, M. Ortuño, A. M. Somoza, V. M. Vinokur, A. Gurevich, *Sci. Rep.* **8**, 15460 (2018).

[151] K. Kanô, S. Naya, *Prog. Theor. Phys.* **10**, 158 (1953).

[152] J. A. M. Paddison, H. S. Ong, J. O. Hamp, P. Mukherjee, X. Bai, M. G. Tucker, N. P. Butch, C. Castelnovo, M. Mourigal, S. E. Dutton, *Nat. Commun* **7**, 13842 EP (2016).

[153] B. Sriram Shastry, B. Sutherland, *Physica B+C* **108**, 1069 (1981).

[154] R. Moessner, J. T. Chalker, *Phys. Rev. B* **58**, 12049 (1998).

[155] A. Honecker, J. Schulenburg, J. Richter, *J. Condens. Matter Phys* **16**, S749 (2004).

[156] G. H. Wannier, *Phys. Rev.* **79**, 357 (1950).

[157] J. Stephenson, *J. Math. Phys.* **11**, 413 (1970).

[158] J. L. Jacobsen, H. C. Fogedby, *Physica A* **246**, 563 (1997).

[159] Y. Shimizu, K. Miyagawa, K. Kanoda, M. Maesato, G. Saito, *Phys. Rev. Lett.* **91**, 107001 (2003).

[160] J. S. Helton, K. Matan, M. P. Shores, E. A. Nytko, B. M. Bartlett, Y. Yoshida, Y. Takano, A. Suslov, Y. Qiu, J.-H. Chung, D. G. Nocera, Y. S. Lee, *Phys. Rev. Lett.* **98**, 107204 (2007).

[161] R. J. C. Dixey, F. Orlandi, P. Manuel, P. Mukherjee, S. E. Dutton, P. J. Saines, *Philos. Trans. R. Soc. A* **377**, 20190007 (2019).

[162] R. J. C. Dixey, P. Manuel, F. Orlandi, P. Mukherjee, S. E. Dutton, G. B. G. Stenning, P. J. Saines, *J. Mater. Chem. C* **8**, 12123 (2020).

[163] S. Mühlbauer, B. Binz, F. Jonietz, C. Pfleiderer, A. Rosch, A. Neubauer, R. Georgii, P. Böni, *Science* **323**, 915 (2009).

[164] J. M. Hopkinson, H.-Y. Kee, *Phys. Rev. B* **75**, 064430 (2007).

[165] D. G. Franco, Y. Prots, C. Geibel, S. Seiro, *Phys. Rev. B* **96** (2017).

[166] T. E. Redpath, J. M. Hopkinson, *Phys. Rev. B* **82** (2010).

[167] F. Kneidinger, I. Zeiringer, A. Siderenko, E. Bauer, H. Michor, P. Rogl, J. G. Sereni, *Phys. Rev. B* **100** (2019).

[168] S. V. Isakov, J. M. Hopkinson, H.-Y. Kee, *Phys. Rev. B* **78**, 014404 (2008).

[169] R. Sibille, N. Gauthier, H. Yan, M. Ciomaga Hatnean, J. Ollivier, B. Winn, U. Filges, G. Balakrishnan, M. Kenzelmann, N. Shannon, T. Fennell, *Nat. Phys.* **14**, 711 (2018).

[170] P. W. Anderson, *Phys. Rev.* **102**, 1008 (1956).

[171] J. N. Reimers, A. J. Berlinsky, A.-C. Shi, *Phys. Rev. B* **43**, 865 (1991).

[172] S. T. Bramwell, M. J. Harris, *J. Condens. Matter Phys* **32**, 374010 (2020).

[173] M. J. Harris, S. T. Bramwell, D. F. McMorrow, T. Zeiske, K. W. Godfrey, *Phys. Rev. Lett.* **79**, 2554 (1997).

[174] S. T. Bramwell, M. J. Harris, *J. Condens. Matter Phys* **10**, L215 (1998).

[175] R. J. Baxter, *Exactly Solved Models in Statistical Mechanics* (Academic Press, London, 1982), third edn.

[176] T. Fennell, P. P. Deen, A. R. Wildes, K. Schmalzl, D. Prabhakaran, A. T. Boothroyd, R. J. Aldus, D. F. McMorrow, S. T. Bramwell, *Science* **326**, 415 (2009).

[177] E. Lhotel, L. D. C. Jaubert, P. C. W. Holdsworth, *J. Low Temp. Phys.* **201**, 710 (2020).

[178] E. Hückel, *Zur Theorie der Elektrolyte* (Springer Berlin Heidelberg, Berlin, Heidelberg, 1924), pp. 199–276.

[179] M. J. P. Gingras, P. A. McClarty, *Rep. Prog. Phys.* **77**, 056501 (2014).

[180] H. W. King, *J. Mater. Sci.* **1**, 79 (1966).

[181] J. W. Heaton, A. C. Rose-Innes, *J. Sci. Instrum.* **40**, 369 (1963).

[182] L. Vegard, *Physik* **5**, 17 (1921).

[183] A. R. Denton, N. W. Ashcroft, *Phys. Rev. A* **43**, 3161 (1991).

[184] M. Castellanos, A. R. West, *J. Chem. Soc., Faraday Trans. 1* **76**, 2159 (1980).

[185] H. Nakaishi, T. Yabutsuka, T. Yao, S. Kitao, M. Seto, W.-J. Chen, Y. Shimonishi, S. Yoshida, S. Takai, *Mater. Chem. Phys.* **303**, 127764 (2023).

[186] R. B. Griffiths, *Phys. Rev. Lett.* **23** (1969).

[187] A. J. Bray, *Phys. Rev. Lett.* **59**, 586 (1987).

[188] Z. Zhang, Y. Shao, B. Lotsch, Y.-S. Hu, H. Li, J. Janek, L. F. Nazar, C.-W. Nan, J. Maier, M. Armand, L. Chen, *Energy Environ. Sci.* **11**, 1945 (2018).

[189] Y. Liu, S. Qi, J. Fang, J. Sun, C. Liu, Y. Liu, J. Qi, Y. Xing, H. Liu, X. Lin, L. Wang, Q.-K. Xue, X. C. Xie, J. Wang, *Phys. Rev. Lett.* **127**, 137001 (2021).

[190] R. S. Silva, C. Santos, M. T. Escote, B. F. O. Costa, N. O. Moreno, S. P. A. Paz, R. S. Angélica, N. S. Ferreira, *Phys. Rev. B* **106**, 134439 (2022).

[191] M. Wortis, *Phys. Rev. B* **10**, 4665 (1974).

[192] S. Nagata, P. H. Keesom, H. R. Harrison, *Phys. Rev. B* **19**, 1633 (1979).

[193] N. D. Mackenzie, A. P. Young, *Lack of Ergodicity in the Infinite-Range Ising Spin-Glass* (WORLD SCIENTIFIC, 1986), vol. 9 of *World Scientific Lecture Notes in Physics*, pp. 185–188.

[194] G. Parisi, *Phys. Rev. Lett.* **50**, 1946 (1983).

[195] S. V. Syzranov, A. P. Ramirez, *Nat. Commun* **13**, 2993 (2022).

[196] M. V. Romitti, F. M. Zimmer, C. V. Morais, S. G. Magalhaes, *Phys. Rev. B* **99**, 014203 (2019).

[197] M. Dove, *Introduction to Lattice Dynamics*, Cambridge Topics in Mineral Physics and Chemistry (Cambridge University Press, 1993).

[198] B. N. Brockhouse, T. Arase, G. Caglioti, K. R. Rao, A. D. B. Woods, *Phys. Rev.* **128**, 1099 (1962).

[199] P. Shearer, *Introduction to Seismology* (Cambridge University Press, 2019).

[200] P. Debye, *Ann. Phys. (Berl.)* **344**, 789 (1912).

[201] G. Burns, B. A. Scott, *Phys. Rev. Lett.* **25**, 167 (1970).

[202] G. Shirane, J. D. Axe, J. Harada, J. P. Remeika, *Phys. Rev. B* **2**, 155 (1970).

[203] P. W. Anderson, *Phys. Rev.* **109**, 1492 (1958).

[204] J. Ziman, *Models of Disorder: The Theoretical Physics of Homogeneously Disordered Systems* (Cambridge University Press, 1979).

[205] Y. Liu, H. Xie, C. Fu, G. J. Snyder, X. Zhao, T. Zhu, *J. Mater. Chem. A* **3**, 22716 (2015).

[206] G. S. Nolas, J. Sharp, H. J. Goldsmid, *The Phonon—Glass Electron-Crystal Approach to Thermoelectric Materials Research* (Springer Berlin Heidelberg, Berlin, Heidelberg, 2001), pp. 177–207.

[207] D. G. Cahill, R. O. Pohl, *Solid State Commun.* **70**, 927 (1989).

[208] D. G. Cahill, S. K. Watson, R. O. Pohl, *Phys. Rev. B* **46**, 6131 (1992).

[209] K. Dychtoń, M. Drajewicz, M. Pytel, P. Rokicki, A. Nowotnik, *J. Therm. Anal. Calorim.* **126**, 1 (2016).

[210] M. R. Winter, D. R. Clarke, *Acta Mater.* **54**, 5051 (2006).

[211] F. Murphy-Armando, S. Fahy, *Phys. Rev. B* **78**, 035202 (2008).

[212] D. Walker, P. K. Verma, L. M. Cranswick, R. L. Jones, S. M. Clark, S. Buhre, *Am. Mineral.* **89**, 204 (2004).

[213] J. M. Ziman, *J. Phys. C: Solid State Phys.* **2**, 1230 (1969).

[214] A. R. Overy, A. B. Cairns, M. J. Cliffe, A. Simonov, M. G. Tucker, A. L. Goodwin, *Nat. Commun.* **7**, 10445 (2016).

[215] A. J. Wright, Q. Wang, Y.-T. Yeh, D. Zhang, M. Everett, J. Neuefeind, R. Chen, J. Luo, *Acta Mater.* **235**, 118056 (2022).

[216] P. G. Arnold, J. Popplewell, *Journal of Physics F: Metal Physics* **3**, 1985 (1973).

[217] J. M. Cowley, *Phys. Rev.* **77**, 669 (1950).

[218] J. R. Stewart, K. H. Andersen, R. Cywinski, *Phys. Rev. B* **78**, 014428 (2008).

[219] S. Mu, J. Yin, G. D. Samolyuk, S. Wimmer, Z. Pei, M. Eisenbach, S. Mankovsky, H. Ebert, G. M. Stocks, *Phys. Rev. Mater.* **3**, 014411 (2019).

[220] A. Silverman, A. Zunger, R. Kalish, J. Adler, *Phys. Rev. B* **51**, 10795 (1995).

[221] C. Wolverton, A. Zunger, *Phys. Rev. Lett.* **75**, 3162 (1995).

[222] B. J. Campbell, S. K. Sinha, R. Osborn, S. Rosenkranz, J. F. Mitchell, D. N. Argyriou, L. Vasiliu-Doloc, O. H. Seeck, J. W. Lynn, *Phys. Rev. B* **67**, 020409 (2003).

[223] K. Huang, N. F. Mott, *Proc. Math. Phys. Eng. Sci.* **190**, 102 (1947).

[224] U. T. Höchli, *Phys. Rev. Lett.* **48**, 1494 (1982).

[225] D. Yang, J. Gao, L. Shu, Y.-X. Liu, J. Yu, Y. Zhang, X. Wang, B.-P. Zhang, J.-F. Li, *J. Mater. Chem. A* **8**, 23724 (2020).

[226] A. von Hippel, *Rev. Mod. Phys.* **22**, 221 (1950).

[227] K. A. Müller, H. Burkard, *Phys. Rev. B* **19**, 3593 (1979).

[228] H. Takenaka, I. Grinberg, S. Liu, A. M. Rappe, *Nature* **546**, 391 (2017).

[229] M. Eremenko, V. Krayzman, A. Bosak, H. Y. Playford, K. W. Chapman, J. C. Woicik, B. Ravel, I. Levin, *Nat. Commun* **10**, 2728 (2019).

[230] V. A. Stephanovich, *Eur. Phys. J. B* **18**, 17 (2000).

[231] F. Li, S. Zhang, T. Yang, Z. Xu, N. Zhang, G. Liu, J. Wang, J. Wang, Z. Cheng, Z.-G. Ye, J. Luo, T. R. Shrout, L.-Q. Chen, *Nat. Commun* **7**, 13807 (2016).

[232] L. Yang, X. Kong, F. Li, H. Hao, Z. Cheng, H. Liu, J.-F. Li, S. Zhang, *Prog. Mater. Sci.* **102**, 72 (2019).

[233] G. Burns, F. H. Dacol, *Solid State Commun.* **48**, 853 (1983).

[234] R. A. Cowley, S. N. Gvasaliya, S. G. Lushnikov, B. Roessli, G. M. Rotaru, *Adv. Phys.* **60**, 229 (2011).

[235] D. Fu, H. Taniguchi, M. Itoh, S.-y. Koshihara, N. Yamamoto, S. Mori, *Phys. Rev. Lett.* **103**, 207601 (2009).

[236] G. Xu, G. Shirane, J. R. D. Copley, P. M. Gehring, *Phys. Rev. B* **69**, 064112 (2004).

[237] H. Hiraka, S.-H. Lee, P. M. Gehring, G. Xu, G. Shirane, *Phys. Rev. B* **70**, 184105 (2004).

[238] H. You, Q. M. Zhang, *Phys. Rev. Lett.* **79**, 3950 (1997).

[239] R. E. Cohen, *Nature* **441**, 941 (2006).

[240] P. M. Gehring, S.-E. Park, G. Shirane, *Phys. Rev. Lett.* **84**, 5216 (2000).

[241] A. Pramanick, S. Nayak, *J. Mater. Res.* **36**, 1015 (2021).

[242] M. E. Manley, J. W. Lynn, D. L. Abernathy, E. D. Specht, O. Delaire, A. R. Bishop, R. Sahul, J. D. Budai, *Nat. Commun* **5**, 3683 (2014).

[243] H. Hu, A. Strybulevych, J. H. Page, S. E. Skipetrov, B. A. van Tiggelen, *Nat. Phys.* **4**, 945 (2008).

[244] J. Hlinka, S. Kamba, J. Petzelt, J. Kulda, C. A. Randall, S. J. Zhang, *Phys. Rev. Lett.* **91**, 107602 (2003).

[245] J. O. Fossum, C. W. Garland, *Phys. Rev. Lett.* **60**, 592 (1988).

[246] J. M. Rowe, J. J. Rush, D. G. Hinks, S. Susman, *Phys. Rev. Lett.* **43**, 1158 (1979).

[247] A. Loidl, K. Knorr, R. Feile, J. K. Kjems, *Phys. Rev. Lett.* **51**, 1054 (1983).

[248] S. Bhattacharya, S. R. Nagel, L. Fleishman, S. Susman, *Phys. Rev. Lett.* **48**, 1267 (1982).

[249] B. D. Silverman, *Phys. Rev. Lett.* **20**, 443 (1968).

[250] P. G. de Gennes, *Solid State Commun.* **1**, 132 (1963).

[251] H. D. Zhou, S. T. Bramwell, J. G. Cheng, C. R. Wiebe, G. Li, L. Balicas, J. A. Bloxsom, H. J. Silverstein, J. S. Zhou, J. B. Goodenough, J. S. Gardner, *Nat. Commun.* **2** (2011).

[252] M. J. Gingras, B. C. den Hertog, *Can. J. Phys.* **79**, 1339 (2001).

[253] T. Fennell, O. A. Petrenko, B. Fåk, S. T. Bramwell, M. Enjalran, T. Yavors'kii, M. J. P. Gingras, R. G. Melko, G. Balakrishnan, *Phys. Rev. B* **70**, 134408 (2004).

[254] B. C. den Hertog, M. J. P. Gingras, *Phys. Rev. Lett.* **84**, 3430 (2000).

[255] B. Tomasello, C. Castelnovo, R. Moessner, J. Quintanilla, *Phys. Rev. B* **92**, 155120 (2015).

[256] S. Pakhira, C. Mazumdar, R. Ranganathan, M. Avdeev, *Sci. Rep.* **7**, 7367 (2017).

[257] A. Tomokiyo, H. Yayama, T. Hashimoto, T. Aomine, M. Nishida, S. Sakaguchi, *Cryogenics* **25**, 271 (1985).

[258] M. E. Zhitomirsky, *Phys. Rev. B* **67** (2003).

[259] D. Chiras, *The Solar House: Passive Heating and Cooling* (Chelsea Green Publishing, 2002).

[260] X. Moya, S. Kar-Narayan, N. D. Mathur, *Nat. Mater* **13**, 439 (2014).

[261] P. Atkins, J. De Paula, J. Keeler, *Atkins' Physical Chemistry* (Oxford University Press, 2018).

[262] C. Kittel, *Introduction to Solid State Physics* (Wiley, 2004).

[263] E. Gopal, *Specific Heats at Low Temperatures*, The International Cryogenics Monograph Series (Springer US, 2012).

[264] P. W. Anderson, *Science* **177**, 393 (1972).

[265] N. E. Phillips, J. P. Emerson, R. A. Fisher, J. E. Gordon, B. F. Woodfield, D. A. Wright, *Physica C* **235-240**, 1737 (1994).

[266] M. A. V. Heringer, D. L. Mariano, D. C. Freitas, E. Baggio-Saitovitch, M. A. Continentino, D. R. Sanchez, *Phys. Rev. Mater.* **4**, 064412 (2020).

[267] Y. Hattori, K. Fukamichi, K. Suzuki, H. Aruga-Katori, T. Goto, *J. Condens. Matter Phys* **7**, 4193 (1995).

[268] T. Liang, S. M. Koohpayeh, J. W. Krizan, T. M. McQueen, R. J. Cava, , N. P. Ong, *Nat. Commun.* **6** (2015).

[269] I. Grosu, T. L. Biter, *Phys. Lett. A* **382**, 3042 (2018).

[270] J. M. Schliesser, B. F. Woodfield, *Phys. Rev. B* **91**, 024109 (2015).

[271] S.-O. Vălu, E. De Bona, K. Popa, J.-C. Griveau, E. Colineau, R. J. M. Konings, *Sci. Rep.* **9**, 15082 (2019).

[272] P. Hidnert, W. Souder, *Thermal Expansion of Solids*, Circular of the National Bureau of Standards (U.S. Government Printing Office, 1950).

[273] B. T. M. Willis, C. J. Carlile, *Experimental Neutron Scattering* (Oxford University Press, Oxford, 2009).

[274] D. Sivia, *Elementary Scattering Theory: For X-ray and Neutron Users* (OUP Oxford, 2011).

[275] R. V. Reid, *Ann. Phys.* **50**, 411 (1968).

[276] R. M. Nicklow, R. M. Moon, S. Kawarazaki, N. Kunitomi, H. Suzuki, T. Ohtsuka, Y. Morii, *J. Appl. Phys.* **57**, 3784 (1985).

[277] J. A. M. Paddison, *Phys. Rev. Lett.* **125**, 247202 (2020).

[278] P. J. Brown, *International Tables for Crystallography* (Kluwer Academic Publishers, Dordrecht, 2004), vol. C, chap. Magnetic Form Factors, pp. 454–460.

[279] P. Debye, *Ann. Phys. (Berl.)* **348**, 49 (1913).

[280] I. A. Blech, B. L. Averbach, *Physics* **1**, 31 (1964).

[281] J. R. Stewart, R. Cywinski, *J. Condens. Matter Phys* **21**, 124216 (2009).

[282] O. Schärpf, *Physica B* **174**, 514 (1991).

[283] D. Richard, M. Ferrand, G. J. Kearley, *Large Array Manipulation Program (LAMP).*

[284] J. Rodríguez-Carvajal, *Physica B* **192**, 55 (1993).

[285] D. S. Kim, O. Hellman, N. Shulumba, C. N. Saunders, J. Y. Y. Lin, H. L. Smith, J. E. Herriman, J. L. Niedziela, D. L. Abernathy, C. W. Li, B. Fultz, *Phys. Rev. B* **102**, 174311 (2020).

[286] Y. Cheng, M. B. Stone, A. J. Ramirez-Cuesta, *Sci. Data* **10**, 54 (2023).

[287] B. E. Meijer, R. J. C. Dixey, F. Demmel, R. Perry, H. C. Walker, A. E. Phillips, *Phys. Chem. Chem. Phys.* **25**, 9282 (2023).

[288] K. Dymkowski, S. F. Parker, F. Fernandez-Alonso, S. Mukhopadhyay, *Physica B* **551**, 443 (2018).

[289] R. Fair, A. Jackson, D. Voneshen, D. Jochym, D. Le, K. Refson, T. Perring, *J. Appl. Crystallogr.* **55**, 1689 (2022).

[290] O. Arnold, *et al.*, *Nucl. Instrum. Methods. Phys. Res. B* **764**, 156 (2014).

[291] C. Paulsen, S. R. Giblin, E. Lhotel, D. Prabhakaran, K. Matsuhira, G. Balakrishnan, S. T. Bramwell, *Nat. Commun* **10**, 1509 (2019).

[292] M. E. J. Newman, G. T. Barkema, *Monte Carlo Methods in Statistical Physics* (Oxford University Press, Oxford, 1999).

[293] J. I. Facio, D. Betancourth, N. R. Cejas Bolecek, G. A. Jorge, P. Pedrazzini, V. F. Correa, P. S. Cornaglia, V. Vildosola, D. J. García, *J. Magn. Magn. Mater.* **407**, 406 (2016).

[294] H. Mori, H. Yashima, N. Sato, *J. Low Temp. Phys.* **58**, 513 (1985).

[295] R. Lora-Serrano, C. Giles, E. Granado, D. J. Garcia, E. Miranda, O. Agüero, L. Mendon ça Ferreira, J. G. S. Duque, P. G. Pagliuso, *Phys. Rev. B* **74**, 214404 (2006).

[296] A. Orchard, *Magnetochemistry* (Oxford University Press, Oxford, 2000).

[297] E. C. Heltemes, C. A. Swenson, *J. Chem. Phys.* **35**, 1264 (2004).

[298] T. Berlijn, G. Alvarez, D. S. Parker, R. P. Hermann, R. S. Fishman, *Phys. Rev. Res.* **3**, 033273 (2021).

[299] D. Neogy, A. Chatterji, *J. Chem. Phys.* **68**, 5647 (1978).

[300] D. Neogy, P. Paul, K. N. Chattopadhyay, *J. Magn. Magn. Mater.* **283**, 164 (2004).

[301] R. Tlili, A. Omri, M. Bekri, M. Bejar, E. Dhahri, E. K. Hlil, *J. Magn. Magn. Mater.* **399**, 143 (2016).

[302] S. Blundell, K. Blundell, *Concepts in Thermal Physics* (OUP Oxford, 2009).

[303] S. Eddahri, A. Razouk, M. Sajieddine, M. Sahlaoui, *Journal of Superconductivity and Novel Magnetism* **35**, 2397 (2022).

[304] K. Binder, *Phys. Rev. Lett.* **45**, 811 (1980).

[305] I. Kuprov, *EPR Newsletter* **23**, 10 (2013).

[306] I. Kuprov, *J. Magn. Reson.* **306**, 75 (2019).

[307] J. A. M. Paddison, A. L. Goodwin, *Phys. Rev. Lett.* **108**, 017204 (2012).

[308] A. A. Markov, *Dynamic Probabilistic Systems* (John Wiley and Sons, New York, 1971), vol. 1, chap. Appendix B.

[309] N. Metropolis, S. Ulam, *J. Am. Stat. Assoc.* **44**, 335 (1949).

[310] R. G. Melko, B. C. den Hertog, M. J. P. Gingras, *Phys. Rev. Lett.* **87**, 067203 (2001).

[311] U. Wolff, *Phys. Rev. Lett.* **62**, 361 (1989).

[312] R. G. Melko, M. J. P. Gingras, *J. Phys.: Condens. Matter* **16**, R1277 (2004).

[313] N. Metropolis, A. W. Rosenbluth, M. N. Rosenbluth, A. H. Teller, E. Teller, *J. Chem. Phys.* **21** (1953).

[314] Z. Wang, C. Holm, *J. Chem. Phys.* **115**, 6351 (2001).

[315] O. Dubay, G. Kresse, *Phys. Rev. B* **67**, 035401 (2003).

[316] J. D. Gale, *J. Chem. Soc., Faraday Trans.* **93**, 629 (1997).

[317] J. D. Gale, *J. Phys. Chem. B* **102**, 5423 (1998).

[318] P. P. Ewald, *Ann. Phys. (Berl.)* **369**, 253 (1921).

[319] R. A. Jackson, C. R. A. Catlow, *Mol. Simul.* **1**, 207 (1988).

[320] W. Press, *Numerical Recipes 3rd Edition: The Art of Scientific Computing*, Numerical Recipes: The Art of Scientific Computing (Cambridge University Press, 2007).

[321] D. F. Shanno, *Math. Comput.* **24**, 647 (1970).

[322] R. E. Schmunk, D. R. Winder, *J. Phys. Chem. Solids* **31**, 131 (1970).

[323] H. Schober, D. Strauch, K. Nutzel, B. Dorner, *J. Condens. Matter Phys* **5**, 6155 (1993).

[324] D. E. Williams, *Journal of Computational Chemistry* **22**, 1154 (2001).

[325] H. Fang, M. T. Dove, L. H. N. Rimmer, A. J. Misquitta, *Phys. Rev. B* **88**, 104306 (2013).

[326] F. Neese, F. Wennmohs, U. Becker, C. Riplinger, *J. Chem. Phys.* **152**, 224108 (2020).

[327] S. Grimme, S. Ehrlich, L. Goerigk, *Journal of Computational Chemistry* **32**, 1456 (2011).

[328] R. S. Mulliken, *J. Chem. Phys.* **23**, 1833 (1955).

[329] R. Bader, R. Bader, *Atoms in Molecules: A Quantum Theory*, International series of monographs on chemistry (Clarendon Press, 1990).

[330] A. J. Stone, *Journal of Chemical Theory and Computation* **1**, 1128 (2005).

[331] S. Thébaud, C. A. Polanco, L. Lindsay, T. Berlijn, *Phys. Rev. B* **102**, 094206 (2020).

[332] N. Roth, A. L. Goodwin, *Nat. Commun* **14**, 4328 (2023).

[333] D. Maspoch, D. Ruiz-Molina, K. Wurst, N. Domingo, M. Cavallini, F. Biscarini, J. Tejada, C. Rovira, J. Veciana, *Nat. Mater* **2**, 190 (2003).

[334] N. Roques, D. Maspoch, I. Imaz, A. Datcu, J.-P. Sutter, C. Rovira, J. Veciana, *Chem. Commun.* pp. 3160–3162 (2008).

[335] A. Datcu, N. Roques, V. Jubera, D. Maspoch, X. Fontrodona, K. Wurst, I. Imaz, G. Mouchaham, J.-P. Sutter, C. Rovira, J. Veciana, *Chem. Eur. J.* **18**, 152 (2012).

[336] E. Coronado, J. Ramón Galán-Mascarós, C. Martí-Gastaldo, *J. Mater. Chem.* **16**, 2685 (2006).

[337] F. Pointillart, C. Train, M. Gruselle, F. Villain, H. W. Schmalle, D. Talbot, P. Gredin, S. Decurtins, M. Verdaguer, *Chem. Mater.* **16**, 832 (2004).

[338] M. G. Yamada, H. Fujita, M. Oshikawa, *Phys. Rev. Lett.* **119**, 057202 (2017).

[339] A. Kitaev, *Ann. Phys.* **321**, 2 (2006).

[340] M. Clemente-León, E. Coronado, C. Martí-Gastaldo, F. M. Romero, *Chem. Soc. Rev.* **40**, 473 (2011).

[341] E. Burzurí, M. J. Martínez-Pérez, C. Martí-Gastaldo, M. Evangelisti, S. Mañas-Valero, E. Coronado, J. I. Martínez, J. R. Galan-Mascaros, F. Luis, *Chem. Sci.* **14**, 3899 (2023).

[342] M. G. Yamada, V. Dwivedi, M. Hermanns, *Phys. Rev. B* **96**, 155107 (2017).

[343] N. Marino, D. Armentano, G. De Munno, F. Lloret, J. Cano, M. Julve, *Dalton Trans.* **44**, 11040 (2015).

[344] M. Grzywa, R. Röß-Ohlenroth, C. Muschielok, H. Oberhofer, A. Błachowski, J. Żukrowski, D. Vieweg, H.-A. K. von Nidda, D. Volkmer, *Inorg. Chem.* **59**, 10501 (2020).

[345] J. G. Park, B. A. Collins, L. E. Darago, T. Runčevski, M. E. Ziebel, M. L. Aubrey, H. Z. H. Jiang, E. Velasquez, M. A. Green, J. D. Goodpaster, J. R. Long, *Nat. Chem* **13**, 594 (2021).

[346] J. G. Park, M. L. Aubrey, J. Oktawiec, K. Chakarawet, L. E. Darago, F. Grandjean, G. J. Long, J. R. Long, *J. Am. Chem. Soc.* **140**, 8526 (2018).

[347] F. Gándara, F. J. Uribe-Romo, D. K. Britt, H. Furukawa, L. Lei, R. Cheng, X. Duan, M. O'Keeffe, O. M. Yaghi, *Chem. Eur. J.* **18**, 10595 (2012).

[348] Y. Meng, Y.-C. Chen, Z.-M. Zhang, Z.-J. Lin, M.-L. Tong, *Inorg. Chem.* **53**, 9052 (2014).

[349] S.-J. Liu, C. Cao, S.-L. Yao, T.-F. Zheng, Z.-X. Wang, C. Liu, J.-S. Liao, J.-L. Chen, Y.-W. Li, H.-R. Wen, *Dalton Trans.* **46**, 64 (2017).

[350] M. Falsaperna, G. B. G. Stenning, I. da Silva, P. J. Saines, *J. Mater. Chem. C* **9**, 13209 (2021).

[351] G. Lorusso, J. W. Sharples, E. Palacios, O. Roubeau, E. K. Brechin, R. Sessoli, A. Rossin, F. Tuna, E. J. L. McInnes, D. Collison, M. Evangelisti, *Adv. Mater.* **25**, 4653 (2013).

[352] J.-P. Zhao, S.-D. Han, X. Jiang, J. Xu, Z. Chang, X.-H. Bu, *Chem. Commun.* **51**, 4627 (2015).

[353] K. Tustain, L. Farrar, W. Yao, P. Lightfoot, I. da Silva, M. T. F. Telling, L. Clark, *Inorg. Chem.* **58**, 11971 (2019).

[354] X. Ma, Z. Zhang, W. Shi, L. Li, J. Zou, P. Cheng, *Chem. Commun.* **50**, 6340 (2014).

[355] D. Tiana, C. H. Hendon, A. Walsh, *Chem. Commun.* **50**, 13990 (2014).

[356] M. Wang, X. Gou, W. Shi, P. Cheng, *Chem. Commun.* **55**, 11000 (2019).

[357] J. P. Renard, M. Verdaguer, L. P. Regnault, W. A. C. Erkelens, J. Rossat-Mignod, W. G. Stirling, *Europhysics Letters* **3**, 945 (1987).

[358] J. B. Goodenough, *J. Phys. Chem. Solids* **6**, 287 (1958).

[359] J. Kanamori, *J. Phys. Chem. Solids* **10**, 87 (1959).

[360] I. E. Collings, R. S. Manna, A. A. Tsirlin, M. Bykov, E. Bykova, M. Hanfland, P. Gegenwart, S. van Smaalen, L. Dubrovinsky, N. Dubrovinskaia, *Phys. Chem. Chem. Phys.* **20**, 24465 (2018).

[361] Z.-M. Wang, Y.-J. Zhang, T. Liu, M. Kurmoo, S. Gao, *Adv. Funct. Mater.* **17**, 1523 (2007).

[362] S. Chen, R. Shang, K.-L. Hu, Z.-M. Wang, S. Gao, *Inorg. Chem. Front.* **1**, 83 (2014).

[363] B. Liu, R. Shang, K.-L. Hu, Z.-M. Wang, S. Gao, *Inorg. Chem.* **51**, 13363 (2012).

[364] R. D. Pierce, S. A. Friedberg, *Phys. Rev.* **165**, 680 (1968).

[365] X. Wang, Z. Wang, S. Gao, *Sci. China Chem.* **55**, 1055 (2012).

[366] D. J. Goossens, A. R. Wildes, C. Ritter, T. J. Hicks, *J. Condens. Matter Phys* **12**, 1845 (2000).

[367] T. Moriya, *Phys. Rev.* **120**, 91 (1960).

[368] W. Wang, L. Q. Yan, J. Z. Cong, Y. L. Zhao, F. Wang, S. P. Shen, T. Zou, D. Zhang, S. G. Wang, X. F. Han, Y. Sun, *Sci. Rep.* **3**, 2024 (2013).

[369] H. L. B. Boström, *CrystEngComm* **22**, 961 (2020).

[370] J. M. Bulled, J. A. M. Paddison, A. Wildes, E. Lhotel, S. J. Cassidy, B. Pato-Doldán, L. C. Gómez-Aguirre, P. J. Saines, A. L. Goodwin, *Phys. Rev. Lett.* **128**, 177201 (2022).

[371] L. Savary, L. Balents, *Phys. Rev. Lett.* **118**, 087203 (2017).

[372] S. V. Isakov, K. Gregor, R. Moessner, S. L. Sondhi, *Phys. Rev. Lett.* **93**, 167204 (2004).

[373] J. A. M. Paddison, J. R. Stewart, A. L. Goodwin, *J. Phys.: Condens. Matter* **25**, 454220 (2013).

[374] M. Moliner, D. C. Cabra, A. Honecker, P. Pujol, F. Stauffer, *Phys. Rev. B* **79**, 144401 (2009).

[375] H. Kawamura, S. Miyashita, *J. Phys. Soc. Jpn.* **54** (1985).

[376] L. Seabra, T. Momoi, P. Sindzingre, N. Shannon, *Phys. Rev. B* **84** (2011).

[377] A. Kitanovski, J. Tušek, U. Tomc, U. Plaznik, M. Ožbolt, A. Poredoš, *Magnetocaloric Energy Conversion: From Theory to Applications*, Green Energy and Technology (Springer International Publishing, 2014).

[378] T. Numazawa, K. Kamiya, T. Okano, K. Matsumoto, *Physica B: Condensed Matter* **329-333**, 1656 (2003).

[379] P. Mukherjee, A. C. S. Hamilton, H. F. J. Glass, S. E. Dutton, *J. Phys.: Cond. Matt.* **29** (2017).

[380] C. Aprea, A. Greco, A. Maiorino, C. Masselli, *Energy* **190** (2020).

[381] A. Simonov, A. L. Goodwin, *Nat. Rev. Chem.* **4** (2020).

[382] J. Bulled, M. Falsaperna, P. Saines, A. Goodwin, Thermodynamic signatures of chain segmentation in dilute quasi-one dimensional ising systems (2022).

[383] T. R. Welberry, S. C. Mayo, *J. Appl. Cryst.* **29** (1996).

[384] J. W. Lynn, M. Iizumi, G. Shirane, S. A. Werner, R. B. Saillant, *Phys. Rev. B* **12** (1975).

[385] A. N. Bloch, D. O. Cowan, T. O. Poehler, *Design and Study of One-Dimensional Organic Conductors II: TTF —TCNQ and Other Organic Semimetals* (Springer US, Boston, MA, 1974), pp. 167–174.

[386] P. K. Kumari, S. Y. Park, *Phys. Rev. B* **106**, 125118 (2022).

[387] S. Furukawa, J. Wu, M. Koyama, K. Hayashi, N. Hoshino, T. Takeda, Y. Suzuki, J. Kawamata, M. Saito, T. Akutagawa, *Nat. Commun* **12**, 768 (2021).

[388] N. Teranishi, R. Kubo, *J. Phys. Soc. Jpn.* **47**, 720 (1979).

[389] K. Hamano, H. Sakata, H. Izumi, K. Yoneda, K. Ema, *Jpn. J. Appl. Phys.* **24**, 796 (1985).

[390] M. Orendáč, P. Farkašovský, L. Regeciová, S. Gabáni, G. Pristáš, E. Gažo, J. Bačkai, P. Diko, A. Dukhnenko, N. Shitsevalova, K. Siemensmeyer, K. Flachbart, *Phys. Rev. B* **102**, 174422 (2020).

[391] Z. Wang, L. Hu, L. Lin, Y. Han, N. Hao, J. Xu, Q. Chen, Z. Qu, *Sci. Rep.* **11**, 14442 (2021).

[392] A. B. Harris, *Phys. Rev. B* **12**, 203 (1975).

[393] B. M. McCoy, T. T. Wu, *Phys. Rev.* **176**, 631 (1968).

[394] H. S. Nair, A. A. El-Gendy, *Magnetic Nanostructured Materials*, A. A. El-Gendy, J. M. Barandiarán, R. L. Hadimani, eds., Micro and Nano Technologies (Elsevier, 2018), pp. 245–268.

[395] Y. ZHUANG, J. DENG, J. LI, Y. ZHAN, Q. ZHU, K. ZHOU, *Rare Metals* **26**, 97 (2007).

[396] T. H. Yang, W. S. Lin, X. T. Jia, M. H. Qin, J. M. Liu, *Physica A: Statistical Mechanics and its Applications* **410**, 253 (2014).

[397] Y. Hu, G. Wu, Y. Liu, X. Yang, , A. Du, *Magn. Magn. Mater* **337**, 46 (2013).

[398] H. Otsuka, *Phys. Rev. B* **92**, 134401 (2015).

[399] Y. Wang, H. De Sterck, R. G. Melko, *Phys. Rev. E* **85**, 036704 (2012).

[400] S.-H. Lee, C. Broholm, W. Ratcliff, G. Gasparovic, Q. Huang, T. H. Kim, S.-W. Cheong, *Nature* **418**, 856 (2002).

[401] X. Ke, R. S. Freitas, B. G. Ueland, G. C. Lau, M. L. Dahlberg, R. J. Cava, R. Moessner, P. Schiffer, *Phys. Rev. Lett.* **99**, 137203 (2007).

[402] T. Lin, X. Ke, M. Thesberg, P. Schiffer, R. G. Melko, M. J. P. Gingras, *Phys. Rev. B* **90**, 214433 (2014).

[403] G.-C. Xu, X.-M. Ma, L. Zhang, Z.-M. Wang, S. Gao, *J. Am. Chem. Soc.* **132**, 9588 (2010).

[404] D. Wu, Q. Zhou, K. K. Shung, S. N. Bharadwaja, D. Zhang, H. Zheng, *Journal of the American Ceramic Society* **92**, 1276 (2009).

[405] P. Timonin, *Low Temp. Phys.* **40** (2013).

[406] C. Djurberg, J. Mattsson, P. Nordblad, *J. Appl. Phys.* **75**, 5541 (1994).

[407] H. Manaka, S. Nagata, Y. Watanabe, K. Kikunaga, T. Yamamoto, N. Terada, K. Obara, *Journal of Physics: Conference Series* **145**, 012080 (2009).

[408] R. Shang, X. Sun, Z.-M. Wang, S. Gao, *Chem.: Asian J.* **7**, 1697 (2012).

[409] J.-P. Zhao, B.-W. Hu, F. Lloret, J. Tao, Q. Yang, X.-F. Zhang, X.-H. Bu, *Inorg. Chem.* **49**, 10390 (2010).

[410] M. Maczka, E. Kucharska, A. Gagor, A. Pikul, J. Hanuza, *J. Solid State Chem.* **258**, 163 (2018).

[411] K. L. Svane, A. C. Forse, C. P. Grey, G. Kieslich, A. K. Cheetham, A. Walsh, K. T. Butler, *J. Phys. Chem. Lett.* **8**, 6154 (2017).

[412] Y.-Y. Li, *Phys. Rev.* **101**, 1450 (1956).

[413] S. A. Serebrinsky, *Phys. Rev. E* **83**, 037701 (2011).

[414] A. B. Bortz, M. H. Kalos, J. L. Lebowitz, *Journal of Computational Physics* **17**, 10 (1975).

[415] M. Fiebig, T. Lottermoser, D. Meier, M. Trassin, *Nat. Rev. Mater.* **1**, 16046 (2016).

[416] C. S. Coates, M. Baise, J. M. Bulled, E. H. Wolpert, J. W. Makepeace, H. C. Walker, A. S. Gibbs, A. D. Fortes, B. Slater, A. L. Goodwin, *Structure and dynamics of the negative thermal expansion material $Cd(CN)_2$ under pressure* (2023). ArXiv:2302.09963.

[417] R. A. Cowley, *Adv. Phys.* **12**, 421 (1963).

[418] A. Erba, J. Maul, M. Ferrabone, P. Carbonnière, M. Rérat, R. Dovesi, *Journal of Chemical Theory and Computation* **15**, 3755 (2019).

[419] R. Mittal, S. L. Chaplot, H. Schober, T. A. Mary, *Phys. Rev. Lett.* **86**, 4692 (2001).

[420] M. G. Kibble, V. Laliena, C. M. Goodway, E. Lelièvre-Berna, K. V. Kamenev, S. Klotz, O. Kirichek, *Journal of Neutron Research* **21**, 105 (2019).

[421] M. D. Le, T. Guidi, R. Bewley, J. R. Stewart, E. M. Schooneveld, D. Raspino, D. E. Pooley, J. Boxall, K. F. Gascoyne, N. J. Rhodes, S. R. Moorby, D. J. Templeman, L. C. Afford, S. P. Waller, D. Zacek, R. C. R. Shaw, *Nuclear Instruments and Methods in Physics Research Section A: Accelerators, Spectrometers, Detectors and Associated Equipment* **1056**, 168646 (2023).

[422] T. R. Ravindran, A. K. Arora, T. A. Mary, *Phys. Rev. Lett.* **84**, 3879 (2000).

[423] R. Pecora, *Basic Concepts – Scattering and Time Correlation Functions* (2008), pp. 2–40.

[424] C. S. Coates, J. W. Makepeace, A. G. Seel, M. Baise, B. Slater, A. L. Goodwin, *Dalton Trans.* **47**, 7263 (2018).

[425] E. Courtens, *Phys. Rev. Lett.* **41**, 1171 (1978).

[426] B. I. Halperin, C. M. Varma, *Phys. Rev. B* **14**, 4030 (1976).

[427] A. Hallil, R. Tétot, F. Berthier, I. Braems, J. Creuze, *Phys. Rev. B* **73**, 165406 (2006).

[428] A. L. Goodwin, *Nat. Commun* **10**, 4461 (2019).

[429] V. V. Shvartsman, A. L. Kholkin, A. Orlova, D. Kiselev, A. A. Bogomolov, A. Sternberg, *Appl. Phys. Lett.* **86** (2005). 202907.

[430] P. Chen, L. Ponet, K. Lai, R. Cingolani, S. Artyukhin, *Npj Comput. Mater.* **6**, 48 (2020).

[431] X. Wu, U. Petralanda, L. Zheng, Y. Ren, R. Hu, S.-W. Cheong, S. Artyukhin, K. Lai, *Sci. Adv.* **3**, e1602371 (2017).

[432] X. Tian, X. Yan, G. Varnavides, Y. Yuan, D. S. Kim, C. J. Ciccarino, P. Anikeeva, M.-Y. Li, L.-J. Li, P. Narang, X. Pan, J. Miao, *Sci. Adv.* **7**, eabi6699 (2021).

[433] T. L. Hughes, H. Yao, X.-L. Qi, *Phys. Rev. B* **90**, 235123 (2014).

[434] R.-J. Slager, A. Mesaros, V. Juričić, J. Zaanen, *Phys. Rev. B* **90**, 241403 (2014).

[435] Y. Deng, W. A. Benalcazar, Z.-G. Chen, M. Oudich, G. Ma, Y. Jing, *Phys. Rev. Lett.* **128**, 174301 (2022).

[436] R. Ewings, R. Bewley, P. Galsworthy, 'mushroom feasibility report', *Tech. rep.*, ISIS Neutron and Muon Source (2021).

[437] M. Klausz, K. Kanaki, T. Kittelmann, R. Toft-Petersen, J. O. Birk, M. A. Olsen, P. Zagyvai, R. J. Hall-Wilton, *J. Appl. Crystallogr.* **54**, 263 (2021).

[438] O. Yaffe, Y. Guo, L. Z. Tan, D. A. Egger, T. Hull, C. C. Stoumpos, F. Zheng, T. F. Heinz, L. Kronik, M. G. Kanatzidis, J. S. Owen, A. M. Rappe, M. A. Pimenta, L. E. Brus, *Phys. Rev. Lett.* **118**, 136001 (2017).

[439] P. DiAntonio, B. E. Vugmeister, J. Toulouse, L. A. Boatner, *Phys. Rev. B* **47**, 5629 (1993).

[440] R. Farhi, M. El Marssi, A. Simon, J. Ravez, *Eur. Phys. J. B* **9**, 599 (1999).

[441] E. G. Meekel, A. L. Goodwin, *CrystEngComm* **23**, 2915 (2021).

[442] V. D. Neverov, A. E. Lukyanov, A. V. Krasavin, A. Vagov, M. D. Croitoru, *Commun. Phys.* **5**, 177 (2022).

[443] D. Chakraborty, T. Löfwander, M. Fogelström, A. M. Black-Schaffer, *npj Quantum Mater.* **7**, 44 (2022).

[444] M. T. Agne, T. Böger, T. Bernges, W. G. Zeier, *PRX Energy* **1**, 031002 (2022).

[445] V. L. Deringer, M. A. Caro, G. Csányi, *Adv. Mater.* **31**, 1902765 (2019).

Appendix

A 2D Triangular Ising Antiferromagnet

A.1 Local statistics

It will prove useful to know the proportion of spins which are 'flippable', *i.e.* surrounded by no net local field. Using a Monte Carlo simulation, we generate a 2D triangular ising antiferromagnet (TIA) (the groundstate of which is disordered [156]) from 20 samples of a 24×24 triangular lattice. Each sample was annealed to $T = 0.1J$, checking that the energy reaches its minimum in each case. A representative ground-state is shown in Fig. A1(a), and the distribution of local environments is shown in Fig. A1(b). We obtain

$$P^* = P(\langle S_i \cdot S_j \rangle = 0) = 0.2891 \pm 0.0032 \tag{A1}$$

as the fraction of Ising states which the local spin product is zero.

A.2 Residual Entropy

According to Wannier [156], we expect the zero point entropy per unit plane-area to be given by

$$S(0) = \frac{2k_{\mathrm{B}}}{\pi} \int_0^{\pi/2} \ln(2\cos\omega)\,\mathrm{d}\omega \simeq 0.3231 k_{\mathrm{B}}. \tag{A2}$$

However, in a bulk sample, we measure entropy per unit volume rather than by unit area. As such, in simulations this contribution to entropy is subextensive

$$S_{\mathrm{3D}}(0) = \frac{0.3231R}{L_z}, \tag{A3}$$

where L_z is the number of unit-cells along the chain axes. Note $S_{\mathrm{3D}}(0) \to 0$ as $L_z \to \infty$.

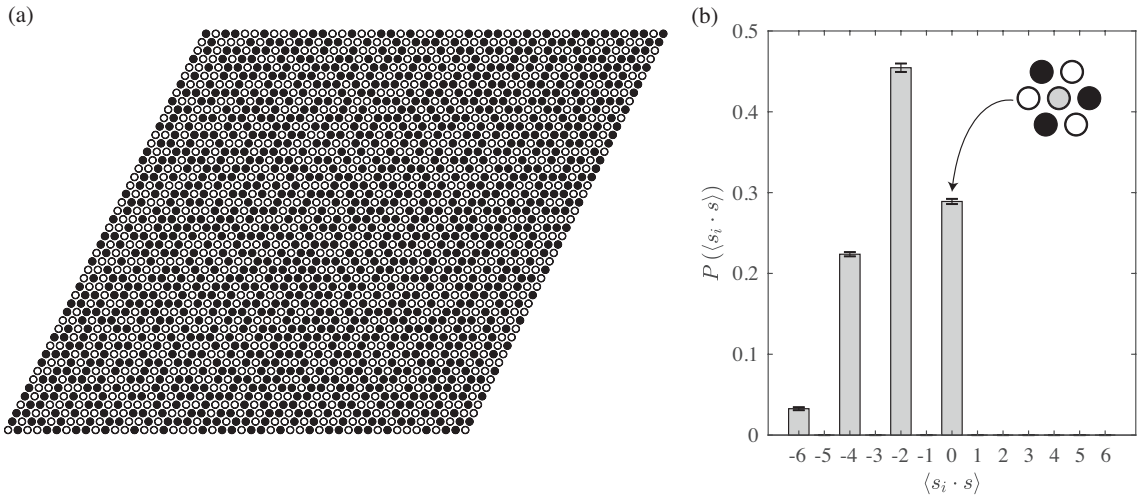

Figure A1: (a) An example TIA configuration as generated by our MC procedure. Each triplet of neighbouring spins sums to ± 1. (b) The distribution of local environments by their local spin product. The single type of local environment corresponding to $\langle S_i \cdot S_j \rangle = 0$ is shown.

B Additional details for $NaMn(HCOO)_3$

B.1 Normalisation of Neutron Diffraction to Nuclear Component

In order to obtain both quantities in absolute units, a scale factor was fitted to the nuclear scattering via a Rietveld refinement using FullProf [284]. Since the Q-space range available for refinement was small, the structure model (see Table B1) was fixed to that obtained in Ref. [89], although the cell parameter and various diffractometer constants were allowed to refine.

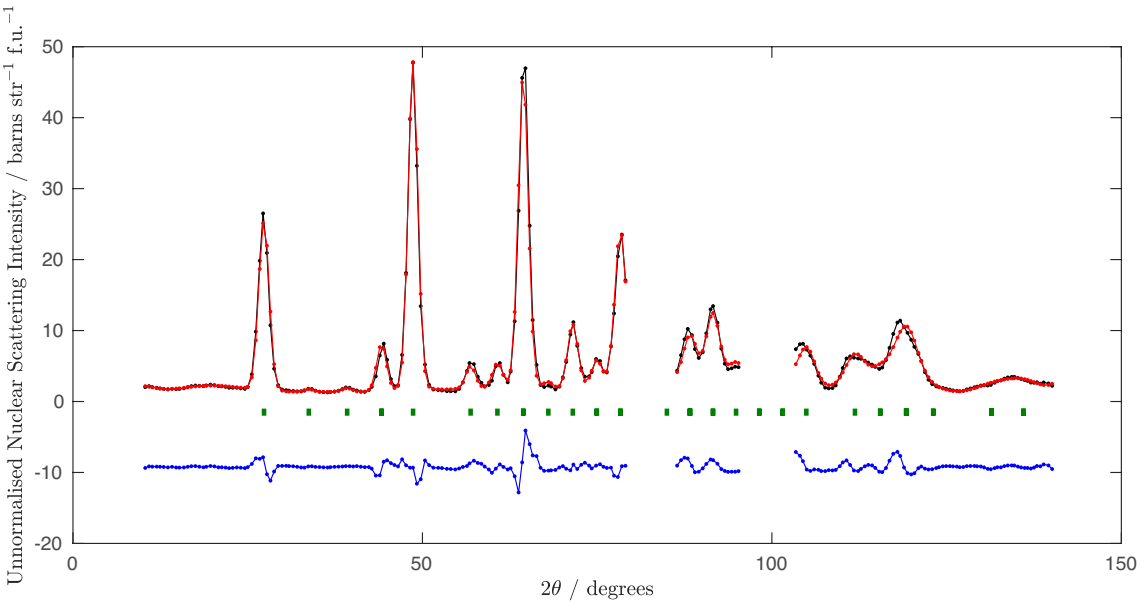

Figure B1: Nuclear neutron scattering function of $Na[Mn(HCOO)_3]$ measured at 1.5 K and corresponding Rietveld fit. Data, fit, and residuals are shown in black, red and blue respectively. Reflection positions are indicated with green tick-marks. Excluded regions surround Bragg peaks from the aluminium sample can. The neutron wavelength $\lambda = 3.1565$ Å.

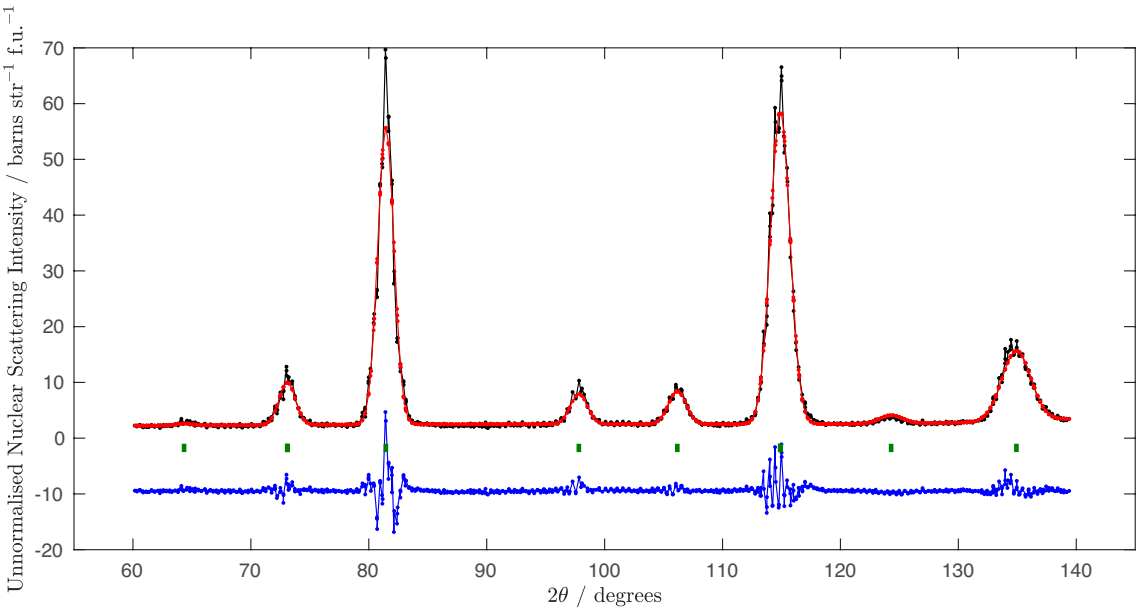

Figure B2: Nuclear neutron scattering function of Na[Mn(HCOO)$_3$] measured at 1.5 K and corresponding Rietveld fit. Data, fit, and residuals are shown in black, red and blue respectively. Reflection positions are indicated with green tick-marks. Excluded regions surround Bragg peaks from the aluminium sample can. The neutron wavelength $\lambda = 4.873$ Å.

Table B1: Atomic coordinates used in the Rietveld refinement of the D7 nuclear scattering data. Coordinates are given relative to the $P2_13$ cell described in Ref. [89] and were not refined in order to reduce the number of free parameters in our Rietveld model.

Atom	Wyckoff site	x	y	z
Mn1	4a	0.88377	0.38377	0.11623
Na1	4a	0.06361	0.06361	0.06361
O1	12b	0.66169	0.45580	0.17151
O2	12b	0.68170	0.53451	0.40118
C1	12b	0.61390	0.51400	0.28560
H1	12b	0.48859	0.54785	0.27599

Table B2: Crystallographic and instrument details determined from the refinement of the lower–wavelength D7 nuclear scattering data.

Empirical formula	$NaMnO_6C_3H_3$
Temperature / K	1.5
Wavelength / Å	3.1565
Space Group	$P2_13$
a / Å	9.310(1)
Number of Parameters	26
Number of background terms	18
Excluded regions	80.0°–85.5°
	96.0°–103.0°
R_f	1.96 %
Bragg R-factor	3.12 %
Scale Factor	0.02501(6)
	$U = 7.5(8)$
Half-width Parameters	$V = -7.7(1.0)$
	$W = 4.3(3)$

Table B3: Crystallographic and instrument details determined from the refinement of the higher–wavelength D7 nuclear scattering data.

Empirical formula	$NaMnO_6C_3H_3$
Temperature / K	1.5
Wavelength / Å	4.873
Space Group	$P2_13$
a / Å	9.13239(3)
Number of Parameters	16
Number of background terms	8
R_f	2.16 %
Bragg R-factor	3.13 %
Scale Factor	0.0655(3)
	$U = 2.37(6)$
Half-width Parameters	$V = -4.0580(9)$
	$W = 4.351(6)$

B.2 Simulation of magnetic ground-state

In order to find the magnetic ground state, simulated annealing was performed on both nnHAF and nnHAF+D Monte Carlo models at zero–field. We used 52 temperatures steps distributed logarithmically between 1.5 and 0.01 K. We show the final supercell configurations in Fig. B3. Fig. B4 shows spin–distribution functions calculated at various temperatures in this simulation.

Averages were performed over instances of the green magnetic unit cells shown in Fig. B3. In the case of the nnHAF model, this ground state exactly reproduces the 120 degree state reported in Refs. [164, 168]. We report the averaged ground state of the nnHAF+D model in Table B4.

Spin orientations in a representative solution to the magnetic ground-state of the nnHAF+D model are given in Table B4. In this particular case, the ordering wave-vectors are $\mathbf{k}_{\rm ord} = [\frac{1}{2}, 0, 0]$ and $[0, 0, \frac{1}{2}]$.

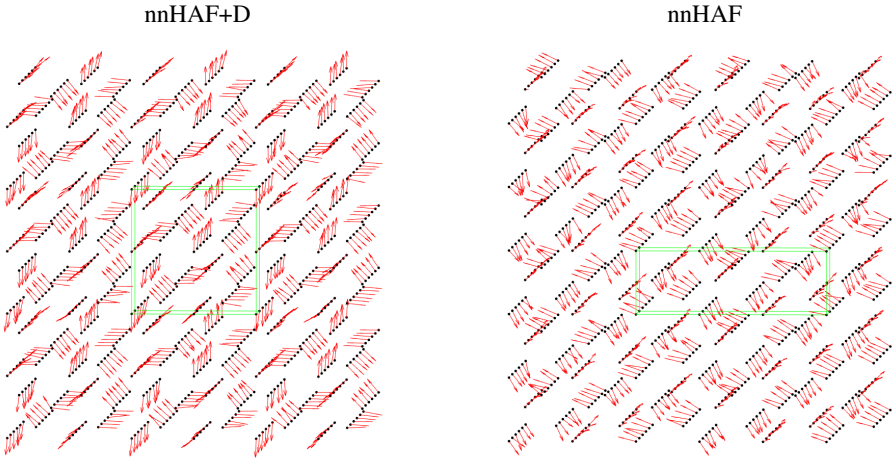

Figure B3: Ground–states (with Monte Carlo simulations annealed to $T = 0.01\,\mathrm{K}$) of zero-field ground–state in the nnHAF+D and nnHAF models. Green boxes show unit cells corresponding to the $\mathbf{k} = \{[1/2, 0, 0], [0, 1/2, 0]\}$ and $\mathbf{k} = [1/3, 0, 0]$ structures respectively.

Table B4: Representative spin orientations in the 2-$\mathbf{k}$ magnetic ground-state of the trillium nnHAF+D model, as determined using Monte Carlo simulations. Atom coordinates are given relative to a $2 \times 1 \times 2$ supercell of the $P2_13$ nuclear unit cell.

x	y	z	S_x	S_y	S_z
0.429355	0.641290	0.179355	0.9780	0.1916	0.0797
0.429355	0.641290	0.679355	0.5328	−0.3884	0.7469
0.929355	0.641290	0.179355	−0.6055	0.3698	−0.7019
0.929355	0.641290	0.679355	−0.9648	−0.1912	−0.0866
0.320645	0.358710	0.429355	0.0505	0.2092	−0.9682
0.320645	0.358710	0.929355	−0.7126	0.3854	0.5853
0.820645	0.358710	0.429355	0.7022	−0.4432	−0.5420
0.820645	0.358710	0.929355	−0.0146	−0.1679	0.9788
0.070645	0.141290	0.070645	0.9732	−0.2164	0.0695
0.070645	0.141290	0.570645	0.6439	0.3933	0.6526
0.570645	0.141290	0.070645	−0.5592	−0.3928	−0.7295
0.570645	0.141290	0.570645	−0.9638	0.1490	−0.1685
0.179355	0.858710	0.320645	−0.6762	−0.4103	0.6110
0.179355	0.858710	0.820645	0.0287	−0.1503	−0.9824
0.679355	0.858710	0.320645	−0.0496	0.2337	0.9668
0.679355	0.858710	0.820645	0.6887	0.3999	−0.6034

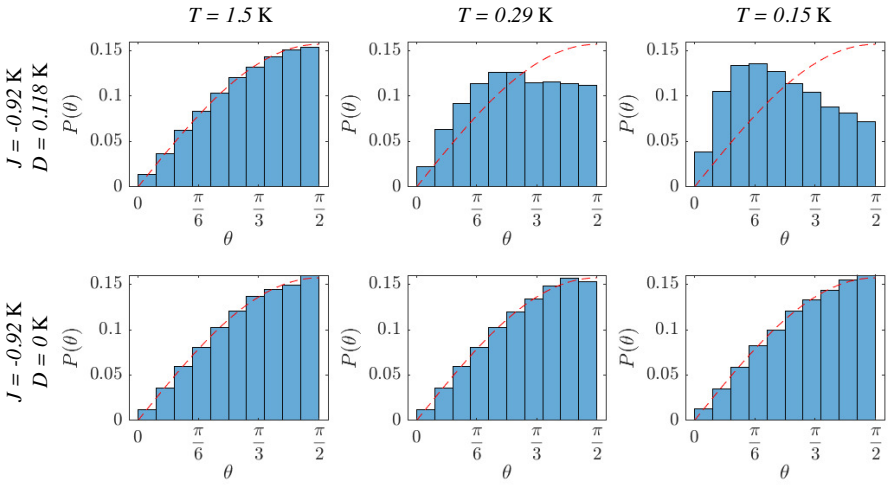

Figure B4: Distribution of polar angle, θ, between the unique axis (a local $\langle 111 \rangle$) and the spin vector. Distribution is averaged over 5 separate cooling cycles with 5 samples per cycle. The red dotted line shows the distribution expected for isotropic systems. At 1.5 K, neither model shows any anisotropy. As the model including a dipolar term is cooled near the ordering temperature, it develops anisotropy. This is evident above the ordering transition but becomes more clear below the ordering transition. The isotropic exchange–only model develops no anisotropy at any temperature.

B.3 Rebinning

For some of the figures (4.1 and 4.4 in the text), it was necessary to rebin the magnetisation data outputted from the simulation. In the case of the former figure, this was done via a gaussian kernal,

$$M_{\mathrm{new}}\left(T_{\mathrm{new}}\right) = \frac{\sum_i M_{i,\mathrm{old}} \exp\left[-\left(\frac{T_{i,\mathrm{old}}-T_{\mathrm{new}}}{\Delta T_{\mathrm{new}}}\right)^2\right]}{\sum_i \exp\left[-\left(\frac{T_{i,\mathrm{old}}-T_{\mathrm{new}}}{\Delta T_{\mathrm{new}}}\right)^2\right]}, \tag{B1}$$

such that the old T–grid was mapped onto a grid of evenly spaced points between 0.2 and 0.3 K. When calculating ΔS, rebinning is especially important, since errors accumulate when integrating. This is illustrated in figure B5.

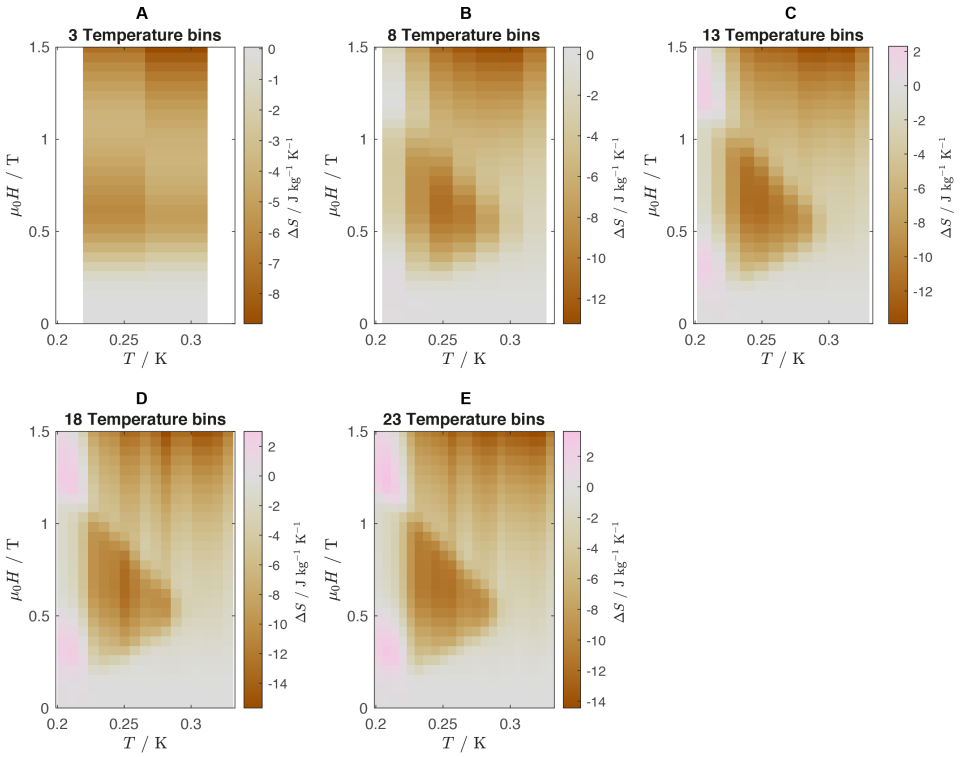

Figure B5: The effect of rebinning on magnetocaloric entropy change. Five versions of Fig. 3(e) of the main text are shown, each corresponding to different bin sizes. The key point of this comparison is to demonstrate that the most extreme value of ΔS_{mag} does not change appreciably with bin size. Since this quantity is calculated from an integral in the field direction, errors accumulate in this direction at high field, leading to the streaks seen in panels **D** and **E**. This artefact is mitigated by rebinning, but at the cost of resolution in the T-direction. It is also clear that this decrease in resolution leads to a decrease in the magnitude of ΔS_{mag}. A compromise is found at 13 temperature bins; this is the value used in the main text.